MASS TRANSFER FROM RISING MIXED GAS BUBBLE IN QUIESCENT LIQUID POOL OF SFR

By

ARJUN PRADEEP

ENGG02201504006

Indira Gandhi Centre for Atomic Research, Kalpakkam

A thesis submitted to the

Board of Studies in Engineering Sciences

In partial fulfillment of requirements

for the Degree of

DOCTOR OF PHILOSOPHY

of

HOMI BHABHA NATIONAL INSTITUTE

January, 2020

Homi Bhabha National Institute[1]

Recommendations of the Viva Voce Committee

As members of the Viva Voce Committee, we certify that we have read the dissertation prepared by Arjun Pradeep entitled "Mass transfer from rising mixed gas bubble in quiescent liquid pool of SFR" and recommend that it may be accepted as fulfilling the thesis requirement for the award of Degree of Doctor of Philosophy.

Chairman - Dr. K. Velusamy		**Date:** 25/6/2021
Guide/Convener - Dr. Anil Kumar Sharma		**Date:**25.06.2021
Examiner – Dr. B. Premachandran		**Date:** 25/6/2021
Member 1- Dr. D. Ponraju		**Date:** 25/6/2021
Member 2- Dr. Anish Kumar		**Date:** 25/6/21

Final approval and acceptance of this thesis is contingent upon the candidate's submission of the final copies of the thesis to HBNI.

I/We hereby certify that I/we have read this thesis prepared under my/our direction and recommend that it may be accepted as fulfilling the thesis requirement.

Date: 25-06-2021

Place: IGCAR - Kalpakkam

25.06.2021

Signature

Guide

[1] This page is to be included only for final submission after successful completion of viva voce.

STATEMENT BY AUTHOR

This dissertation has been submitted in partial fulfillment of requirements for an advanced degree at Homi Bhabha National Institute (HBNI) and is deposited in the library to be made available to borrowers under rules of the HBNI.

Brief quotations from this dissertation are allowable without special permission, provided that accurate acknowledgement of source is made. Requests for permission for extended quotation from or reproduction of this manuscript in whole or in part may be granted by the Competent Authority of HBNI when in his or her judgment the proposed use of the material is in the interests of scholarship. In all other instances, however, permission must be obtained from the author.

25/6/2021

Arjun Pradeep

DECLARATION

I, hereby declare that the investigation presented in the thesis has been carried out by me. The work is original and has not been submitted earlier as a whole or in part for a degree/diploma at this or any other Institution/University.

25/6/2021

Arjun Pradeep

List of Publications arising from the thesis

Journal

1. "Semiempirical model for wet scrubbing of bubble rising in liquid pool of sodium-cooled fast reactor", Arjun Pradeep, Anil Kumar Sharma, *Nuclear Engineering and Technology*, **2018**, *50(6)*, 849-853. https://doi.org/10.1016/j.net.2018.04.003

2. "Numerical investigation of single bubble dynamics in liquid sodium pool", Arjun Pradeep, Anil Kumar Sharma, *Sadhana*, **2019**, *44(3)*, 56. https://doi.org/10.1007/s12046-018-1041-5

3. "Numerical and experimental investigation of air-water system to simulate bubble dynamics in liquid sodium pool", Arjun Pradeep, Anil Kumar Sharma, M P Rajiniganth, N Malathi, M Sivaramakrishna, D Ponraju, B K Nashine, P Selvaraj, *Brazilian Journal of Chemical Engineering*, **2019**, *36(4)*, 1475-1485. https://dx.doi.org/10.1590/0104-6632.20190364s20190268

Chapters in books and lectures notes

1. Numerical investigation of single gas bubble rising in liquid column, Arjun Pradeep, Anil Kumar Sharma, D Ponraju, B K Nashine, P Selvaraj, *Advances in Fluid and Thermal Engineering. Lecture notes in Mechanical Engineering*, **2019**, Springer, Singapore. https://doi.org/10.1007/978-981-13-6416-7_3

Conferences

1. Numerical simulation of gas bubble rising in liquid pools of SFR, Arjun Pradeep, Anil Kumar Sharma, D Ponraju, B K Nashine, K Velusamy, P Selvaraj, G Srinivasan, *MSMNA-2015, Indo-UK workshop on Modelling and Simulation of safety and Materials for Nuclear Application*, **2015**, December 16-17, Anupuram, India.

2. Numerical modelling of inert gas bubble rising in liquid metal pool, Arjun Pradeep, Anil Kumar Sharma, D Ponraju, B K Nashine, *Proceedings of the 6th International*

and 43rd National Conference on Fluid Mechanics and Fluid Power, **2016**, December 15-17, MNNITA, Allahabad, U.P., India.

3. Bubble rise dynamics in water column, Arjun Pradeep, Anil Kumar Sharma, M P Rajiniganth, N Malathi, M Sivaramakrishna, D Ponraju, B K Nashine, P Selvaraj, *Proceedings of the 24th National and 2nd International ISHMT-ASTFE Heat and Mass Transfer Conference (IHMTC-2017)*, **2017**, December 27-30, Indian Institute of Technology Madras, Chennai, India.

   http://dx.doi.org/10.1615/IHMTC-2017.990

4. Aerosol removal efficiency of gravel bed scrubber, Arjun Pradeep, Anil Kumar Sharma, D Ponraju, B K Nashine, P Selvaraj, *Proceedings of the 7th International and 45th National Conference on Fluid Mechanics and Fluid Power*, **2018**, December 10-12, Indian Institute of Technology Bombay, Mumbai, India.

5. Aerosol penetration in submerged gravel bed scrubber, Arjun Pradeep, Anil Kumar Sharma, D Ponraju, B K Nashine, P Selvaraj, *The 7th Asian Symposium on Computational Heat Transfer and Fluid Flow-2019*, **2019**, September 3-7, Tokyo University of Science, Tokyo, Japan **(best paper award)**.

25/6/2021

Arjun Pradeep

Dedicated to my family

ACKNOWLEDGEMENTS

I wish to express my sincere gratitude to my guide Dr. Anil Kumar Sharma for his invaluable guidance, keen interest, motivation, continuous support and valuable suggestions during my research work. His patience, enthusiasm, and immense knowledge helped me throughout the time of my research and writing thesis.

I am very much grateful to Mrs. G. Punitha, Dr. D. Ponraju, Dr. B. K. Nashine and Dr. P. Selvaraj for motivation and encouragement.

I convey my sincere thanks to my Division colleagues Mr. K. E. Jebakumar, Mrs. G. Lydia, Mr. Sanjay Kumar Das for their kind help and wholehearted support.

It is my great privilege to acknowledge members of the doctoral committee: Dr. K. Velusamy (Chairman), Dr. D. Ponraju (Member) and Dr. Anish Kumar (Member) for their critical review and valuable comments.

I take this opportunity to sincerely acknowledge Dr. P. Selvaraj, Director FRTG and Dr. Arun Kumar Badhuri, Director IGCAR for allowing experiments in SED, FRTG, IGCAR and SED colleagues for helping in conduction of experiments.

Finally, I thank one and all who have helped me during research work.

25/6/2021

Arjun Pradeep

CONTENTS

LIST OF FIGURES

LIST OF TABLES

CHAPTER-7

BROAD CONCLUSIONS AND FUTURE SCOPE OF STUDY

Chapter-7: Broad conclusions and future scope of study

A semiempirical pool scrubbing model is developed to estimate the scrubbing efficiency of liquid pools in SFRs. This model is useful for in-vessel bubble transport radiological source term evaluation. The model evaluates scrubbing efficiencies of about 80 % for 1 μm sodium iodide aerosol sizes in SFR pool of 5 m height.

Three-dimensional numerical simulations are observed to simulate the realistic bubble dynamics than the two- dimensional simulations, with the limitation being increase in computational time. Similarity of bubble dynamics between water and sodium systems helps to reduce number of experiments in liquid sodium systems for in-vessel radiological source term evaluations in SFR.

To study the retention of iodine vapours during mixed gas bubble rising through water pool, an experimental facility (IBEX) is setup. Experiments carried out in IBEX showed increase of iodine retention in water with increase in water pool height. The study is useful in evaluating bubble transport radiological source term under fuel pin failure scenario in spent fuel storage bay of SFR.

Engineering scale model of a wet scrubber (SGBS) is setup to study the scrubbing efficiency of sodium fire aerosols during mixed gas bubble rising through water submerged gravel bed. Numerical simulations are also performed to evaluate aerosol removal efficiency in a submerged gravel bed scrubber. At low gas flow rates, semiempirical model underpredicts the removal efficiency for aerosols smaller than 10 μm; however, present CFD study predicts efficiencies above 90 % as observed during in-house experiments for the typical size range of sodium combustion aerosols (1-10 μm), hence, proving the suitability of SGBS as a passive device for sodium combustion aerosol removal.

The problems associated with bubble dynamics and mass transfer issues during bubble movements in the pools of nuclear industries have been dealt to date using a judicious mix of analytical correlations and few experiments. In short, though many studies are available in literature confining to analytical evolution of bubble dynamics and semiempirical correlations, scarce are the studies that focus on bubble dynamics in liquid pools by means of computational fluid dynamics. The present work is an attempt to fill the existing gap areas in this field of study. Here, the semiempirical model is developed to first understand the concept of pool scrubbing. This is followed by reliable simulation of bubble dynamics using OpenFOAM software and then validating the model with in-house experimental data. Finally similarity between water and sodium systems on bubble dynamics is carried out. Hence, a judicious mix of computational methodology with in-house experiments is presented in the thesis for simulating the pool scrubbing phenomena encountered in SFRs.

Future scope of work

The future works proposed based on the study are as follows:

1. Improvement of the semiempirical model for bubble dynamics with mass transfer towards evaluating the relative importance scrubbing efficiency for iodine in vapour (I_2) and aerosol (CsI, NaI) forms.

2. Iodine retention experiments can be extended in sodium pool to understand the bubble transport in-vessel source term in sodium pool.

3. Submerged gravel bed scrubber experiments can be carried out for higher gas flow rates and higher inlet aerosol concentrations to study its performance.

SUMMARY

The important issues associated with bubble dynamics and related mass transfer in pools of nuclear industries have been dealt to date using a judicious mix of analytical correlations and few experiments. Though many studies are available in literature confining to analytical evolution of bubble dynamics along with semiempirical correlations, scarce are the studies that focus on bubble dynamics in liquid pools by means of computational fluid dynamics (CFD).

The present work is an attempt to fill gap areas in the field of bubble scrubbing related safety studies in SFRs. Here, a semiempirical model is developed to first understand the concept of pool scrubbing. The main phenomena governing the removal of aerosol and vapours from rising bubbles are identified. This is followed by reliable numerical simulation of bubble dynamics using OpenFOAM software to verify the empirical correlations used in the pool scrubbing model. The interFoam solver of OpenFOAM, which uses volume of fluid (VOF) method to track the interface between gas and liquid phases, is used in the present study. We tested the solver in OpenFOAM 3.0.0 and validated the method against experimental results by simulating bubbles rising in stagnant 2-D, 2-D axisymmetric and 3-D liquid domains. The simulated terminal velocity and shapes of the rising bubble were found to agree well with the experimental results.

Custom made pulsating type conductance based sensor with enamel coated copper wire probes was tested in water medium to evaluate effect of bubble rise velocity on rise height and related uncertainties.

Finally similarity between water and sodium systems on bubble dynamics is brought out to simplify SFR safety studies. The understanding from CFD and experimental studies have been extended to analyze mass transfer/scrubbing of vapours and aerosols encountered in liquid pool of SFR systems. Hence, a judicious mix of computational methodology with in-house

experiments is presented in the thesis for simulating the pool scrubbing phenomena encountered in SFRs.

CHAPTER-1

INTRODUCTION

Chapter-1: Introduction

1.1 Background

SFRs as shown in fig. 1.1 are posed with advantages such as low pressure operation, high core power density, low containment design pressure, passive decay heat removal systems and few inherent safety features. However, it is also associated with certain disadvantages such as reactor core is not in most reactive configuration, reaction of liquid sodium with air, water and concrete and also difficulties for in-service inspection due to opaque nature of sodium.

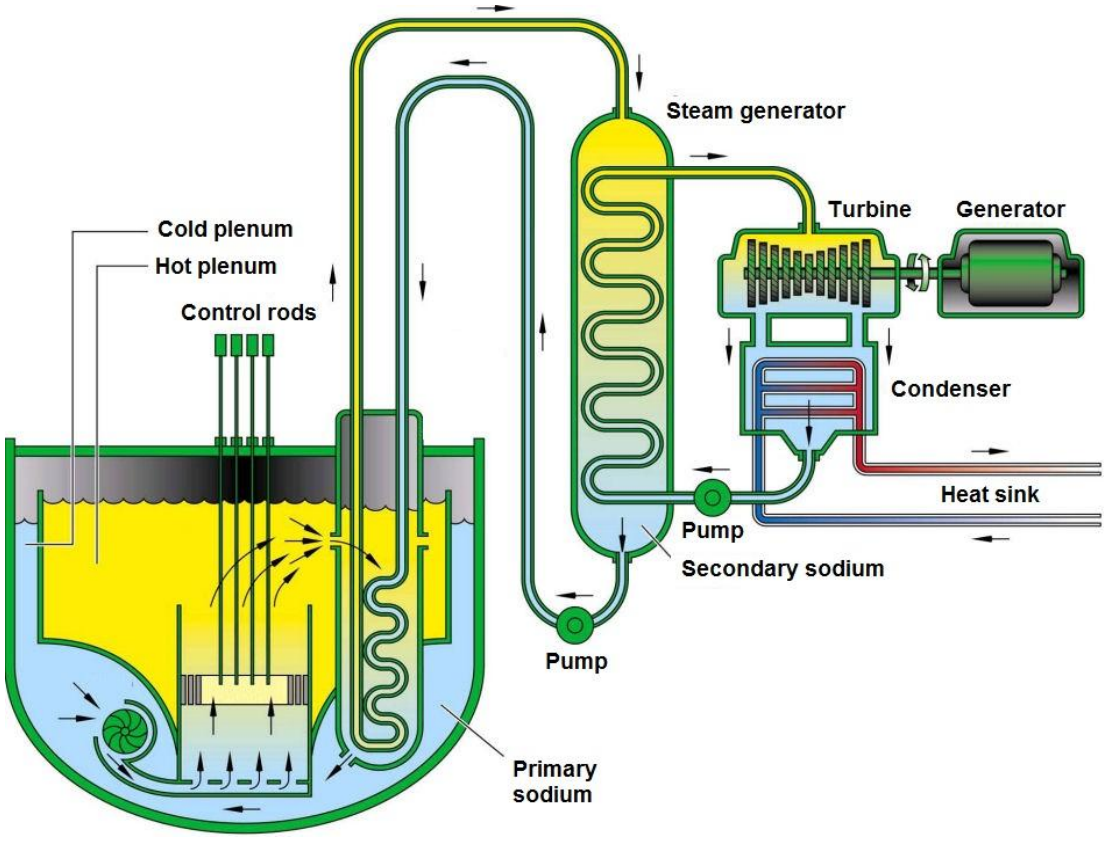

Fig.1.1 Sodium-cooled fast reactor (Lineberry and Allen, 2002)

The accidental sodium leakages and associated chemical reactions related incidents encountered in SFR plants to date resulted in losses of plant capacity factor and hence, reduced SFRs economic competitiveness compared to other nuclear reactors. Hence, to overcome these issues, it is essential for practically eliminating all the risks (associated with severe accidents, sodium fire etc.) posed to public and environment by incorporating related safety measures at the SFR design stage itself.

The history of SFR dates back from experimental breeder reactor (EBR)-1 commissioned in 1950 to its current position as the most developed generation (GEN) IV reactor design concept based on considerable operating experience gained in several countries. The categorization of reactors as various generations was carried out by generation IV international forum (GIF) setup in 2000, for which the technical secretariat is nuclear energy agency (NEA) of organization for economic coordination and development (OECD) and consisted of 14 member countries. The various generations of reactors as per the GIF classification are shown in table 1.1. A technology roadmap was laid down by GIF to improve SFR systems by incorporating features such as sustainability, safety and reliability, economic competitiveness, proliferation resistance and physical protection (PR&PP) in their design before the deployment of GEN IV reactors.

To ensure the GIF goal of sustainability in terms of energy i.e., availability of fuel and minimization of nuclear waste, a closed fuel cycle is opted for SFRs. The various options considered are advanced aqueous reprocessing for minor actinide (MA) bearing mixed (uranium-plutonium) oxide fuel and pyrometallurgical processing for mixed metal alloy (uranium-plutonium-MA-zirconium) as fuel. The licensing of GEN IV SFR systems also requires meeting of stringent safety and reliability goals in instrumentation and control for reducing the likelihood of reactor core damage and eliminating the need for offsite emergency response. The GIF goal of

economic competitiveness for SFR can be achieved by usage of advanced instrumentation (ultrasonics, robotics) for in-service inspection and repair (ISI&R), improved instrumentation for detection of sodium leaks, advanced energy conversion systems, increased fuel burnup, extended plant lifetime of 60 years and many more for reducing capital costs. The final GIF goal of PR&PP in SFR can be achieved by use of advanced separation technologies which include MAs and hence, making diversion unattractive. For achieving its goal areas, GIF is also working hands in hands with international atomic energy agency (IAEA) projects such as international project on innovative nuclear reactors and fuel cycles (INPRO) established in 2000 having 42 member countries towards making SFR a GEN IV reactor.

Table 1.1 Classification of nuclear reactors based on GIF (Horvath and Rachlew, 2016; Brady and MacKinlay, 2016; Findlay, 2010; Behar, 2014)

Reactor type	**GEN I (1955-1965)**	**GEN II (1965-1995)**	**GEN III (1995-2010)**	**GEN III+ (2010-2030)**	**GEN IV (>2030)**
PWR	Shippingport	Mihama 1	AP 600	AP 1000	SCWR
BWR	Dresden-1	Grand Gulf		ABWR	
SFR	Fermi-1				ASTRID, TWR
GCR	Calder Hall	AGR		PBMR	HTTR, HTR-10
PHWR	Douglas Point		CANDU 6	ACR 1000	
VVER	Kola 1-2	Kalinin			
RBMK		Kursk 1-4			
GFR					ALLEGRO, EM^2
LFR					ALFRED, ELSY
MSR					CMSR, LFTR

The generation IV international forum system research plan (SRP) considers four sodium-cooled fast reactor design concepts (Sagayama, 2017), i.e., loop option (Japan sodium-cooled fast reactor design track), pool option (Korea advanced liquid metal reactor design track), pool option

(European sodium fast reactor design track) and small modular option (AFR-100 design track). The safety work package of safety and operations project reviews and assesses passive/active safety, severe accident issues and identify additional research and development activities from safety issues. Till date, sodium-cooled fast reactors used deterministic, bounding assessments for radiological source term under severe accidents (non-energetic core melt accident and energetic hypothetical core disruptive accident), thus bringing out the requirement of mechanistic source term (MST) development as a key safety and operations project subject to be analyzed during the design stage towards obtaining generation IV status for the sodium-cooled fast reactor. Following 2011 accident at Fukushima Daiichi nuclear power station, CSNI, nuclear energy agency launched activities related to assessment of source term from spent fuel failure inside the storage bay water pool for addressing certain technical issues related to its mitigation. For the purposes of defense-in-depth (DiD) (Apostolakis *et al.*, 2011), the sodium-cooled fast reactor containments may be provided with additional barrier in terms of filtered containment venting systems (FCVSs) as a safety measure for energetic severe accident scenarios (hypothetical core disruptive accident).

1.2 Indian SFR program

Sodium-cooled fast reactor program started in India with the advent of fast breeder test reactor (FBTR) having an installed capacity of 40 MWt as shown in fig. 1.2. Figure 1.2 also shows the upcoming/under construction oxide and metal fuelled Indian SFRs designed by Indira gandhi centre for atomic research (IGCAR), department of atomic energy (DAE), along with their corresponding reprocessing facilities.

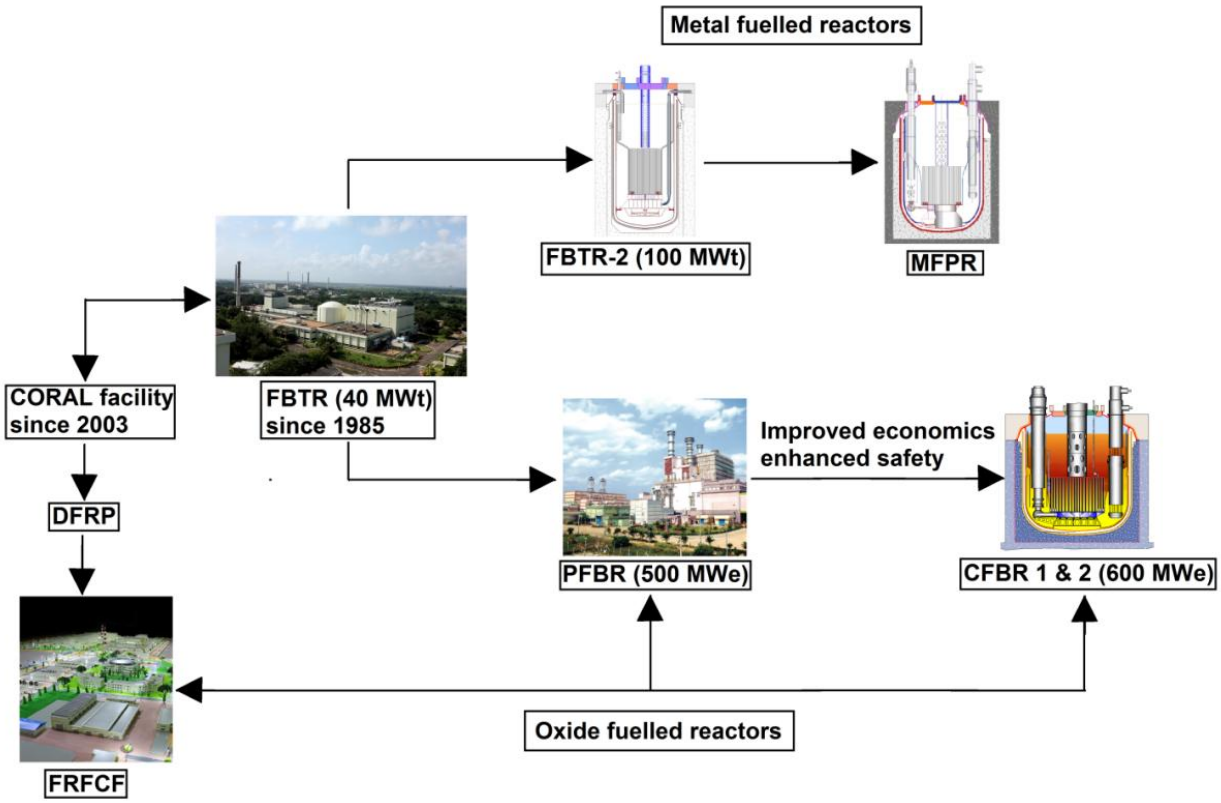

Fig.1.2 Indian SFR program (Puthiyavinayagam *et al*., 2018)

1.2.1 Fast breeder test reactor (FBTR)

FBTR is a sodium-cooled, loop type research reactor that operates using fast neutron fission of a unique plutonium rich mixed (Pu, U) carbide (MC) fuel. The reactor consists of several components, i.e., FSA, RA, IHX, SGs to produce super heated steam. The steam from the four SG modules is fed into turbine generator (TG) to produce electricity and further cooled by main/dump condensers. The final heat sink is a wet type induced cooling tower which dissipates the heat to atmosphere. The schematic of various sections viz., reactor vessel (RV), IHXs, primary and secondary sodium pumps, SGs, steam turbine and cooling tower in the flow diagram are shown in fig. 1.3. The RV is surrounded by a safety steel vessel and further by two types of concrete namely biological shield and structural concrete. The biological shield concrete is

cooled by circulating water through approximately 180 coils embedded in concrete. The primary sodium flows into the RV from bottom and comes out from the two outlet pipes located on the sides of RV.

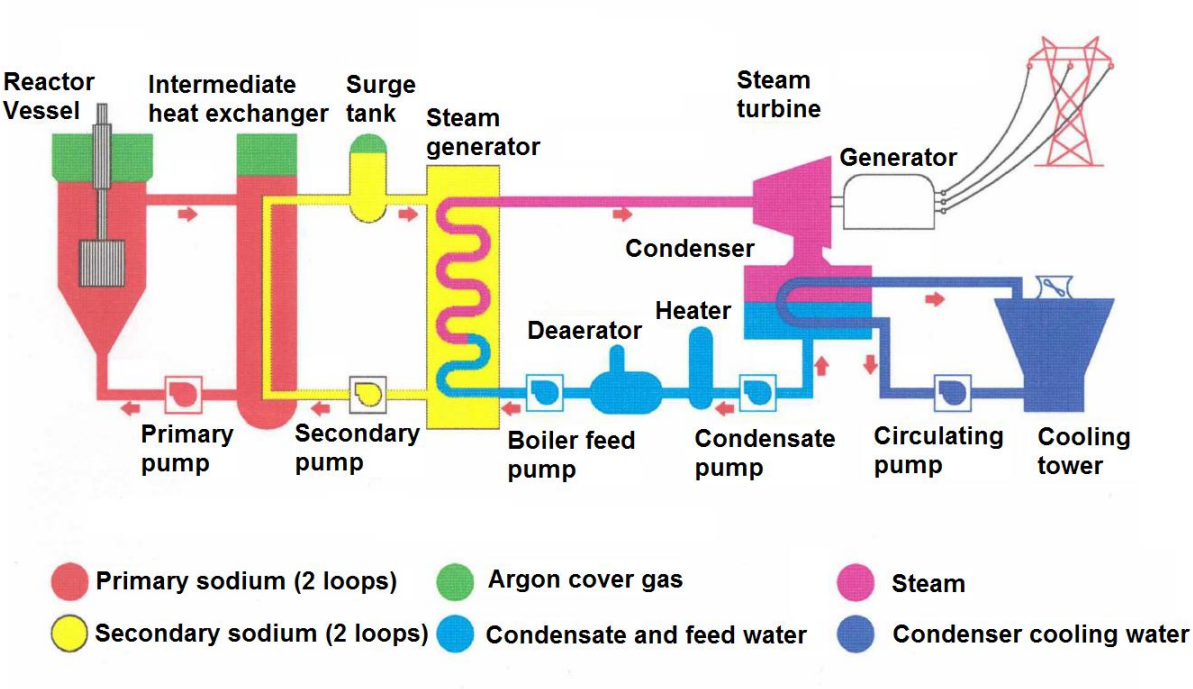

Fig.1.3 FBTR flow sheet (Srinivasan *et al*., 2007; Puthiyavinayagam *et al*., 2017)

The over flow tank in the primary circuit maintains sodium coolant at required level in reactor vessel. The primary sodium inlet temperature is maintained at 180 °C and ~380 °C during shutdown and high power operation respectively. Reactor vessel cover gas (RVCG) is a protective gas layer sandwiched between primary sodium in reactor vessel and top axial shield (Sarangapani *et al*., 2019) with a volume of 4 m^3. During reactor operation, a mixture of argon and helium is used as reactor vessel cover gas to maintain the reactor vessel temperature at radial locations within the acceptable levels. RVCG is maintained at a pressure of 30 mbar above the air pressure in reactor containment building (RCB) to prevent air ingress. The schematic reactor

assembly showing RV, core, cover gas, top axial shield, biological and structural shields etc. is shown in fig. 1.4.

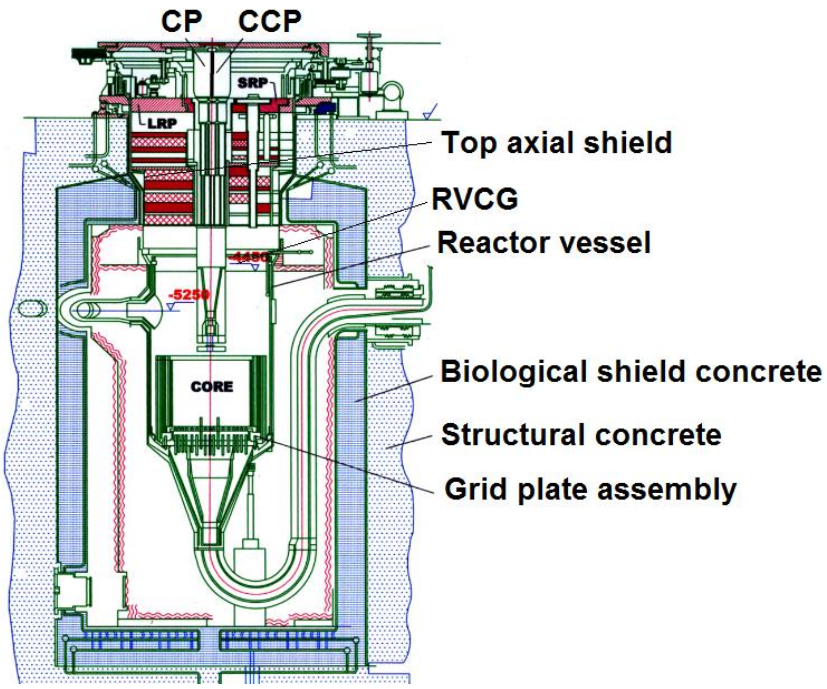

Fig.1.4 FBTR reactor assembly cross-section (Ashok *et al*., 2019)

1.2.2 Prototype fast breeder reactor (PFBR)

PFBR designed for a life of 40 years with a load factor of 75% has a NSSS composed of PSPs, IHX and SGs (Fig. 1.5). Steam water system adopts a regenerative reheat rankine cycle for thermal to mechanical energy conversion with 40% thermal to electric energy conversion efficiency. The SG is a once through type vertical shell and tube heat exchanger made of modified 9Cr-1Mo (grade 91, P91) with sodium on the shell side and water/steam on the tube side (Narayanan, 2018; Perumalsamy, 2019; Srinivas, 2019). The balance of plant components include LP, HP heaters and BFPs. Steam produced in SG at high pressure (170 bar) and temperature (495 °C) is supplied to the TG to produce electric power of 500 MWe. The

generator is directly coupled to turbine. The turbine is of tandem compound design with separate HP, IP and LP cylinders.

The PFBR sodium loops consists of main circuit, fill and drain, purification and allied circuits like argon and nitrogen. The entire sodium piping and its components are located in the RCB and steam generator buildings (SGB). Sodium piping in PFBR has SS 316LN/SS 304LN as material of construction (MOC). RCC confines the FPs leaked from fuel under hypothetical core disruptive accident (HCDA), so that dose limits are not exceeded. Decontamination facility is located inside RCB to avoid transport of highly active sodium wetted components prior to decontamination. Apart from RCB, PFBR also consists of FB, SGBs, building for rad-waste etc. The stack, 100 m tall, is located close to the rad-waste building. The condenser pump house is located offshore. The passive SGDHR composed of DHX, AHX and active OGDHR are the two DHRSs available in PFBR.

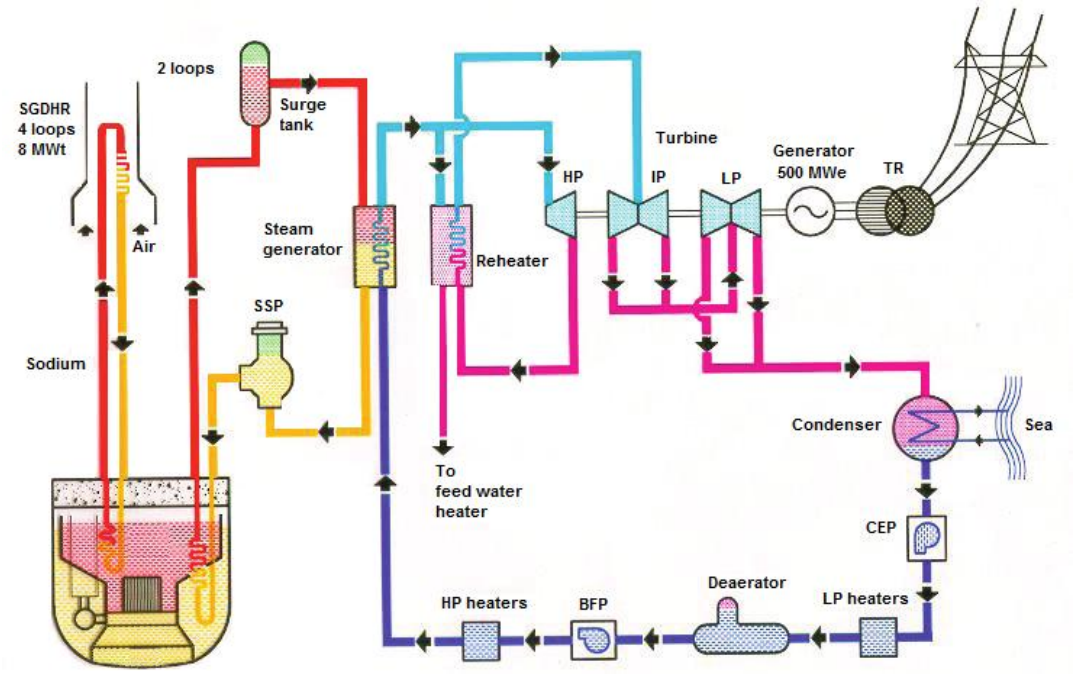

Fig.1.5 PFBR flow sheet of heat transfer circuit (Sarathy *et al*., 2004; Babu and Roy, 2017)

In SGDHR, the intermediate sodium and air flow are by natural circulation. Among the four loops, two loops run from the RCB to SGB-1 and the other two loops runs from the RCB to SGB-2. Each loop can remove 8 MWt when hot pool temperature is 803 K.

1.2.3 Commercial fast breeder reactor (CFBR)

Safety design criteria are evolving continuously internationally. Some of them are IAEA specific safety requirements (SSR)-2/1, western european nuclear regulators association (WENRA) and GEN IV. Accordingly safety design criteria for CFBR 1&2 have been evolved. Many innovative design features are introduced to achieve improved safety and significant cost reduction. The conceptual design of CFBR started in 2009 as a 500 MWe MOX fuelled SFR with enhanced safety and improved economic features compared to PFBR (500 MWe). The cross-sectional view of CFBR RA is given in fig. 1.6.

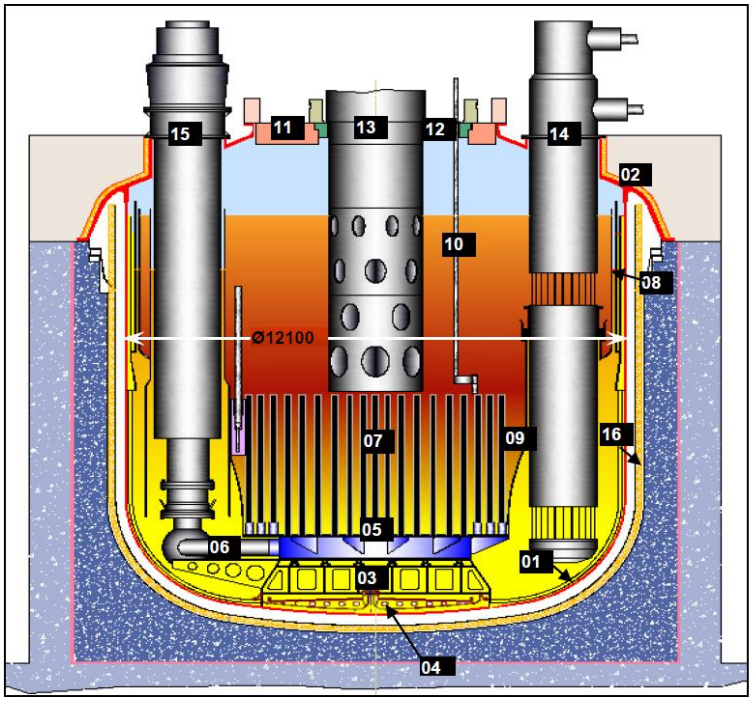

Sl. No	Components
01	Main Vessel
02	Roof Slab
03	Core Sup. Structure
04	Core Catcher
05	Grid Plate
06	Primary Pipe
07	Core
08	Thermal Baffle
09	Inner Vessel
10	Transfer Arm
11	LRP + Support
12	SRP + Support
13	Control Plug
14	IHX- 4 Nos.
15	Primary Pump- 2Nos.
16	Safety Vessel + Thermal Insulation

Fig.1.6 CFBR reactor assembly cross-section (Gupta *et al.*, 2013)

Based on the experience gained during design, manufacture and erection of PFBR components, detailed and exhaustive design optimization exercises were initiated. As an outcome of this exercise, several design features and improvements have been considered for incorporation in the design of CFBR 1&2 (Gupta *et al*., 2013; Puthiyavinayagam *et al*., 2017; Gupta *et al*., 2017; Selvaraj *et al*., 2017; Raghupathy *et al*., 2017; Azhagarason *et al*., 2017; Sundaran *et al*., 2017; Kale *et al*., 2018; Pawar *et al*., 2018; Raja, 2018; Krovvidi *et al*., 2018; Gnanasekaran *et al*., 2019; Bharasi *et al*., 2019; Chandran *et al*., 2019).

1.3 Project proposal

The use of inherent passive nature of SFR systems to reduce the consequences/risks of severe accidents, sodium fires etc. for public and environment is an important step in SFR design for enhancing safety and improving economic competitiveness of Indian SFR program. In an event of fuel failure accident including severe accidents in SFRs, FPs released from the failed fuel will be transported into cover gas region through liquid sodium of reactor MV. Among the FPs, release of VFPs (I, Cs) is very important for assessment of radiological consequences due to its high volatility, making them major contributors to public health hazard. In SFRs, the chemical form of released iodine would be primarily sodium iodide and cesium iodide, and that for Cs would be primarily Cs vapour but also CsNa and CsI. If the iodine and cesium are retained before release into cover gas region, health hazards of such an accident can be greatly reduced. Fortunately, the reaction of iodine and cesium solubility makes sodium as an important retention medium for VFPs in SFRs. The retention factor (*RF*) of VFPs in sodium for the PFBR design is considered based on deterministic release fractions values recommended by OECD/NEA to date. GEN IV SRP R&D for SFRs requires development of a mechanistic pool scrubbing model to evaluate the *RFs* of VFPs under sever accident scenarios.

In an event of fuel failure accident in SSSB of SFRs, FPs released from the failed fuel will be transported through water pool. The volatile fission products of primary importance are I-131, Cs-137 and Cs-134. Under postulated accident scenarios, the iodine would be primarily released as CsI aerosols and gaseous iodine, whereas Cs would be released as CsI, cesium molybdate and cesium hydroxide. The molybdenum in spent fuel would decrease the availability of cesium to form cesium iodide, and consequently, increase the gaseous iodine fraction. The cesium isotopes are likely to be the largest contributors to latent cancer fatalities and land contamination. In the case of fast breeder fuels, high burnups and short cooling times allows only a very limited reduction of the I-131 content by the time the fuel is moved to the spent fuel storage pool and hence I-131 can be an important contributor to early health effects, eventhough it has short half life. In case of fuel failure in SSSB, to the extent that iodine is released in elemental form along with noble gas bubbles, the dissolution of iodine in water towards its retention is an important data for SSSB design as few experimental studies exist till date.

Under a scenario of sodium fire in RCB during severe accident, RCB will be pressurized and contained with sodium combustion aerosols. The RCB wall dampers will be closed immediately within 60 s to prevent the venting of aerosols to the environment. Use of FCVSs in the RCB exhaust to capture sodium fire aerosols reduces the pressurization of RCB and release of aerosols in environment. This helps in reducing the containment wall thickness at design stage and hence, improves SFR economic performance and maintains adequate safety towards meeting GIF goals. PFBR incorporates HEPA, charcoal and delay beds in the RCB exhaust which are typically used as FCVS for water reactors. Hence, a low cost and simple prescrubber named submerged gravel bed scrubber (SGBS) is proposed for future Indian FBR RCB exhaust. FCVS designs to take

care of sodium fire aerosols with constant ventilation to reduce the capital cost of reactor containment building.

Answers to the above mentioned project goals can be obtained by carrying out a detailed research and development program on mass transfer from mixed gas bubble rising in quiescent liquid pool for SFR systems both theoretically and experimentally. The incorporation of such inherent passive features of SFR pools and passive FCVS in RCB exhaust system can improve the safety features of Indian SFR program, make SFR economically competitive and enhance its potential towards commercialization.

1.4 Scope of the study

Mass transfer from gas bubble rising in liquid pools finds applications in the suppression pools of nuclear reactors during severe accidents as discussed in previous sections. Figure 1.7 shows the scope of the study w.r.t to SFRs in the areas of reactor and SSSB, for which only few prototypic experimental and theoretical studies are available to date.

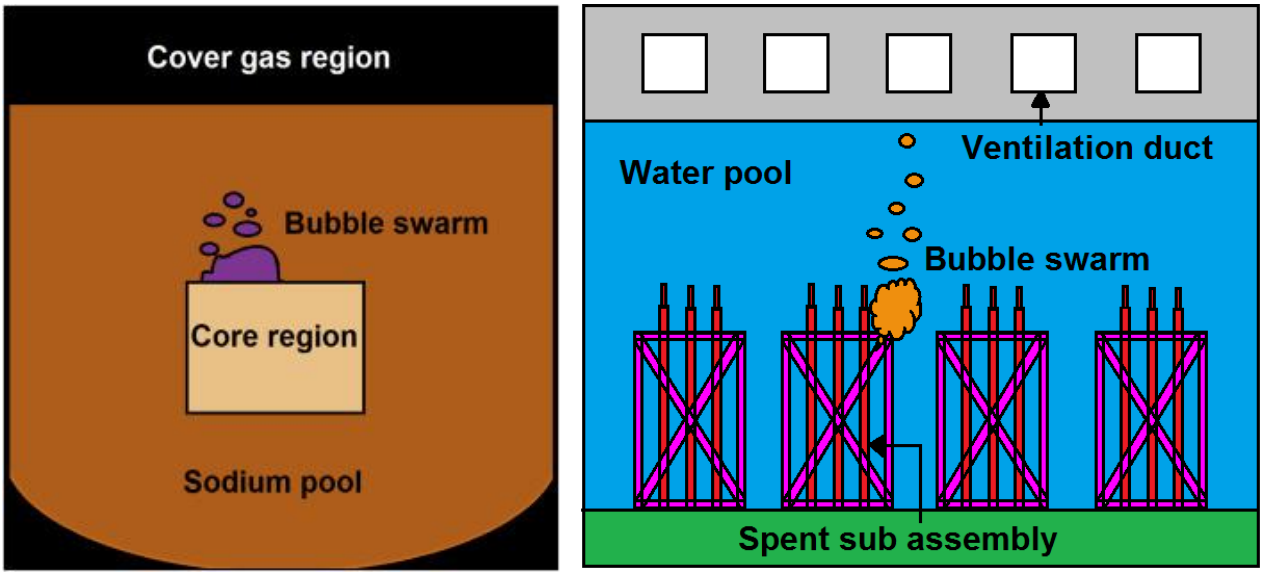

(a) (b)

Fig.1.7 Pool scrubbing during VFP bubble transport (a) reactor (b) SSSB

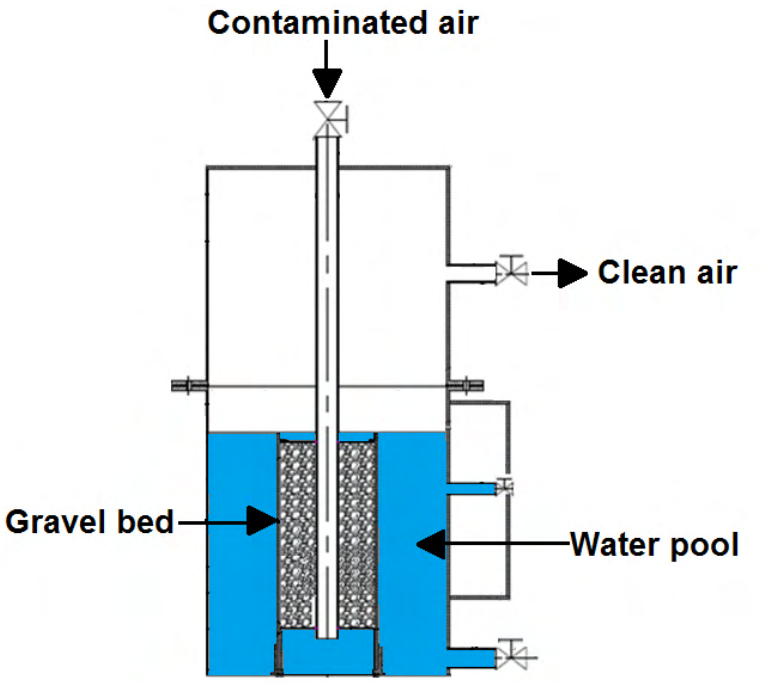

Fig.1.8 Pool scrubbing in EACS

Submerged graved bed scrubber (SGBS) as shown in fig. 1.8 is a passive emergency air cleaning system (EACS), which can be used to remove sodium fire aerosols from the gas during containment venting in SFRs. Scarce are the experimentally and theoretically available studies to evaluate the air cleaning efficiency of Submerged gravel bed scrubber.

Hence, the scrubbing of aerosol/vapour by liquid pools of SFR play vital role in its safe operation. Therefore, in this thesis, mass transport from rising bubble to liquid pools of SFR is studied systematically both theoretically and experimentally for better understanding of the phenomena. The study is carried out in two parts, (i) understanding the bubble dynamics and (ii) bubble dynamics with mass transfer. Both the interacting phenomena are analyzed in detail. Firstly, literature survey is carried out to find gap areas in the R&D project and to frame the objectives. The insight to the problem was given theoretically from the range of semiempirical correlations to numerical simulations. Finally the computational results are validated with in-house experiments towards predicting the phenomenon by well validated computational model.

1.5 Closure

This chapter briefs the SFR technology available worldwide with main focus on Indian program towards successful developments to achieve the second stage of nuclear program. Basic design and safety features were highlighted. Finally the objective of the thesis is brought out clearly after careful consideration of the existing literature. Next chapter is dedicated to the literature review related to area of research presented in the thesis.

CHAPTER-2

LITERATURE REVIEW

Chapter-2: Literature review

In this chapter detailed literature survey on mass transfer from mixed gas bubble rising in liquid pool of SFR is described.

2.1 Radionuclide bubble transport

Following fuel pin failure, gases (mostly noble gases) released from the fuel pin will create bubbles within the primary sodium. Some of the VFPs released from the fuel pin will become entrained within the bubbles as aerosols/vapours. As the bubble moves through the sodium, a fraction of these aerosols/vapours will be removed from the bubble. However, the fraction which will not be removed from the bubble will bypass the sodium pool and be released to the cover gas. Bubble transport is the most influential phenomenon/highest ranking gap area for assessment of transport and release of radionuclides from a reactor system to the environment under severe accident scenarios, since it provides a mechanism to bypass the sodium pool, a major radionuclide barrier, and has large uncertainties with little available data.

2.1.1 Review of experiments

Iodine bubble experiments were conducted at atomics international (AI) in 1962 to study the sorptive properties of liquid sodium at 260 °C and 537 °C for iodine. Capsules containing iodine were punctured at depths of 1.8 m and 3 m in a liquid sodium pool, nitrogen gas was used to sweep out the cover gas and passed through charcoal filter, and the filter was analyzed for iodine after the cover gas was displaced ~5 times. The amount of iodine retained in sodium varied from 98.5% for a total amount of 0.6 mg to about 99.9% for 60 mg (Begley, 1962; Kunkel, 1966). The capsules, were fabricated either of 39/29 ml tubing sealed by flat SS top and bottom sheets. To facilitate puncturing, the top sheet was of 0.1524 mm shim stock. The capsule was first purged

with nitrogen sweep gas through a 6.35 mm tube welded in the side, and preweighed iodine crystals were placed in the capsule. The nitrogen pressure in capsule was varied from 0-90 wt. %. The iodine nitrogen capsules were rigidly attached to rings which were in turn welded to a steel frame suspended in the test column. The test column consisted of a 101.6 mm diameter pipe, 3657.6 mm long, which included attached heaters, thermocouples, and insulation. A SS rod was operated through a sliding seal in the top plate. The bottom end of rod terminated in a conical plunger and was used to rupture the capsule lid and release N_2 + iodine gas to the sodium pool. The depth of sodium in the test column was 3048 mm and temperatures were maintained constant with controllers. The iodine N_2 mixture was released from one capsule at a time by driving the plunger through each thin capsule cap. The released gas traveled up through sodium column and entered the 609.6 mm deep cover gas region above the sodium pool. Before each capsule was ruptured, sweep gas flow was initiated. Neutron activation techniques utilized to determine the total iodine in the charcoal filters.

The earlier bubble experiment was repeated in 1965 with more realistic insertion of FP activity. The plenum simulator was a SS 304 cylinder, with 177.8 mm ID and 482.6 mm, inside height. A circular ring was welded in the center of the bottom plate to hold the irradiation capsule in the proper position. The irradiation capsule was also of SS, with a volume of 26 ml. A rupture disc mounted on top of the capsule was calibrated to rupture at 8.62 bar gauge pressure for ambient temperature and 5.1 bar gauge pressure at 260 °C. A 0.0381 mm thick disc of uranium metal (93% U-235) weighing 129 mg was supported on three pillars at the base of capsule. The capsule was evacuated inside a helium atmosphere chamber, purged with helium, and loaded with the fuel disc. There was no sodium inside the capsule in the experiment. Following the placement of the capsule in position, the lid of plenum simulation chamber was secured and plenum simulator

evacuated and purged with helium several times. The temperature was then raised to 204 °C and 4.53 kg of liquid sodium was introduced from the fill chamber. The temperature of the plenum simulator was next stabilized at 537 °C for 2 hr, the flow of helium over the top of the chamber was established at 0.2 lpm, and the firing chamber loaded with argon gas. The rupture disc was opened by 6.89 bar gauge pressure, as was noted by a sudden decrease on the pressure gauge affixed to the firing chamber. Following the initial burst of rupture disc, the firing chamber was again charged with argon, and this was introduced to the small capsule. Temperature of sodium in the plenum simulator was maintained at 537 °C for 2.5 hour, at which time the off gas sampling stream was diverted from both the May pack and the diffusion tube sampler, and the valve closed preparatory to removing filter components and diffusion tube samples for gamma spectrometric analysis. At the end of sampling period, the temperature of sodium in the plenum simulator was lowered to 204 °C, and as the sodium was drained from bottom of the simulator tank, samples of the sodium were taken for analysis. Ten samples of sodium were obtained varying in weight ranging from 7-13 g sodium. The May pack components were disassembled, and each filter disc removed for radioactivity analysis. Similarly, the diffusion tube sampling network was disassembled and the tubes were sectioned into approximately ten samples, for gamma counting. The original inventory of fuel disc at the time of rupture is estimated to be 48 μCi of I-131 and 2.6 μCi of Xe-133. By relating the approximate limit of I-131 detected in sodium by chemical separation and gamma spectrometry to the amount in the cover gas, a retention factor of 85% was obtained (Kunkel, 1966; Atomics International, 1965).

Based on half size SFR model studies with air bubbles in water at Hanford engineering development laboratory (HEDL), Dickinson and Nunamaker (1975) projected the bubble diameter and behaviour of fission gas discharged from SFR FSAs into sodium pool upon

potential Loss of Clad Integrity (prototype). The scaling for appropriately simulating bubble behaviour in sodium by a water test was achieved by matching the model's Froude and Weber numbers to those of the prototype at the same time. The diameter of the bubble would then be scaled in the same way as the other linear dimensions. In the test model, a scale factor of 0.512 was chosen rather than the optimum 0.625 to allow for the use of readily available lucite tubing for the chimney and to save vertical space. Tests were performed with water in a 0.51 scale model to determine the bubble sizes and degree of contact of liquid and gas in the clinch river breeder reactor (CRBR) outlet plenum following a hypothetical large sudden release of fission gas from the fuel. The test assembly simulated the tops of six FSAs encircling a control rod, as well as the chimney above them and the free area in the outlet plenum up to the suppressor plate. By rapidly opening a valve from a pressurized storage reservoir, a known volume of gas was introduced. The number of FSAs with gas release (1 and 6), liquid flow rate (modelling 0, 10, and 50% CRBR flow), volume of gas released (modelling 40 and 100 percent of end-of-life gas inventory) and the speed of gas release (less than 1 s and 8 s) were all investigated. All of the settings examined showed effective breakdown of the gas discharged into tiny bubbles. Gas was spread in a cloud of bubbles with a typical diameter of 6.35 mm between the fuel outlets and the bottom of the chimney. The bubbles collected into a dense cloud, froth, or, in some circumstances, a continuous cylinder of gas as they made their way up the chimney. The gas erupted from the top of the chimney in a column of either extremely concentrated bubbles or pure gas, often with powerful pulsations that resulted in gigantic surges or bubbles with a diameter slightly larger than the chimney's diameter. Discrete bubbles are difficult to recognize and quantify in the area below the chimney, however they do not appear to be larger than 6.35 mm with few exceptions. Individual bubbles following breakup were visible in the area above

the chimney. The largest visible bubbles have diameters of ~7.62 mm, while most are 5.08 mm or smaller. In the top of plenum, the one largest bubble is 20.32 mm diameter, a few others are 7.62-12.7 mm, and the great majority is in neighborhood of 5.08 mm. To apply to sodium in CRBR, the bubble sizes seen in this test should be scaled up by a factor of two. As a result, nearly all of the fission gas created in CRBR would travel through the sodium pool in bubbles of 12.7 mm diameter or smaller under the conditions tested. The authors also indicated that rather of using observed bubble sizes in conjunction with independent studies of iodine removal from single quiescent bubbles, it might be able to establish the degree of iodine removal expected in SFR solely from gas release studies.

Nelson *et al*. (1976) conducted an experiment to determine the decontamination factor (DF), which is defined as the ratio of the initial iodine mass in the mixed gas bubble to the discharged mass into the cover gas. The experimental settings, on the other hand, were restricted to areas with smaller bubble sizes, lower sodium temperatures and larger concentrations.

Based on the 1/2" (12.7 mm) bubble diameter predicted at HEDL, series of tests were conducted at AI (1976) to determine attenuation factor (*AF*) as a function of pool depth for elemental iodine within a bubble of mixed xenon and krypton rising in sodium. *AF*/*DF* was evaluated as the product of constant initial attenuation (10) and rise time dependent specific attenuation. A series of tests were conducted to determine the attenuation of elemental iodine within a bubble of mixed xenon and krypton rising in sodium. The test apparatus consisted of a pressure vessel of 430 mm diameter by 1800 mm high. The vessel was filled with 145 kg of sodium, providing a 1400 mm high sodium column. The simulant fission gas mixture (xenon, krypton, and iodine) was introduced into a separate 5 liter reservoir. The concentration of gaseous iodine in this externally heated reservoir was maintained constant by the vapour pressure of iodine at 154 °C.

The test vessel was modified to accept various test nozzles and provided with a bubble collection apparatus. The bubble generator, which was connected to xenon, krypton, and iodine reservoir, consisted of a section of 6.4 mm OD tubing with a 6.4, 12.7, or a 38 mm diameter nozzle attached. As the bubbles were generated, simultaneous sampling of the cover gas collection volume was made by passing the collected xenon, krypton, unreacted iodine, and sodium iodide through a prefilter and charcoal sample train. The volume of gases which passed through the filter train was measured with a wet test meter. The quantity of iodine injected into sodium column was determined by observing the pressure decrease of mixed gas (xenon, krypton, and iodine) reservoir during the injection period. The mass of iodine collected on the millipore and charcoal filters and the activated charcoal filter train was determined by neutron activation analysis (NAA). The sample train filters and the standards were irradiated in the AI L-85 reactor and analyzed using a gamma detector and a 4000-channel analyzer. Iodine attenuation tests were conducted using the 6.4-38 mm diameter nozzles positioned at sodium depths ranging from 10-540 mm. Twenty tests were conducted at low sodium temperatures, 105-227 °C, to minimize the amount of sodium vapour in rising bubble. Fourteen tests were conducted at high sodium temperature, 450 °C, to show the effect of iodine reaction with vapour within the rising bubble. The measurement of iodine attenuation due to the formation of sodium iodide within the bubble and the reaction of iodine with the sodium bubble surface was conducted in a two part series. In the first series of tests, bubbles ranging in volume from 0.22-9.65 ml were produced by various diameter nozzles. The nozzles were positioned at various depths in the sodium column, which was held to 105-227 °C bulk temperature. The sodium vapour pressure was low compared to iodine at these temperatures, therefore only a minor reaction between sodium vapour and iodine was expected. Under these conditions, the loss of iodine diffusing to the bubble surface during

the bubble rise period would dominate. The second series of iodine attenuation tests were conducted with a bulk temperature of 450 °C to verify the magnitude of the iodine sodium, vapour reaction. Optical microscopy (40X) observations were made of samples collected in both low and high temperature sodium tests. Samples collected in the low temperature tests showed the presence of sodium iodide crystals with absorbed condensed iodine. Volatization tests showed that these samples were ~ 45% by weight sodium iodide and 55% by weight iodine. All of the samples collected in high temperature tests were sodium iodide. The 6.4-12.7 mm diameter nozzles produce bubbles bracketing the 12.7 mm diameter SFR bubbles predicted by HEDL based on half scale SFR model experiments. There is an initial attenuation factor, A_1 of ~10-20 independent of bubble size. This indicates an initial reaction of the iodine vapour as soon as the bubble forms in contact with sodium. The subsequent attenuation, A_2, per meter depth (specific attenuation) occurs as bubble rises. The study showed that out of the total iodine vapour released/injected a large fraction (~90% or more) gets trapped in the pool as sodium iodide (Heisler *et al*., 1975).

The SABER experiment by PNC (Miyahara *et al*., 1995a; Miyahara *et al*. 1996) was carried out to understand the in-vessel source term. The bubble was created in the sodium pool by shattering a quartz ball containing xenon iodine mixed gas, and the mixed gas was subsequently discharged into argon cover gas to determine the iodine mass transferred to the pool in the SABER tests. Chen-type void sensors were mounted vertically in the pool to detect the rising bubble velocity. During the rising time, the bubbles disintegrated into multiple smaller spherical cap bubbles. The SS test vessel carries 180 kg of sodium and has an inner diameter of 300 mm and a height of 3000 mm. At the bottom of the vessel is a bubble generating device consisting of a quartz glass ball containing mixed xenon iodine gas and a cracking device for the ball. To collect the mixed

gas, a funnel device is attached to the sodium surface in the cover gas. Two Chen type sensors with an outside diameter of 0.65 mm make up a void sensor assembly. They're attached to four arms that extend toward the test vessel's center axis. To measure the rising velocity of mixed gas bubbles, the four assemblies are mounted at 450, 750, 1050, and 1350 mm from the quartz ball in the vessel. The bubbles were created instantly by splitting the quartz ball at the vessel's bottom. Signals from sensors mounted vertically in a sodium pool were used to calculate the speed of rising bubbles. To capture sodium iodide aerosols, the bubbles reaching the surface of the sodium pool were passed through an aerosol filter sampling device. In distilled water, the materials that had accumulated on the filters were dissolved. An inductively coupled plasma mass spectrometer (ICP-MS) was used to determine the amount of iodine in the solution. The diameter of the quartz ball was changed from 50 to 120 mm, resulting in an initial bubble volume of 65-900 ml, which is similar to the fission gas volume in a fuel pin at an 80 GWd/T burnup. The ball's gas pressure was set to match the surrounding sodium pressure. Throughout the experiment, the cover gas pressure was kept at atmospheric pressure. Iodine concentrations in the ball ranged from 1 to 40% initially. 4 mol percent is the fraction of iodine produced with a burnup of 80 GWd/T among the values. Because the sodium coolant is 500 degrees Celsius, the temperature of the sodium pool was varied between 300 and 600 degrees Celsius. To study the bubble rise time, the depth of the sodium pool was adjusted from 30-2000 mm. With the exception of the initial phase, the bubble rises linearly with time. With a rise in the initial bubble volume, the bubble's rising velocity also increases. The measured velocities are found to be lower than Clift's calculated terminal velocity of a spherical cap shaped bubble, and the divergence grows as the initial bubble volume increases, implying that the bubble broke up into multiple smaller bubbles. The rising bubble's behaviour was observed in a water pool that was

1500 mm deep, 300 mm long and 300 mm broad (Miyahara *et al*. 1996). Similar to the sodium pool experiment, the bubbles were formed by fracturing a quartz ball containing air. The water tests were carried out in the same conditions as the sodium experiments, with the same range of dimensionless numbers. It was also discovered that changes in the initial bubble volume and sodium temperature have no effect on the transferred mass. With rising iodine concentration, the mass transfer rate (which declines immediately shortly after bubble production and then gradually for subsequent periods) is observed to increase. This means that a more mechanistic analysis is needed to accurately predict *DF* over a long period of time, as well as just after the bubble has formed. Depending on the initial iodine concentration, sodium temperature, bubble rise time and bubble diameter the release fraction ranged from 1-100 percent.

2.1.2 Review of theoretical models

Miyahara *et al*. (1995b) developed analytical model to clarify the process of the iodine mass transfer observed during the SABER experiments. Analytical models for mass and heat transfer in the xenon iodine mixed gas bubble are built based on observations of bubble rising through sodium pool and simulated water pool. The study employed the following models: (1) Diffusion model in which heat transfer is controlled by conduction and radiation and mass transfer is controlled by diffusion for a short time from the static spherical bubble (2) Convection model in which mass transfer is controlled by the aerosol deposition processes from a spherical cap bubble as it rises through the pool. The following assumptions were employed in the research: (a) Initially iodine vapour is uniformly dispersed in the bubble (b) The sodium is saturated at surface temperature and evaporates at the bubble's interface (c) On a spherical reaction front, iodine vapour reacts with sodium vapour, generating heat of reaction and sodium iodide aerosols with a mass median diameter of 0.1 μm (d) Chemical reaction has no effect on the spherical bubble size

and pressure (e) Aerosols settle on the bubble surface by diffusiophoresis, thermophoresis and brownian motion (f) Aerosol concentration gradients between the reaction front and the bubble surface are roughly proportional to sodium concentration and temperature gradients and (g) Convective flow in the rising bubble enhances aerosol settling in the convection model. The reaction front advances from the bubble surface to the bubble center over time, generating heat and sodium iodide aerosols in the process. The rate at which aerosols are produced is determined by the reaction rate. The following results were drawn from the analytical investigation. The heat generation at the reaction front increases as the initial iodine concentration rises, raising the temperature at the reaction front. The contribution of thermophoresis to the deposition of sodium iodide aerosols on the bubble surface is significantly increased when the temperature difference between the reaction front and the bubble surface is raised. The diffusion model's *DF* predicted in the spherical bubble accurately represents the measured DFs' quick growth in the first stage, as well as their increase with the initial iodine concentration. The fact that the measured *DF*s are between the *DF* curves with the bubble diameter of 10-30 mm is consistent with the original bubble breaking up into little bubbles during rising through the sodium pool. The convection model-derived DF curve in a spherical cap bubble demonstrates a gradual increase in measured *DF*s over time.

The computer code TRACER (transport phenomena of radionuclides for accident consequence calculation of reactor) was developed by Japan in 1996 to evaluate the in-vessel source term; the species and quantities of FPs released into the cover gas (Miyagi *et al*., 1996). Important transport phenomena analyzed in the code included the transport behavior of FP gas bubbles and aerosols in connection with bubble dynamic behavior and the sodium flow, evaporation into cover gas and deposition onto structure wall. The code uses the earlier developed analytical

model for evaluation of *DF* for fission gases. The code validation for iodine bubble decontamination was performed with the results of SABER experiment on gas bubble behavior. The code yields the time histories of FP concentrations in the cover gas as well as in coolants and bubbles. The TRACER code (Nakagiri *et al*., 2000) has been developed since early 1990's and continued to be modified and expanded as understandings of various FP transport phenomena improved in time. The TRACER version 1.0 was described in the report published in 2002 (Toyahara *et al*., 2002). The code has been improved in terms of the models and its structure since then. More recently, the manual of the TRACER version 2.3 was issued in 2005 (Toyahara *et al*., 2005).

The transport of FPs by bubble transport to cover gas in SFR is evaluated using RCS code (Umbel, 2011). Sedimentation, inertial impaction and diffusion are the three deposition modes that determine the transmitted fraction. Gravitational settling is sedimentation, and inertial impaction happens when molecules are unable to follow the flow lines. Brownian motion and the random nature of gas molecule collisions cause diffusion. The terminal velocity and diameter of the bubble are required to calculate the deposition fraction. The transfer of fission gas in vapour form rather than as an aerosol was also considered. The release fraction for vapours was evaluated using fitted equation based on molecular diffusion.

2.2 Iodine retention in water

Following fuel handling accident, the water pool above spent fuel storage racks plays an important role in scrubbing and reducing the amount of radionuclides (I-131) available for release. Hence, the radiological source term evaluation for spent fuel pool under such accidents for SFRs is also equally important to the MST evaluation of radionuclide bubble transport mentioned in the earlier section. However, this work received little attention in the literature, but

for SFRs that use a water pool system for fuel storage, the GIF-SFR-SDC/SDG ensures that future designs will prevent the uncovering of FSAs in all plant states relevant to the spent fuel pool, therefore eliminating the conditions that could lead to a substantial radioactive release.

Few experimental and theoretical studies were carried out till date towards evaluating the *DF* of iodine in suppression pools of light water reactors (LWRs). These experiments showed that even a boiling water pool can have an appreciable *DF* (Cunnane *et al*., 1986; Merilo, 1986; Paul *et al*. 1985). Until the mid-1990s, a number of experimental programmes have attempted to resolve the pool scrubbing problem in LWRs (Fuchs, 1964; Demitrack and Moody, 1983; Powers and Brockmann, 1986; Kuhlman *et al*., 1986; Hashimoto *et al*., 1988; McCormack *et al*., 1989; Güntay, 1990a; Güntay, 1990b; Hashimoto *et al*., 1991; Furrer and Passalaqua, 1992; Ramsdale *et al*., 1992; Marcos *et al*., 1993; Peyres, 1995; Fischer *et al*., 1996; Fischer *et al*., 1997; Dehbi *et al*., 2001).

2.2.1 Review of experiments

In part, iodine retention experiments in water was carried out aiming at quantifying the retention of iodine vapours by the final barrier in the DiD strategy (wet well/pressure suppression pools) of BWRs. Findings from these experiments indicated the retention of volatile iodine compounds had influence of certain geometric and physicochemical parameters. The role played by hydrolysis reaction regarding the *DF* has shown that the aqueous concentration of iodine and the pH may be influencing parameters, and that the aqueous chemistry of iodine may be an important boundary condition in the pool scrubbing processes for volatile iodine. In the literature survey Diffey *et al*. (1965) experimental programme seemed to be the most suitable to test the computer models.

They (Diffey *et al*., 1965), performed a series of experiments at the united kingdom atomic energy authority (UKAEA) for investigating the retention of molecular iodine in water pool, from the point of view of accident conditions. The retention of molecular iodine in water pools depended on proportion of air in the inlet gas, the final concentration of iodine in the pool and its chemical reactivity. As shown mainly by the POSEIDON and ORNL (General Electric) experiments, the most relevant geometric parameters for *DF* are submergence and diameter of the injector. Submergence increases the residence time of the gas in the pool, and consequently the *DF*. Injection via small orifices contributes to the formation of smaller bubbles, thus increasing the transfer surface area and *DF*. Especially outstanding among the physicochemical parameters are the steam fraction in the inlet gas, the pool temperature and the iodine mass injected. The presence of sufficient steam in the inlet gas to promote condensation contributes to removal of iodine present inside the gas, as was concluded in the UKAEA Hillary and Diffey *et al*. (1965) experiments. Temperature has a complex influence, since it affects diffusion, partition coefficient, and chemical reactivity of iodine in the pool and under favorable conditions, may promote evaporation inside the bubble. Therefore, the overall effect of temperature on *DF* depends on balance of all these processes. Finally, the chemical reactivity of iodine in aqueous phase, which depends to a large extent on mass of iodine present, may under certain conditions affect retention of iodine in the pool. In this regard, the UKAEA (Diffey) experiments concluded that the concentration of molecular iodine in the water had an important influence on the *DF*. At low concentrations ($<10^{-6}$ M), an important fraction of the iodine suffered reactions with water giving low volatility compounds and contributing to increase the partition coefficient, and consequently *DF*. The role played by chemical additives has not been widely explored. Nevertheless, mention might be made of the UKAEA (Diffey) and ORNL experiments, which

found that certain chemical additives in the pool might enhance chemical reactions tending to decrease the volatility of the system, thus increasing the *DF*. In all the tests it was found that the mass released to the atmosphere was less than 1.8% of the mass injected.

2.2.2 Review of theoretical models

Fuchs (1984) articulated quantitative models for aerosol deposition processes within spherical bubbles. Moody and coworkers (Demitrack and Moody, 1983) have published expressions for the deposition rates in ellipsoidal bubbles. The computer model VANESA was developed in 1986 at sandia national laboratories (SNL), USA to determine aerosol decontamination for evaluation of LWR ex vessel source term (Powers and Brockmann, 1986; Powers and Sprung, 1992). In connection with the boiling pool experimental works two computer codes have been developed, suppression pool aerosol removal code (SPARC) (Owczarski at al., 1985) and suppression pool retention analysis (SUPRA) (Wassel *et al*., 1985; Wassel *et al*., 1985). SUPRA, bubble scrubbing analysis (BUSCA) (Ramsdale et. al, 1992) and SPARC90 (Owczarski and Burk, 1991) which were primarily created in the 1980s, contained a large portion of the LWR experimental inquiry. The codes predict retentions ranging from 97-99% for molecular iodine in water. Both SPARC and BUSCA model the retention of volatile iodine compounds on the basis of the penetration theory of diffusion. Penetration theory evaluates the iodine removal during bubble rise using diffusive mass transfer coefficients calculated for the gas and liquid sides of bubble interface. Diffusive mass transport velocities u_D are calculated as

$$u_D = \sqrt{D/\pi t_e} \tag{2.1}$$

Where D is the diffusivity of iodine in the gas or liquid phase, and t_e is the time of surface exposition. The interfacial concentration c_i is calculated from the continuity of the diffusive mass flow as

$$c_i = \left(c_l u_{D,l} + c_g u_{D,g}\right) / \left(He u_{D,l} + u_{D,g}\right) \quad (2.2)$$

where $u_{D,l}$ and $u_{D,g}$ are the diffusive transport velocities (mass transfer coefficients) at the liquid and gas side, respectively; c_l and c_g are the associated bulk molar concentrations, and *He* is the Henry number.

Despite the similarity in two models, there exist some differences mainly focused on the boundary conditions in the aqueous phase and in the species involved in models. Thus, in SPARC both molecular iodine and methyl iodide are considered as well as an approach to the aqueous chemistry of iodine is included. BUSCA only deals with molecular iodine and does not have any chemical model. The sensitivity analysis performed for both models has shown that different sensitivity of SPARC and BUSCA codes is due to the differences regarding the chemistry between both models. Despite the uncertainties associated with the Diffey *et al*. (1965) experimental data, the results of SPARC and BUSCA have been qualitatively compared and rationalized. The SPARC results showed a good agreement with the experimental trend. On the contrary, the BUSCA predictions were not influenced by the iodine concentration in the pool. In consequence, the aqueous chemistry model included in SPARC makes it more suitable to the modelling of pool scrubbing phenomena for volatile iodine.

2.3 Filtered containment venting system (FCVS)

The most expensive system/component in SFR plant design is the containment. The use of low design pressure and vent/filter containment is found to have the potential to reduce plant capital costs by approximately 5%. Filtered containment venting systems (FCVS) have been used historically in United States at fast flux test facility (FFTF) of Hanford site (Postma and Hilliard, 1980). A filtered vent design was also planned for the CRBR. The conventional method for filtering radioactive aerosols is to utilize HEPA filters, which are capable of removing even

submicron particles with great efficiency. HEPA filters, on the other hand, have a finite amount of loading capacity. The pressure drop rises as the amount of aerosol on the filter increases, and the filter fails. A substantial release of radioactive material is invariably accompanied by a huge emission of sodium aerosols, which have typically interacted with air to generate sodium oxide aerosols in SFR severe disaster scenarios. As a result, any filter evaluated for an SFR vent/filter system must be able to contain a significant amount of sodium compound aerosols. Hence, several experiments were carried out to find the most suitable passive FCVS for SFRs.

2.3.1 Review of experiments

The EACSs typically used for sodium fire aerosol control are dry filters (HEPA filters, sand and gravel beds) and wet scrubbers (spray chamber, pool, venturi and PBSs). The dry filters feature high aerosol removal efficiency but has lower mass loading. When loaded with moist aerosols to 1.6-10 kg/m^2, dry fibre filters and sand and gravel beds clogged, giving lower loadings. To handle the effluent from a massive sodium fire, a very large installation would be necessary. Wet scrubbers are suitable for high mass loadings and have high aerosol removal efficiency when used in series and not individually. Several types of traditional aqueous scrubbers were investigated (ejector venturi, irrigated fibre bed and spray chamber). There was no single stage scrubber that could match both the high efficiency and high mass loading capacity requirements. When these components were connected in series, they provided outstanding efficiency (>99.9%) and loading capabilities limited only by the amount of water available. However, the ideal scrubber for containment venting in SFRs require features such as low electricity demand, high aerosol removal efficiency and high mass loading, which are not met by commercially available wet scrubbers. Several EACSs were experimentally tested at HEDL, USA to find the most ideal scrubber suitable for sodium fire aerosol removal in SFRs.

The SGBS designed in 1979 by HEDL, USA satisfactorily met most of the requirements of an ideal scrubber for SFR. The SGBS adds the advantages of both dry (sand and gravel bed) and wet (pool) scrubbers and hence, has characteristics of both high mass loadings and aerosol removal efficiency when used individually for sodium aerosol removal. The self cleaning SGBS featured a passive (no electrical demand), low cost scrubber that occupies less space compared to commercially available wet scrubbers. Its efficiency as a stand-alone air cleaner was >99%, and it was >99.9% when combined with a fibre demister. Except for the alkalinity of aqueous solution confined to 5 M due to corrosion reasons, its mass loading capacity was 100 times greater than that of a sand and gravel bed.

The SGBS conceived at HEDL, consisted of a water pool submerged gravel bed. Air carrying sodium fire aerosols entered the SGBS through a down comer inlet pipe. Aerosols were scrubbed from the air while rising up through the submerged gravel bed and cleaned air left the SGBS via an outlet pipe. Removal of sodium fire aerosols takes place primarily by inertial impaction on the gravels in SGBS. The presence of air in gravel bed region reduced the liquid density inside the bed, resulting in natural circulation of water in the SGBS pool. The cleaning of aerosols collected in bed by natural circulation of water resulted in a self cleaning bed. Several studies were carried out in the past from 1978-1995 (Postma and Hilliard, 1980; Owen and Postma, 1980; Owen, 1980; Hilliard and Muhlestein, 1982; de Cuy, 1978; Boehm and Jordan, 1976; Barreca and McCormack, 1980; Hilliard *et al*., 1981; Boehm *et al*., 1974; Hilliard *et al*., 1979; Eckardt and Losch, 2012; Knaus, 1995) related to improving SGBS aerosol removal efficiency and scaling up for bigger containments.

For the 90% removal efficiency case, even though both eductor venturi and SGBS were rated as prime candidates, the SGBS was superior to the eductor venturi in passivity and mechanical

simplicity but it lacks an extensive use history (Postma and Hilliard, 1980). Similarly, for the 99% removal case, both eductor venturi and the SGBS were also prime candidates when SGBS was upgraded by adding a packed bed back-up stage of polypropylene fibers. A 0.61 m deep bed of crushed rock with a diameter of 0.95-1.27 cm is an appropriate bed design option. For gas superficial velocities ranging from 0-0.5 m/s, scrubber performance is maintained. The gas-induced liquid circulation through the bed is a unique feature of SGBS. The pressure drop in the scrubber is roughly equivalent to a static head of water. The removal efficiency of three chemical types of sodium aerosol studied, Na_2CO_3, Na_2O_2, and NaOH, was practically the same.

A hydraulic scale-up for a bed capable of handling 275 real m^3/hr has been demonstrated. For inlet gas temperatures up to 120 °C, cooling to within 2 °C of the liquid temperature was demonstrated. The SGBS/HEFD test article's overall performance was outstanding, with great aerosol removal, strong flow control, stable pressure differentials, great gas cooling, and high aerosol mass loading. Except for the addition of water to offset evaporation losses, the unit was completely passive. The SGBS/HEFD system outperformed a commercial system that consisted of a water spray quench tank, ejector venturi, and fibrous scrubber connected in series. The SGBS unit had a little higher particle removal efficiency (99.987 percent vs. 99.956 percent) and more consistent pressure differentials. The SGBS/HEFD system has a significant benefit over the quench/venturi/fibrous scrubber method in that it does not require pumps (passive). It operates at a larger pressure drop (9.0 kPa vs. 2.0 kPa), which could be a disadvantage. Hydraulic tests on three scale models of the SGBS show that scaling up to units of 10-20 m^3/s (20,000-40,000 ft^3/min) may be possible, but large-scale hydraulic testing should be done to verify flow distribution. The gravel bed for a 10 m^3/s scrubber would be 5.0 m in diameter, based on a recommended superficial gas velocity of 0.5 m/s.

The SGBS/HEFD System has an excellent efficiency at eliminating sodium fire aerosol particles, averaging 99.987 percent which translates to a *DF* of 7700. The SGBS had very high removal efficiency without the demister, averaging 99.24 percent (*DF* of l30). Only two operating parameters, aerosol particle size and sodium content in the SGBS liquid pool, had any discernible effect on the measured efficiency. The change in sodium fire aerosol's aerodynamic mass median diameter (AMMD) from 3.4 to 8.4 μm had only a slight impact, however submicron particles were collected with lesser efficiency, as expected. Due to entrainment carryover, which is a property of all scrubbers, a high sodium concentration in the scrubber liquid caused the efficiency to fall significantly. Small particles which penetrated the SGBS were captured efficiently (98%) by diffusion in the HEFD (Owen and Postma, 1980). The EACS is highly efficient and adaptable because to the SGBS's high mass loading capacity and the HEFD's effective small particle retention (Owen and Postma, 1980). The pressure drop across the scrubber system changed predictably with gas flow rate and did not appreciably change over time. This demonstrates the system's ability to capture significant amounts of aerosol without clogging. The system's total mass loading capacity is determined by the amount of water available. Aerosol deposition was significant in the duct leading from containment to the scrubber (Owen, 1980).

2.3.2 Review of theoretical models

Theoretically, the SGBS efficiency were evaluated to date using semiempirical correlations available for PBSs. Jackson and Calvert (1966) model considered the scrubber bed as a series of channels in nonsubmerged condition through which the air carrying aerosols passes through and aerosol capture primarily occurred by inertial impaction phenomenon on the gravels. Empirical constants related to channel width were used in the Calvert model making it semiempirical.

SGBS aerosol removal efficiency was considerably underestimated by the mathematical model based on impaction. Two mechanisms believed responsible for higher than predicted performance are: (a) particle growth due to water condensation, and (b) enhanced turbulence due to energy dissipation. Particle size increase due to water condensation and greater turbulence due to energy dissipation are two factors thought to be responsible for better-than-predicted performance.

2.4 Gap areas and objectives

It is clear from the extensive review of literature presented in previous sub-section that experiments carried out till date related to iodine retention in sodium pool under fuel pin failure scenario, were limited to the initial iodine masses between 0.6-2697 mg, bubble sizes between 7.5-120 mm, sodium temperatures between 105-600 °C and pool heights ranging from 25.4-3000 mm. Iodine retention in sodium pool varied from about 60-100 %, depending upon the bubble diameter, bubble rise time, initial iodine concentration and pool temperature. However, the experimental results were highly scattered and hence, iodine retention and mass transfer rate could not be successfully correlated with experimental parameters till date. The computer codes available in literature to evaluate the retention of iodine in sodium pool were based on empirically evaluated bubble dynamic parameters such as bubble shape (spherical, ellipsoidal and spherical cap), rise time, velocity and trajectory which were well developed for normal liquids (water) than liquid metals (sodium) and report about 0-99 % retention. Even though similarity in bubble dynamics between water and sodium is considered in literature, a systematic study to prove this similarity is missing in literature. Hence, there is still scope in the research field both experimentally and theoretically to bring out the effects of various parameters on iodine retention in liquid pools of SFR clearly.

Pool scrubbing experiments have been previously carried out aiming at quantifying the scrubbing efficiency for removal of iodine vapours in water (Polo *et al*., 1996). SPARC, SUPRA, and BUSCA, codes intended to calculate iodine scrubbing in accident situations, are acknowledged to rely on speculative modelling (Beghi *et al*., 2018). The validation of these algorithms is based on a single series of trials (Diffey *et al*., 1965; Guentay *et al*., 1996), and the verified parameter range is limited, as Fischer *et al*. (1997) pointed out. Despite this, there is currently a lack of a systematic assessment of iodine scrubbing and an intelligible data set for model development. Hence, there are still more scopes in the research field both experimentally and theoretically to bring out the effects of various parameters on iodine retention in water pool.

Experiments carried out in recent past in SGBS evaluated the aerosol scrubbing efficiencies for sodium fire aerosol up to 96-99.9 %, for specific experimental conditions. The conditions considered were aerosol size of 1.5-15 μm, aerosol concentration of 0.01-50 g/m^3, bed height of 0.305-0.610 m, crushed basalt rock size of 6.4-15.9 mm and air flow rate of 120-2100 liter/minute. Theoretically, the SGBS efficiency were evaluated to date using semiempirical correlations available for PBSs. Jackson and Calvert (1966) model considered the scrubber bed as a series of channels in nonsubmerged condition through which the air carrying aerosols passes through and the aerosol capture primarily occurred by inertial impaction phenomenon on gravels. Empirical constants related to channel width were used in Calvert model making it semiempirical. Even though, the passive SGBS gives high aerosol removal efficiencies at low air flow rates in reality, the Calvert semiempirical model is observed to under predict the SGBS efficiency at low air flow rates. Hence, to reduce the dependence on empirical constants and to uphold the passive nature of scrubber at low air flow rates, better and advanced theoretical models have to be brought out for capturing aerosol scrubbing efficiency of SGBS. These gap

areas were clearly identified from the literature survey and formed the basis and objective of the Ph. D thesis.

2.5 Closure

This chapter was dedicated to extensive review of existing literature in area of bubble dynamics, aerosol removal efficiency and iodine retention in water pool. The major findings were highlighted in detail and gap areas are identified. These gap areas framed the objectives of the thesis. Next chapter is dedicated to semiempirical model correlations for bubble dynamics with mass transfer.

CHAPTER-3

SEMIEMPIRICAL MODEL FOR BUBBLE DYNAMICS WITH MASS TRANSFER

Chapter-3: Semiempirical model for bubble dynamics with mass transfer

3.1 Introduction

The aerosol/vapour mass transfer from rising gas bubbles in liquid pools typical of SFR is evaluated in this chapter using a basic wet scrubbing model. Classical mass transfer theories, which were developed for the scenario of an isolated bubble rising through liquid, are used in this theoretical model. It calculates the aerosol scrubbing efficiency by evaluating deposition coefficients for ellipsoidal bubble shape and the vapour scrubbing efficiency by solving the Fick's diffusion equation analytically. This chapter also goes through the parametric tests that were done to see how several important parameters like aerosol size, inert gas component, pool height and bubble rise time affected pool scrubbing.

3.2 Description of model

Modules for evaluating bubble dynamics and mass transport of aerosol/vapour make up the wet scrubbing model. Based on literature correlations, the bubble dynamics module calculates the terminal velocity, shape and diameter. The aerosol/vapour scrubbing for bubble rise through the liquid pool is evaluated using the mass transport module.

3.2.1 Model assumptions

The primary system in SFR works at atmospheric pressure. As a result, in the current model, atmospheric pressure is assumed above the pool. Because the maximum stable bubble diameter is limited by hydrodynamic instability during bubble rise, the same is used in the model as the initial bubble size. Sedimentation, inertial impaction and diffusion are the scrubbing processes studied for the aerosol sub-module. Scrubbing of VFPs by vapour phase condensation is not explored since the quantity of evaporative flow at the gas liquid interface may augment or inhibit

efficiency. As a result, at the bubble entry site, the current model assumes instantaneous thermal equilibrium between the liquid and gas phases. The vapour scrubbing module's process entails vapour diffusion to the bubble surface, followed by instantaneous dissolution/reaction at the gas-liquid interface and removal into sodium. The assumption is based on fast reaction rate of iodine vapour with sodium at the bubble boundary and cesium's high solubility in sodium.

3.2.2 Module for bubble dynamics

The correlations available in the literature are used to evaluate the bubble dynamic parameters. The diameter and terminal velocity of a rising bubble affect the amount of mass transported. The Levich (1962) correlation was used to calculate the maximum stable bubble diameter. The parameterization equation derived by Park *et al*. (2017) determines the variation of bubble terminal velocity with diameter.

$$d_b = \frac{3.6\sigma_l}{u_T^2\left(\rho_g\rho_l^2\right)^{1/3}} \tag{3.1}$$

$$u_T = \frac{1}{\sqrt{\frac{144\mu_l^2}{g^2\rho_l^2 d_b^4} + \frac{\mu_l^{4/3}}{0.14425^2 g^{5/3}\rho_l^{4/3} d_b^3} + \frac{1}{\frac{2.14\sigma_l}{\rho_l d_b} + 0.505 g d_b}}} \tag{3.2}$$

Dimensionless numbers like Reynolds number, Morton number, Eötvös number and Tadaki number characterize bubble dynamics in terms of shape and rise velocity.

3.2.3 Module for mass transfer

During bubble rise, the mass transfer module has sub-modules for aerosol and vapour scrubbing by liquid pool. The module is divided into sub-sections as follows.

3.2.3.1 Scrubbing of aerosols in liquid pool

The reaction between sodium vapour and iodine is substantial and dominant at higher pool temperatures, resulting in the generation of NaI aerosols at the reaction front produced inside a

bubble. Aerosol removal models were used to determine the liquid pool's aerosol scrubbing efficiency for mixed gas bubbles (Bucknor *et al*., 2017; Umbel, 2007; Powers and Sprung, 1992). Sedimentation, inertial impaction and diffusion are the deposition mechanisms studied in this model. For a variety of particle sizes (d_p), the amount deposited was estimated. The terminal velocity and bubble diameter anticipated by the bubble dynamic module are used to calculate the deposition fractions.

$$SE_a(\%) = \left[1 - \frac{C_a}{C_{a0}}\right] \times 100 = \left[1 - exp\left(-h * \left(\alpha_{diff} + \alpha_{sed} + \alpha_{iner}\right)\right)\right] \times 100 \quad (3.3)$$

3.2.3.2 Scrubbing of vapour in liquid pool

During liquid pool scrubbing, VFPs (I, Cs) can be also be transported in vapour form. If the vapour reacts/dissolves quickly at the gas-liquid interface and is removed into the liquid pool owing to sodium flow, Fick's law can be used to describe the volatile species mass transport from a bubble into a pool. Because of its high solubility, cesium vapour that reaches the gas-liquid interface dissolves in the sodium pool. At the gas-liquid interface, iodine vapour interacts instantly with liquid sodium, releasing the product NaI into the sodium (Miyahara and Shimoyama, 1995). When compared to iodine, sodium vapour pressure is low at lower pool temperatures, and only a minor reaction occurs between sodium vapour and iodine. During the rising stage, diffusive iodine loss to the bubble surface thus takes precedence. Starting with uniform concentration inside and zero boundary condition, the model for vapour scrubbing solves Fick's second law of diffusion in spherical geometry (Welty *et al*., 2009).

$$\frac{C_v - C_{v0}}{C_{vs} - C_{v0}} = 1 + 2\sum_{n=1}^{\infty}(-1)^n\, exp\left(\frac{-D_{vi}n^2\pi^2 t}{R^2}\right), \quad r = 0, n = 1,2,3,\ldots \quad (3.4)$$

$$\frac{C_v - C_{v0}}{C_{vs} - C_{v0}} = 1 + \frac{2R}{\pi r}\sum_{n=1}^{\infty}\frac{(-1)^n}{n} sin\left(\frac{n\pi r}{R}\right) exp\left(\frac{-D_{vi}n^2\pi^2 t}{R^2}\right), \quad r \neq 0, n = 1,2,3,\ldots \quad (3.5)$$

$$SE_v(\%) = \left[1 - \frac{6}{\pi^2}\sum_{n=1}^{\infty}\frac{1}{n^2}exp\left(\frac{-D_{vi}n^2\pi^2 t}{R^2}\right)\right] \times 100 \quad (3.6)$$

where SE_v is the vapour scrubbing efficiency, C_{v0}, C_v, C_{vs} are the bubble's starting, final, and surface vapour concentrations, R is the bubble's radius, t is the time of bubble ascent, r is the radial coordinate, and D_{vi} is the inert gas vapour diffusion coefficient. The Chapman-Enskog theory (Welty *et al*., 2009) was used to calculate the vapour diffusion coefficient in an inert gas.

3.3 Experimental and theoretical comparison of model

For the aerosol scrubbing sub-module of the wet scrubbing model, an experimental comparison was conducted. The scrubbing efficiency of sodium pool for nitrogen iodine mixture gas bubbles rising in sodium pool was investigated in the iodine bubble experiment (Kunkel, 1966). Initial bubble volume of 39 ml, iodine concentrations of 10, 50, and 100 percent, pool depths of 1.8-3 m, pool temperatures of 260-538 °C were used in the experiment. Using experimental data at high pool temperatures, an experimental comparison of the aerosol scrubbing sub-module of the wet scrubbing model was carried out. In comparison to the diffusion transfer of iodine vapour to the bubble surface during the rise period, the iodine sodium vapour reaction dominates at high temperatures. As shown in fig. 3.1, the experimental pool scrubbing efficiency at 538 °C for pool depths of 1.8 and 3 m was found to be closer to the scrubbing efficiency anticipated by the current model for aerodynamic particle diameter $\left(d_a = d_p\left(\rho_p/\rho_w\right)^{1/2}\right)$ of 5.7 μm (particle diameter, d_p of 3 μm).

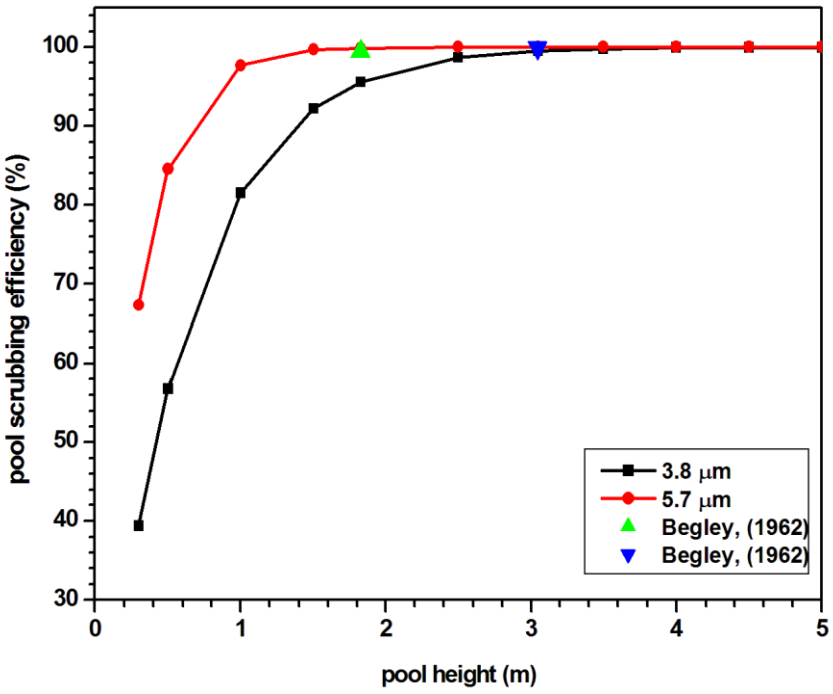

Fig.3.1 Aerosol sub-module experimental comparison

The vapour scrubbing sub-module was compared theoretically using estimated values for the xenon cesium mixed gas bubble obtained in the literature. Umbel (2011) looked at how successful sodium was at scrubbing cesium from a xenon cesium mixed gas bubble rising in a pool. Pool temperature and depth of 510 °C and 4.47 m, respectively, were considered for the evaluation. Umbel evaluated the efficiencies as 99 percent and 99.99 percent at pool rise times of 3 s and 12 s, respectively, using fitted equations valid for spherical diffusion at long time scales ($Fo > 0.5$). Figure 3.2 demonstrates that the current model's estimated efficiencies are 11 percent and 0.07 percent lower than Umbel's figures. The discrepancy in fig. 3.2 at 3 s is due to Umbel's model's larger time scale assumption.

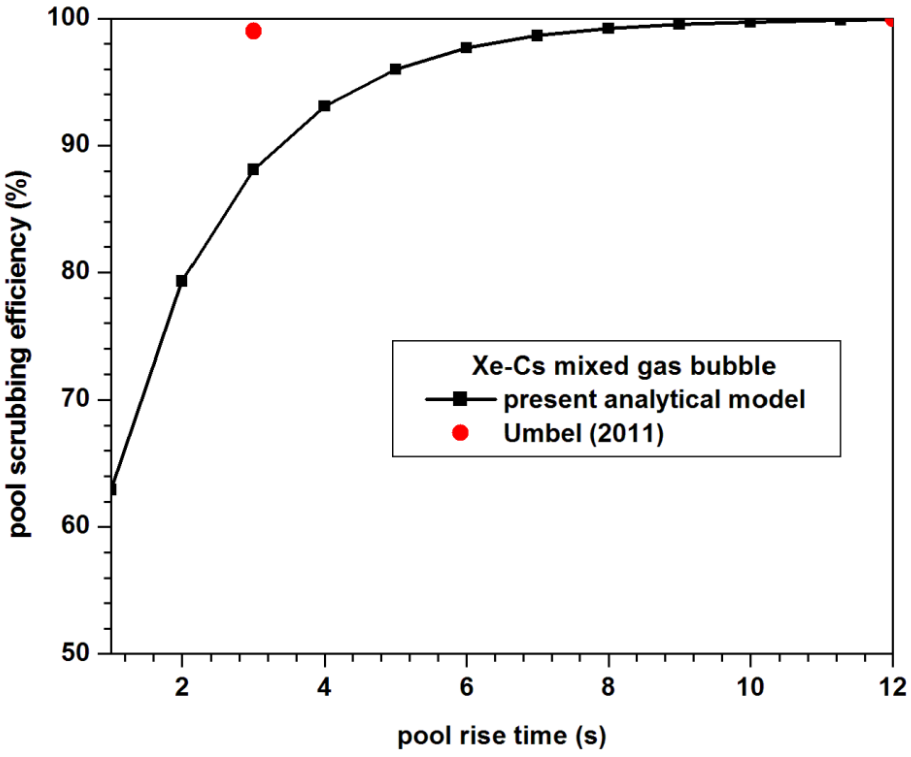

Fig.3.2 Vapour sub-module theoretical comparison

3.4 Discussion of the findings

The variation of bubble terminal velocity with diameter was evaluated using the bubble dynamic module, as illustrated in fig. 3.3 for a rise height of 1 m. The terminal velocity in fig. 3.3 reduces as the bubble diameter increases in the range of 1-10 mm due to the shift of the bubble shape from spherical to ellipsoidal, then increases. In table 3.1, the sizes and shapes of bubbles for the three gas-liquid systems are also listed. The results demonstrate that for bubble diameters greater than 10 mm, the shape is ellipsoidal/spherical cap for all three systems tested. The model was used to study the dynamics of a xenon bubble rising in a sodium pool at 527 degrees Celsius. The temperature of the gas bubbles is assumed to be the same as that of the pool. The height of the rise taken into account for bubble rise is 4.47 m.

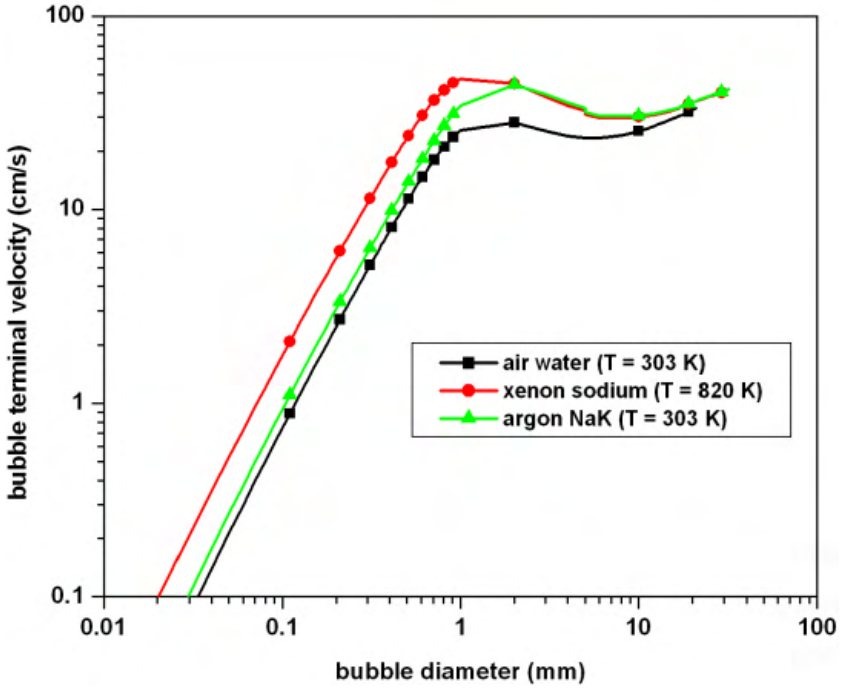

Fig.3.3 Terminal velocity of bubble as a function of its diameter

Table 3.1 **S**hape of bubbles as a function of size

G-L system	Ar-NaK	Xe-Na	Air-H_2O
Diameter for spherical to ellipsoid transition (mm)	9.4	9	5.6
Diameter for ellipsoid to spherical cap transition (mm)	29	27.6	17.1
Maximum diameter for stable bubble (mm)	32.9	30.2	21.2

The bubble diameter is 28.9 mm at 527 °C, and the terminal velocity is 39.7 cm/s, resulting in a rise time of 11.26 seconds. Based on liquid and gas temperatures, the transport characteristics of liquid sodium and xenon gas (Fink and Leibwitz, 1995; Kestin and Wakeham, 1972) were studied. Re = 41930.1, Eo = 43.7, M = 8.3 x 10^{-15}, and Ta = 24.2 are the non-dimensional numbers considered for bubble ascent. According to Levich (1962), the bubble diameter grows with increasing temperature up to 527 °C and then drops due to the balance of density and surface tension forces. Surface tension, liquid and gas density all decrease when liquid and gas

temperatures rise. The fluctuation of bubble terminal velocity with temperature follows the same pattern as bubble diameter. Bubble diameter and terminal velocity fluctuations in relation to temperature are projected to be within 3.5 percent and 1.3 percent, respectively. As a result, these characteristics are unaffected by the temperature of the sodium pool.

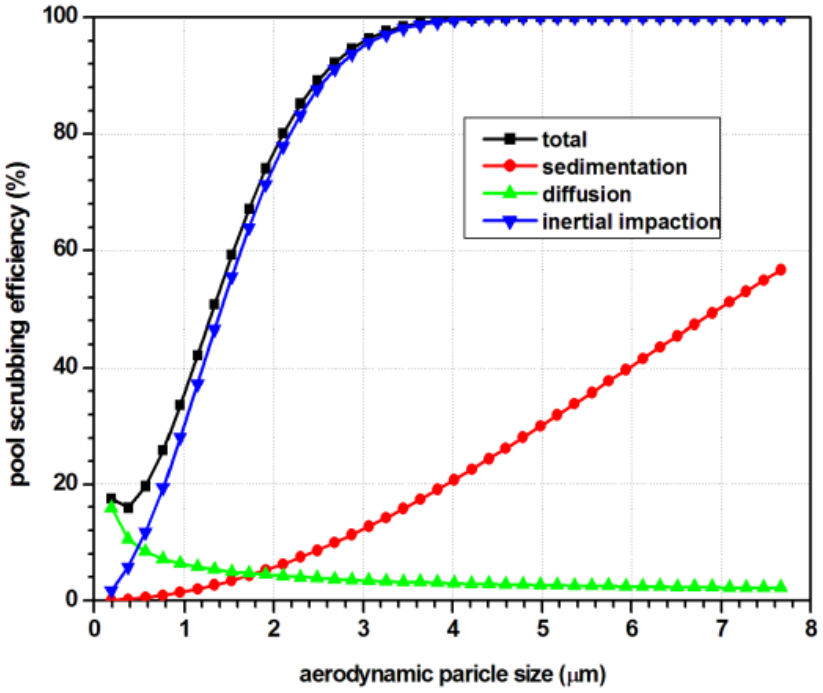

Fig.3.4 NaI aerosol scrubbing as a function of its size

The scrubbing efficiency of the liquid pool for NaI aerosols contained in xenon bubble has been determined based on the model evaluated bubble dynamics of xenon bubble rising in sodium pool at 527 °C. Figure 3.4 shows the total scrubbing efficiency of NaI aerosols contained in xenon bubbles rising via sodium pool as a function of aerodynamic particle size, which can be calculated by combining the individual contributions due to sedimentation, inertial impaction and diffusion deposition mechanisms. The inertial impaction mechanism provides for the majority of overall scrubbing efficiency in the larger size range, whereas the diffusion mechanism accounts for the majority of overall scrubbing efficiency in the smaller size range, as shown in fig. 3.4. As

shown in fig. 3.4, scrubbing efficiency is small for aerodynamic particle sizes less than 1 μm and is mostly dictated by diffusional deposition, but scrubbing efficiency is substantial for particles higher than 1 μm.

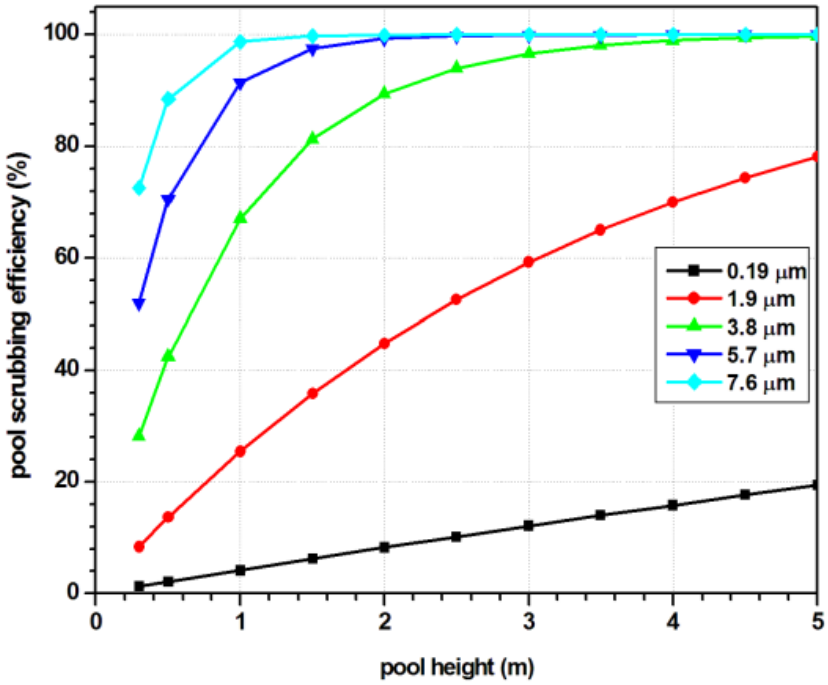

Fig.3.5 NaI aerosol scrubbing as a function of pool height

The overall scrubbing efficiency as a function of pool height for various aerodynamic particle sizes is shown in Figure 3.5. In a sodium pool at 527 °C, 100% removal of aerosols occurs within 1 m of rise height for aerodynamic particle sizes bigger than 7.6 μm for NaI aerosols, and the inertial impaction mechanism accounts for the majority of the overall scrubbing efficiency.

The scrubbing efficiency of the liquid pool for Cs vapour contained in xenon bubble has been determined based on the model evaluated bubble dynamics of xenon bubble rising in sodium pool at 527 °C. The diffusion coefficient of cesium in a xenon bubble at 527 °C is predicted to be 2.3 x 10^{-5} m^2/s. For bubble rising through SFR pool of 4.47 m, the vapour scrubbing effectiveness is 99.99 percent. Figure 3.6 depicts the variation in cesium concentration along the radial coordinate of the bubble at various bubble rise times.

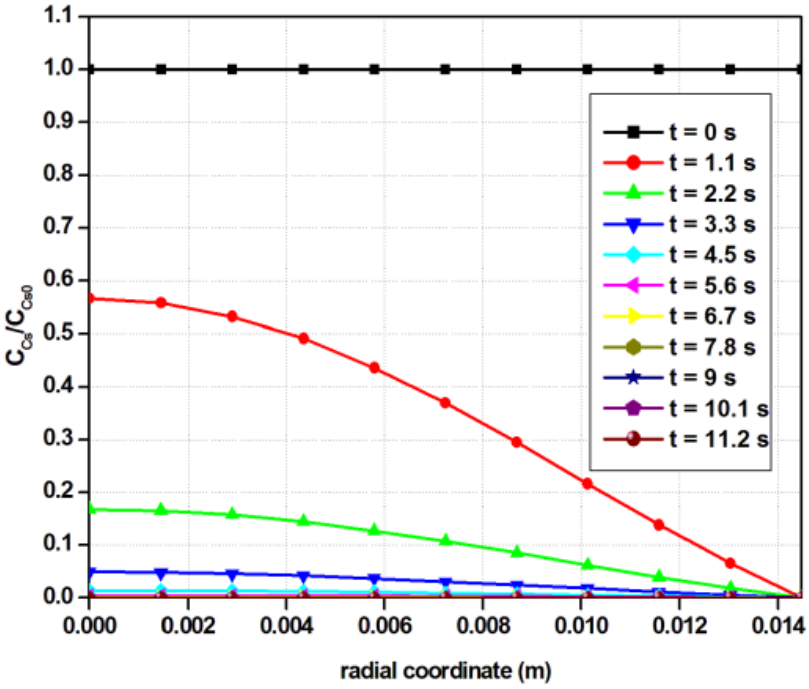

Fig. 3.6 Relative variations of Cs concentration along radial coordinate inside bubble

However, when the initial flow velocity, bubble expansion in the channel, and swarm effect are taken into account, the bubble rise time is significantly reduced. Scrubbing efficiency is 97.74 percent with a rising time of 3 seconds. Cesium vapour diffusing in xenon gas was used in these computations. Krypton and helium are also likely to be present in the bubble. As demonstrated in fig. 3.7 and table 3.2, the diffusion coefficient for cesium diffusion in helium is nearly an order of magnitude higher, resulting in a higher scrubbing efficiency. For inert gases with lower molecular weight, these results in a smaller amount of cesium vapour bypassing the pool via bubble transfer.

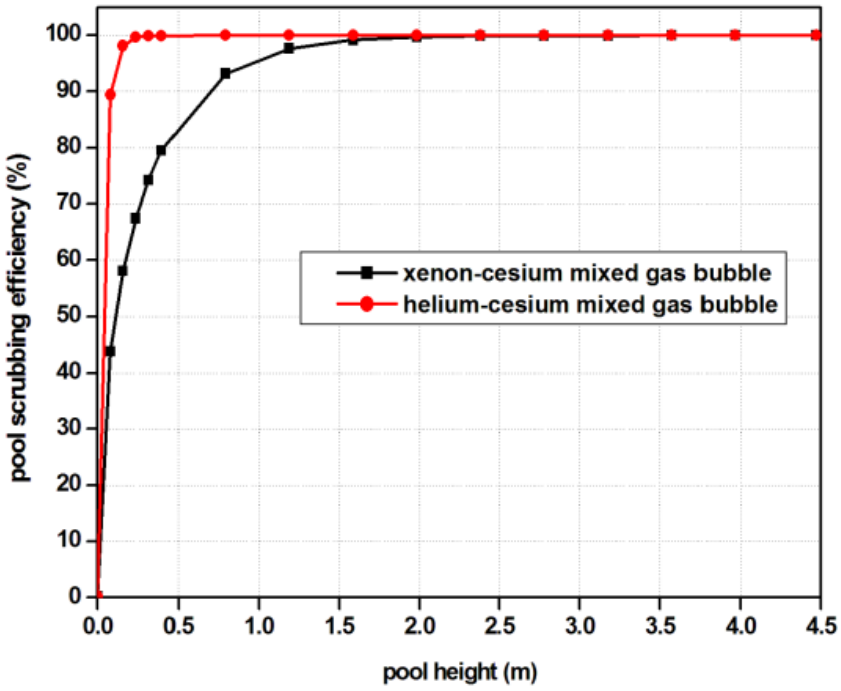

Fig.3.7 Pool scrubbing efficiency for Cs vapour as a function of pool height

Table 3.2 Scrubbing efficiency for change of inert gas component.

Gas	Xenon	Helium
Time of rise (s)	3	3
Coefficient of diffusion (m^2/s)	2.3×10^{-5}	1.8×10^{-4}
Efficiency (%)	97.74	99.99

Inertial impaction and diffusion, respectively, are responsible for the majority of liquid pool scrubbing of very big and very minute aerosol particles, according to this model. According to the findings, during bubble rise through a 1 m deep pool, virtually all big particles larger than 4 μm are eliminated. Due to the higher vapour diffusion coefficient, vapour scrubbing efficiency is higher for lower molecular weight inert gas.

3.5 Closure

The creation of a pool scrubbing model to analyze the scrubbing efficiency of aerosol/vapour from rising gas bubbles in SFR liquid pools was highlighted in this chapter. Modules for

evaluating bubble dynamics and aerosol/vapour mass transport are included in the model. Starting with uniform concentration inside and zero boundary condition, the model simulates the scrubbing of volatile vapours (I, Cs) based on molecular diffusion in spherical shape. Aerosol (NaI) capture through gravitational sedimentation, inertial deposition and brownian diffusion are all considered in the model. The vapour scrubbing efficiency is found to be higher when the vapour diffusion coefficient in the gas bubble is higher. The size over which scrubbing efficiency becomes significant in aerosols was also established. The efficiency of vapour and aerosol scrubbing rises as the pool height/rise time increases. The pool scrubbing model is useful for assessing the scrubbing effectiveness of liquid pools in SFRs and evaluating source terms. Bubble dynamics significantly influence the mass transfer of vapours and aerosols from rising mixed gas bubbles. Therefore, next chapter is dedicated to the bubble dynamic studies carried out.

CHAPTER-4

INVESTIGATION OF BUBBLE DYNAMICS IN LIQUID POOL

Chapter-4: Investigation of bubble dynamics in liquid pool

4.1 Introduction

The semiempirical model developed for pool scrubbing of aerosols/vapours is highly dependent on the bubble dynamics module, which uses correlations available for bubble terminal velocity in water. To understand the applicability of correlations used for water in the pool scrubbing model developed for liquid sodium, a thorough understanding of bubble dynamics in liquid water and sodium based on numerical and experimental studies is essential. Evaluation of bubble dynamics is essential for determining SFR in-vessel source term arising from to core melt accident fuel failures. In SFR liquid pools, the rise velocity is a crucial parameter that controls heat and mass transfer from rising bubbles. The bubble deformation in a stagnant sodium pool is a basic study to be carried out towards understanding its dynamics. The major parameters influencing bubble dynamics are bubble diameter, gas-liquid system, domain aspect ratio and dimension. Understanding single bubble dynamics is the first step towards development of a numerical model for pool scrubbing in SFRs involving complex heat and mass transport phenomena.

Experimentally, single gas bubbles are generated using low gas injection rates. Bubble dynamic experiments were mainly conducted for air-water system due to the transparent nature of water (Clift *et al*., 1975). Experiments carried out in liquid metals such as liquid sodium and NaK were few due to the limited measuring techniques available for opaque liquids. Both invasive and non-invasive techniques such as soft field tomography and hard field tomography are used to measure gas-liquid metal flows (Clift *et al*., 1975). However, the most used technique for liquid metals is X-ray attenuation (Han and Holappa, 2003; Guézennec *et al*., 2004; Shevchenko *et al*., 2013). The advent of computational fluid dynamics (CFD) has made it possible to theoretically study

bubble dynamics in a cost-effective manner. Such studies supplement experimental measurements and provides for a more detailed physical explanation of the phenomena. To date, several CFD studies have been conducted on bubble dynamics for better understanding of the same (Krishna and Baten, 1999; Wang and Tong, 2008; Raees *et al*., 2011; Islam, 2013; Klostermann *et al*., 2013; Zahedi, 2014; Xu *et al*., 2015; Wang, 2015; Verma *et al*., 2017). The majority of these studies are run on commercial software platforms like CFX and Fluent and only few studies employ open source programme, OpenFOAM for such simulations. The OpenFOAM-based researches were limited to 2-D/2-D axisymmetric domains, which under/over predicted rise velocities and were not validated by experimental tests. This brings in the requirement of validated OpenFOAM-based studies to predict realistic bubble dynamics.

In literature, few studies characterized bubble dynamics in sodium using water experiments (Atomics International, 1965; Dickinson and Nunamaker, 1975). Based on the bubble sizes determined from HEDL water experiments simulating SFR fuel failure scenario and similarity of non-dimensional numbers, the average bubble diameter predicted for sodium pool was 1.27 cm. Sodium experiments were carried out at AI for bubble sizes in the range from 1.1-4.1 cm based on water tests at HEDL. Bubbles in the size range between 1-3 cm are typically studied in sodium experiments for SFR in-vessel source term analysis (Miyahara *et al*., 1995a; Miyahara *et al*., 1996). Based on similarity of non-dimensional numbers, Miyahara *et al*. (1996) conducted water experiments to model bubble dynamics in a sodium system. However, theoretical studies on bubble dynamics in sodium pool were limited to terminal velocity correlations and computing the equation of motion. Theoretical studies on bubble dynamics to establish similarity between water and sodium systems are also scarce in literature. Although bubble dynamics similarities between water and sodium systems have been documented in the literature, most investigations

lack a quantitative investigation.

Bubble dynamics in liquid sodium and water pool are investigated in this work using the interFoam solver of open field operation and manipulation (OpenFOAM) for 2-D, 2-D axisymmetric, and 3-D situations. The interFoam module used in present study is verified against 2-D and 3-D numerical benchmark data (Hysing *et al*., 2009; Adelsberger *et al.*, 2014) available in literature. The solver is also validated using 2-D experimental data available in literature and in-house 3-D experimental results. The optimal mesh size for simulating bubble rise in liquid sodium is determined after a rigorous grid independence research. The bubble dynamics in liquid sodium is studied for various domain aspect ratio and range of bubble diameters to understand their influence on bubble behavior.

For the first time, 3-D numerical studies and experiments are wisely coupled to prove the quantitative nature of bubble dynamics similarities between water and sodium systems. A similarity criterion obtained from the numerical work is used to set up an experimental facility for researching bubble dynamics in sodium systems using water. Terminal velocity and shape of the bubble in water system is monitored using void sensors and camera recording. Numerical predictions are validated using the experimental measurements and correlations available in literature. The research reveals open source numerical methods for capturing bubble dynamics as well as a novel way for measuring bubble velocity in vast pools of fluids utilizing void sensors created in-house. The current research is also a first step towards creation of an OpenFOAM-based pool scrubbing model for SFR fuel failure accident scenario involving complex heat and mass transfer processes.

4.2 Experiment

The bubble dynamic similarity between water and sodium systems can be obtained by equating

the non-dimensional Weber and Froude numbers (Dickinson and Nunamaker, 1975).

Equating Weber numbers

$$\frac{\rho_w u_w^2 d_w}{\sigma_w} = \frac{\rho_{sod} u_{sod}^2 d_{sod}}{\sigma_{sod}} \tag{4.1}$$

Equating Froude numbers

$$\frac{u_w^2}{d_w g} = \frac{u_{sod}^2}{d_{sod} g} \tag{4.2}$$

The mass and momentum transport parameters determine the bubble dynamic similarity between water and sodium. Table 4.1 gives the mass and momentum transport properties of water and liquid sodium.

Table 4.1 Transport properties of water and liquid sodium

Properties	**Water**	**Sodium**
T (°C)	30	200
ρ_l (kg/m^3)	995	904.3
μ_l (Pa.s)	0.0008	0.0004
σ (N/m)	0.071	0.189

From Eqs. 4.1 and 4.2,

$$d_w = d_{sod}\left(\frac{\sigma_w \rho_{sod}}{\sigma_{sod} \rho_w}\right)^{0.5} \tag{4.3}$$

According to this similarity, the bubble diameter of 0.58-2.38 cm in water system corresponds to diameter of 1-4.1 cm in sodium system. The similarity between water and sodium systems, on the other hand, has never been investigated using bubble aspect ratio as the basis. The present

study fills the gap area of establishing quantitative similarity between bubble dynamics in sodium and water systems numerically. The bubble rise velocity is measured using conductance-based void sensors in this experiment, and the bubble aspect ratio is measured using image analysis. The experimental methodology is discussed in depth in the following sub-sections.

4.2.1 Experimental setups

Two experimental facilities are developed and used to carry out these studies. The experimental setup-I for studying 0.5 cm bubble case consists of a cylindrical tank with diameter of 10 cm and height of 80 cm as shown in fig. 4.1a.

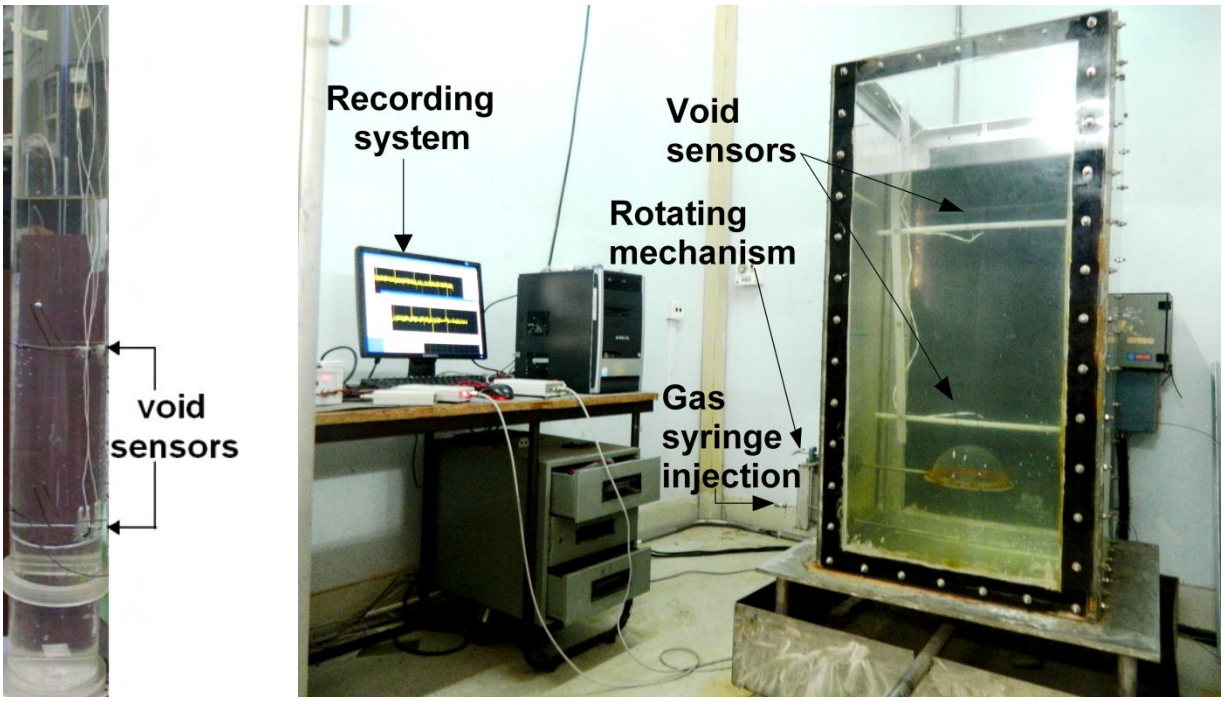

(a) (b)

Fig.4.1 Experimental setups for air bubble dynamics in water (a) I (b) II

It is made of transparent acrylic walls and provided with arrangements for filling and draining water upto desired level. Air was introduced via a nozzle at the bottom of the tank into the water column by means of syringe injection system. The air volume injected from the graduated syringe is used to determine the initial bubble volume. The experimental setup-II is used to study

rise behavior for higher bubble sizes. It comprises of a tank (see fig. 4.1b) with dimensions of 61 cm x 61 cm x 122 cm and a single bubble generating device (see fig. 4.2).

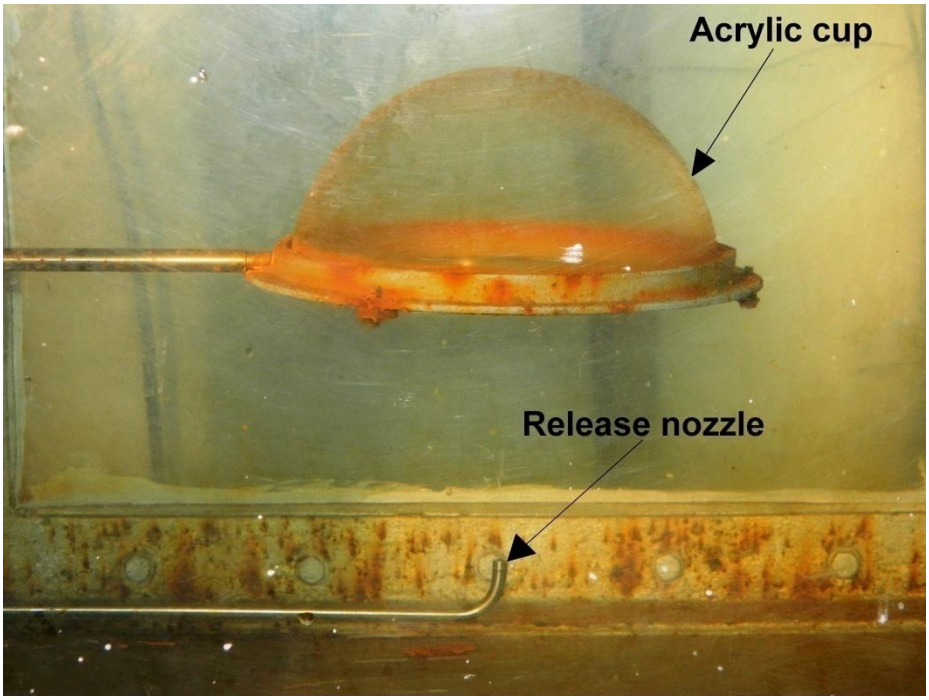

Fig.4.2 Single bubble generating system

The experimental tank made of acrylic is filled with water upto a depth of 117 cm. An acrylic cup (ID=17.8 cm) is mounted 22 cm above the tank bottom via a shaft that passes through a rotary seal housing attached to the column side wall. A plummer block kept outside the tank supports the other end of shaft which can be rotated around its axis. A nozzle made of SS tube (ID = 0.6 cm) is positioned centrally 7 cm above the tank bottom to introduce air into the cup. A compression fitting is attached at the other end of the steel tube, which consists of a rubber septum compressed between a back ferrule and the fitting nut.

The septum fitting prevented backflow of water into the syringe during air injection. The bubble is initially confined inside the cup till required air volume is injected using syringe, followed by rotating the cup to release the bubble. By controlling the rotation rate of shaft, the generation of secondary bubbles during bubble release can be avoided.

4.2.2 Void-detection sensors

The bubble rise velocities in water setups I and II are measured using void-detection sensors developed using a conductance technique. As part of a miniaturized resistance capacitance type logic gate oscillator (LGO), the conductance sensor consists of a pair of electrodes inserted in the sensing medium. In the LGO, the probe served as the resistance component of the tank circuit, while the capacitor component had a fixed value. The LGO oscillates and creates pulses of 5V amplitude when powered by 5V DC. The resistance and capacitance components of the tank circuit determine the number of pulses generated by the LGO. The change in resistance provided by bubbles flowing between the electrodes in the aqueous medium causes a change in resistance component, which is quantified in terms of pulse output from the LGO in this study. For further measurement, the pulse output is converted to frequency.

Customized conductance probes are designed and made for use in the experimental settings to detect bubble velocity. For great sensitivity and to eliminate the wall effect, wire electrodes are utilized. The bubbles travelled between the electrodes in the wire type electrodes in a few milliseconds, which is less than the gate time. During test runs, the two sets of probes are fixed apart at a given vertical distance. The change in conductance observed by the probes due to the passage of air bubbles is used to calculate the time it takes for an air bubble to move from the first to the second probe.

4.2.3 Details of instruments

Two single channel rapid counter units receive the frequency output from two void-detection sensors. A 5V DC battery power supply, optical isolator circuit, microcontroller-based data acquisition circuit (DAQ) and 5V DC regulated power supply from the mains compose the channel quick counter card that interfaces the PC and LGO. A 5V DC battery source powers

LGO, while the hardware system is powered by a controlled 5V DC mains supply (50 Hz, 230V AC). The LGO generated pulses are optically isolated to avoid ground interference with the interface counter card's mains power supply. Figure 4.3 shows a block schematic of interfacing electronics.

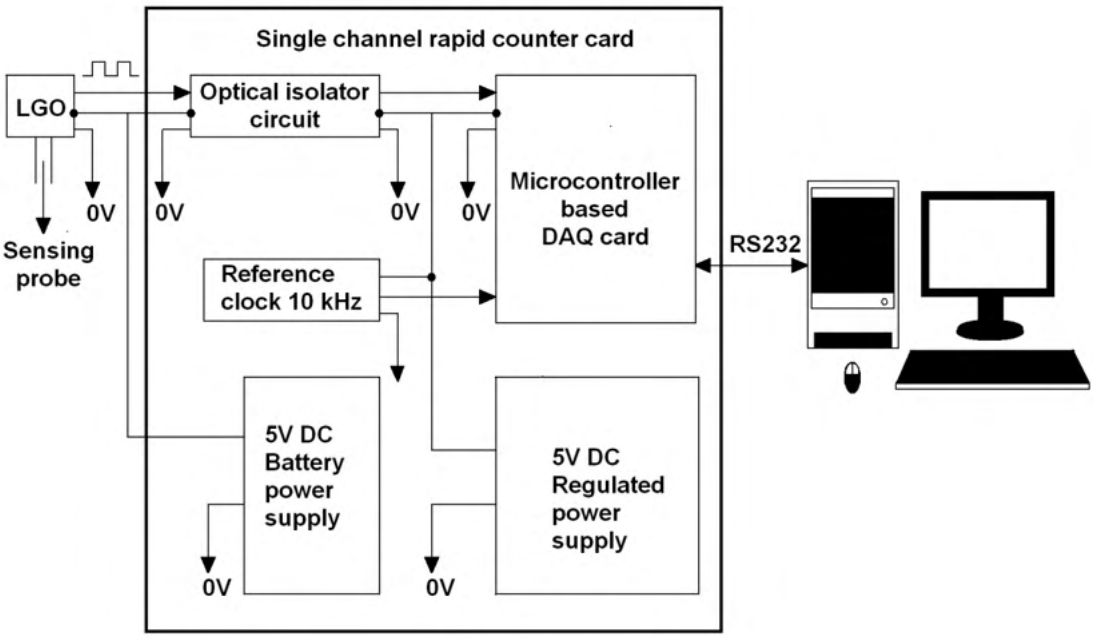

Fig.4.3 Rapid counter interface unit block diagram

Design of single channel digital pulse counter card was carried out to sample LGO pulse output with a user-defined gate time. In this study, the gate time for logging the change in frequency output from the void-detection sensors is standardized to 50 ms. The 8-bit microcontroller ATMEL 89C4051 is used in the rapid counter unit's counter card. One of the microcontroller's three 16-bit timers has been set up as a counter. A 1 MHz crystal-based frequency generator circuit is used to generate a 10 kHz reference clock. The strobe pulse for the counter is generated using this reference clock. The counter is latched every 50 milliseconds to keep track of how many pulses are generated at the LGO output.

The frequency value is calculated by dividing the number of pulses emitted by the LGO by the time period during which the pulses are counted, and the firmware is written in C++ to connect to the PC through an RS 232 serial port interface. Through the serial port on the PC, application-specific graphical user interface (GUI) software written in Visual Basic gets data from the single channel rapid counter interfacing unit. This value is plotted in real time online and recorded for later examination. Options for recording time, data logging file path, parameter display and calibration coefficients can all be customized by the user. Windows 98, 2000, and XP are all supported by the application software. Figure 4.4 depicts a screenshot of the GUI. The frequency output from two void-detection sensors is logged using two rapid counter units. A time marker is used to keep a common reference time for both GUIs. The actual travel time of bubbles recorded in the GUI is estimated separately using this reference time.

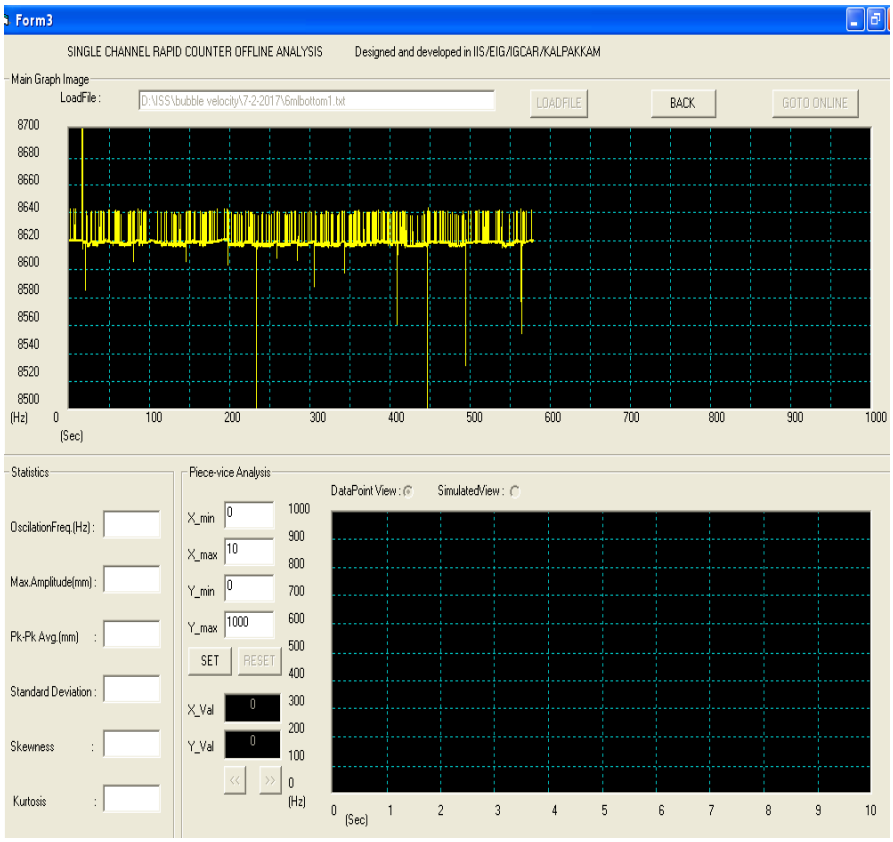

Fig.4.4 Screen capture of GUI

4.2.4 Methodology for sensing

Voids in a two-phase medium can be detected in a variety of ways, including sensing the changes in the medium's magnetic property as bubbles travel through an inductor, resistance provided by the bubbles in the conductance channel, or capacitance change induced by the bubbles while passing through the capacitor arrangement. What kind of sensor can be used to measure the bubble rise velocity depends on the intrinsic properties of the fluid and bubble dynamics. Based on water properties, it was chosen to employ conductance-based sensing approach in order to achieve greater detection capability and repeatability than other sensing approaches. The conductance-based sensors used to detect bubbles will be referred to as 'void-detection sensors' from now on. The novelty and strength of this sensing technology is its ability to precisely detect bubbles regardless of their size, shape, or course of passage. By using two void-detection sensors of the same type separated at a specified distance and sensing the existence of a bubble, it is possible to determine the bubble velocity. A dip in conductance can be seen as the bubble passes between the sensor electrodes. The sensor output is used to calculate the time difference between two such dips from two void-detection sensors. Bubble velocity is estimated using the information from the computed time difference in the basic equation of motion.

4.2.5 Electronics for sensors

The current work utilized a novel class of digital sensors called as pulsating sensors (Praveen *et al*., 2010; Sahoo *et al*., 2010; Malathi *et al*., 2015), which have been developed and applied in a variety of physicochemical applications. Pulsating sensors basic electrical response, unlike traditional sensors, is in pulse form, i.e. in the digital domain, bypassing intermediate signal processing stages like preamplification, postamplification, and analog to digital conversion. In a

physical or physicochemical system, pulsating sensors can be designed to employ one of four basic electrical properties: (i) electromotive force (ii) dielectric permeability (iii) resistance/resistivity (or conductance/conductivity) and (iv) inductance. Any parameter that indirectly/directly affects either of the above properties becomes measurable. These four independent sensing parameters allow a lot of versatility for redundantly monitoring a parameter, whether used individually or in combination. The signal output from each of these sensors is a digital pulse frequency that conveys information about the physical parameter being detected. Appropriate in situ calibration is used to determine the relationship between frequency and the sensed parameter. Pair of electrodes is put in the sensing medium and are part of the timing circuit of a tiny resistance capacitance type LGO. The sensing electrodes constitute resistance of the LGO. In the oscillator's timing circuit, a fixed value capacitor is used. When powered by 5V DC, the LGO oscillates between two logic states: "0" and "1." The LGO signal is a series of rectangular pulses with 5V amplitude from which the pulse frequency is calculated. Without any additional amplification or signal processing, these digital pulses can be interfaced with any digital input/output card for further data processing. A simplified block diagram of signal routing from the probe end to the Graphical user display in the PC is shown in Figure 4.5.

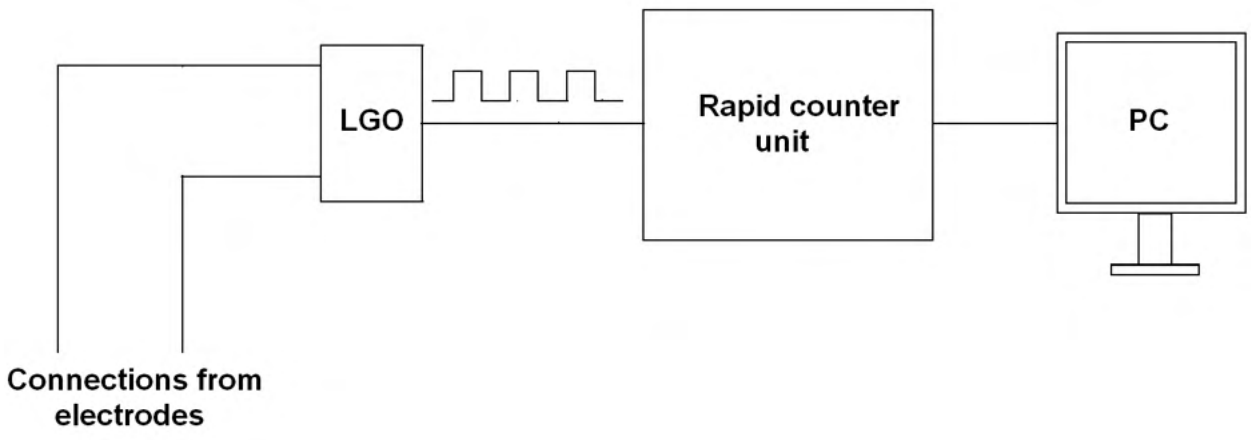

Fig.4.5 Signal flow from probe end to PC display in block diagram

4.2.6 Construction of sensing probe

The main purpose of a void-detection sensor is to determine how quickly a void rises in a static pool. As a result, the sensor for the void sensing probe is immersed in a static pool. Electrodes of various designs are already constructed and optimized for conductance-based void detection because they give good results in such situations (Aggarwal *et al*., 2012). Mesh type, ring type, and wire type electrodes were among the designs tested earlier. Because of their high sensitivity, wire electrodes were chosen to avoid the wall effect and generate more consistent results. A pair of enamel coated copper wires with a diameter of 2 mm, arranged parallel to each other, were chosen as the probe material. To ensure sufficient insulation and serve as a fixture, wires were placed into a 12 mm diameter teflon rod. Figure 4.6 shows a schematic of an electrode fixture.

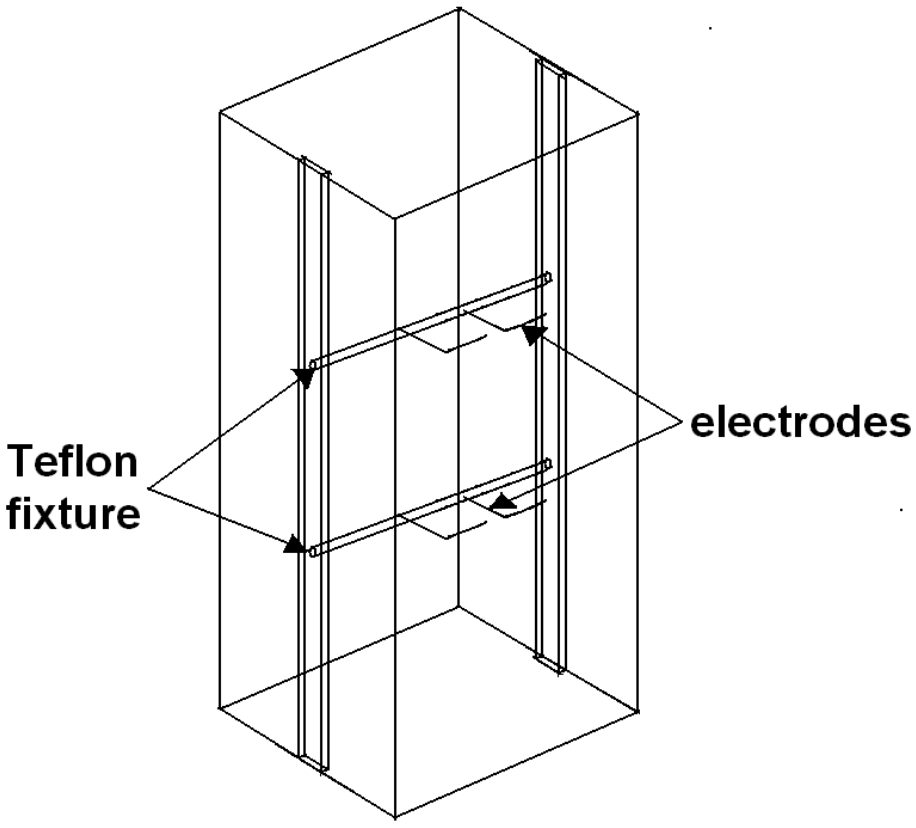

Fig.4.6 Schematic diagram of electrode fixture

Depending on the water column height, two similar electrode pairs were mounted one above the other at appropriate distances. To prevent lateral movement of the sensors, they were tightly attached with bolts at the top of the experimental tank.

4.2.7 Experimental campaign

In setup-I, there is only one campaign in the bubble rise experiment. In a water column with a specified aspect ratio, the campaign assessed the rise velocity of a 0.5 cm bubble. For the campaign, a bubble volume of 65 μl and pool height of 55 cm is used to determine the bubble rise velocity. The supporting fixtures are positioned such that the distance between two sets of conductance probes is set at 20 cm. To increase the accuracy of the rising time estimation, the tests are repeated ten times. Three campaigns make up the bubble rise experiment in setup-II. The rise velocity of three bubble sizes was measured for each campaign for a certain aspect ratio of the water column. For this experiment, bubble volumes of 2 ml, 4 ml, and 6 ml were explored. To investigate the impacts of water column aspect ratio on bubble rise velocity, three pool heights of 75 cm, 95 cm, and 107 cm are fixed. The spacing between two sets of conductance probes is modified during each campaign. Aspect ratios of 1.2, 1.5, and 1.9 are achieved by spacing the probes 25 cm, 50 cm, and 75 cm apart, respectively. To increase the accuracy of the rise time estimation, each bubble diameter test is done ten times.

4.3 Theoretical study

The next sub-sections go over the available theoretical correlations as well as an in-house numerical research that was utilized to characterize bubble dynamics.

4.3.1 Empirical correlations

Bubble dynamics are defined by the velocity, shape and size of the bubbles. In order to determine bubble terminal velocity, correlations available in the literature require information on

bubble shape, which requires information on bubble size. As indicated in table 4.2, there are several correlations available in the literature for analyzing clean water terminal velocity (Davies and Taylor, 1950; Mendelson, 1967; Talaia, 2007).

Table 4.2 Bubble terminal velocity correlations

	Shape	**Correlation**
Davies and Taylor (1950)	spherical cap	$0.707\sqrt{gd}$
Mendelson (1967)	ellipsoidal	$\sqrt{\frac{2.14\sigma}{\rho_l d} + 0.505gd}$
Talaia (2007)	spherical cap	$(0.691 \pm 0.021)\sqrt{\frac{gd\Delta\rho}{\rho_l}}$

Grace (1973) and Park *et al*. (2017) used bubble shape diagrams to show the link between bubble size and shape. As indicated in table 4.3, correlations for measuring the bubble aspect ratio of water are also available in the literature (Taylor and Acrivos, 1964; Lee and Choi, 2014).

Table 4.3 Bubble aspect ratio correlations

	Correlation
Taylor and Acrivos (1964)	$\mathbf{1}/\left(\mathbf{1}+\frac{\mathbf{5}}{\mathbf{32}}\boldsymbol{We}\right)$
Moore (1965)	$\mathbf{1}/\left(\mathbf{1}+\frac{\mathbf{9}}{\mathbf{64}}\boldsymbol{We}\right)$
Lee (2014)	$\mathbf{1.7}/(\mathbf{1}+\mathbf{1.2}\boldsymbol{Eo}^{\mathbf{0.27}})$

4.3.2 Numerical model

The correlations available in literature as mentioned in earlier sub-section are mostly developed for normal liquids and not liquid metals. Hence, the applicability of these interrelated correlations for bubble dynamic parameters in case of liquid sodium systems has to be verified

numerically. The following sub-sections illustrate the numerical studies carried out for understanding bubble dynamics.

4.3.2.1 The problem's physical description

In two-dimensional, axisymmetric, and three-dimensional domains, single bubble (fluid 2) dynamics in liquid sodium (fluid 1) pools are investigated numerically. Figure 4.7 shows the geometry and boundary conditions used for simulations in both two-dimensional and three-dimensional domains.

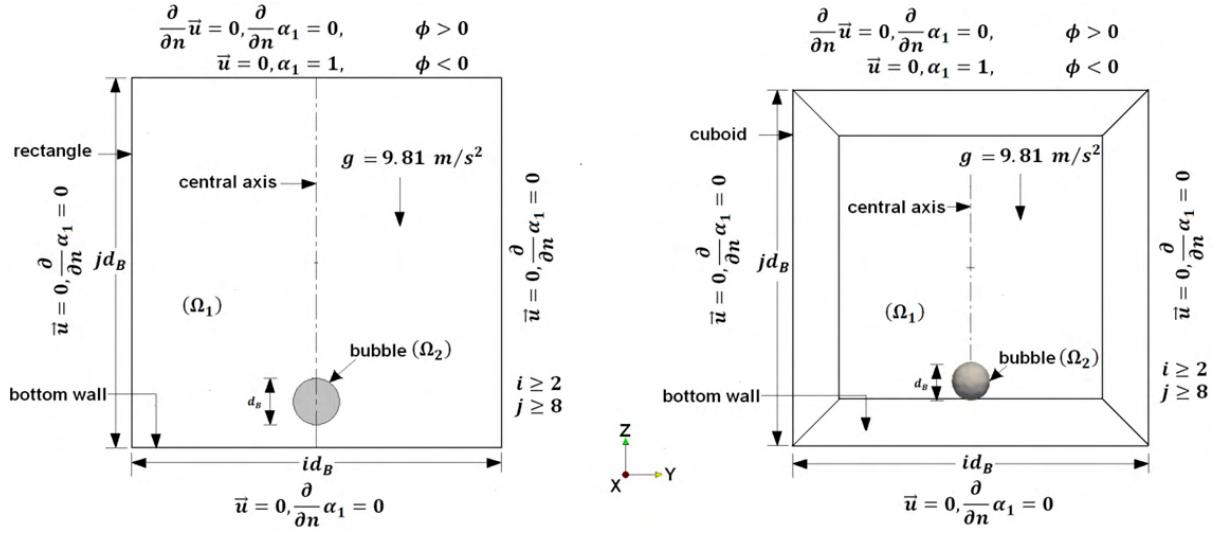

(a) (b)

Fig.4.7 Computational domain (a) 2-D (b) 3-D

The spherical bubble, with a diameter of d_B, is placed at $0.5d_B$ above the bottom wall, along the central vertical axis. The analysis takes into account a gravitational acceleration of 9.81 m/s^2. The current study focuses on the gas bubble and liquid pool's thermal equilibrium condition.

4.3.2.2 Method of computation

The interFoam solver (Damián, 2012) from OpenFOAM version 3.0.0 (Greenshields, 2016), an open source CFD application, is used to numerically investigate the ascent of an inert gas bubble in a liquid sodium pool.

4.3.2.2.1 Equations that govern

The mass, momentum, and phase fraction conservation equations are listed below.

Equation of continuity

$$\nabla \cdot \vec{u} = 0 \tag{4.4}$$

$$\vec{u} = \alpha_1 \vec{u}_1 + (1 - \alpha_1)\vec{u}_2 \tag{4.5}$$

The volume fraction of fluid 1

$$\alpha_1 = \begin{cases} 1 & in\ fluid\ 1 \\ 0 & in\ fluid\ 2 \\ 0 < \alpha_1 < 1 & at\ the\ interface \end{cases} \tag{4.6}$$

Momentum equation

$$\frac{\partial(\rho\vec{u})}{\partial t} + \nabla \cdot (\rho\vec{u}\vec{u}) = -\nabla p_{rgh} + \nabla \cdot [\mu(\nabla\vec{u} + (\nabla\vec{u})^{\mathrm{T}})] - \vec{g} \cdot \vec{x}\nabla\rho + \sigma\kappa\nabla\alpha_1 \tag{4.7}$$

$$\rho = \alpha_1\rho_1 + (1 - \alpha_1)\rho_2 \tag{4.8}$$

$$\mu = \alpha_1\mu_1 + (1 - \alpha_1)\mu_2 \tag{4.9}$$

$$p_{rgh} = p - \rho\vec{g} \cdot \vec{x} \tag{4.10}$$

Volume fraction equation for phase 1 (Damián, 2012)

$$\frac{\partial\alpha_1}{\partial t} + \nabla \cdot (\vec{u}\alpha_1) + \nabla \cdot [\vec{u}_r\alpha_1(1 - \alpha_1)] = 0 \tag{4.11}$$

$$\vec{u}_r = \vec{u}_1 - \vec{u}_2 \tag{4.12}$$

curvature of the interface is given by,

$$\kappa = -\nabla \cdot \hat{n} = -\nabla \cdot \left(\frac{\nabla\alpha_1}{|\nabla\alpha_1|}\right) \tag{4.13}$$

4.3.2.2.2 Conditions at boundaries

A no-slip boundary condition has been added to the bottom and side walls. The gradient of the volume fraction of fluid 1 in the direction normal to the wall boundary has been set to zero, as has the velocity. Based on the velocity boundary condition anticipated boundary flux (ϕ), the

gradient of pressure normal to the wall boundary is determined. The top barrier is open to the atmosphere, allowing in and outflow. As a result, the upper boundary is subjected to a mixed boundary condition. Outflow has a fluid 1 volume fraction gradient of zero in the direction corresponding to the top boundary, whereas inflow has a fluid 1 volume fraction of unity. For outflow ($\phi > 0$), the gradient of velocity in the direction normal to the top boundary is set to zero, and for inflow ($\phi < 0$), velocity is set to zero. By subtracting the dynamic pressure from the required total pressure, the static pressure at the top boundary is derived.

4.3.2.2.3 Method of solving

The interFoam solver solves the governing conservation equations by combining the volume of fluid (VOF) method (Hirt and Nichols, 1981) with surface compression (Brackbill *et al*., 1992). Klostermann *et al*. (2013) explains the interFoam solver's algorithm and the discretization of governing equations in great detail (2013).

4.3.2.2.3a Details of discretization

The implicit Euler approach is utilized for temporal discretization and the finite volume gaussian integration approach is employed for spatial discretization. The convective term in the momentum equation is interpolated using a limited linear technique. The van Leer scheme (Van Leer, 1979) and a specific interface compression strategy were utilized to interpolate the first and second convective terms in the phase fraction equation, resulting in smoother interfaces. To keep the volume fraction limited when solving volume fraction equations, the Multidimensional universal limiter for explicit solution (MULES) technique is used (Damián, 2012).

4.3.2.2.3b Algorithm for solution

PIMPLE (merged pressure implicit with splitting of operator (PISO) and semi implicit method for pressure linked equations (SIMPLE) algorithm) is used for pressure velocity coupling. It has

three correction steps for pressure and two sub-cycles for interface correction. The PIMPLE method has two loops, one inner and one outer, in which the outer loop solves all equations and the inner loop only solves the continuity equation. To obtain time accuracy, the pressure equation is solved in the outer loop for three correction steps. For transitory flow, the total number of loops over fluid 1 volume fraction equals one, and the number of sub-cycles for which fluid 1 volume fraction is calculated equals two. In the phase fraction equation, conservative compression is utilized for the compression term. Pressure correction, first pressure loop, second and last pressure loops, and the velocity equation are among the equations that have been solved. For velocity equations containing asymmetric matrices, the preconditioned bi-conjugate gradient (PBiCG) with diagonal incomplete-lower upper (DILU) preconditioner is employed, while for pressure equations containing symmetric matrices, the diagonal incomplete cholesky (DIC) preconditioned conjugate gradient is employed.

4.3.2.2.3c Details of computation

The computer used for simulation has an Intel Core 2 Duo processor running at 2.4 GHz and 4 GB of RAM, and it runs Ubuntu 14.04 OS. For a grid size of 544 x 544, the typical computational time for a 10 mm argon bubble in a two-dimensional domain of liquid sodium is 4 days. For a grid size of 128 x 128 x 128, the typical calculation time for a 10 mm argon bubble growing in a three-dimensional domain of liquid sodium is 4 days.

4.3.2.3 Data processing after simulation

The Swiss Army Knife for Foam (swak4Foam) toolbox is used for post-processing. The user can apply a few conditions to the retrieved data, as well as construct expressions that incorporate the fields, using the toolbox. In this study, the center of mass (COM) position coordinates of the

bubble and the bubble rise velocity in the y direction were analyzed using swak4Foam. The following equation is used to calculate the bubble's center of mass location coordinates.

$$\vec{X}_c = \frac{\int_{\Omega_1 \cap \Omega_2} \alpha_1 \vec{x}_c dA}{\int_{\Omega_1 \cap \Omega_2} \alpha_1 dA} \tag{4.14}$$

where, $\vec{x}_c = (x_c, y_c)$ denotes the individual cell's center of mass position in the computational mesh. Dividing the axial displacement of the center of mass by the rise time at any given moment yields the average bubble rise velocity.

In the *y* direction, the bubble rise velocity is given as:

$$U_y = \frac{\int_{\Omega_1 \cap \Omega_2} \alpha_1 u_y dA}{\int_{\Omega_1 \cap \Omega_2} \alpha_1 dA} \tag{4.15}$$

where u_y signifies a single computational mesh cell's velocity in the *y* direction. The terminal velocity is computed by averaging the non-fluctuating rise velocity readings.

4.3.2.4 Computational domain

Numerical simulations are carried out using two-dimensional, axisymmetric and three-dimensional domains to investigate the dependence of bubble dynamics on size of computational domain.

4.3.2.4.1 Effect of domain aspect ratio for 2-D case

The effect of domain aspect ratio on bubble dynamics in the argon-sodium system in 2-D is studied using simulations. By altering the domain height and width independently, the effect of aspect ratio on bubble dynamics is investigated in depth.

4.3.2.4.1a Domain height effect

For a fixed domain width of 160 mm, the aspect ratio is adjusted by adjusting the height of the domain. For the purposes of analysis, the domain aspect ratios of 1, 1.25, and 1.5 for a fixed

bubble diameter of 20 mm are used. Figures 4.8 and 4.9 depict the temporal fluctuation of bubble dynamics as a function of cavity aspect ratio by varying domain height. Figure 4.8 demonstrates that for all aspect ratios studied, the 20 mm bubble rise velocity reaches 0.2 m/s in 0.025 s.

As shown in fig. 4.9a, the highest horizontal deviation from the central axis is ~4% at half width of the domain cavity and is inconsequential. The rising trajectory of the 20 mm bubble is thus rectilinear, regardless of the aspect ratio investigated. Figure 4.9b further shows that the difference in rise height between *AR* = 1.5 and *AR* = 1 at 0.425 s is less than 1%, indicating that the deviation is minor.

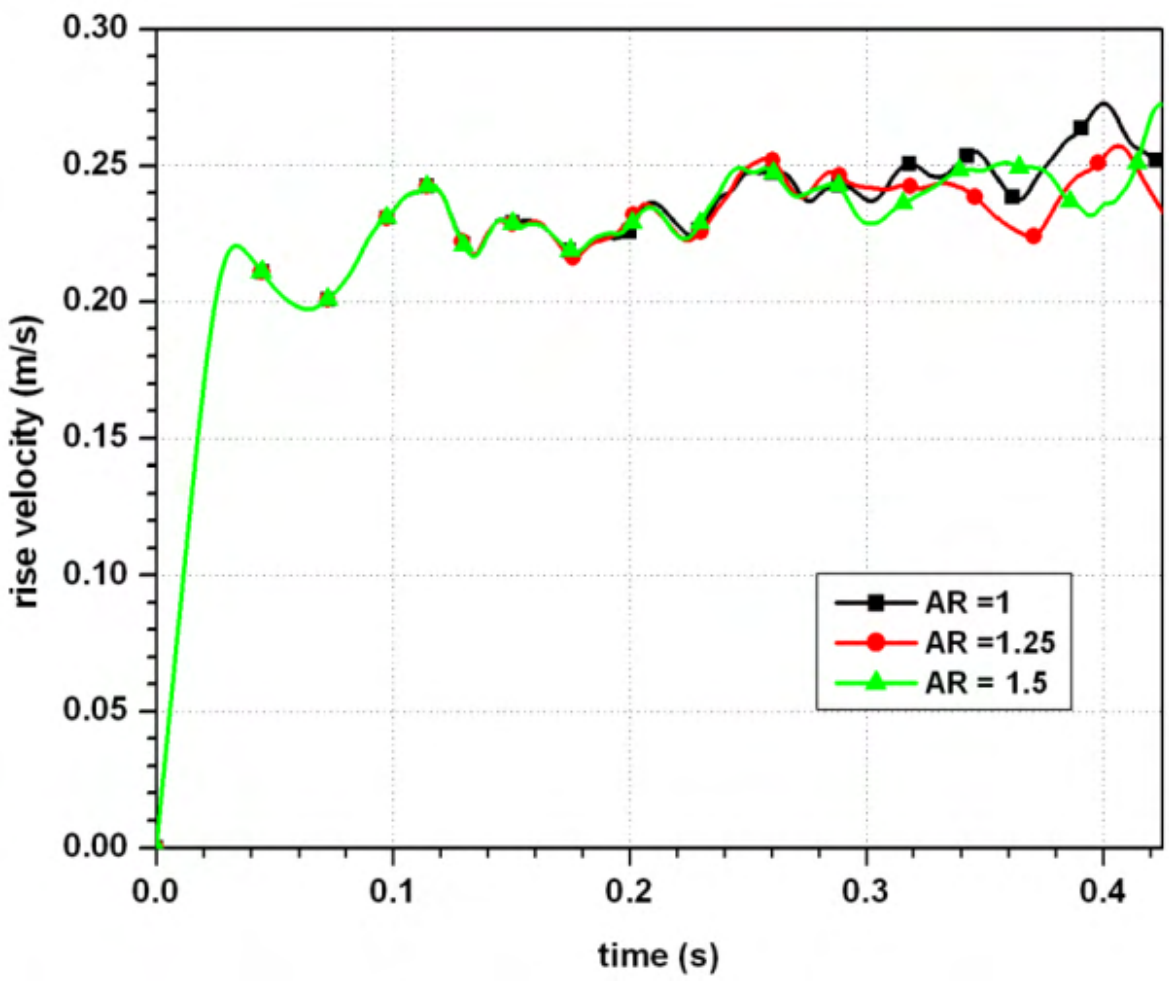

Fig.4.8 Bubble rise velocity variation with domain height for 2-D case

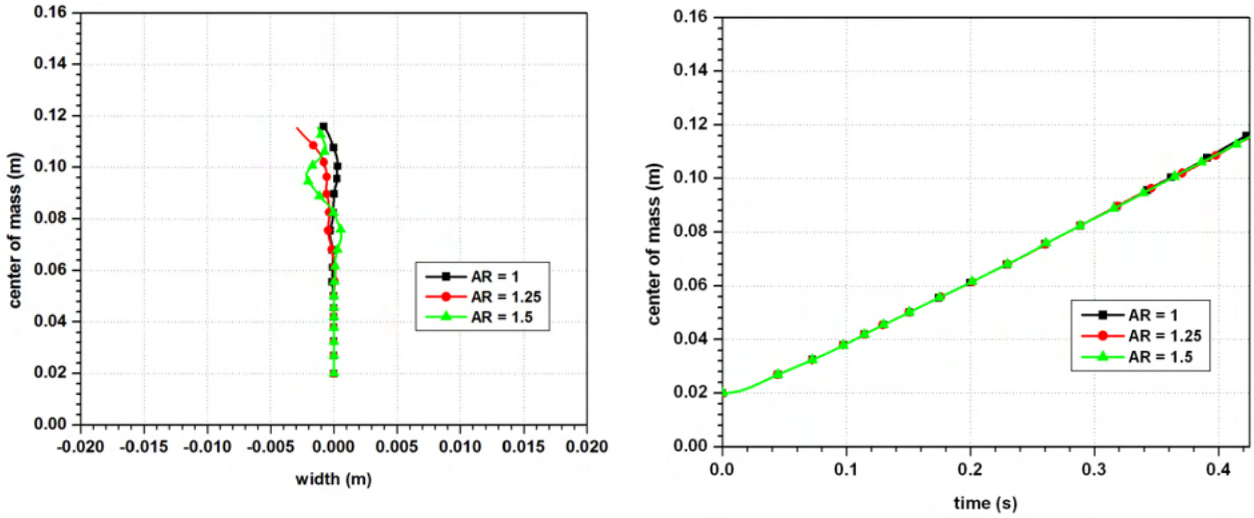

(a) (b)

Fig.4.9 Bubble (a) path (b) rise height variation with domain height for 2-D case

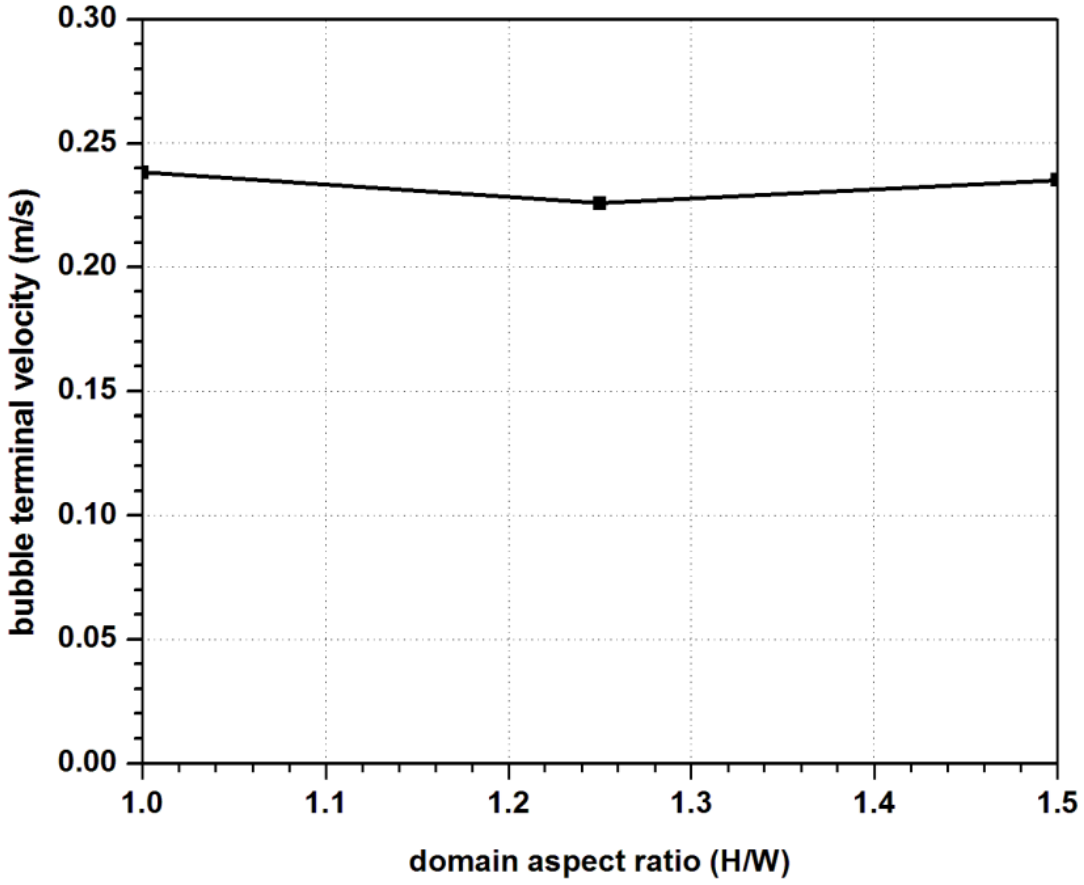

Fig.4.10 Terminal velocity variation with domain height for 2-D case

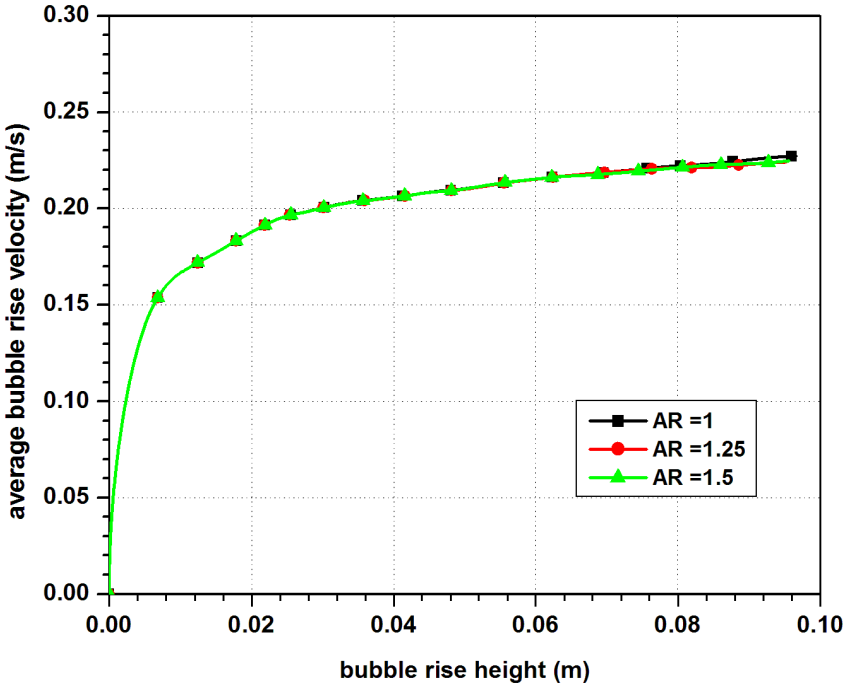

Fig.4.11 Average bubble rise velocity variation with domain height for 2-D case

As illustrated in fig. 4.10, the average bubble terminal velocity is 0.23 m/s for aspect ratios of 1 to 1.5 for varied domain height. For AR = 1 and 1.5, the terminal velocity is found to be 0.238 m/s and 0.235 m/s, respectively, with no significant difference between them. Figure 4.11 shows the variation in average rise velocity with rise height of a 20 mm bubble for various aspect ratios as a function of domain height. The domain height of $8d_B$ is hence clearly suitable for bubble dynamic simulation in this investigation.

4.3.2.4.1b Domain width effect

This section presents the results of the effect of domain width for a fixed domain height of 160 mm. For a given bubble diameter of 20 mm, the three domain aspect ratios examined for the analysis are 0.73, 1 and 1.6. Figures 4.12 and 4.13 depict the temporal fluctuation of bubble dynamics as a function of cavity aspect ratio for varied domain width.

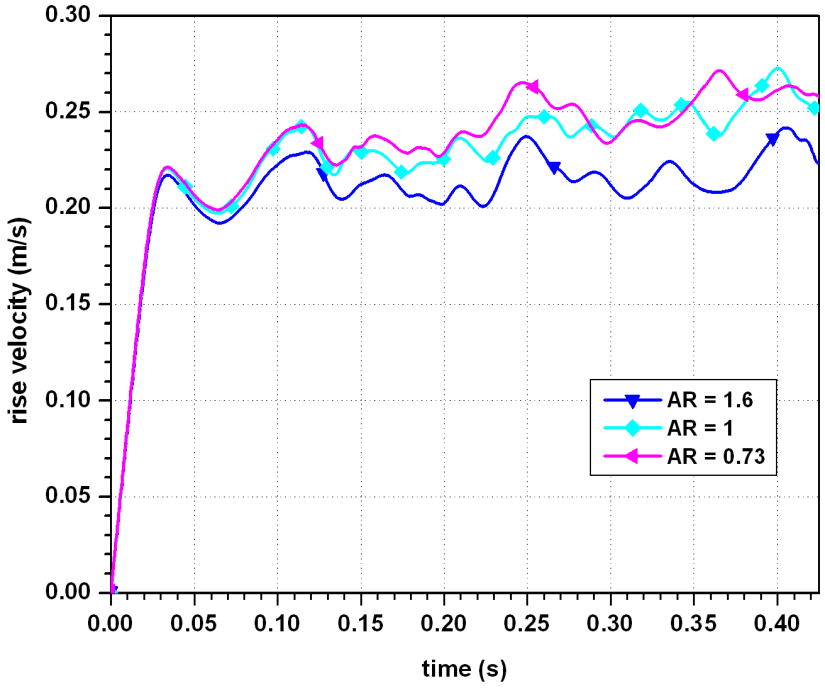

Fig.4.12 Bubble rise velocity variation with domain width for 2-D case

The rise velocity for a 20 mm bubble size reaches 0.2 m/s in 0.025 s for all aspect ratios examined, as shown in fig. 4.12. The largest horizontal deviation from the central axis at the half width of the domain cavity for an aspect ratio of 0.73 is 4.2 percent, while the least divergence is 0.75 percent for an aspect ratio of 1.6, which is modest, as shown in fig. 4.13a. The rise trajectory of the 20 mm bubble is thus rectilinear for aspect ratios of 1 and 1.6. At 0.425 s, the bubble rise height for *AR* = 1 and 1.6 is 10.1 percent and 1.9 percent lower than that for *AR* = 0.73. (fig. 4.13b). For a range of aspect ratios from 0.73 to 1.6 for varied domain widths, the average terminal velocity is 0.24 m/s (fig. 4.14).

For *AR* = 1.6, the terminal velocity is 0.22 m/s, which is 13.6 percent lower than the terminal velocity of 0.25 m/s obtained for *AR* = 0.73. Figure 4.15 shows the fluctuation of average rise velocity with rise height of 20 mm bubble as a function of domain width for various aspect

ratios. To eliminate wall effects, the investigation reveals that a minimum domain width of $W = 8d_B$ must be provided.

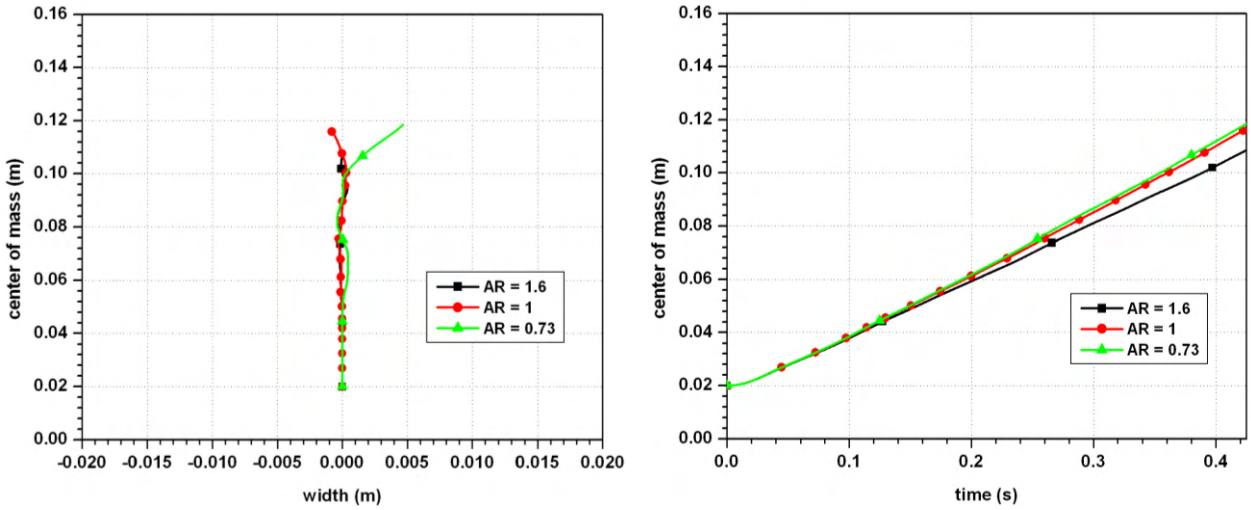

(a) (b)

Fig.4.13 Bubble (a) path (b) rise height variation with domain width for 2-D case

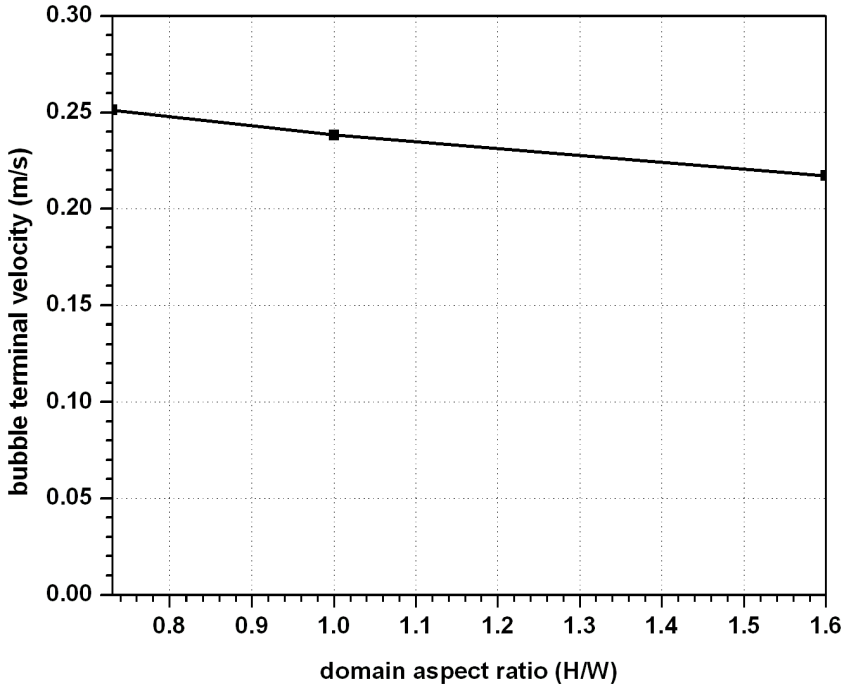

Fig.4.14 Terminal velocity variation with domain width for 2-D case

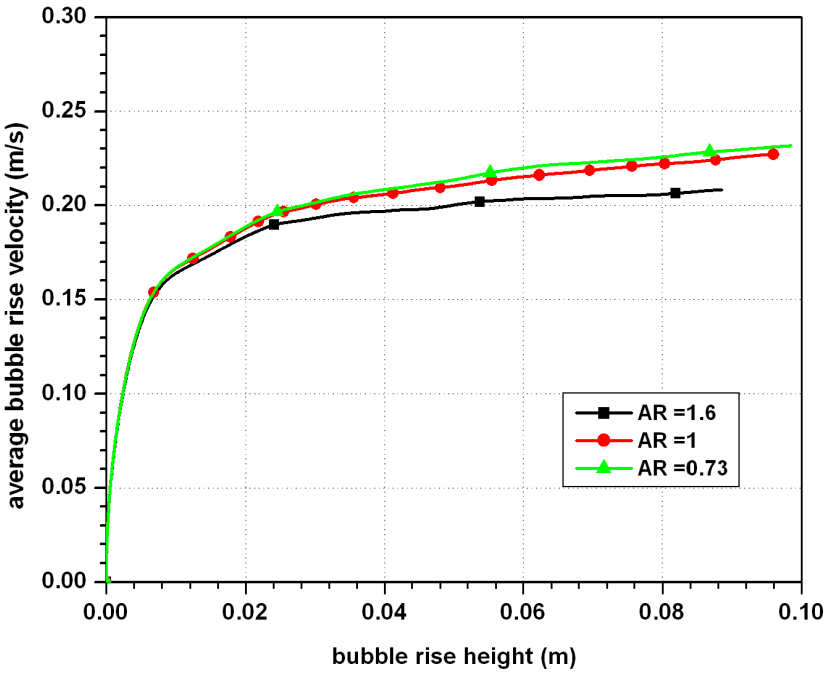

Fig.4.15 Average bubble rise velocity variation with domain width for 2-D case

4.3.2.4.2 Effect of domain aspect ratio for 2-D axisymmetric case

The effect of domain aspect ratio on bubble dynamics in the argon-sodium system in a 2-D axisymmetric scenario is studied using simulations. By altering the domain height and width independently, the effect of aspect ratio on bubble dynamics is investigated in depth.

4.3.2.4.2a Domain width effect

To explore the effects of the sidewall on bubble behavior, the physical diameter of vessel, W, is increased from $6d_B$ to $10d_B$ corresponding to model domain widths of $3d_B$ to $5d_B$ respectively. Figures 4.16a and 4.16b show the temporal fluctuation of instantaneous rising bubble velocity and center of mass for a 0.9 cm argon bubble rising in sodium. For the three domain widths tested, the bubble behavior is observed to be in close agreement. As a result, the study demonstrates that in axisymmetric simulations, $W = 8d_B$ is sufficient to eliminate side wall effect.

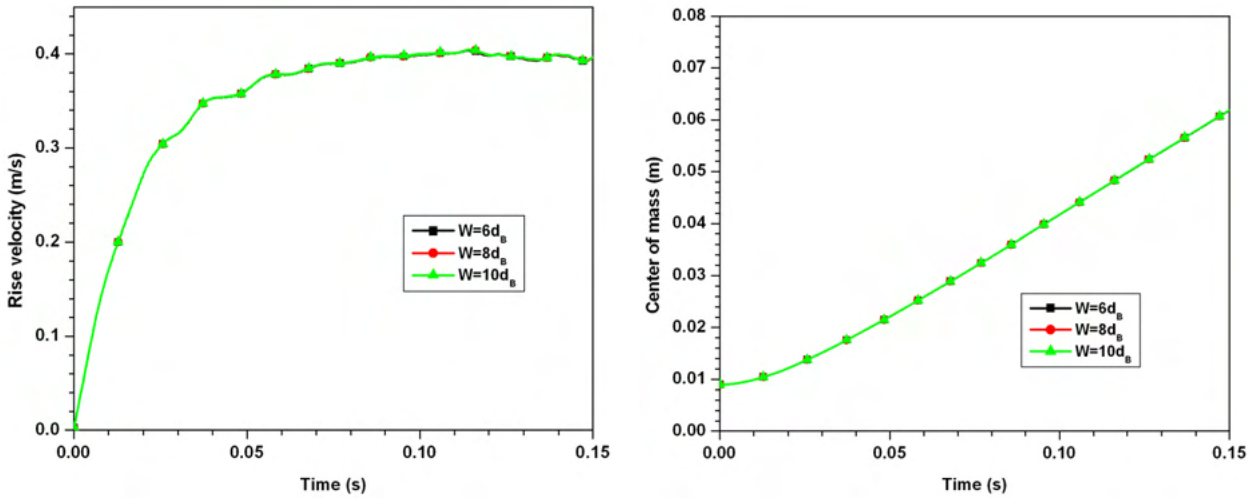

(a) (b)

Fig.4.16 Bubble (a) instantaneous rise velocity (b) COM variation with domain width for 2-D axisymmetric case

4.3.2.4.2b Domain height effect

The solution domain height, H is varied from $6d_B$-$10d_B$, so that the effect on bubble behavior can be studied. For a 0.9 cm argon bubble rising in sodium, figure 4.17 depicts the temporal fluctuation of bubble dynamics in terms of instantaneous rising velocity and center of mass.

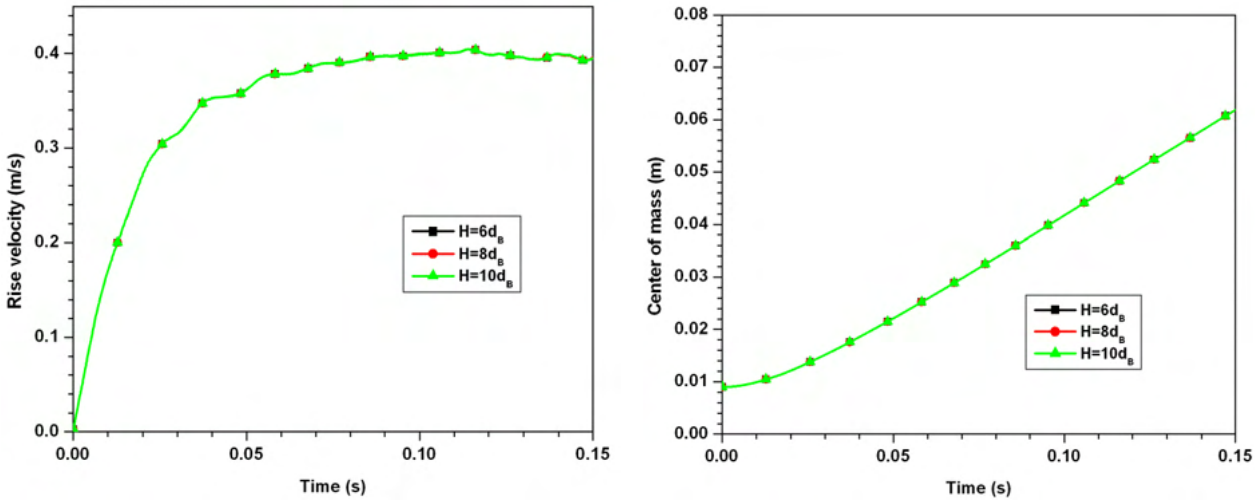

(a) (b)

Fig.4.17 Bubble (a) instantaneous rise velocity (b) COM variation with domain height for 2-D axisymmetric case

For the three domain heights tested, the bubble behaviour is observed to be in close agreement. As a consequence of the research, it was discovered that an $8d_B$ domain height is sufficient for the bubble to attain terminal velocity.

4.3.2.4.3 Effect of domain aspect ratio for 3-D case

The effect of domain aspect ratio on bubble dynamics in the argon-sodium system in 3-D is studied using simulations. By altering the domain height and width independently, the effect of aspect ratio on bubble dynamics is investigated in depth.

4.3.2.4.3a Domain width effect

To explore the effects of the sidewall on bubble behavior, the domain width, W, is increased from $6d_B$ to $10d_B$. Figures 4.18a and 4.18b show the temporal fluctuation of instantaneous rising bubble velocity and center of mass for a 0.9 cm argon bubble rising in sodium. For the three domain widths tested, the bubble behaviour is observed to be in close agreement. As a result, the research shows that an $8d_B$ domain width is sufficient to prevent side wall effect.

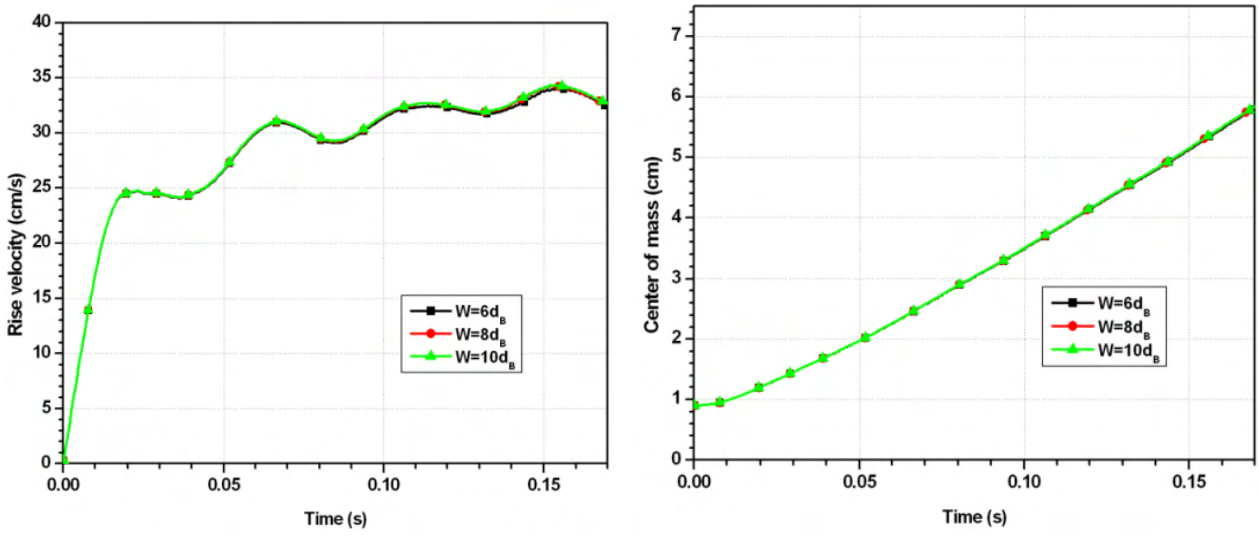

(a) (b)

Fig.4.18 Bubble (a) instantaneous rise velocity (b) COM variation with domain width for 3-D case

4.3.2.4.3b Domain height effect

To explore the effect on bubble behavior, the height of the solution domain, H, is increased from $6d_B$ to $10d_B$. Figures 4.19a and 4.19b demonstrate the temporal variation of bubble dynamics in terms of instantaneous bubble rise velocity and center of mass for a 0.9 cm argon bubble rising in sodium. For the three domain heights tested, the bubble behaviour is observed to be in close agreement. As a result, the study reveals that a domain height of $8d_B$ is sufficient for the bubble to attain terminal velocity in 3-D case.

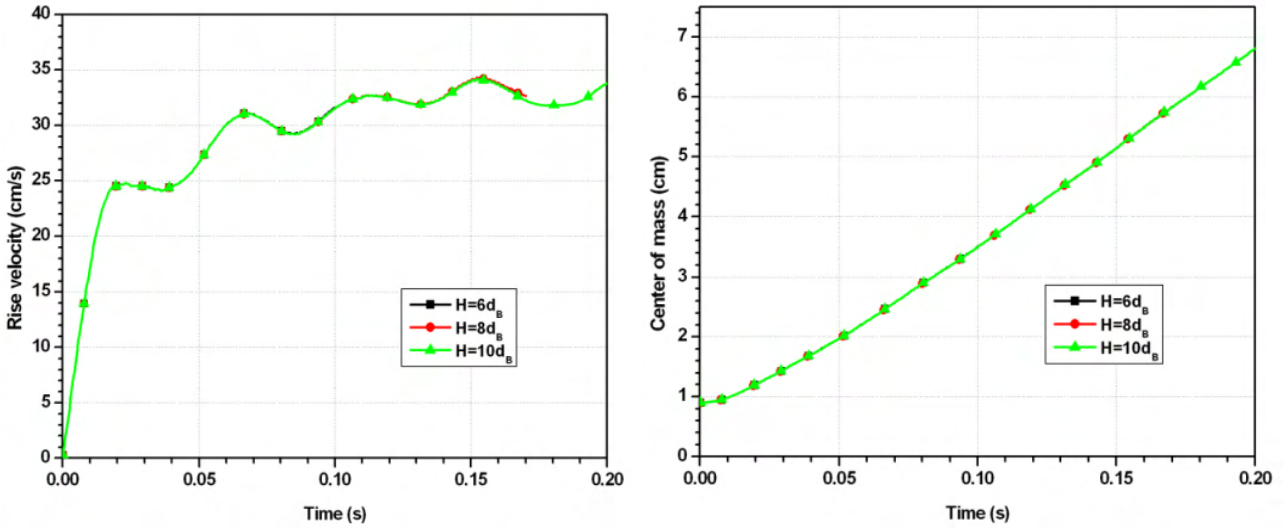

(a) (b)

Fig.4.19 Bubble (a) instantaneous rise velocity (b) COM variation with domain height for 3-D case

4.4 Grid sensitivity study

The grid size for simulating bubble rise in quiescent liquid sodium pool is determined through a grid sensitivity research. The studies are carried out for argon gas bubble rising in liquid sodium pool by evaluating temporal variation of rise velocity and center of mass position. The results of two-dimensional, axisymmetric and three-dimensional domains for different grid sizes are presented in the following sub-sections.

4.4.1 Grid independence for 2-D case studies

For the two-dimensional investigation, an argon gas bubble with an initial diameter of 20 mm is used. A domain height and width of 160 mm is considered for the study. At 200 °C, the thermophysical characteristics of sodium (Na) and argon (Ar) are assessed. For the current system, grid sensitivity is achieved by modelling the case for three grid sizes: 576 × 576 (fine), 544 x 544 (medium) and 512 x 512 (coarse). In fig. 4.20, the study's results for various grid sizes are compared.

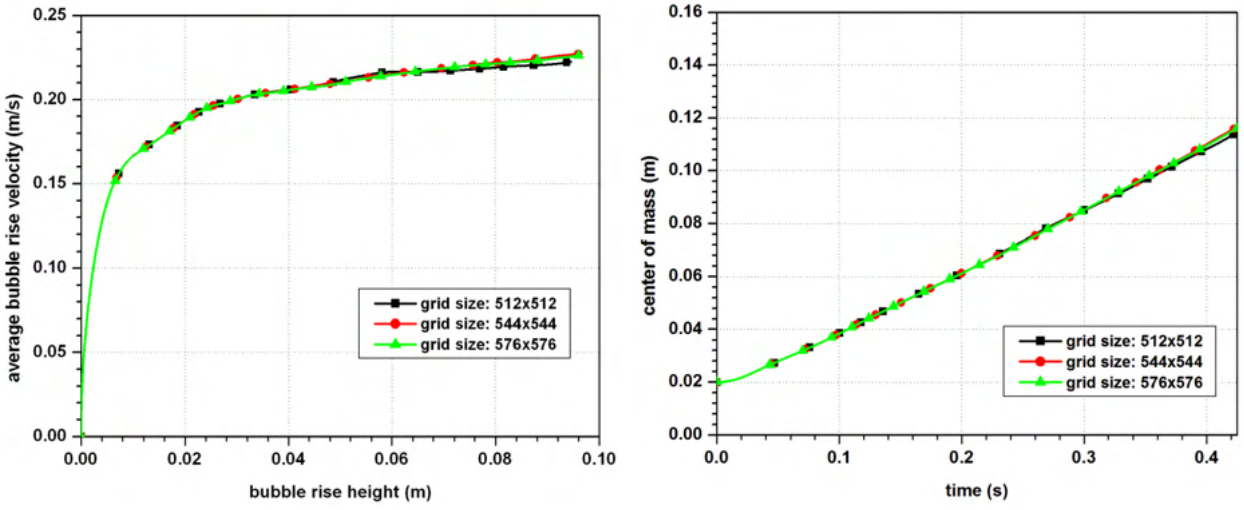

(a) (b)

Fig.4.20 Bubble (a) average rise velocity (b) COM variation with mesh size for 2-D case

Figures 4.20a and 4.20b show that the average bubble rise velocity and center of mass position are nearly identical for all three grid sizes investigated. As a result, in this investigation, a domain with a grid size of 544 × 544 was used. Simulating a grid size of 544 × 544 takes around 4 days of computation time.

4.4.2 Grid independence for 2-D axisymmetric case studies

For the argon-sodium system, the dynamics of a 0.9 cm bubble in a 2-D axisymmetric domain with dimensions of $4d_B$ x $8d_B$ are explored. The study was carried out using three grids, coarse

(150 x 350), medium (200 x 400) and fine (250 x 450). Figure 4.21a demonstrates that the greatest percentage departure of the medium grid from the coarse grid in the case of rising velocity is 6.5 percent, whereas the maximum percentage deviation of the fine grid from the medium grid is only 3.9 percent. The highest percentage divergence of the medium grid from the coarse grid in the case of the center of mass is 1.5 percent, as shown in Figure 4.21b. The fine grid, on the other hand, only accounts for 0.6 percent of the medium grid. In 2-D axisymmetric cases, the medium grid (200 x 400) is chosen based on the grid independence analysis.

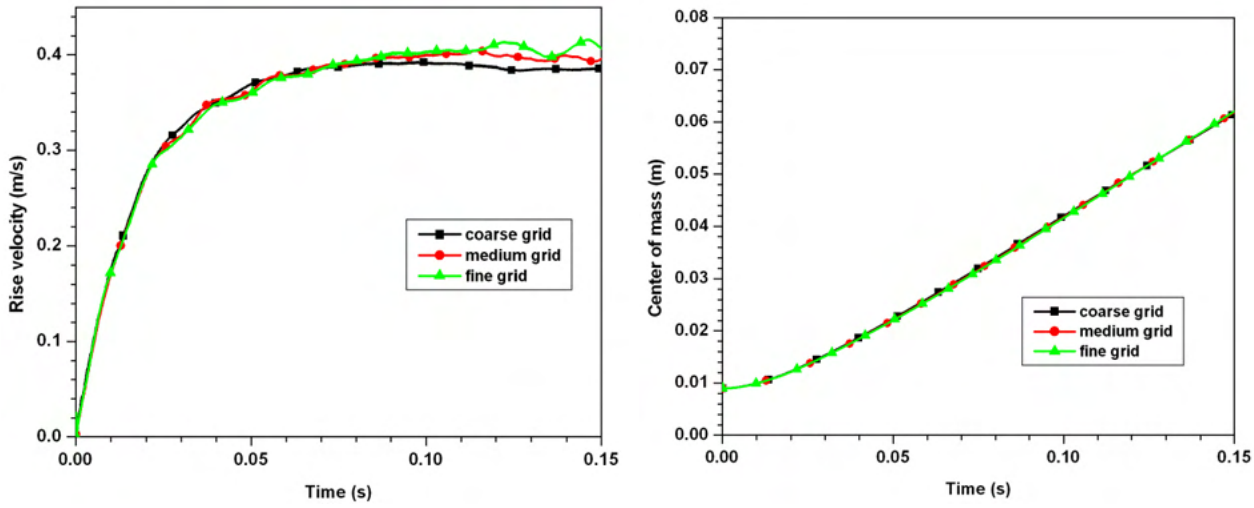

(a) (b)

Fig.4.21 Bubble (a) instantaneous rise velocity (b) COM variation with mesh size for 2-D axisymmetric case

4.4.3 Grid independence for 3-D case studies

In a 3-D cubic domain with dimensions of $8d_B$ x $8d_B$ x $8d_B$, the dynamics of a 0.9 cm bubble are investigated for the argon-sodium system. The research was conducted using three distinct grids: fine (144 x 144 x 144), medium (128 x 128 x 128) and coarse (112 x 112 x 112). Figure 4.22a demonstrates that the highest percentage departure of the medium grid from the coarse grid in the case of rising velocity is 8.3 percent, whereas the maximum percentage deviation of the fine grid from the medium grid is only 3.4 percent. Figure 4.22b indicates that the greatest percentage

departure of the medium grid from the coarse grid is 1.3 percent, whereas the highest percentage departure of the fine grid from the medium grid is just 0.4 percent. For the current 3-D domain simulation, a medium grid of 128 x 128 x 128 was chosen after extensive grid independence investigation.

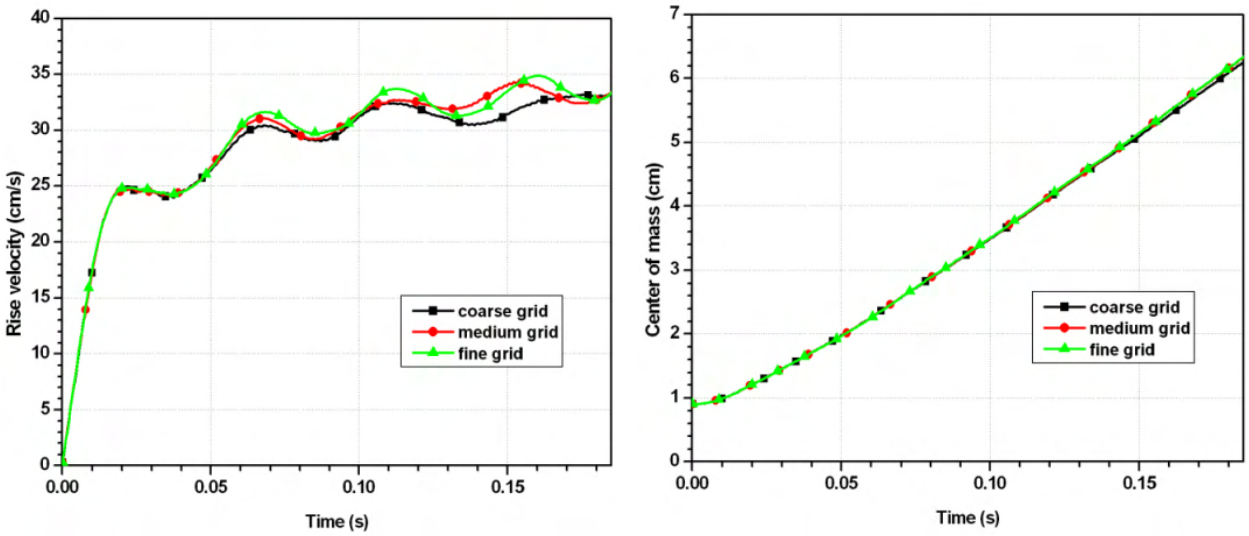

(a) (b)

Fig.4.22 Bubble (a) instantaneous rise velocity (b) COM variation with mesh size for 3-D case

4.5 Verification and validation studies

The numerical benchmark results available in literature for rising bubble are used to verify the interFoam solver utilized in this study. The solver is additionally validated against published correlations as well as in-house experimental data. The following sub-sections go into the numerical verification and experimental validation of the solver for 2-D and 3-D domains.

4.5.1 Solver verification

The interFoam solver's VOF module is verified using two-dimensional and three-dimensional numerical benchmark results for single bubble dynamics from the literature. The verification domain is 2 metres in height and 1 metre in width, and it is filled with fluid 1. In the domain, a bubble holding fluid 2 is initially positioned with its center of mass at 0.5 m above the bottom

wall along the central axis. For d_B = 0.5 m, verification studies are conducted using two benchmark cases: (1) high surface tension and (b) low surface tension. The fluid properties in each of the benchmark cases are as shown in table 4.4.

Table 4.4 Two benchmark validation cases fluid characteristics

Case	1	2
Density of fluid 1 (kg/m^3)	1000	1000
Density of fluid 2 (kg/m^3)	100	1
Viscosity of fluid 1 (kg/ms)	10	10
Viscosity of fluid 2 (kg/ms)	1	0.1
Surface tension (kg/s^2)	24.5	1.96
Gravitational acceleration (m/s^2)	0.98	0.98

The top and bottom boundaries have no-slip ($\vec{u} = 0$) conditions, while the side boundaries have slip conditions. In the direction normal to the top, bottom, and side boundaries, the gradient of volume fraction of fluid 1 is set to zero. For the top and bottom boundaries, the velocity is set to zero. The normal velocity component is set to zero, and the gradient of the tangential velocity component in the normal direction is set to zero in the slip boundary conditions for the side wall. The dynamic pressure gradient in the direction normal to the bottom and side borders is set to zero, and the top boundary is set to constant pressure.

4.5.1.1 Two-dimensional numerical verification

Hysing *et al*. (2009) used FreeLIFE, MooNMD and TP2D numerical codes to produce quantitative 2-D benchmark solutions of bubble rise dynamics for two different cases. To track the location of the interface between two fluids, the TP2D (transport phenomena in 2D) algorithm and FreeLIFE (free-surface library of finite element) use finite element (FE) discretization using a level set technique. MooNMD (mathematics and object-oriented numerics

in magdeburg) is also based on FE discretization and uses the arbitrary Lagrangian Eulerian (ALE) technique to analyse incompressible two-phase flows. TP2D and FreeLIFE numerical benchmarks have grid sizes of h = 1/320 and h = 1/160, respectively, with time steps of h/16 and h/2. Štrubelj *et al*. (2009) adopts an enhanced two-fluid model with a conservative level set method to sharpen the interface. Klostermann *et al*. (2013) used VOF technique in OpenFOAM version 1.5.1 to perform numerical simulations for the two different benchmark situations. Klostermann *et al*. (2013) employed a grid size of h = 1/320 with a time step of h/2. The benchmark cases 1 and 2 are investigated using four alternative mesh sizes, h = 1/40, 1/80, 1/160, and 1/320, in order to verify the interFoam solver with current discretization schemes. As indicated in table 4.5, a grid size dependent time step of $t = h/16$ is used for simulating bubble rise time (t_{final}) of 3 s.

Table 4.5. Computation parameters for 2-D benchmark verification cases.

Grid refinement (1/h)	40	80	160	320
number of elements	3200	12800	51200	204800
time step (Δt)	1.5×10^{-3}	7.8×10^{-4}	3.9×10^{-4}	1.9×10^{-4}
Computation time for case 1	3.5 minutes	52 minutes	13.5 hour	13 days
Computation time for case 2	3.7 minutes	1.7 hour	10.1 hour	12 days

Table 4.5 shows the compute times for both test scenarios for a better understanding of the operating system's computing performance. The bubble profile produced for benchmark case 2 at t = 3 s is compared to the forms computed by other authors (fig. 4.23). Although the shapes are very close, it is impossible to determine the solver verification just on a visual qualitative comparison.

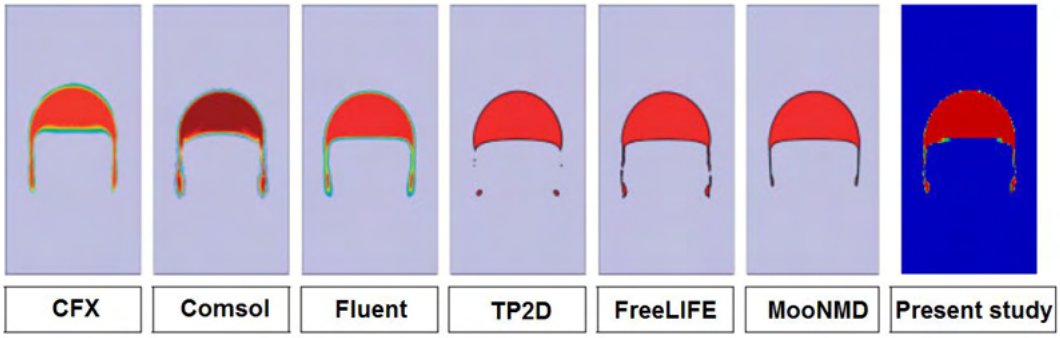

Fig.4.23 Qualitative verification of case 2 for 2-D case

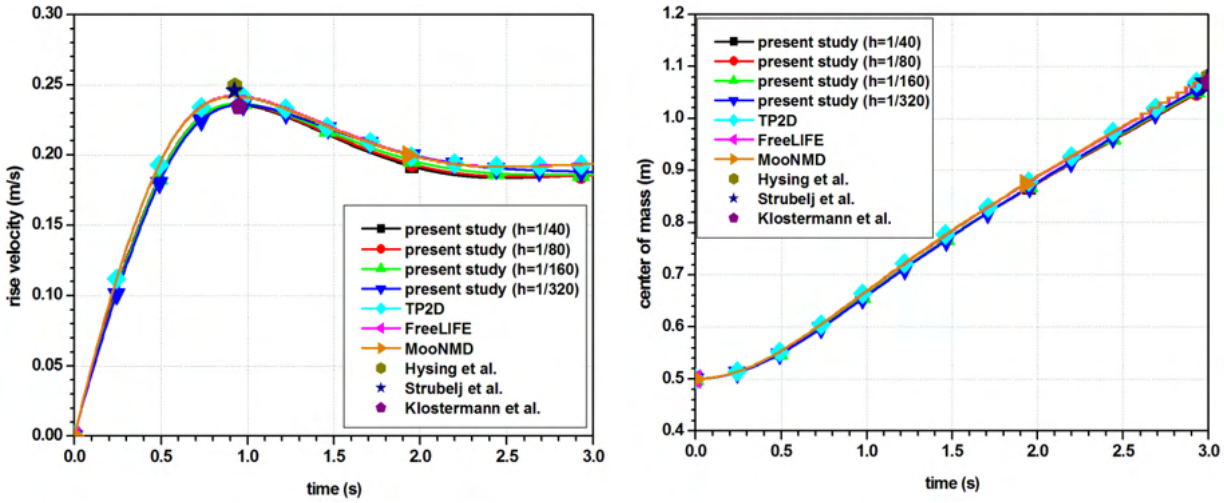

(a)

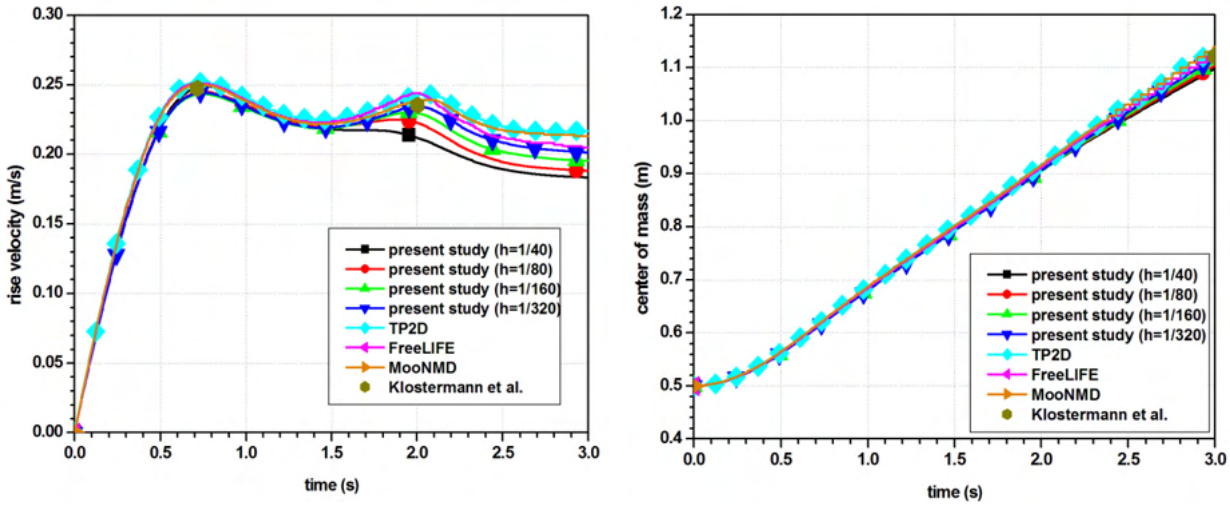

(b)

Fig.4.24 Quantitative verification of (a) case 1 (b) case 2 for 2-D case

Table 4.6 Verification of 2-D benchmark data for case 1

	COM (m)	u_{max} **(m/s)**	
	at *time* = 3 s	***time* (s)**	**maximum**
h = 1/40	1.062	0.941	0.236
h = 1/80	1.063	0.938	0.236
h = 1/160	1.065	0.944	0.237
h = 1/320	1.069	0.967	0.236
TP2D (Hysing *et al.*, 2009)	1.081	0.921	0.242
FreeLIFE (Hysing *et al.*, 2009)	1.080	0.931	0.242
MooNMD (Hysing *et al.*, 2009)	1.081	0.924	0.242
Hysing *et al.* (2009)	1.081	0.927	0.242
Štrubelj *et al.* (2009)	1.068	0.924	0.246
Klostermann *et al.* (2013)	1.070	0.952	0.235

At h = 1/320, a percentage deviation of 1% is recorded for the final position of the COM at t = 3 s, 5% for the incidence time of maximum velocity (u_{max}), and 3% for u_{max}. However, the percentage difference of the current study for h = 1/320 compared to Klostermann *et al*. (2013) OpenFOAM results is 1% for all benchmark case 1 parameters. Grid independence is not observed as mesh refinement increases in case 1, when surface tension is high, although the predictions are within a respectable range of the benchmark data.

As demonstrated in fig. 4.24 and table 4.7, increased mesh refinement combined with lower surface tension resulted in estimates that were comparable to those obtained using the FreeLIFE method. At h = 1/320, a percentage deviation of 1% is detected for the ultimate position of the COM at t = 3 s and incidence time of second maximal velocity (u_{max2}), 3% for incidence time of first maximum velocity (u_{max1}) and u_{max1}, and 4% for u_{max2}. However, when h = 1/320 is compared to Klostermann *et al*. (2013) OpenFOAM results, the percentage difference is less than 1% for all parameters except the incidence time of u_{max1}, which is roughly 5% for benchmark

case 2. VOF solver used in this study is capable of predicting bubble rise benchmark results for both low and high surface tension fluids, according to the verification investigations.

Table 4.7 Verification of 2-D benchmark data for case 2

	COM (m) at *time* = 3 s	**u_{max} (m/s)**			
		***time* (s) of first maximum**	**first maximum (m/s)**	***time* (s) of second maximum**	**second maximum (m/s)**
h = 1/40	1.099	0.767	0.249	1.706	0.218
h = 1/80	1.104	0.753	0.245	1.872	0.225
h = 1/160	1.111	0.746	0.242	1.953	0.230
h = 1/320	1.119	0.749	0.244	2.003	0.234
TP2D (Hysing *et al.*, 2009)	1.138	0.733	0.252	2.07	0.243
FreeLIFE (Hysing *et al.*, 2009)	1.125	0.728	0.251	1.984	0.244
MooNMD (Hysing *et al.*, 2009)	1.139	0.732	0.250	2.06	0.239
Klostermann *et al.* (2013)	1.122	0.716	0.247	2.005	0.235

4.5.1.2 Three-dimensional numerical verification

Verification of interFoam module is also done for 3-D benchmark data available in literature. A cuboid of 1 m length, 1 m width, and 2 m height is the 3-D domain examined for verification. Along the center axis, a bubble containing fluid 2 is positioned 0.5 m above the bottom of the 3-D domain filled with fluid 1. The fluid characteristics from table 4.4 were used to verify d_B = 0.5 m. A mesh size of h = 1/40 was used to study the benchmark cases. In order to better understand computing performance, table 4.8 compares 2-D and 3-D simulations for a rising time of 3 s and the accompanying computation times for both test cases. The top and bottom boundary conditions were no-slip, whereas the sides were slip. Verification has been done for quantitative parameters of bubble vertical velocity and center of gravity.

Table 4.8 Computation parameters for 2-D and 3-D benchmark verification cases

Dimension of domain	Two-dimension	Three-dimension
Grid refinement	40	40
Number of elements	3200	128000
Case 1 computing time	3.5 minutes	1.8 days
Case 2 computing time	3.7 minutes	1.5 days

With a mesh size of 1/40, figure 4.25 displays the verification of rise velocity and COM in the 3-D domain for benchmark cases 1 and 2. The results of the simulation are compared to the benchmark results. For benchmark cases 1 and 2, Adelsberger *et al*. (2014) employed the VOF methodology in OpenFOAM version 2.2.2 to execute three-dimensional numerical simulations. As seen in fig. 4.25, the vertical position of the bubble in this study is higher than the values anticipated by DROPS and NaSt3D.

Figure 4.25 depicts the bubble's ascent velocity in benchmark case 1 with high surface tension. The vertical velocity increases from zero to 0.384 m/s at around 0.95 s in the early stages of simulation. In DROPS, the highest velocity is 0.357 m/s, in NaSt3D it's 0.35 m/s, and in OpenFOAM V 2.2.2 it's 0.33 m/s. In the current investigation, the COM location is shown to be higher due to changes in rise velocity during the last stage of simulation, as shown in fig. 4.25.

The rise velocity plot of bubble in fig. 4.25 for benchmark case 2 with low surface tension is likewise in good agreement for all flow solvers considered. At 0.54 s, all solvers attain maximum velocities in the order of 0.37 m/s, whereas at 0.56 s, the current study reaches a maximum rise velocity of 0.395 m/s. The velocity of the bubble decreases over time, peaking at 0.31 m/s after 3 seconds.

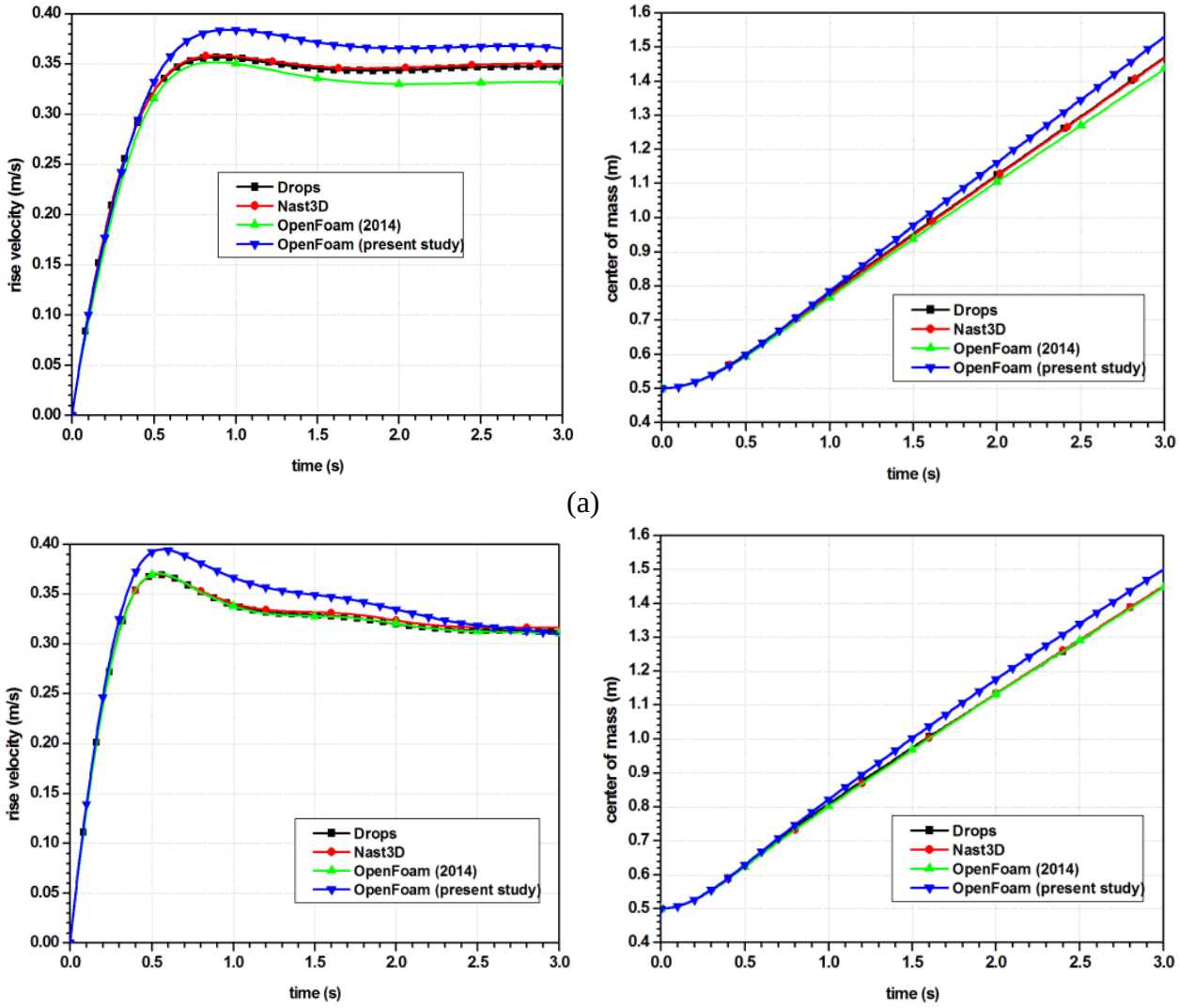

(a)

(b)

Fig.4.25 Quantitative verification of (a) case 1 (b) case 2 for 3-D case

4.5.2 Experimental validation of solver

The experimental validation of solver is carried out for both 2-D and 3-D domains. The 2-D bubble dynamics is validated using terminal velocity correlations available in literature (Krishna and Baten, 1999). Similarly, the 3-D bubble dynamics is validated using both available correlations and in-house 3-D experimental results. The details of validation are described in the following sub-sections.

4.5.2.1 Two-dimensional experimental validation

The experimental validation of solver is carried out with correlations for bubble terminal velocity. The test case 2-D domain considered for validation study is shown in fig. 4.7a. The validation of the Froude number $\left(Fr = \frac{U_T}{\sqrt{g d_B}}\right)$ for an air-water system is shown in Figure 4.26.

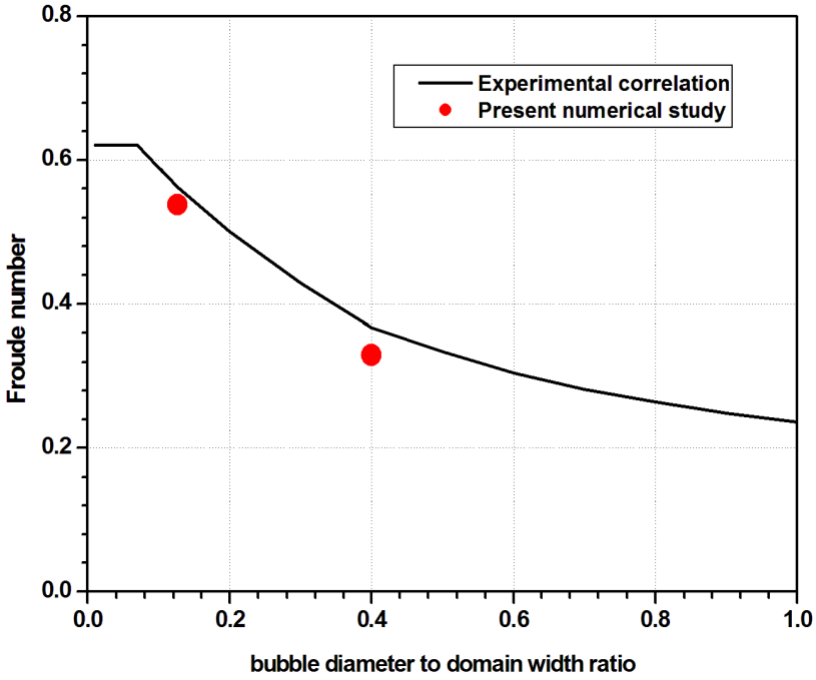

Fig.4.26 Validation of solver for 2-D case

For bubble diameter to domain width ratios of 0.125 and 0.4, simulations are run for a 20 mm air bubble rising in a water column. As demonstrated in fig. 4.26, a good connection between numerical prediction and experimental correlation (Krishna and Baten, 1999) is obtained, proving the validity of the interFoam solver for this study.

4.5.2.2 Three-dimensional experimental validation

The in-house experimental data for the air-water system and the Mendelson (1967) correlation were used to validate the 3-D numerical model. Because the solution domain is set to $W = 8d_B$, the sidewall influence on bubble behavior is minimal. The temporal variations in bubble

dynamics are studied to validate the 3-D numerical model for the water system. Effect of bubble diameter for air bubble rising in water is depicted in fig. 4.27 for diameters ranging from 0.5-0.7 cm.

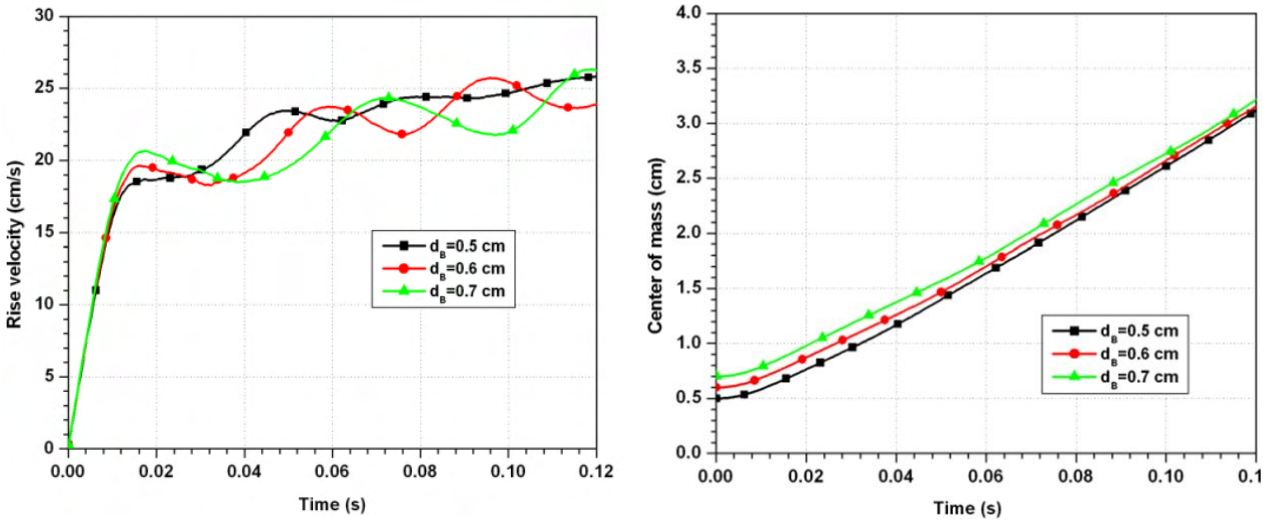

(a) (b)

Fig.4.27 Air-water system (a) instantaneous rise velocity (b) COM variation with bubble size for 3-D case

For a 0.5 cm, 0.6 cm, and 0.7 cm bubble in water, the numerically anticipated terminal velocity is 23.5 cm/s, 23.8 cm/s, and 22.7 cm/s, respectively. A 0.5 cm bubble's terminal velocity, measured experimentally is 24.6 cm/s, with an uncertainty of 2.5 cm/s. The in-house experiment and Mendelson (1967) correlation used to validate numerically predicted terminal velocity for an air-water system are shown in Figure 4.28. For the 0.5 cm bubble scenario, the numerically predicted terminal velocities are in close accord with Mendelson (1967) correlation and are -4.5 percent lower than the in-house experimental result. The numerically anticipated aspect ratio of a 0.5 cm bubble in water is 0.62, which is quite near to the values of 0.624 obtained from Taylor and Acrivos (1964) correlation and 0.6 acquired from an in-house experiment following extensive image analysis.

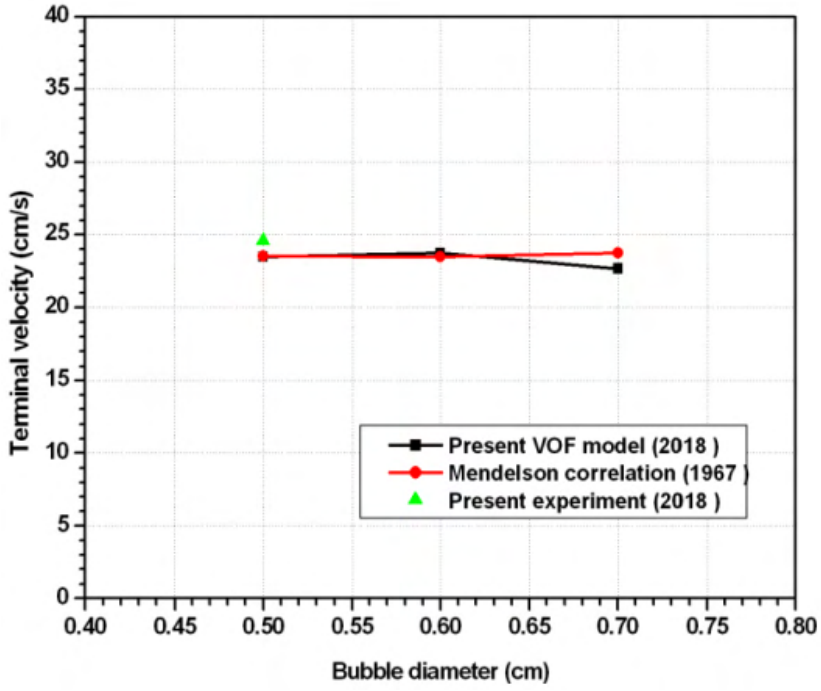

Fig.4.28 Validation of solver for 3-D case

4.6. Results and discussion

Numerical simulations are carried out using two-dimensional, axisymmetric and three-dimensional domains to evaluate the effects of various parameters influencing bubble dynamics for gas-liquid systems.

4.6.1 Two-dimensional bubble dynamics in sodium system: numerical study

The influence of bubble size and gas-liquid components on inert gas bubble dynamics in a liquid sodium/NaK pool is examined systematically using a 2-D numerical simulation. The evaluation is broken down into the sub-sections below.

4.6.1.1 Bubble size effect

For the argon gas and liquid sodium system at 200 °C, simulations are carried out to study the effect of initial bubble diameter on bubble dynamics. To ensure that the side wall effects are avoided and bubble reaches terminal velocity, the domain height 'H' and width 'W' are set to "$8d_B$". The diameters of the bubbles used for analysis were 10 mm, 15 mm, and 20 mm. The

characteristic bubble velocity $U_T = \sqrt{gd_B}$ is used to calculate the non-dimensional parameters for bubble dynamics, as given in table 4.9.

Table 4.9 Argon-sodium system's bubble conditions

Bubble diameter (mm)	10	15	20
Morton number	6.7×10^{-14}	6.7×10^{-14}	6.7×10^{-14}
Reynold number	6262.0	11505.7	17714.0
Eötvös number	4.7	10.6	18.8
Capillary number	7.5×10^{-4}	9.1×10^{-4}	1.1×10^{-3}

Figure 4.29 shows the simulation results of bubble rising trajectories and shapes in liquid sodium for various bubble sizes. Table 4.10 shows the rising time, number of elements, and computing time for various bubble diameters in the current investigation.

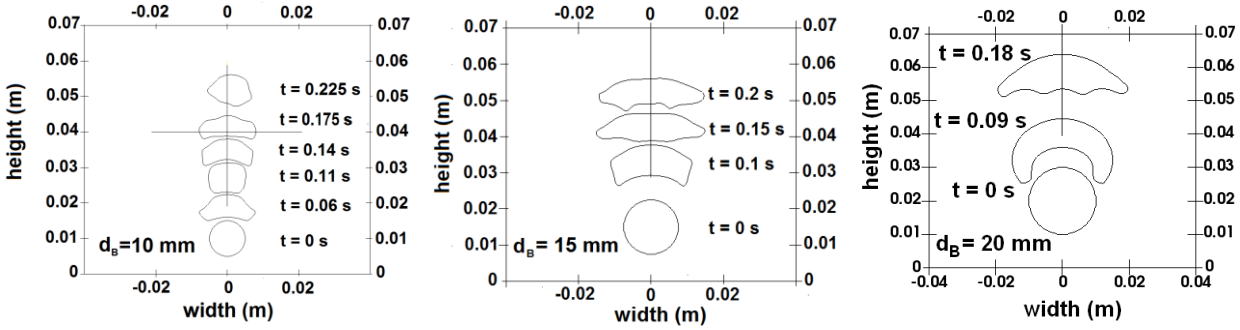

(a) (b) (c)

Fig.4.29 Bubble contours for sizes (a) 10 mm (b) 15 mm (c) 20 mm in 2-D case

Table 4.10 Computation parameters for 2-D case in current study

d_B **(mm)**	**Rise time (s)**	$n_{elements}$	**Computation time**
10	0.225	295936	4 days
15	0.350	295936	4 days
20	0.425	295936	4 days

The 20 mm bubble is relatively stable in comparison to previous case studies, as seen in fig. 4.29(a-c), and its ascending trajectory is essentially rectilinear. Figures 4.30 and 4.31 demonstrate the temporal variation of bubble dynamic characteristics and the rise trajectory for COM position of bubble sizes ranging from 10 to 20 mm. Figure 4.30 demonstrates that the bubble rise velocity for 10 mm, 15 mm, and 20 mm bubbles reaches 0.2 m/s in 0.104 s, 0.062 s, and 0.025 s, respectively. Because of the effects of horizontal velocity components, oscillations in the bubble vertical velocity component are visible and predicted. Smaller bubbles have more prominent oscillations, and the amplitude diminishes as the bubble diameter grows. With increasing bubble diameter, the greatest deviations in rise velocities for 10 mm and 15 mm bubble diameters from the 20 mm case are observed to decrease. The largest variations in rise velocity of 10 mm and 15 mm from the 20 mm bubble example, as shown in fig. 4.30, are 31.6 percent and 28.1 percent, respectively.

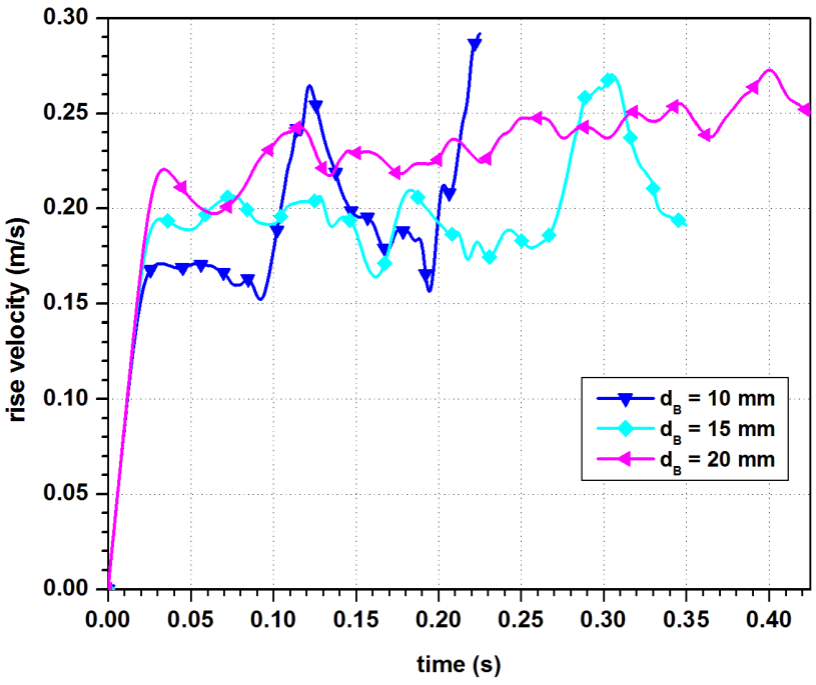

Fig.4.30 Bubble rise velocity variation with diameter for 2-D case in current study

As shown in fig. 4.31a, the departure from rectilinear motion is least for 20 mm, with a maximum divergence of 0.0009 m from the central axis at 0.425 s. It denotes that at a bubble diameter of 20 mm in an argon-sodium system, the bubble ascent becomes rectilinear. For bubble sizes of 10 mm, 15 mm, and 20 mm, Figure 4.31b depicts the temporal fluctuation of COM position. The discrepancy in starting sizes and elevation for each bubble causes the offsets at time t = 0 s. The 20 mm bubble travels 0.047 m vertically in 0.225 s, as shown in Figure 4.31b. The vertical distance traversed by a 10 mm bubble at t = 0.225 s is 12% less than that of a 20 mm bubble due to its lower rise velocity. Table 4.11 shows the largest horizontal deviations from the center axis. The variance for 20 mm is 1% at the half width of the domain cavity, as can be shown from table 4.11. When compared to 10 mm and 15 mm bubbles, a 20 mm bubble's rising trajectory is rectilinear because its horizontal departure from the central axis is the least. For bubble diameters ranging from 10 to 20 mm, the average bubble terminal velocity is 0.21 m/s. As shown in fig. 4.32, the maximum value of bubble terminal velocity is 0.24 m/s for a 20 mm bubble and the lowest is 0.18 m/s for a 10 mm bubble.

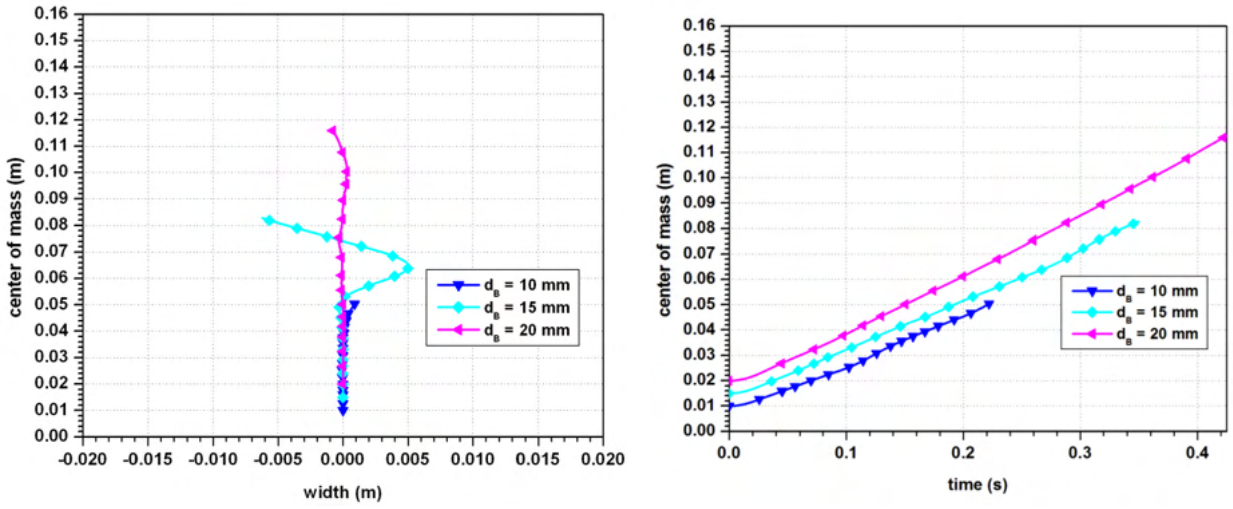

(a) (b)

Fig.4.31 Bubble (a) path (b) rise height variation with diameter for 2-D case in current study

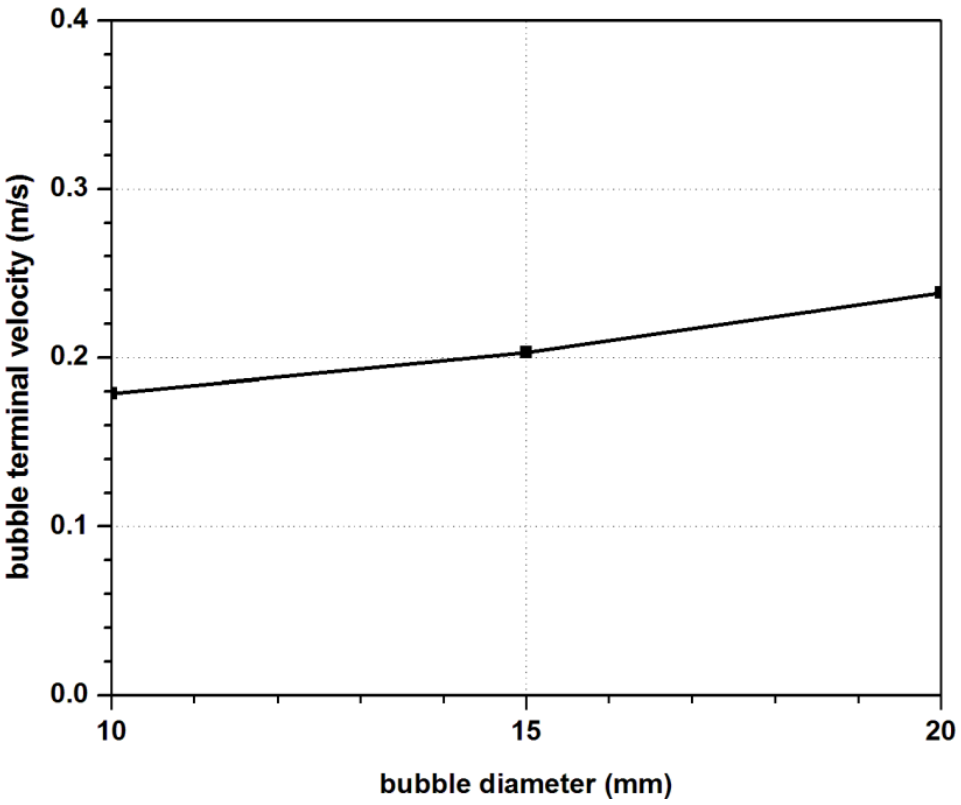

Fig.4.32 Terminal velocity variation with diameter for 2-D case in current study

Table 4.11 Ar-Na system maximum horizontal deviation from central axis (*AR* = 1)

Bubble diameter (mm)	10	15	20
Horizontal deviation from the central axis at its maximum (m)	9.8×10^{-4}	6.2×10^{-3}	9.1×10^{-4}
% of horizontal divergence from domain cavity's half width	2.5	10.3	1.1

4.6.1.2 Gas-liquid component effect

To better understand the impact of various gas-liquid system components on bubble dynamics, simulations are run. The argon-NaK system at 30 °C, argon-sodium system at 200 °C and xenon (Xe)-sodium system at 547 °C are the gas-liquid systems studied. The height (*H*) and width (*W*)

of the domain are set to "8d_B". The analysis is based on a bubble diameter of 20 mm. Table 4.12 shows the transport parameters of the gas-liquid systems under consideration for investigation.

Table 4.12 Inert gas-liquid system fluid properties

Case	Argon-NaK (T = 30 °C)	Argon-sodium (T = 200 °C)	Xenon-sodium (T = 547 °C)
Density of fluid 1 (kg/m^3)	874	904	820
Density of fluid 2 (kg/m^3)	1.63	1.04	1.97
Viscosity of fluid 1 (kg/ms)	5.3 x 10^{-4}	4.5 x 10^{-4}	2.2 x 10^{-4}
Viscosity of fluid 2 (kg/ms)	2.8 x 10^{-5}	3.2 x 10^{-5}	5.6 x 10^{-5}
Surface tension (kg/s^2)	0.177	0.189	0.155

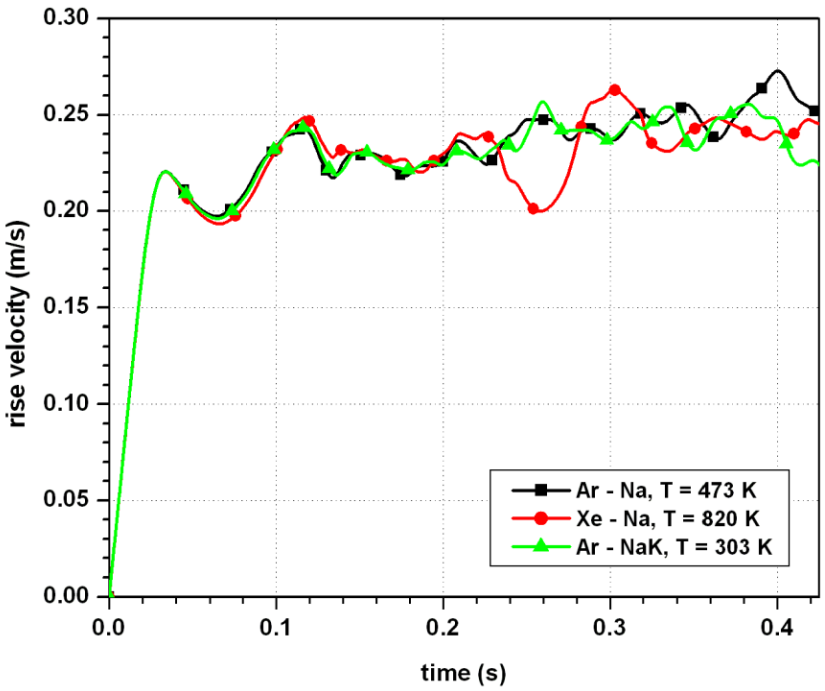

Fig.4.33 Bubble rise velocity variation with gas-liquid systems for 2-D case in current study

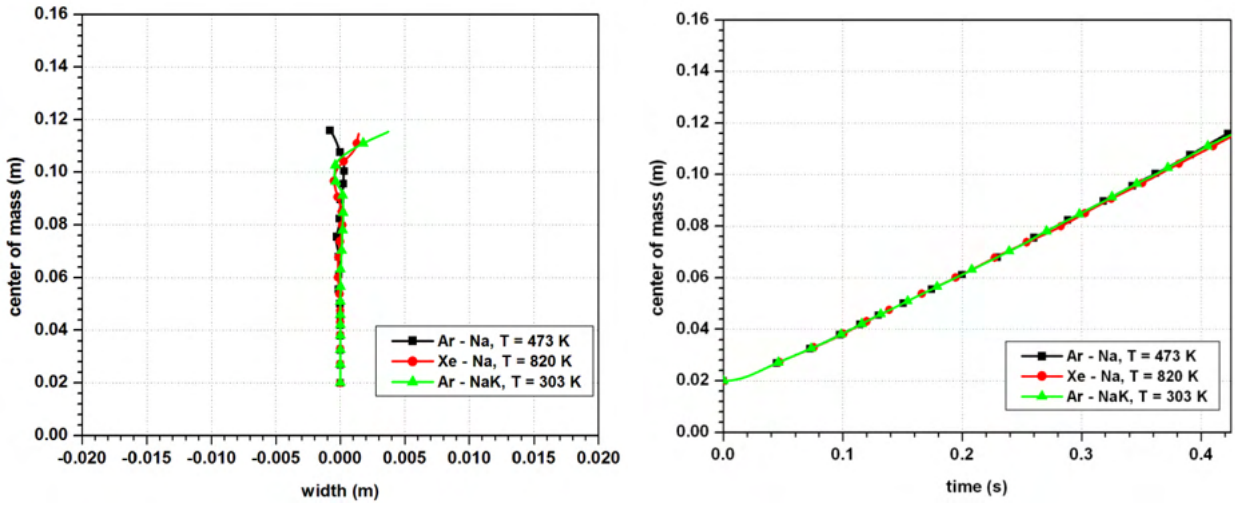

(a) (b)

Fig.4.34 Bubble (a) path (b) rise height variation with gas-liquid systems for 2-D case in current study

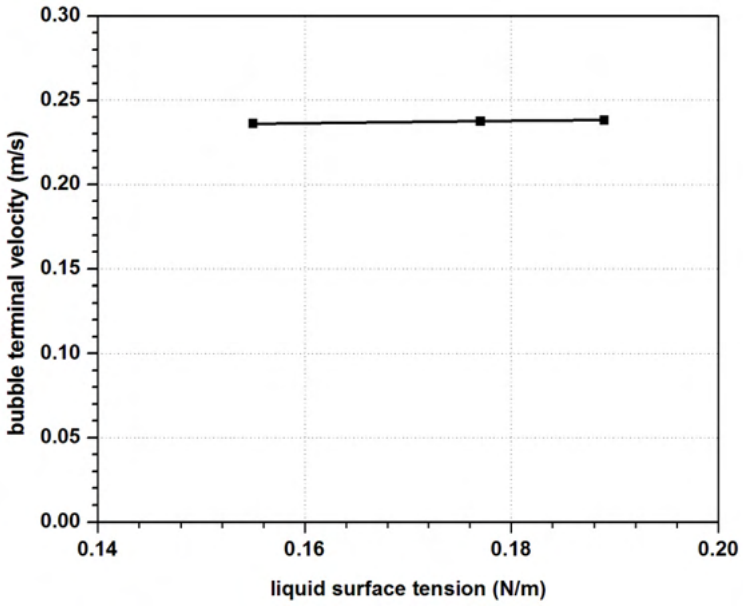

Fig.4.35 Terminal velocity variation with gas-liquid systems for 2-D case in current study

Figures 4.33 and 4.34 depict bubble dynamics as a function of the gas-liquid component. For all three gas-liquid systems studied, the bubble rise velocity approaches 0.2 m/s in 0.025 s, as shown in Figure 4.33. With increasing surface tension, the maximum deviation in rise velocities for various gas-liquid components from the argon-sodium system scenario is shown to decrease. The rise velocities of the xenon-sodium system (= 0.155 N/m) and argon-NaK system (= 0.177 N/m)

are 19 percent lower at 0.26 s and 13 percent lower at 0.41 s, respectively, than the argon-sodium system (= 0.189 N/m). For the argon-NaK system, the maximum horizontal deviation from the central axis for the gas-liquid component investigated is 5% at half width of the domain cavity (fig. 4.34a). The rising trajectory of the 20 mm bubble is thus rectilinear, regardless of the gas-liquid component investigated. The highest bubble rise height for the argon-sodium system is at 0.425 s, as shown in Figure 4.34b. The xenon-sodium system has a 1.7 percent lower rise height than the argon-sodium system, therefore the difference is negligible. As a result of this research, it is obvious that the effect of the gas-liquid component on bubble dynamics is negligible for bubbles with a diameter of 20 mm. With varied gas-liquid system components, the average bubble terminal velocity remains nearly constant (0.24 m/s), as illustrated in fig. 4.35. The argon-sodium system's bubble terminal velocity is 0.238 m/s, while the xenon-sodium system's is 0.236 m/s, with the divergence being minor.

4.6.1.3 Water and sodium bubble dynamics

Bubble dynamics for 20 mm initial bubble diameter are studied between air-water and argon-sodium systems to see if there is a similarity between regular liquid and liquid metal single bubble dynamics. Table 4.13 shows the transport parameters of the fluids utilized to simulate the air-water and argon-sodium systems. Figures 4.36 and 4.37 exhibit the temporal fluctuations of bubble dynamics for 20 mm air-water and argon-sodium systems, respectively. Figure 4.38 depicts the bubble contour for a 20 mm bubble in both air-water and argon-sodium systems at t = 0.425 s. In both argon-sodium and air-water systems, the rise velocity reaches 0.2 m/s in 0.025 s, as shown in Figure 4.36. The largest departure in air-water rise velocity from an argon-sodium system is 39%, and it occurs at a time interval of 0.135 s, owing to bubble breakup. As demonstrated in fig. 4.37a, the deviation from rectilinear motion is lower for the air-water system

(highest departure of 0.0003 m from the central axis at 0.425 s) and larger for the argon-sodium system (highest departure of 0.0009 m from the central axis at 0.425 s).

Table 4.13 20 mm bubble fluid characteristics for argon-sodium and air-water systems

Case	Argon-sodium (T = 200 °C)	Air-water (T = 30 °C)
Density of fluid 1 (kg/m^3)	904	995
Density of fluid 2 (kg/m^3)	1.0	1.2
Viscosity of fluid 1 (kg/ms)	4.5×10^{-4}	8.0×10^{-4}
Viscosity of fluid 2 (kg/ms)	3.2×10^{-5}	1.8×10^{-5}
Surface tension (kg/s^2)	0.189	0.07
Morton number	6.7×10^{-14}	1.1×10^{-11}
Reynold number	17714	10953
Eötvös number	18.8	54.9

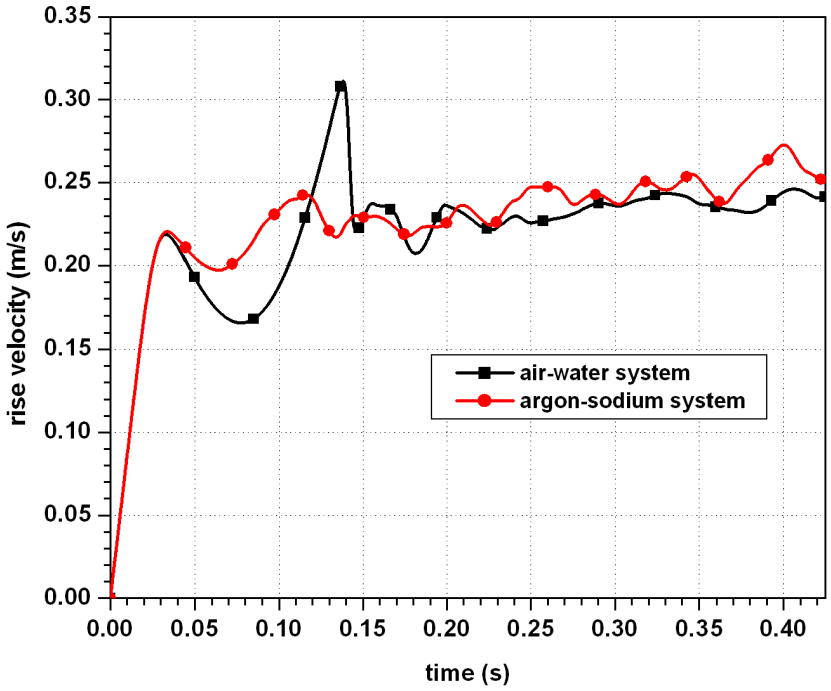

Fig.4.36 Simulation results of 20 mm bubble for instantaneous rising velocity of bubble in 2-D

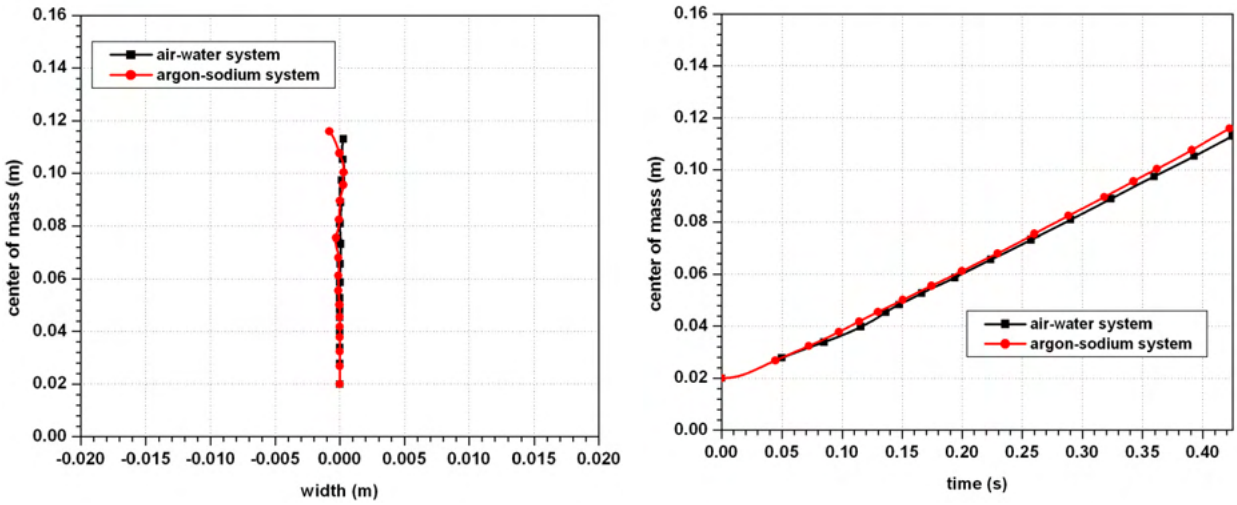

(a) (b)

Fig.4.37 Bubble (a) path (b) rise height similarity between water and sodium systems for 2-D case

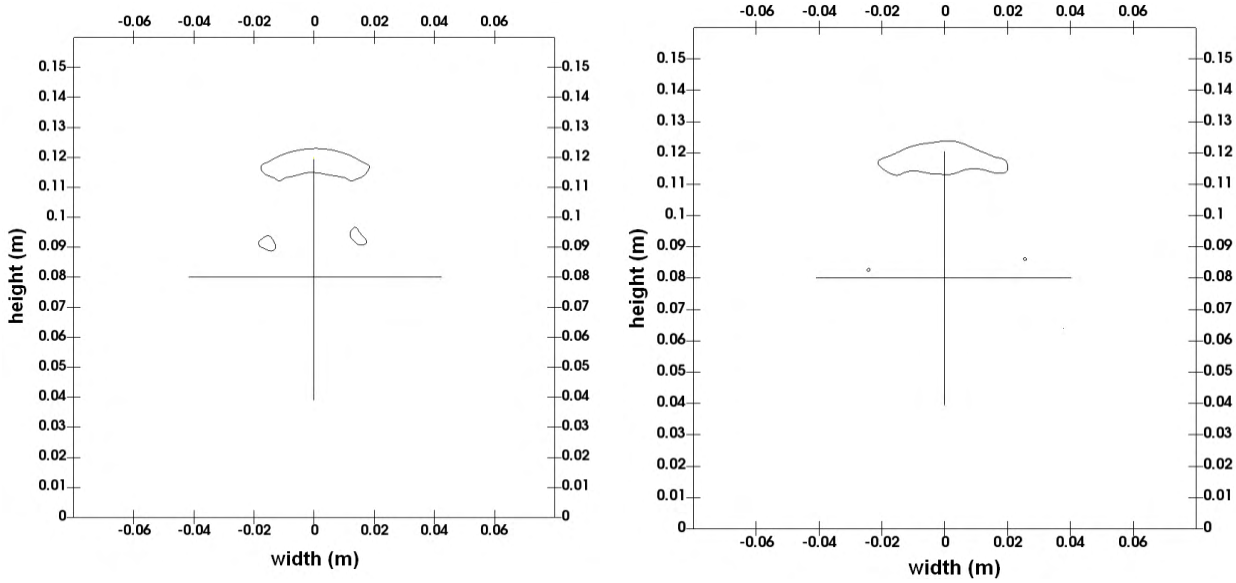

(a) (b)

Fig.4.38 Bubble contour for (a) air-water system (b) argon-sodium system in 2-D case

For the argon-sodium system, the highest horizontal deviation from the central axis is 1% at half width of the domain cavity, which is negligible. The rise trajectory of the 20 mm bubble is thus rectilinear for both systems. The rising height of the argon-sodium system is higher than that of the air-water system at 0.425 s, as shown in Figure 4.37b. The rise height of an air-water system is 3% lower than that of an argon-sodium system, making the difference

inconsequential. In an air-water system, the bubble terminal velocity of a 20 mm bubble is 0.233 m/s, which is 2% lower than in an argon-sodium system. Except for the bubble breakup, the systems bubble dynamic properties appear to be similar.

The air-water system has substantially more secondary bubble breakup than the argon-sodium system, as shown in Figure 4.38. This shows that, as anticipated by Levich (1962), bubble breakage occurs at smaller diameters for liquids with reduced surface tension. At 0.425 s, the bubble bottom oscillations are stronger in the argon-sodium system than in the air-water system, as shown by comparisons of figs. 4.38a and 4.38b. This is owing to sodium's higher surface tension when compared to water, and it agrees with Wang and Tong's findings (2008).

4.6.2 Three-dimensional bubble dynamics in sodium system: numerical study

A systematic numerical investigation of the argon bubble rising in the sodium system is carried out after a comprehensive numerical validation of the three-dimensional computational model using theoretical correlations identified in the literature and in-house experiments. The following sub-sections go through the most important findings regarding the effects of various critical parameters on bubble dynamics. Figure 4.7b depicts the three-dimensional domain used in numerical simulations.

4.6.2.1 Effect of bubble diameter

Figures 4.39a and 4.39b demonstrate the temporal fluctuation of bubble dynamics in terms of bubble rise velocity and COM for an argon bubble rising in sodium.

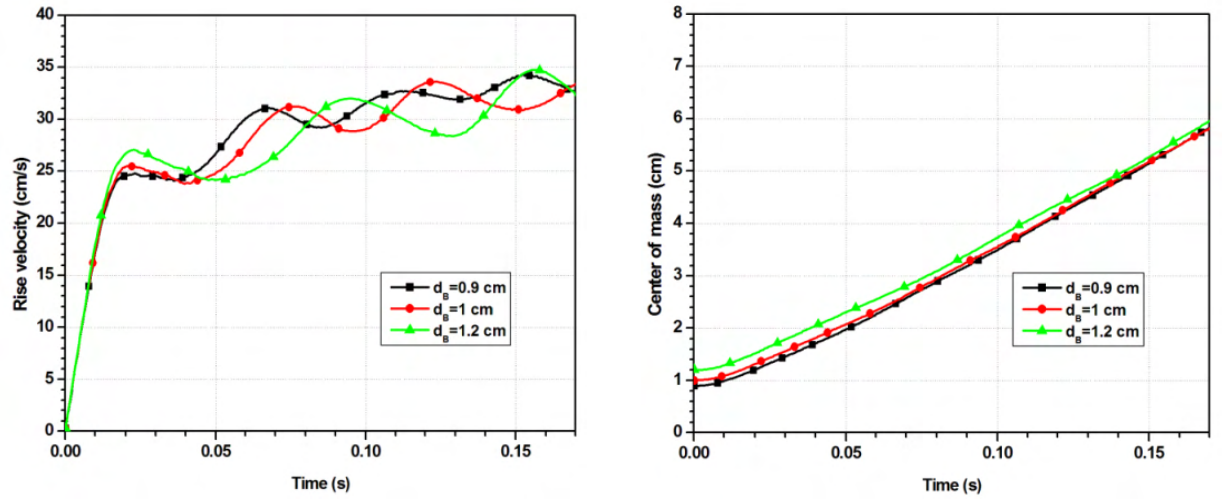

(a) (b)

Fig.4.39 Bubble (a) instantaneous rise velocity (b) COM variation with bubble size for 3-D case in current study

For 0.9, 1 and 1.2 cm bubble sizes in sodium, the numerically evaluated terminal velocity is 30.2, 29.8, and 28.87 cm/s, respectively. For the 1.2 cm bubble case, the estimated terminal velocity is determined to be 6.9% lower than the value obtained from the Mendelson (1967) correlation (fig. 4.40).

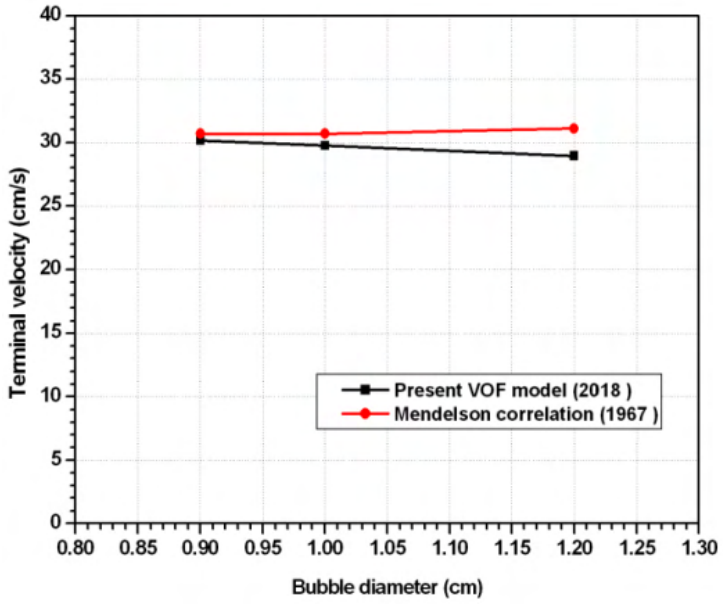

Fig.4.40 Current study bubble terminal velocity with correlation for 3-D case

4.6.2.2 Effect of domain dimension

Using a 5 mm bubble rise case, the effect of domain dimension on bubble velocity is simulated. The argon-sodium system evaluated for investigation at 200 °C is listed in Table 4.14.

Table 4.14 Fluid properties for argon-sodium system at 200 °C

Case	Argon-sodium (T = 200 °C)
Density of fluid 1 (kg/m^3)	904
Density of fluid 2 (kg/m^3)	1.0
Viscosity of fluid 1 (kg/ms)	4.5 x 10^{-4}
Viscosity of fluid 2 (kg/ms)	3.2 x 10^{-5}
Surface tension (kg/s^2)	0.189
Gravitational acceleration (m/s^2)	9.8

Figures 4.41 and 4.42 give the bubble's evolution with time and bubble quantitative parameters variation with domain dimension respectively.

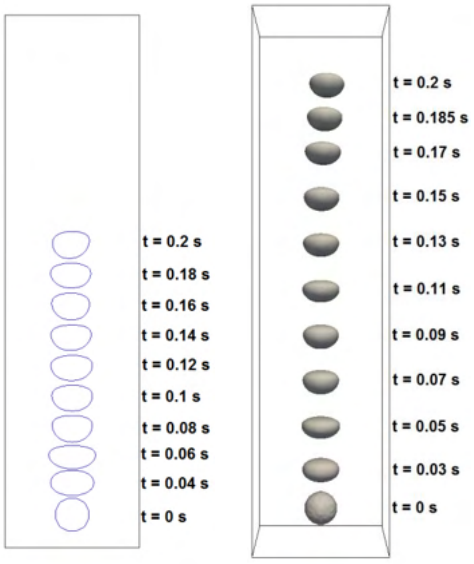

(a) (b)

Fig. 4.41 Bubble contours (a) 2-D (b) 3-D

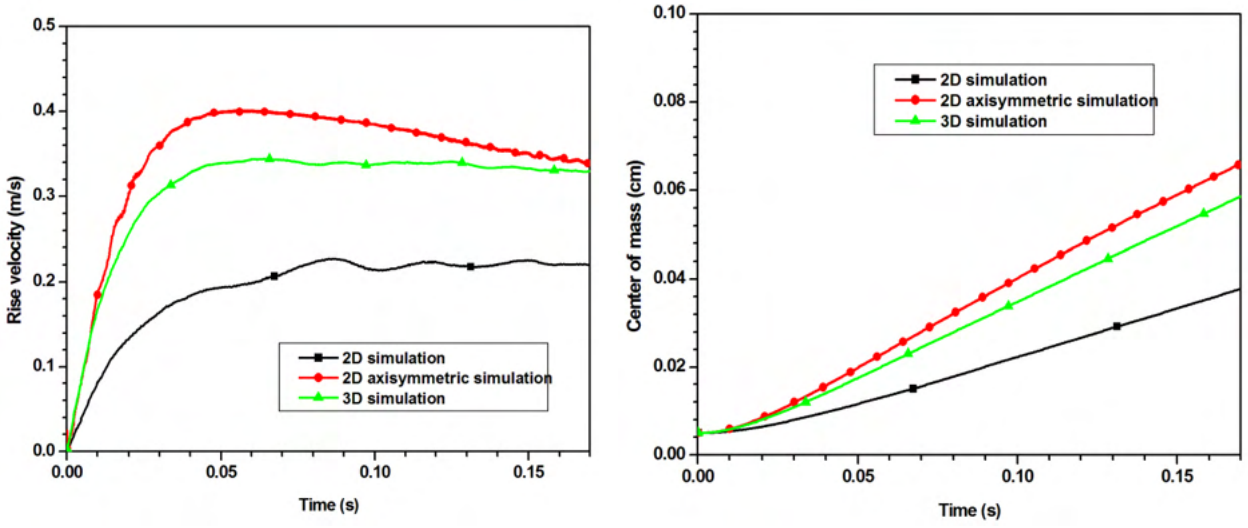

(a) (b)

Fig. 4.42 Bubble (a) instantaneous rise velocity (b) COM variation with domain dimension in current study

Table 4.15 Computation parameters for 2-D and 3-D cases in current study.

Dimension	Two-dimension	Three-dimension
Grid refinement	4	4
Number of elements	28000	2048000
Simulation time	11.3 minutes	6 days

Figure 4.42 indicates that terminal velocities of 0.224 and 0.331 m/s are computed using two-dimensional and three-dimensional simulations, respectively. To understand computing efficiency, Table 4.15 illustrates the computing times for 2-D and 3-D. A realistic velocity is predicted by the three-dimensional scenario, which is quite similar to Mendelson's (1967) correlation value of 0.338 m/s. The axisymmetric case even though has a low computation time (~12 hours) than the 3-D case, it limits the bubble movement confined to the axis and hence over predicts the terminal velocity (fig. 4.42) compared to the realistic 3-D case.

4.6. Water and sodium similarity

To date, the similarity requirements between water and liquid sodium have been determined by equating the non-dimensional numbers. The equivalent bubble diameter in the water system is 0.58 of the corresponding diameter in the sodium system to imitate a bubble of a certain dimension in the sodium system. To get the terminal velocity in the sodium systems, the terminal velocity obtained from the water experiment has to be divided by 0.76. The bubble dynamics of a 0.5 cm bubble in a water system and a 0.9 cm bubble in a sodium system are numerically examined in this section. The numerical value for the ratio of terminal velocities between the water and sodium systems is 0.77, which is quite similar to the value obtained using non-dimensional numbers. The resemblance in bubble profiles produced from 3-D numerical simulation for the sodium and water systems is shown in Figure 4.43. A 0.5 cm water bubble and a 0.9 cm sodium bubble have aspect ratios of 0.62 and 0.61, respectively (fig. 4.44).

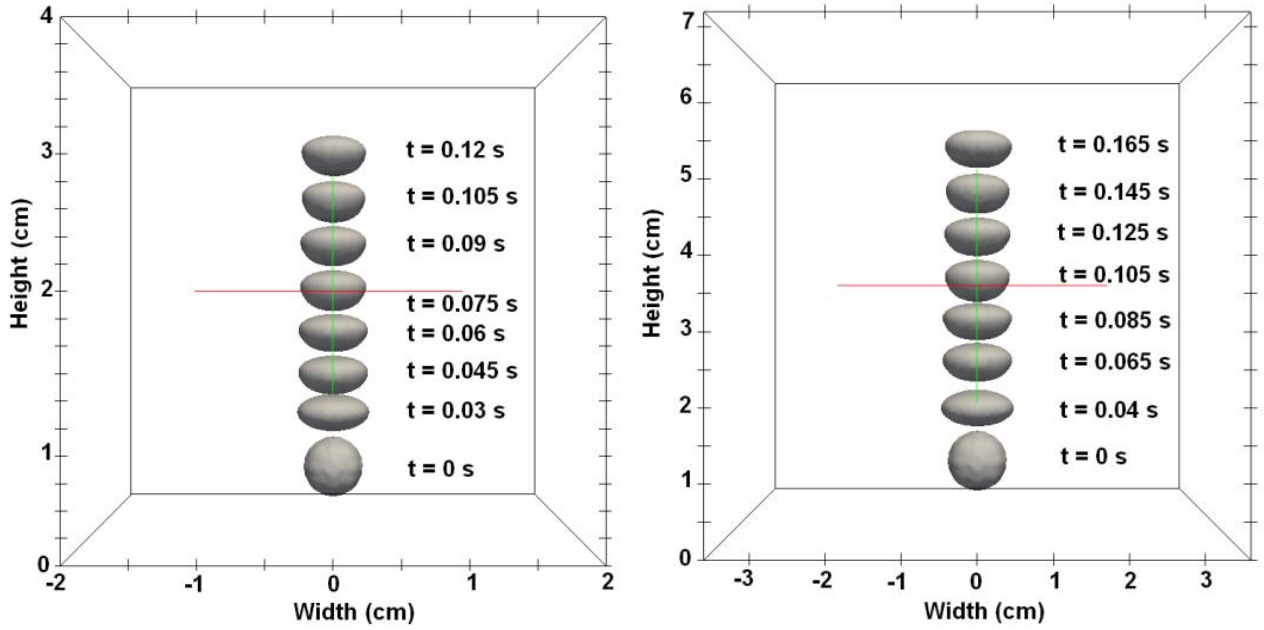

(a) (b)

Fig.4.43 3-D numerical model for (a) 0.5 cm bubble in water (b) 0.9 cm bubble in sodium

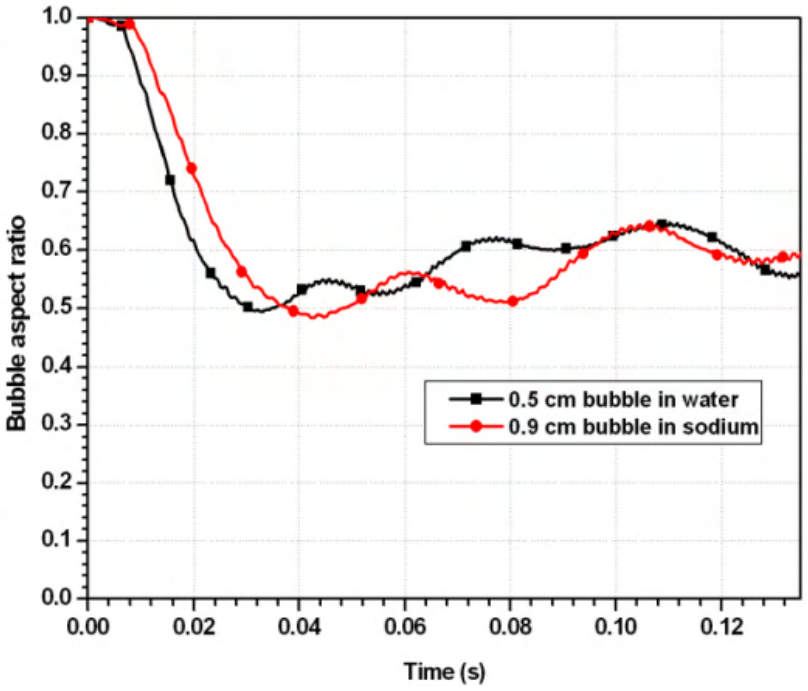

Fig.4.44 3-D simulation results of aspect ratio for rising bubble

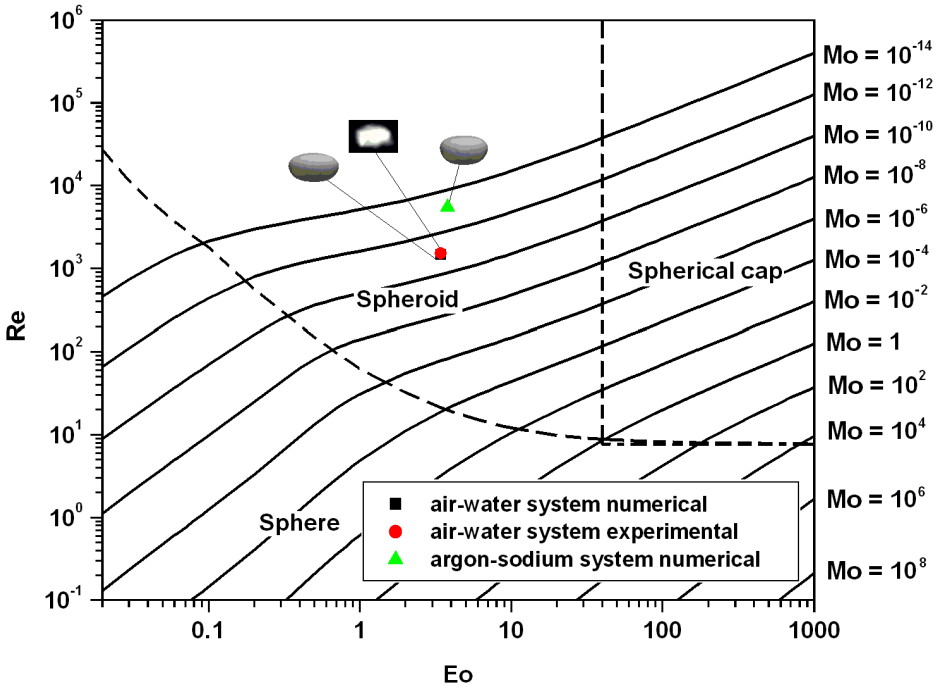

Fig.4.45 Bubble shape diagram

It can also be noted that the 0.9 cm bubble aspect ratio in the sodium system agrees well with the 0.5 cm bubble aspect ratio in water. As demonstrated in fig. 4.45, the observed bubble sizes from similarity investigations in sodium and water systems fall into the spheroidal domain of the bubble shape diagram. As a result, a sufficiently scaled-up water system can be utilized to simulate sodium system for bubble dynamic research connected to SFR in-vessel source term evaluation, taking into account the similarity criterion developed for medium to large-sized bubbles.

4.6.4 Experimental study of bubble dynamics in water system to replicate sodium system

An in-house water experimental facility has been established to simulate sodium system bubble dynamics based on the similarity criteria created between water and liquid sodium systems using the numerical model in the previous section. Bubble rise velocities for diameters of 0.5-2.25 cm ranged from 24.6 ± 2.5 cm/s to 29.1 ± 3.5 cm/s, according to in-house bubble dynamic research. When the experimentally measured bubble rise velocities in the water system for diameters ranging from 0.5 to 2.25 cm are scaled up, the rise velocities in the sodium system are 31.9-40.9 cm/s for diameters ranging from 0.84 to 3.8 cm. The results are quite close to the values anticipated by Mendelson (1967) for the argon-sodium system, which are 30.8-44.7 cm/s. The proposed water set-up can be used to examine bubble dynamics in SFR pools connected to in-vessel bubble transport source term studies since the corresponding diameter range of bubbles created from the in-house water setup simulates the diameter range in sodium research.

The experimentally measured average rise velocity of 0.5 cm bubble, for a pool height of 55 cm is 24.6 cm/s. For a pool height of 75 cm, the experimentally measured rise velocity of a 1.97 cm bubble ranged from 24.5 cm/s to 32.8 cm/s, with an average value of 27.9 cm/s. For a pool height of 95 cm, the rise velocity ranged from 24.6 cm/s to 27.7 cm/s, with an average of 26.0

cm/s. The rise velocity for a pool height of 117 cm ranged from 28.0 cm/s to 29.0 cm/s, with an average of 28.5 cm/s. Because of the attainment of terminal velocity, the variances in rise velocity for a given bubble diameter decreased as the rise height increased. As a result, the 1.97 cm bubble's actual measured rise velocity is 28.5 cm/s. Similarly, for bubble diameters of 1.56 cm and 2.25 cm, the rise velocities are 25.7 cm/s and 31.5 cm/s, respectively. As the bubble diameter grows larger, the rise velocity increases.

Non-dimensional numbers like Morton number, Reynolds number, Capillary number and Eötvös number characterize bubble dynamics in terms of shape and rise velocity. The Morton number for an air-water system, which is dependent on fluid characteristics, is 1.1×10^{-11}. The thermophysical parameters of the air-water system are used to calculate the Reynolds number (ratio of inertial to viscous force), Capillary number (ratio of viscous to surface tension force) and Eötvös number (ratio of gravitational to surface tension force) as shown in table 4.16 and 4.17. The experimentally obtained rise velocities are used to estimate the non-dimensional numbers in table 4.17. Table 4.16 shows the thermophysical characteristics at 30 degrees Celsius.

Table 4.16 Properties of air-water system

Case	Air-water (T = 30 °C)
Density of fluid 1 (kg/m^3)	995
Density of fluid 2 (kg/m^3)	1.26
Viscosity of fluid 1 (kg/ms)	8.0×10^{-4}
Viscosity of fluid 2 (kg/ms)	1.86×10^{-5}
Surface tension (kg/s^2)	0.071

Table 4.17 and fig. 4.46 illustrate the results of evaluating bubble dynamics for four different bubble sizes. The Levich correlation predicts that the maximum stable bubble diameter for an

air-water system at 30 °C is 2.1 cm, after which bubble breakup occurs. Figure 4.46 depicts the air-water system's terminal velocity as well as the bubble velocity predicted from literature correlations.

Table 4.17 Experiment-derived dimensionless numbers

Case	Air-water (T = 30 °C)			
Bubble diameter (cm)	0.5	1.56	1.97	2.25
Bubble velocity (cm/s)	24.6	25.7	28.5	31.5
Weber number	4.24	14.44	22.49	31.32
Reynold number	1529	4968	6959	8787
Eötvös number	3.43	33.47	53.14	69.63
Capillary number	0.0027	0.0029	0.0032	0.0035

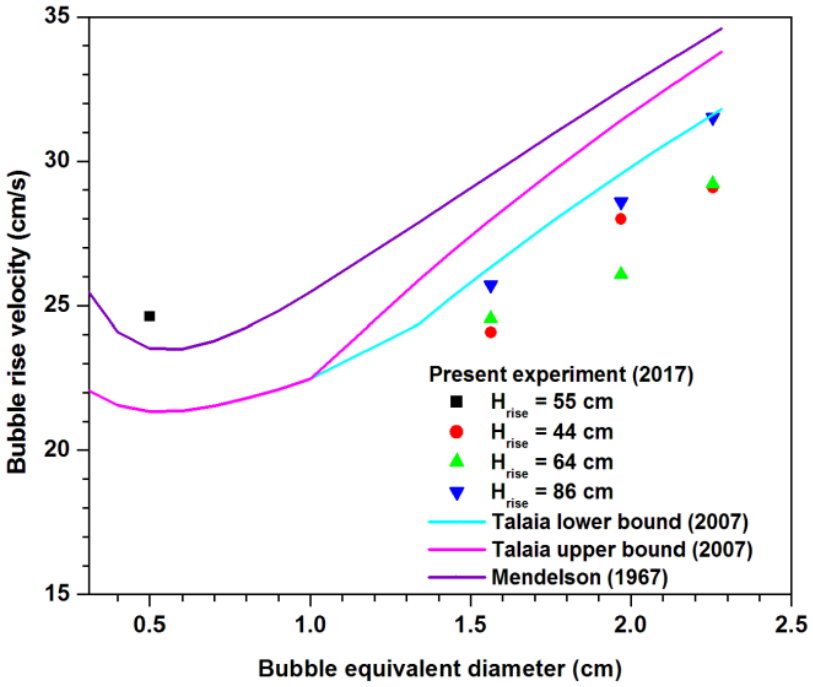

Fig.4.46 Experimental variation of rise velocity with bubble equivalent diameter

The relationship between the Weber number (*We*) and the Reynolds number (*Re*) is investigated, with both dimensionless values derived from bubble rise velocity measurements. For the domain

under consideration, the results show that *We* increases with *Re*. As illustrated in fig. 4.47, the predicted Weber number was compared to the value derived via Raymond and Rosant correlation for the appropriate Reynolds number. For the Morton number range of *Mo* ~ 9 x 10^{-7} to 7, the Raymond and Rosant correlation was derived as follows:

$$We = 0.42Mo^{0.35}Re^{(5/3)} \qquad (4.16)$$

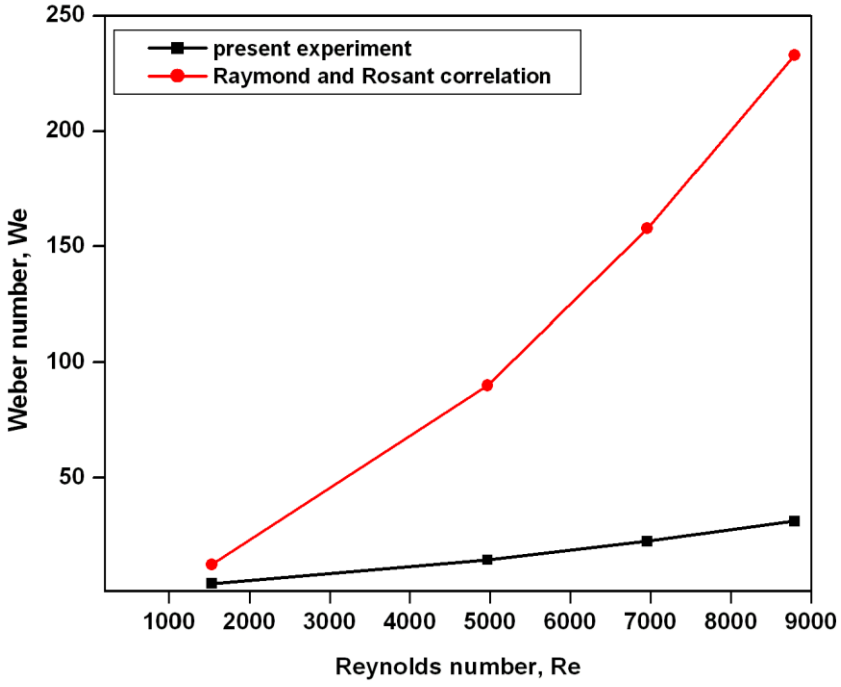

Fig.4.47 Weber number as a function of Reynolds number

The present experimental study predicted Weber numbers around 86% lower than the correlation. Islam (2013) numerically predicted Weber numbers around 32% lower than the correlation for 0.5 cm air bubble in water as observed in the present experiment. Raymond and Rosant (2000) projected a larger value for the air-water system, which could be owing to the low *Mo* ~ 1x10^{-11} for water. According to the current experimental investigation and numerical results of Islam (2013), the deviation of Raymond and Rosant correlation from air-water experimental measurements increases with increasing bubble diameters.

During the rising time, photographs and films of the four bubble sizes are shot. In the air-water system, the bubble diameters of 1.97 cm and 2.25 cm show slight breakup during the rising period, as illustrated in fig. 4.48. The photos in fig. 4.48 were created by adjusting the saturation of a captured movie and then using a video to image converter to create still photos. The breaking of a 1.97 cm bubble into secondary bubbles (fig. 4.48c) matches the 2-D numerical research prediction for a 2 cm bubble quite well.

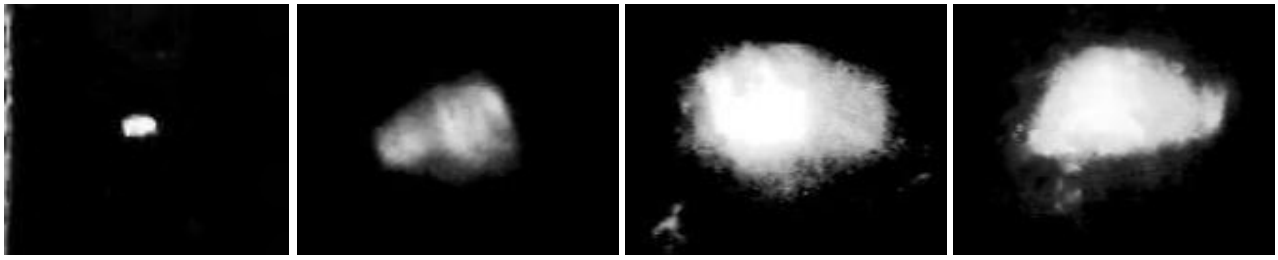

(a) (b) (c) (d)

Fig.4.48 Images for bubble sizes of (a) 0.5 cm (b) 1.56 cm (c) 1.97 cm (d) 2.25 cm in the air-water system

4.7 Closure

In 2-D, 2-D axisymmetric, and 3-D domains, the interFoam solver of the open source CFD program OpenFOAM version 3.0.0 is used to simulate the rise dynamics of a single gas bubble in a liquid sodium pool. The solver's VOF module, as well as the discretization techniques employed in this study, have been validated against numerical benchmark data and experimental results. To better understand the mechanics of air bubble ascent in the water column, experiments are being carried out. The bubble's rise velocity is measured in the pool using void-detection sensors created in-house. For various equivalent bubble diameters and water column aspect ratios, the experimental study investigated bubble rise velocity in a water column. With an increase in the initial bubble diameter, the measured bubble rise velocity increases. The bubble velocity is measured using a new type of digital sensors called pulsating void-detection sensors,

which are based on conductance measurement. The chapter's research looks into the dynamics of an inert gas bubble rising in a liquid sodium/sodium-potassium alloy (NaK) pool. To better understand the impacts of domain aspect ratio, bubble diameter and gas-liquid system on bubble rise dynamics, parametric simulations are conducted. For liquid sodium systems, the bubble rise velocity rises with diameter, according to the research. The bubble dynamics for 20 mm size in liquid sodium and water systems are comparable, with the exception of lower breakup and stronger bubble bottom oscillations in sodium systems due to higher surface tension. For both 2-D and 3-D situations, bubble behaviour was simulated for a 5 mm bubble rise in sodium. The terminal velocity data from the literature backs up the 3-D bubble simulation. The findings reveal that terminal velocity varies with domain dimension, and that the 3-D scenario accurately predicts true velocity values. As a result, the study backs up the use of water as a sodium system simulant in bubble dynamic tests, as proposed in the literature for SFR source term research. For the first time, we provide novel similarity criteria for understanding bubble dynamics in liquid sodium systems using water as a working fluid by intelligently combining computational and experimental data. The bubble aspect ratios of water and scaled up sodium systems are similar, according to the experiment and numerical study. A remarkable resemblance in bubble aspect ratio exists between a water bubble of dimension 0.5 cm and a sodium bubble of diameter 0.9 cm. As a result, the defined water-to-sodium similarity criteria will be useful in performing water-based experiments to investigate bubble dynamics in sodium systems. Chapter 5 details the investigation of bubble dynamics with mass transfer for vapours.

CHAPTER-5

INVESTIGATION OF BUBBLE DYNAMICS WITH MASS TRANSFER FOR VAPOURS

Chapter-5: Investigation of bubble dynamics with mass transfer for vapours

5.1 Introduction

The extent to which radioactive iodine ($^{131}_{53}I$) is released in elemental form from failed fuel pin of fast breeder reactors (FBRs) into environment is an important safety issue to be addressed with reference to its radiotoxicity. Radioiodine ($^{131}_{53}I$) is a short lived fission product $\left(t_{\frac{1}{2}} = 8.02\ days\right)$ and decays to $^{131}_{54}Xe$ with beta and gamma emissions, but is highly radioactive with a specific radioactivity of 124 MCi/kg. Radioactive $^{131}_{53}I$ may enter human body via contaminated water, milk or air. The ingested $^{131}_{53}I$ is dangerous, since it accumulates in thyroid gland of human body, which plays a fundamental role in childhood development and increases the risk of thyroid cancer. Radioactive iodine toxicity varies greatly with age, with children and adolescents being far more sensitive than adults.

The spent fuel subassemblies in typical SFR are cooled in the in-vessel storage locations for 185 effective full power days towards reducing the decay heat to less than 5 kW/SA before being shifted to spent fuel storage bay (Chetal *et al*., 2015). Storage is in a pool of demineralized water, which has a capacity to store 710 subassemblies. The bay is designed to hold spent FSA, BSA and also failed SA housed in partially water-filled leak tight containers for ~240 days, till the decay heat is reduced sufficiently to less than 2 kW/SA. SSSB houses spent SA storage racks with storage locations for storing spent SA & containers. Under the postulated design basis events of failure of fuel cladding during storage, fall of SA during handling and complete draining of SSSB releases gaseous and volatile fission products to the water pool. In the case of fast breeder fuels, high burnups and short cooling times allows only a very limited reduction of

the I-131 content by the time the fuel is moved to the spent fuel storage pool. Iodine may exist in spent fuel either in the free state or in a number of complex molecular forms with uranium, other fission products, or with other species present in the fuel or sodium such as alloying metals, cladding materials, impurities, etc. In case of fuel failure in SSSB, to the extent that iodine is released in elemental form along with noble gas bubbles, it is required to understand its scrubbing efficiency by the overhead water pool. This chapter is dedicated to iodine absorption in water pool during its travel to cover gas region above the pool and also demonstrates the mass transfer for a vapour.

An experimental facility to assess the iodine bubble retention in water is setup in the laboratory. The experimental setup consisted of three parts: bubble injection system, bubbler tank and bubble collection system. The bubble injection system is used to mix the inert gas with contaminant (i.e. iodine), followed by release of mixed gas bubbles into the liquid pool. The bubbler tank contains water and is used for interaction of water and mixed gas bubbles. The collection system is used to collect the off gas for analysis. The schematic of iodine bubble experiment (IBEX) facility is depicted in fig. 5.1.

As discussed in previous part, the objective of this experimentation is to study the iodine retention in water pool. The scslvofMassTransfer solver (Taqieddin, 2018) in OpenFOAM v4.1 has been validated against experimental results by simulating bubble rising in stagnant 2-D liquid domains with mass transfer. The solver couples one-fluid species transport model of Haroun (2010, 2012) with s-CLSVOF (Albadawi, 2013) two phase flow solver considering the interface changes due to the mass transfer. The simulated scrubbing efficiency of iodine agrees with the experimental results.

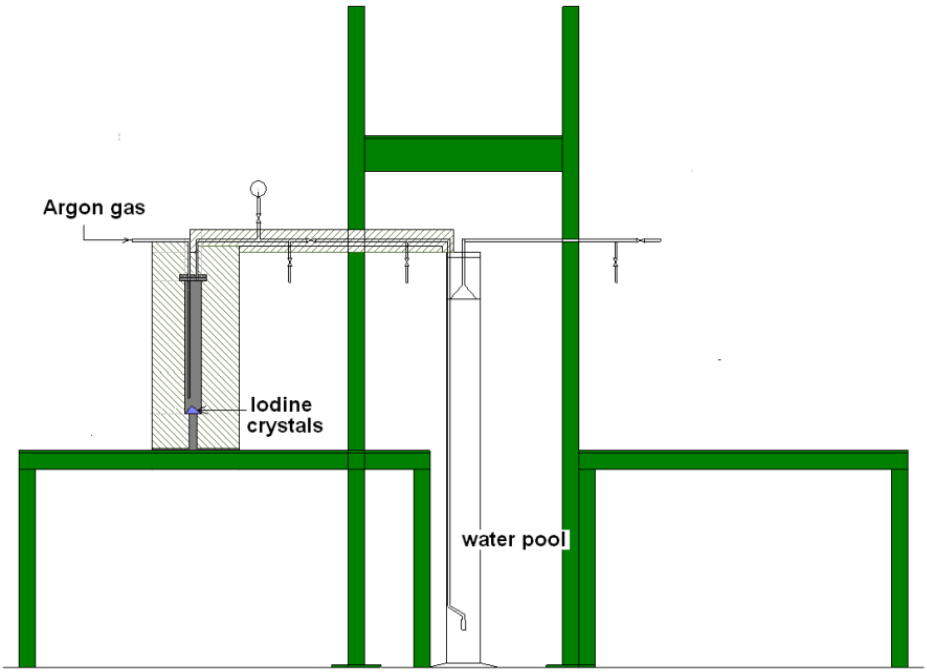

Fig.5.1 Schematic of iodine bubble experiment (IBEX) facility

5.2 Theory

Iodine is a chemical element with atomic number 53. It is heaviest of the stable halogens and its thermodynamics can be observed from the phase diagram (fig. 5.2).

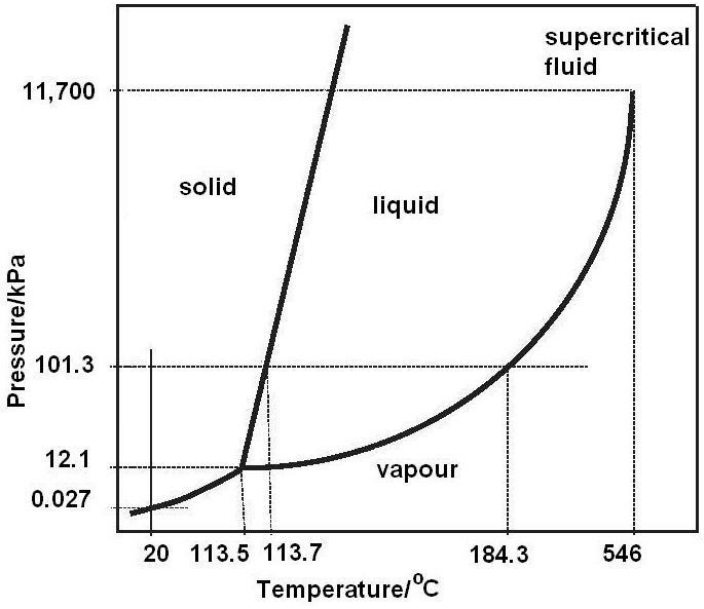

Fig.5.2 Phase diagram of iodine (Yolcu and Gürses, 2016)

The quantity of iodine injected into the water column is determined by observing the pressure decrease of the gas reservoir during the injection period using the following equation.

$$q = \frac{SVD}{760} \times \frac{273}{T} \times \frac{\Delta p}{p - (\Delta p/2)} \tag{5.1}$$

Table 5.1 Maximum mass of iodine injected as a function of temperature

Temperature (°C)	**Vapour pressure of iodine (atm)**	**Maximum mass of iodine injected, $m_{I2,in}$ (g)**
120	0.146	1.21
130	0.207	1.68
140	0.286	2.26
150	0.387	2.99
160	0.518	3.91
170	0.686	5.06
180	0.893	6.44
190	1.143	8.07

The maximum mass of iodine injected for a specified temperature is obtained when the system pressure reduces to zero from initial reservoir pressure. The maximum mass of iodine injected as a function of temperature is given in table 5.1.

The hydrolysis of iodine is an important reaction which controls the overall absorption rate of iodine vapour contained in argon gas by water. Hydrolysis of iodine results in formation of hydrated iodine cation and hypoiodous acid. The chemical reactions involved are as follows:

$$I_2(g) \leftrightarrow I_2(l) \tag{5.2}$$

Formation of hydrated iodine cation (H_2OI^+) which is precursor of hypoiodous acid (HOI)

$$I_2(l) + H_2O \leftrightarrow H_2OI^+ + I^- \tag{5.3}$$

Formation of hypoiodous acid (HOI)

$$I_2(l) + H_2O \leftrightarrow H^+ + I^- + \text{HOI} \quad (5.4)$$

$$3I_2(l) + 3H_2O \leftrightarrow IO_3^- + 5I^- + 6H^+ \quad (5.5)$$

The triiodide ion is formed as a result of reaction of iodine with iodide ion (Eq. 5.6) produced by hydrolytic reactions of iodine (Eq. 5.3, 5. 4 and 5.5).

$$I_2(l) + I^- \leftrightarrow I_3^- \quad (5.6)$$

$$H_2O \leftrightarrow H^+ + OH^- \quad (5.7)$$

The chemical reactions change the solubility of iodine in water due to the formation of triiodide ions.

The retention factor (*RF*) of iodine in water pool $= \left[\frac{m_{pool}}{m_{i2,in}}\right] \times 100\%$ (5.8)

5.3 Experimental setup

Figure 5.3 depicts the IBEX setup for experimentation to analyze the removal efficiency of iodine. The bubbler tank is made of acrylic tube and is filled with water upto the desired height. Bubble injection system comprises of argon gas cylinder, gas reservoir, pressure gauge, needle valves and gas inlet line extending upto the nozzle (Table 5.2). The bubbler collection system is comprised of collecting funnel, needle valves, activated charcoal filter, wash bubbler, vacuum pump and rotameter (Table 5.2).

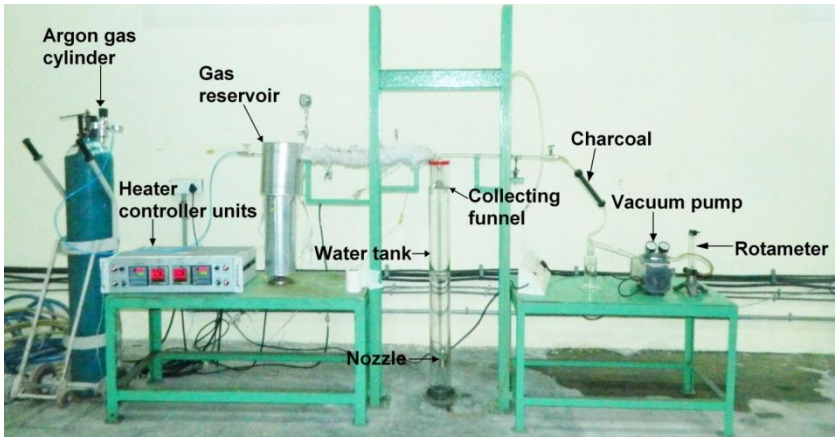

Fig.5.3 Experimental facility to carry out the experiments of iodine removal efficiency

Table 5.2 Experimental setup details

	Component	**Purpose**	**Location**
A	cylinder	To supply argon	-
B	regulator	Filling of argon in gas reservoir	After the cylinder
C	needle valve-1	To isolate the gas reservoir from cylinder after required pressurization of the gas reservoir	After the pressure regulator
D	gas reservoir	To store the iodine flakes	After the needle valve-1
E	pressure gauge	To read the pressure at the inlet of gas reservoir	Prior to bubbler tank
F	needle valve -2	To control the quantity of iodine injected	In the connection line
G	bubbler tank	The contain water pool for interaction with mixed gas	After needle valve-2

Fig.5.4 Gas reservoir with heater

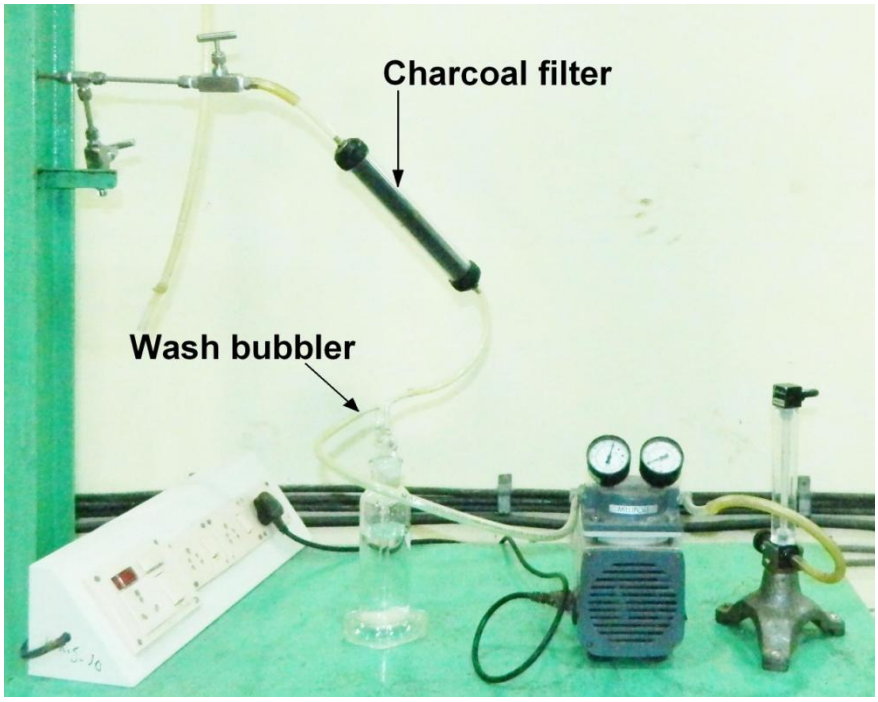

Fig.5.5 Bubble collection system

The gas reservoir and inlet line of bubble injection system are provided with insulations and heater controller units for maintaining required temperatures. The gas reservoir is provided with two different extension lines: pressurization line and release line (fig. 5.4). The bubble collection system consists of activated charcoal filter and wash bubbler sampler as shown in fig. 5.5 to trap iodine released from water pool. The quantity of activated charcoal in the outlet filter is decided based of the amount of iodine to be trapped.

5.4 Procedure for experiment

During the test run, a known amount of iodine flakes is taken into a stainless steel crucible (fig. 5.6), which is placed inside the gas reservoir. The reservoir is initially pressurized using argon gas via the pressurization line to the required pressure. The reservoir and gas inlet lines are properly insulated and heated to required temperatures (above iodine melting point) using corresponding heater controller units. The iodine vapours generated during heating mix with

argon gas inside the pressurized heated gas reservoir. The initial pressure of gas reservoir after heating is monitored before the start of gas release into bubbler tank.

The needle valve in the release line of gas reservoir is opened in a controlled manner to adjust the gas release duration during the test run. Distilled water is used as the scrubbing medium in the bubbler tank and experimental test runs are carried out by varying the water pool heights from 25-92 cm as shown in fig. 5.7.

Fig.5.6 Iodine in crucible before experiment

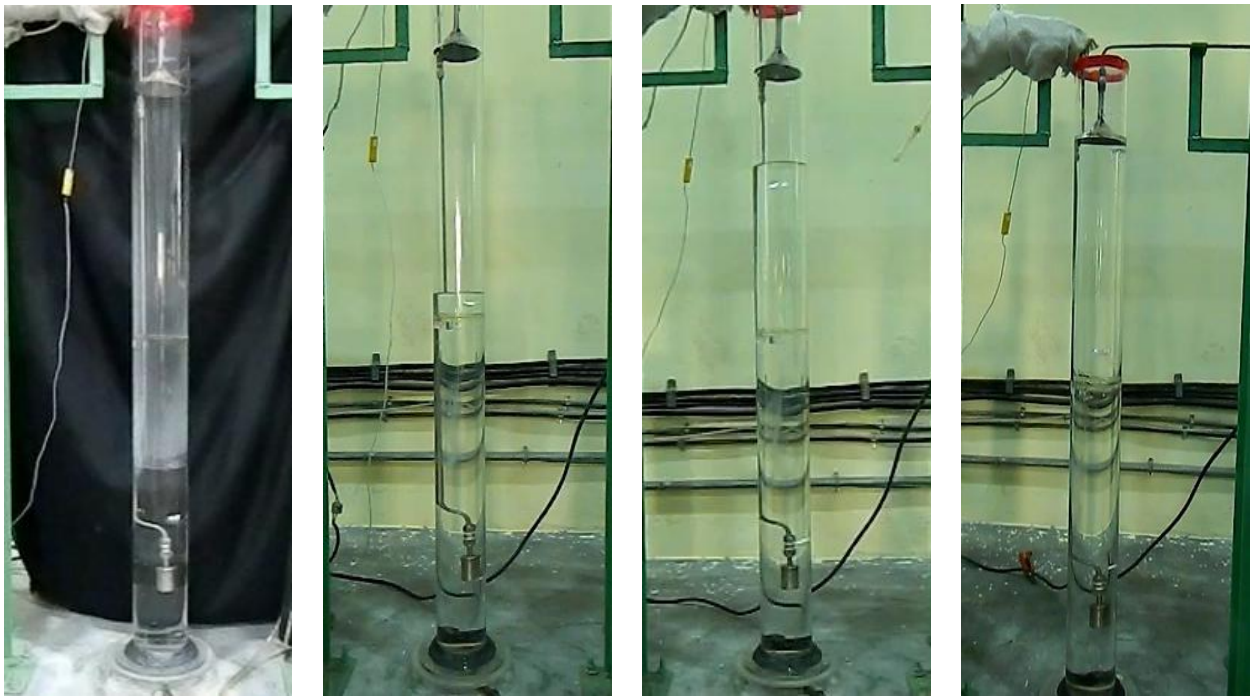

(a) (b) (c) (d)

Fig.5.7 Test runs in IBEX facility for various pool heights

The bubble collection system is simultaneously operated using vacuum pump during the bubble injection period of the test run to collect the non-retained iodine in activated charcoal and wash bubbler samplers. The release line needle valve is closed post-experiment and heaters are switched off before samples are collected for iodine measurements. The post-experimental image of iodine above the water pool is shown in fig. 5.8. Samples of water are collected from the bubbler tank and outlet tank for analysis. The activated charcoal filter after the test run is rinsed with distilled water, which is further analyzed for iodine content.

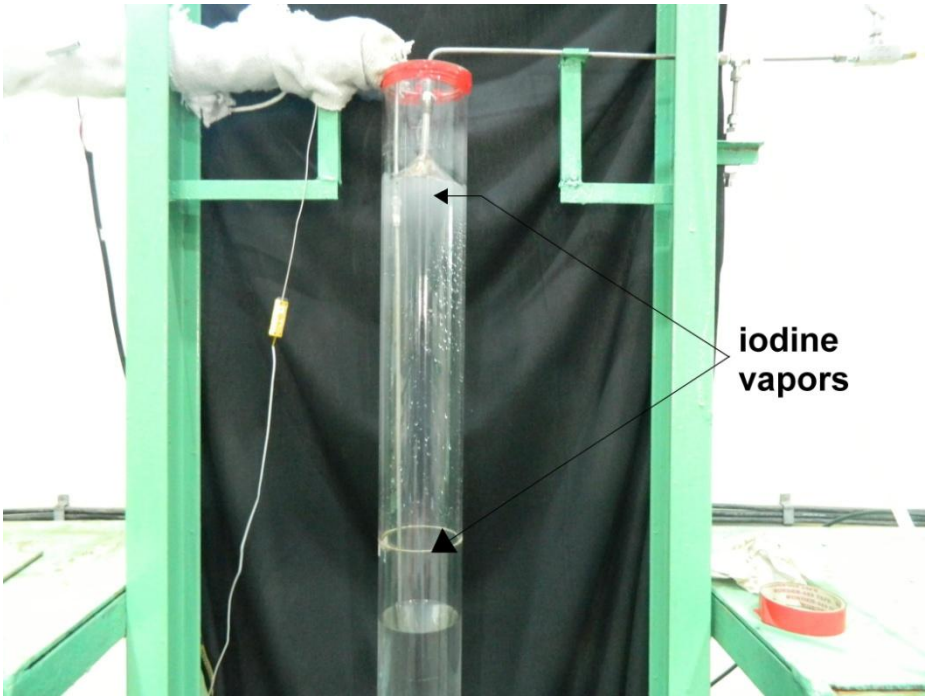

Fig.5.8 Iodine vapours collected at the top of the bubbler tank

Iodimetric titration is used in the present study to determine quantities of iodine in distilled water samples because of its accuracy, relatively easy to use and low cost sampling. Earlier studies used methods such as inductively coupled plasma mass spectrometry (ICP-MS)/neutron activation analysis (NAA) which are either very expensive or require several stages of manipulation for routine analysis.

(a) (b)

Fig.5.9 (a) sample (b) sample with acetic acid and potassium iodide

Fig.5.10 Sample solution after starch test

Samples of water containing iodine are collected in the sampling bottles. Starch test is carried out initially to find the presence of iodine. About 40 ml of sample in taken in a conical flask as shown in fig. 5.9a to which about 0.5 ml of acetic acid and 0.5 g of potassium iodide is added, resulting in an yellow solution as shown in fig. 5.9b. When starch is added to the resultant solution, it turns dark blue as shown in fig. 5.10. This indicates presence of iodine in water samples collected after the experiment.

Next step is an iodimetric titration as shown in fig. 5.11, which uses 0.001 N sodium thiosulfate solution as the titrant. The analyte consists of water sample mixed with acetic acid and potassium iodide. Starch is used as indicator.

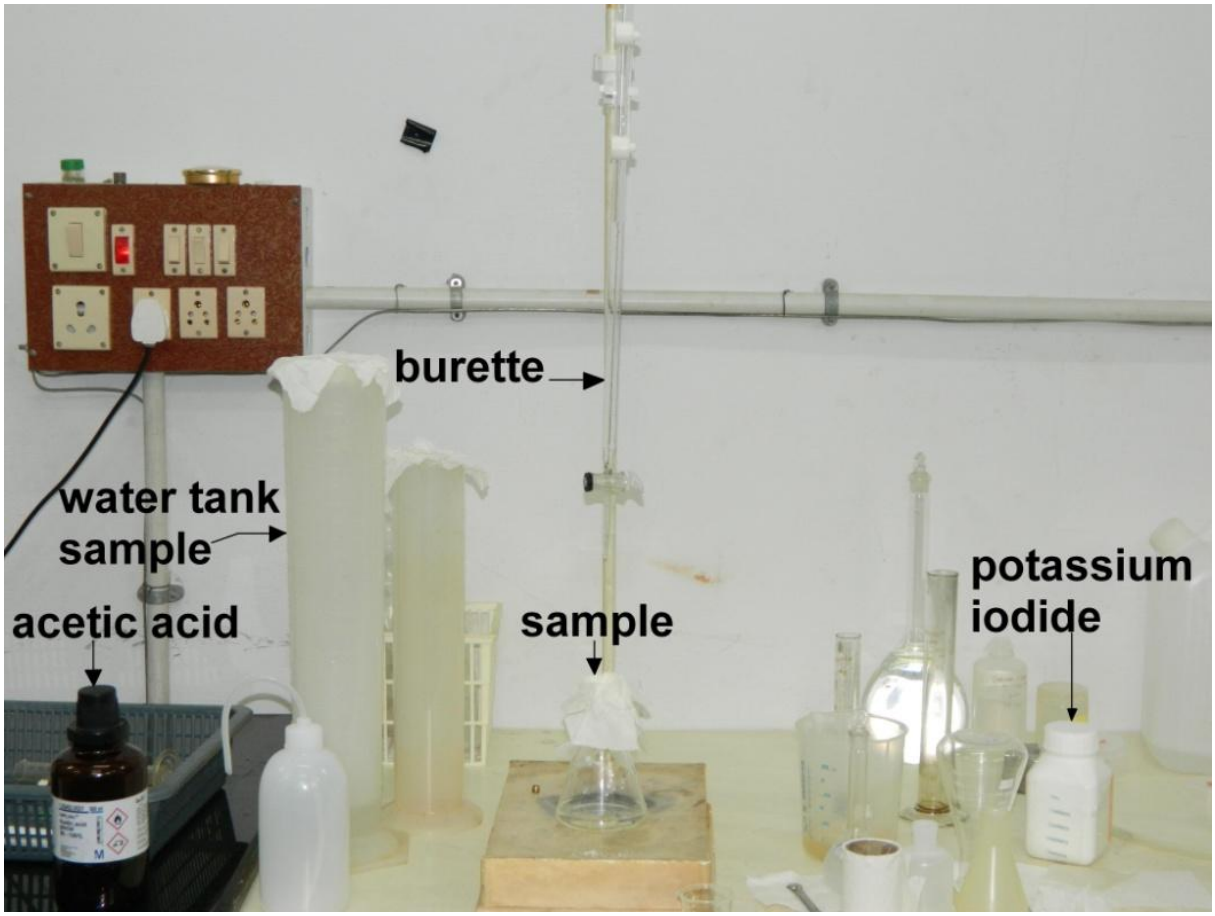

Fig.5.11 Iodimetric titration in chemical lab

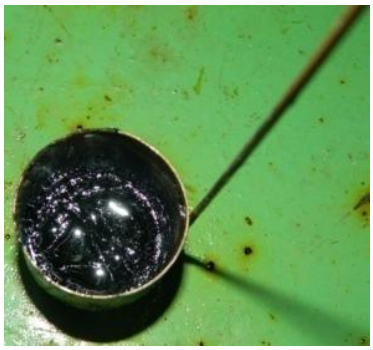

Fig.5.12 Iodine in crucible post experiment

The iodine left behind in the crucible post experiment is shown in fig. 5.12. The iodine deposited inside the gas reservoir after the experiment is cleaned by rinsing the gas reservoir with sufficient inventory of water, followed by titrating the resultant mixture with sodium thiosulphate in presence of acetic acid (0.5 ml), potassium iodide (0.5 g) and using starch solution as indicator as shown in fig. 5.13. The iodine deposited in the pipeline is estimated by heating the pipeline to required temperature, followed by flushing argon gas through the pipeline into the bubbler tank containing 1 m water column as shown in fig. 5.14. The iodine collected in the water column is determined using iodimetric titration.

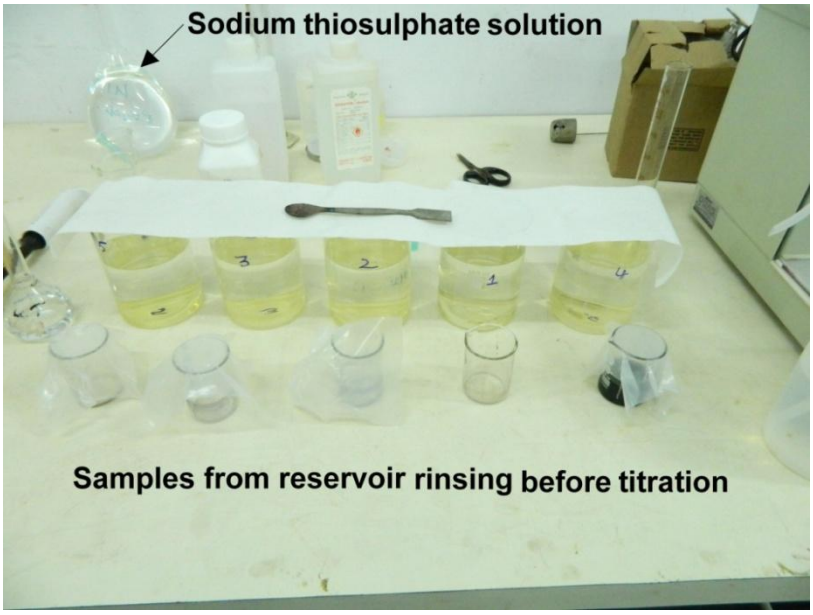

Fig.5.13 Iodine left behind in the gas reservoir

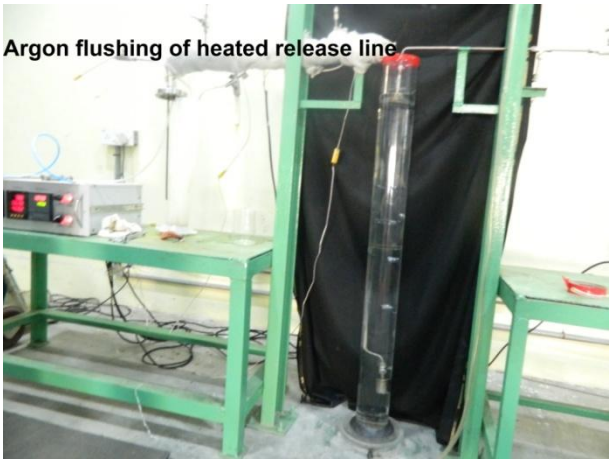

Fig.5.14 Iodine left behind in the gas inlet line

5.5 Numerical model

In the present study sclsvofMassTransfer solver is setup in OpenFOAM v.4.1 and used to investigate the iodine retention in water pool.

5.5.1. Physical description of the problem

The numerical investigation of iodine mass transfer is carried out in a two-dimensional domain of width 30 mm and height 480 mm as shown in fig. 5.15. Initially, the spherical bubble of diameter d_B = 10 mm contains 1 mol/m^3 iodine.

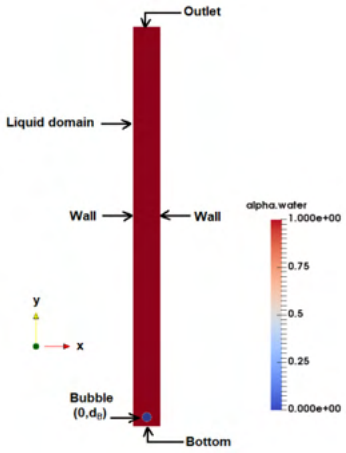

Fig. 5.15 Computational setup of bubble rising with species transport in a stagnant viscous liquid.

5.5.2. Computational model

The sclsvofMassTransfer solver setup in OpenFOAM v.4.1 is used to simulate the bubble rise dynamics with mass transfer. The governing equations, boundary conditions and solution algorithm are described in the following sections.

5.5.2.1. Equations that govern

The mass, momentum, phase fraction, and species transport conservation equations are listed below.

$$\nabla \cdot \vec{u} = \dot{v}_s \tag{5.9}$$

where $\dot{v}_s$ is the source term due to the interfacial mass transfer and represents the total mass transfer of all chemical species.

$$\dot{v}_s = A\left(\frac{1}{\rho_g} - \frac{1}{\rho_l}\right)\sum_{i=1}^{I} \dot{m}_i MW_i \tag{5.10}$$

where A is the interfacial area, I is the total number of chemical species, and MW_i (kgmol^{-1}) is the molecular weight of species i. Calculating the total mass transfer in Eq. (5.10) requires computation of interfacial area, A, at which the species transfers across the interface. The value of A can be determined as follows

$$A = |\nabla\alpha| V_{cell} \tag{5.11}$$

where V_{cell} (m^3) is the volume of the computational cell at the interface and $|\nabla\alpha| = 0$ inside the fluid phases and $|\nabla\alpha| \neq 0$ at the interface.

The mass transfer, $\dot{m}_i$ (mol/s) from the single species transport between two phases can be defined as:

$$\dot{m}_i = \left(-D_i \nabla c_i + D_i\left(\frac{c_i(1-He_i)}{\alpha + He_i(1-\alpha)}\right)\nabla\alpha\right)\cdot \hat{n} \tag{5.12}$$

Where $\hat{n}$ is the interface normal vector, which can be obtained from the LS model

$$\hat{n} = \frac{\nabla\psi}{|\nabla\psi|} \tag{5.13}$$

The LS function, ψ, is constructed from the field of α as:

$$\psi_0 = (2\alpha - 1)0.75\Delta x \tag{5.14}$$

The momentum conservation equation is given as:

$$\frac{\partial(\rho\vec{u})}{\partial t} + \nabla\cdot(\rho\vec{u}\vec{u}) = -\nabla p' + \nabla\cdot[\mu(\nabla\vec{u} + (\nabla\vec{u})^T)] + \rho\vec{g} + \vec{F}_\sigma \tag{5.15}$$

where p' is the relative pressure which accounts for the hydrostatic variations avoiding sudden changes and is defined as

$$p' = p - \rho g h \tag{5.16}$$

The first two terms in Eq. (5.15) accounts for the volume temporal and convection variations in the fluid momentum. In the right side of Eq. (5.15) the body and surface forces on the fluid, balance the momentum variations in the fluid to satisfy the conservation of momentum. In the presented framework, the surface tension force is calculated based on the interface identified by the LS model as shown in Eq. (5.17)

$$\vec{F}_\sigma = \sigma\kappa(\psi)\delta(\psi)\nabla\psi \tag{5.17}$$

where σ is the surface tension coefficient and κ is the interface curvature which is defined as

$$\kappa = -\nabla\cdot\hat{n} \tag{5.18}$$

One of the aspects of the LS method is the accuracy in calculating the surface tension, which is satisfied numerically by the Dirac function, δ in the form:

$$\delta = \begin{cases} 0 & if\ |\psi| > 1.5\Delta x \\ \frac{1}{3\Delta x}\left(1 + \cos\left(\frac{\pi\psi}{1.5\Delta x}\right)\right) & if\ |\psi| \le 1.5\Delta x \end{cases} \tag{5.19}$$

The δ function is used to limit the surface tension influence to a narrow region at the interface, where the function is centered at the interface, which has thickness of $3\Delta x$, and has a zero value in both phases.

The physical properties of the fluid (i.e. density and viscosity) are calculated based on the VOF method as given in Eqs. (5.20) and (5.21).

$$\rho = (1-\alpha)\rho_g + \alpha\rho_l \tag{5.20}$$

$$\mu = (1-\alpha)\mu_g + \alpha\mu_l \tag{5.21}$$

When computational cell is located in the liquid phase then $\alpha = 1$ and the fluid properties correspond to the liquid properties since the term $1-\alpha = 0$. The later term represents the volume fraction that is occupied by the gas phase, noticing that the sum of the liquid and gas volume fractions equals 1. On the other hand, when $\alpha = 0$ the cell will be located in the gas phase and the fluid properties are the same as the gas phase properties. In fact, the properties averaging takes place in the computational cells of the interface at which $0 < \alpha < 1$.

$$\alpha = \begin{cases} 0 & for\ cells\ filled\ only\ gas \\ 1 & for\ cells\ filled\ only\ liquid \\ 0 < \alpha < 1 & for\ cells\ representing\ the\ interface \end{cases} \tag{5.22}$$

The conservation equation of the volume fraction is given as:

$$\frac{\partial \alpha}{\partial t} + \nabla \cdot (\alpha \vec{u}) = \dot{\alpha}_s \tag{5.23}$$

where α is the volume fraction of liquid phase and $\dot{\alpha}_s$ (s^{-1}) is the source term due to mass transfer which is defined as:

$$\dot{\alpha}_s = A\frac{1}{\rho_l}\sum_{i=1}^{I} \dot{m}_i MW_i \tag{5.24}$$

The species transfer conservation model as follows:

$$\frac{\partial c_i}{\partial t} + \nabla \cdot (\vec{u} c_i) = \nabla \cdot \left(D_i \nabla c_i - D_i \left(\frac{c_i (1 - He_i)}{\alpha + He_i (1 - \alpha)} \right) \nabla \alpha \right) + R_i \tag{5.25}$$

where c_i is the concentration, D_i is the diffusion coefficient, and R_i is the source term of the chemical reaction for the chemical species i.

where, He_i is Henry's constant and is defined as per the chemical equilibrium as:

$$He_i = \frac{c_i^g}{c_i^l} \tag{5.26}$$

For I_2 in water, partition coefficients (inverse of Henry's constant) have been measured and are used as function of temperature only (Hasty, 1968):

$$log_{10}\left(PC_{I_2}\right) = 6.29 - 0.0149T(K) \tag{5.27}$$

The Haroun model determines the concentration of the one-fluid domain based on the arithmetic mean of volume fraction,

$$c_i = \alpha c_i^l + (1 - \alpha) c_i^g \tag{5.28}$$

Where c_i^g and c_i^l are, respectively, the concentration at the interface from bubble and liquid sides for species i and the diffusion coefficients are obtained based on harmonic averaging,

$$D_i = \frac{D_i^l D_i^g}{\alpha D_i^l + (1 - \alpha) D_i^g} \tag{5.29}$$

where D_i is the diffusion coefficient for the chemical species i, and the harmonic averaging of the diffusion coefficients reduces the spurious fluxes compared to the linear averaging. Diffusion coefficient in gas were calculated by the Hirshfelder, Bird and Spotz (1949) equation with the Wilke and Lee (1955) modification.

$$D_i^g = \frac{BT^{1.5}\left(1/MW_i + 1/MW_g\right)^{0.5}}{P\sigma_{ig}^2 \omega_D} \tag{5.30}$$

$$B = 0.00214 - 0.000492\left(1/MW_i + 1/MW_g\right)^{0.5} \tag{5.31}$$

Where, MW_g is the molecular weight of gas, P(atm) is the total pressure.

The collision diameter, σ_{ig} (Å) is given as

$$\sigma_{ig} = \frac{1}{2}(\sigma_i + \sigma_g) \tag{5.32}$$

ω_D is the collision integral for mass diffusivity and is a function of kT/ε_{ig}

Where

$$\varepsilon_{ig}/k = \sqrt{\left(\frac{\varepsilon_i}{k}\right)\left(\frac{\varepsilon_g}{k}\right)} \tag{5.33}$$

where ε is the characteristic energy of interaction between molecules and k is the Boltzmann constant.

On the basis of data tabulated by Hirschfelder, Curtiss, and Bird (1954)

$$\omega_D = 0.7075 + 0.7341/\left(kT/\varepsilon_{ig}\right) \tag{5.34}$$

Range $1.0 \leq kT/\varepsilon_{ig} \leq 2.5$ with average deviation of 0.1% from tabulated data.

Wilke and Chang (1955) presented a relationship for calculation of diffusion coefficients in liquids:

$$D_i^l = \frac{7.4 \times 10^{-8}(xMW_l)^{0.5}T}{\mu_l V^{0.6}} \tag{5.35}$$

where V is the molecular volume of diffusing substance, 71.5 cm^3/gmol for iodine. The viscosity of liquid water, μ_l (cP) is given as:

$$\frac{100}{\mu_l} = 2.1482\{(T - 281.615) + [8078.4 + (T - 281.615)^2]^{0.5}\} - 120 \tag{5.36}$$

5.5.2.2. Boundary conditions

The boundary conditions at the bottom are set to fixedValue uniform (0 0 0), zeroGradient, and zeroGradient for the velocity, pressure and volume fraction, respectively. At the walls, the boundary conditions for the velocity, pressure, and volume fraction are, respectively, noSlip,

fixedFluxPressure, and zeroGradient. Finally, the boundary conditions at the outlet are selected as inletOutlet uniform (0 0 0), totalPressure uniform 0, and zeroGradient for the velocity, pressure, and volume fraction, respectively, and the level set function is set to zeroGradient boundary condition at all boundaries.

5.5.2.3 Solution methodology

Figure 5.16 shows the computational algorithm that is implemented to evaluate the governing equations of mass, momentum, concentration, and volume fraction conservation models using the sclsvofMassTransfer solver. We note that the discretization schemes of the sclsvofMassTransfer solver are based on the finite volume approach in OpenFOAM v4.1. Starting with initializing the u, p, c and α and setting the boundary condition, OpenFOAM starts the sclsvofMassTransfer algorithm as shown in Fig. 5.16. Then ψ field is constructed from α using Eq. (5.14). After that the time marching of the simulation takes place ensuring the time stability. The numerical stability is associated with Courant number, Co, which controls simulation stability by satisfying the Courant-Friedrichs-Lewy (CFL) condition that is defined as:

$$Co = \sum_{i=1}^{n} \frac{u_{x_i} \Delta t}{\Delta x_i} \leq Co_{max} \tag{5.37}$$

where Δt is the time step size, n is spatial dimension (i.e. one, two, or three dimensional), u_{x_i} is the fluid velocity, Δx_i is the cell size, and Co_{max} is the maximum Courant number which is $Co_{max} = 1$. Following the time stability, advection of volume fraction is carried out. OpenFOAM solves the advection equation of α using the MULES algorithm which is based on the method of flux corrected transport.

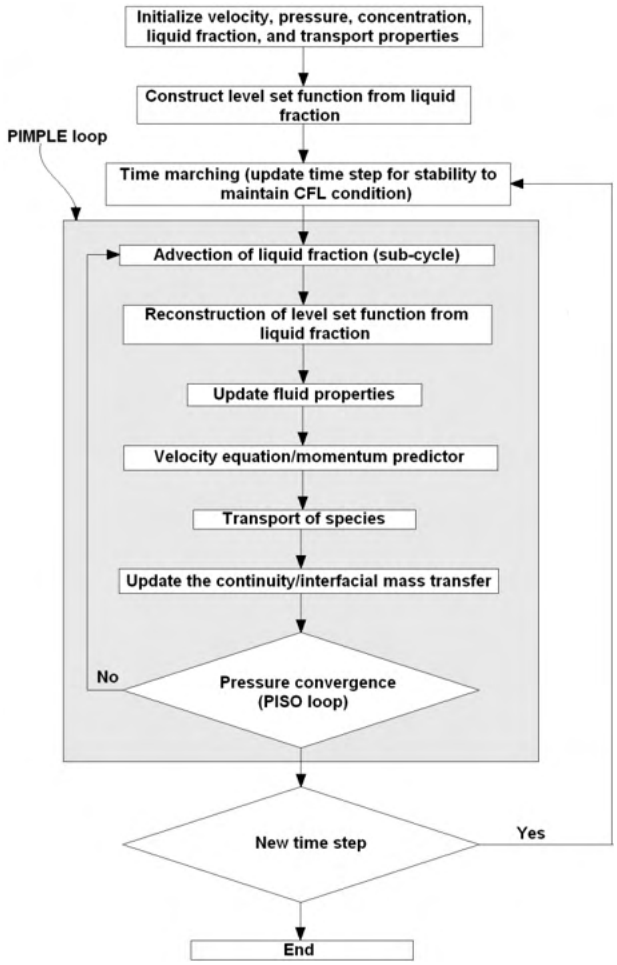

Fig. 5.16 Schematic algorithm of the proposed sclsvofMassTransfer solver

This algorithm implements an additional limiter cutoff on the face-fluxes at the critical values. Following the advection of α, ψ is reinitialized and the fluid properties gets updated. Then ψ computes the normal vectors, evaluate the interface curvature and the surface tension. After that the velocity field is predicted, then transport of species is carried out. From the transport of species, the interfacial mass transfer can be calculated. Lastly, the pressure convergence is checked using pressure-implicit with splitting of operators algorithm, PISO loop. At this stage the updated continuity equation is implemented in calculating the pressure.

$$\nabla \cdot \left(\frac{1}{\alpha_D} \nabla p'\right) = \nabla \cdot \vec{u} - \dot{v}_s \tag{5.38}$$

where p' is the corrected pressure, α_D is the pressure matrix equation coefficients. The pressure is called corrected since it is evaluated based on the corrected velocity field and updated mass transfer of the cell faces by satisfying the continuity in Eq. (5.9) as last step of the algorithm, where the pressure at the beginning of the computational algorithm is guessed in the momentum predictor step to evaluate the velocity equation.

The coefficients α_D are evaluated from the discretized momentum equation to determine the pressure. If the pressure convergence is not achieved the solver goes back to the advection of α step re-evaluating and correcting the fields till reach the pressure convergence condition. Once the pressure convergence criteria is satisfied the computational algorithm in Fig. 5.17 leaves the PIMPLE loop starting a new time step or stopping the simulation in case the final time is reached.

5.5.2.4 Post processing

The post processing has been carried out using paraView. We have used the velocity of the center of gravity of the bubble to approximate the rise velocity of the bubble (Raees *et al*, 2011). In OpenFOAM, it can be written as

$$Rise\ velocity = \frac{\int (1-\alpha_1) U d\Omega}{\int (1-\alpha_1)} \tag{5.39}$$

5.5.3 Verification

This section provides a verification test to show the accuracy of the s-CLSVOF solver in OpenFOAM v4.1 by simulating a stationary bubble in 3-D liquid domain. We compare the interfacial pressure to Young-Laplace pressure and the pressure that obtained from VOF. In the same section, we run another verification test for the one-fluid transport of species model by simulating a transport of species between a two phase planar layers. We compare the concentration results with published computational results.

5.5.3.1 Verification of bubble dynamics solver

At the interface between two fluid phases the, the capillary pressure between two static fluids is described by the Young-Laplace equation.

$$\Delta p = \frac{2\sigma}{r} \tag{5.40}$$

Pressure discontinuity across the interface occurs as part of the equilibrium with the surface energy (i.e. surface tension). Young-Laplace pressure is considered as a fundamental and direct approach to compare the computational result to a well-established analytical equation. In this manner, we perform a case study by simulating a stationary bubble in a 3-D liquid domain as shown in Figure 5.17.

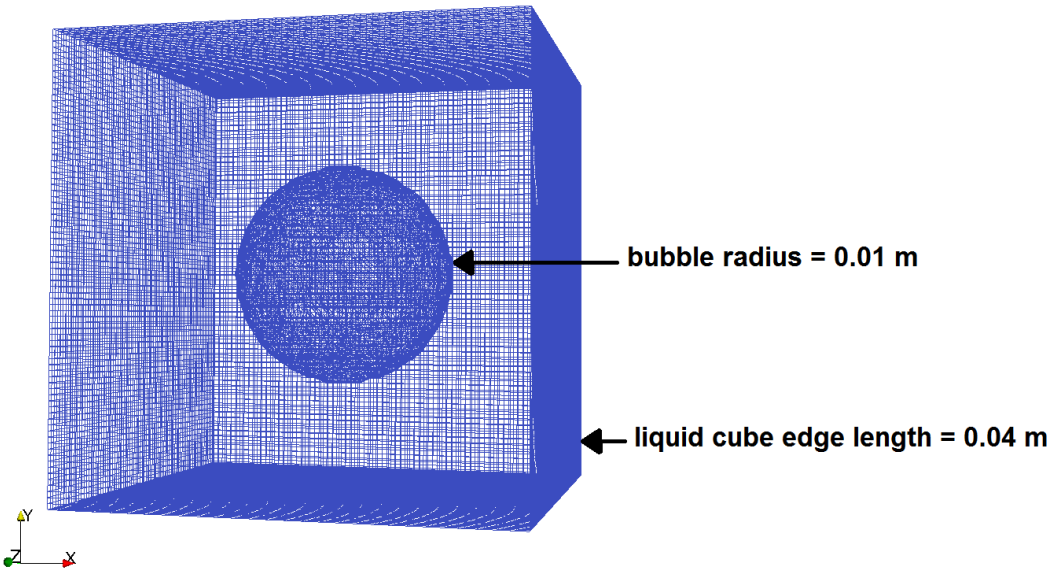

Fig. 5.17 Spherical bubble is positioned in stagnant liquid

The simulation is performed one time using interFoam and another using s-CLSVOF with bubble radius = 0.01 m, $\sigma = 1\,N/m$, and a cubic domain with edge length=0.04 m and computational mesh of 80x80x80. The results are shown in Figure 5.18. The density and viscosity ratios between the two phases are, respectively, 10 and 1. The pressure profile calculated by the s-CLSVOF solver is closer to the theoretical result compared to the interFoam

solver as shown in Fig. 5.18. The estimated error of the s-CLSVOF is approximately 2.5 % as compared to the interFoam which underestimates the pressure by 12.85 % compared to the analytical result by Young-Laplace equation. Therefore, this test case proves the improvement and accuracy of s-CLSVOF compared to interFoam.

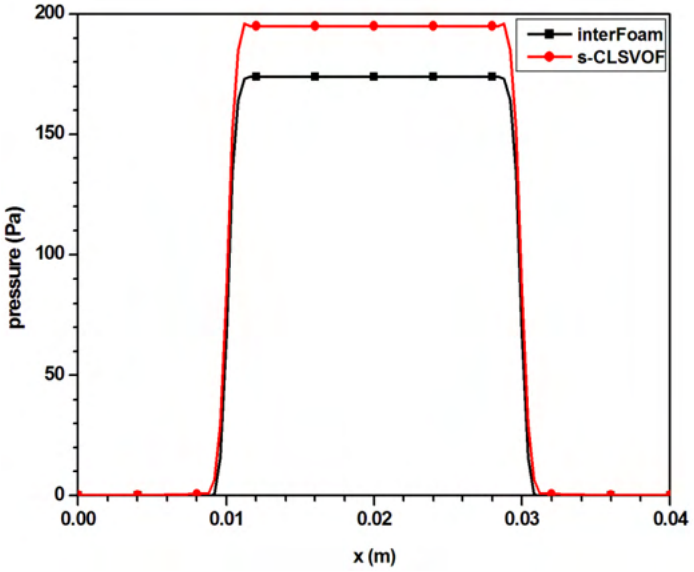

Fig. 5.18 Pressure distribution in the x direction along the central axis

5.5.3.2 Verification of species transport solver

Here, we reproduce two tests to validate our transport of species in one-fluid model. Verification test studies the concentration profile across the planar domain which is shown in Fig. 5.19. In this test, Henry's constant is selected to be $He_i = 100$ and the diffusion coefficients ratio are $D_i^g/D_i^l = 1$ and $D_i^g/D_i^l = 100$ respectively. The initial condition c_0^g and c_0^l are respectively, the initial concentration of the gas and liquid phases, which are taken for this problem as $c_0^g = 0$ and $c_0^l = 1$, and h is the elevation of the computational domain which is selected to be 1 cm. The boundary conditions are $c(y = 0, t) = 1$ and $\partial c/\partial y\,(y = h, t) = 0$.

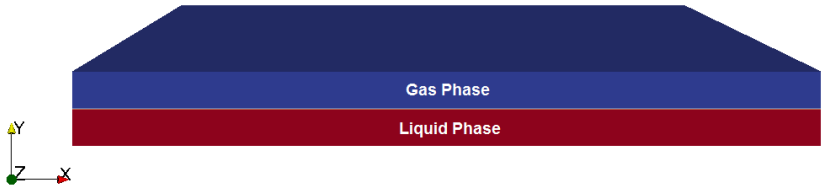

Fig. 5.19 Schematic of planar transport of species between two phases to validate the one-fluid model of species transport in OpenFOAM

The obtained results are shown in Figs. (5.20) and (5.21) respectively for the two diffusion coefficient cases. These simulation results match the computed profiles by Nieves-Remacha *et al*. (2015) who compared the OpenFOAM simulations to MATLAB models. The jump in concentration at the interface reveals a smooth transition between the two phases at the final time. By this, the constructed one-fluid transport of species model works as expected in OpenFOAM with interFoam.

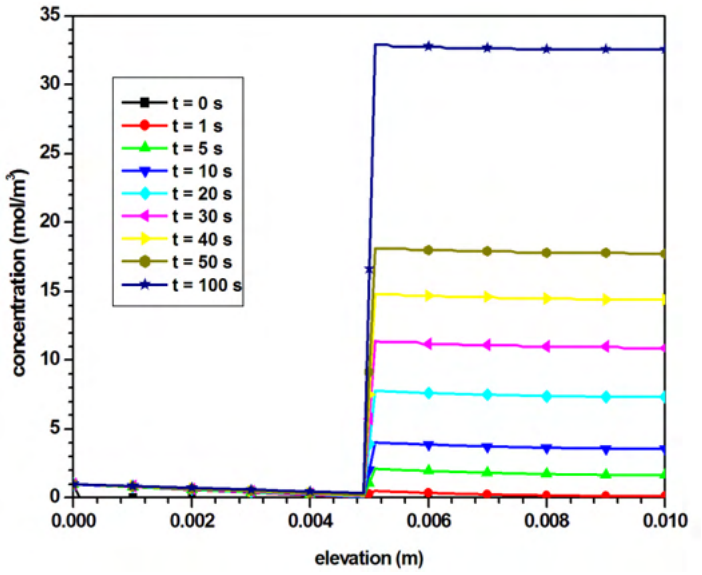

Fig. 5.20 Concentration profiles using OpenFOAM over time across a planar domain with He = 100 and diffusion coefficients ratio equals 1

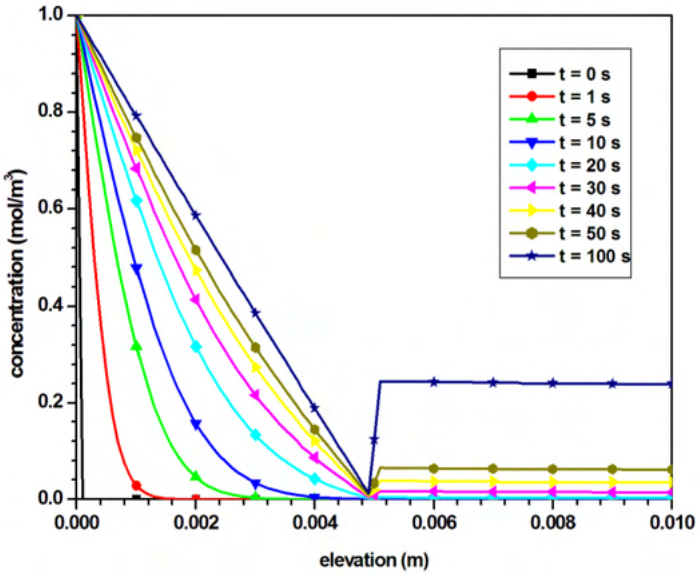

Fig. 5.21 Concentration profiles using OpenFOAM over time across a planar domain with He = 100 and diffusion coefficients ratio equals 100

5.6 Results and discussion

By analyzing the experimental data, it is found that the water setup is able to remove ~80 % of the iodine from the argon gas for ~1 m water pool height. The efficiency is low compared to earlier studies because of absence of steam condensation and presence of non volatile iodine species as in earlier experiments by Diffey *et. al*. (1965) and low solubility of iodine in water. Table 5.3 illustrates the results of the experimental study on iodine removal efficiency. The variation of iodine scrubbing efficiency with pool height is also given in fig. 5.15.

Table 5.3 Iodine removal efficiency of water facility

S. No.	P_i **(kg/cm^2)**	P_f, **(kg/cm^2)**	T **(°C)**	$m_{I2,c}$ **(g)**	$m_{I2,in}$ **(g)**	H_p **(cm)**	t **(min)**	$m_{I2,pool}$ **(g)**	RF **(%)**
1	6.3	0	190	30.021	6.77	25	4	0.181	2.67
2	6.7	0	190	20.002	7.71	92	8	6.16	79.87
3	6.9	0	190	20.004	2.05	75	40	1.655	80.72
4	6.3	0	190	20.0294	1.28	50	4	0.595	46.36

In test no. 1 the mass of iodine left behind in the crucible post experiment is 8.176 g. The iodine deposited inside the gas reservoir post experiment is collected by rinsing the gas reservoir with ~6 liters of water. The mass of iodine left behind in gas reservoir is estimated to be 14.49 g. The iodine deposited in the pipeline is estimated by heating the pipeline to required temperature (190 °C) maintained during experiment, followed by flushing argon gas through the pipeline into the bubbler tank containing 1 m water column. In the test no. 1 the mass of iodine deposited in pipeline is estimated to be 0.2 g.

The numerical study is performed by running 2-D simulation of bubble flow with transport of iodine species across the bubble. The initial concentrations inside the bubble and in the liquid medium are 1 mol/m^3 and zero respectively. The boundary conditions of the species are set to zero gradient everywhere, with He = 0.017, MW= 254 g/gmole, and D_g/D_l= 5498. For the 2-D simulation Δx = 0.00015 m was used with an adaptive time step for fixed values of Co_{max} = 0.2 and Δt_{max}= 0.0005 sec. The comparison of numerical model with experimental results for iodine retention in water obtained from in-house experiments and those from Beghi *et al*. (2018) are presented in fig. 5.22. Beghi *et al*. (2018) used a bubbling volume absorbent scrubber to purify gaseous molecular iodine. A bubble column reactor was 1.5 m high and 0.2 m in diameter loaded with DI water kept at constant level of 0.96 m. The numerical model was observed to predict more closely with Beghi *et al*. (2018) experimental results. The scrubbing efficiency experimental results showed close results at rise time of 3.3 s, but was observed to decrease with increase in inlet iodine concentration at rise time of 0.73 s. Since the numerical model does not model the chemical reaction between iodine and water, the variation of scrubbing efficiency with inlet concentrations could not be modeled.

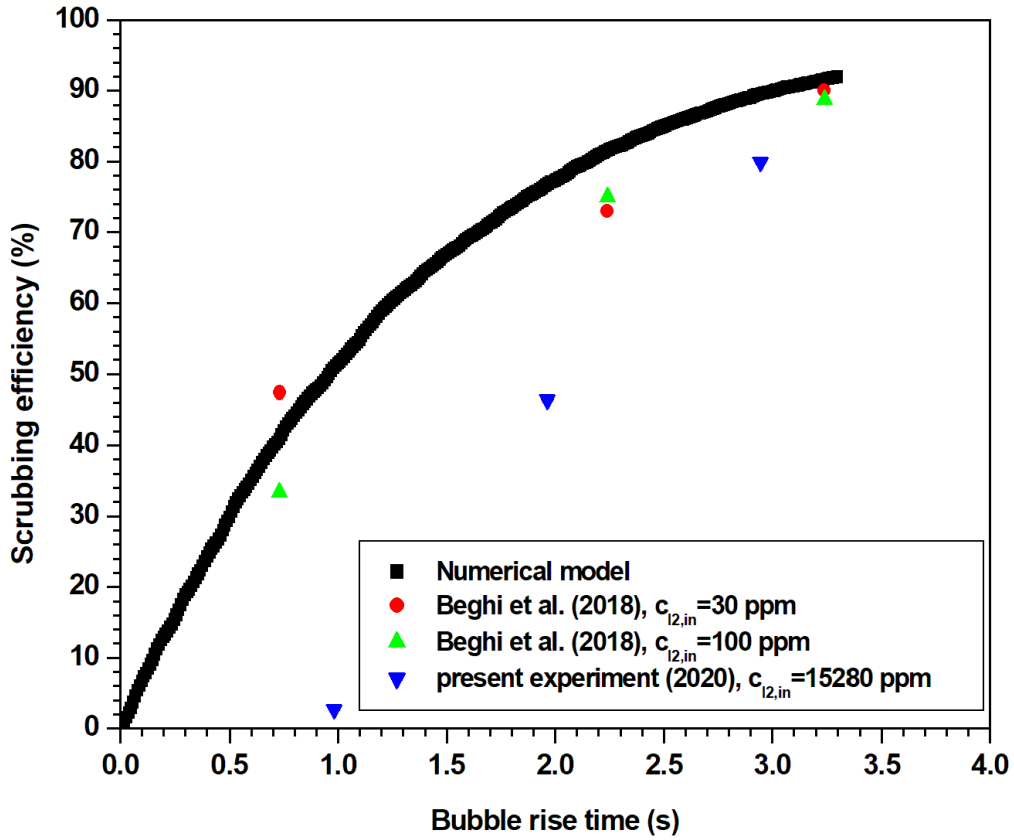

Fig. 5.22. Comparison of numerical model with experimental results for iodine retention in water

5.7 Closure

An experimental water setup, IBEX has been designed, fabricated and installed at Indira gandhi centre for atomic research (IGCAR) to study iodine retention in water pool. The setup consists of iodine bubble injection system, bubbler tank and bubble collection systems. This work uses the rapid, simple, reliable, affordable, and flexible iodimetric titration method for the measurement of iodine concentration in water samples. The maximum iodine removal efficiency of ~80 % is obtained for the water pool of ~1 m height from the present study. A numerical study on iodine retention in water pool is also carried out and is in good agreement with experimental results. Next chapter is dedicated towards bubble dynamics with mass transfer for aerosols.

CHAPTER-6

INVESTIGATION OF BUBBLE DYNAMICS WITH MASS TRANSFER FOR AEROSOLS

Chapter-6: Investigation of bubble dynamics with mass transfer for aerosols

6.1 Introduction

Accidental leakage of hot liquid sodium into contained air atmospheres of SFRs may result in sodium fire. The sodium fire generates sodium compound aerosols, which are harmful for public safety due to its chemical and radiological effects (Ballif *et al*., 1979). The aerosols can impair vision and upon inhalation damages mucous membrane of respiratory tract.

Several EACS were experimentally tested at HEDL, USA (Hilliard *et al*., 1976) to find the most ideal scrubber suitable for sodium fire aerosol removal in SFRs. The SGBS designed in 1979 by HEDL, USA satisfactorily met most of the requirements of an ideal scrubber for SFR, due to its passive and self cleaning nature. The air carrying aerosols is drawn in through the central duct downwards and later bubbles up through the submerged gravel bed as shown in fig. 6.1.

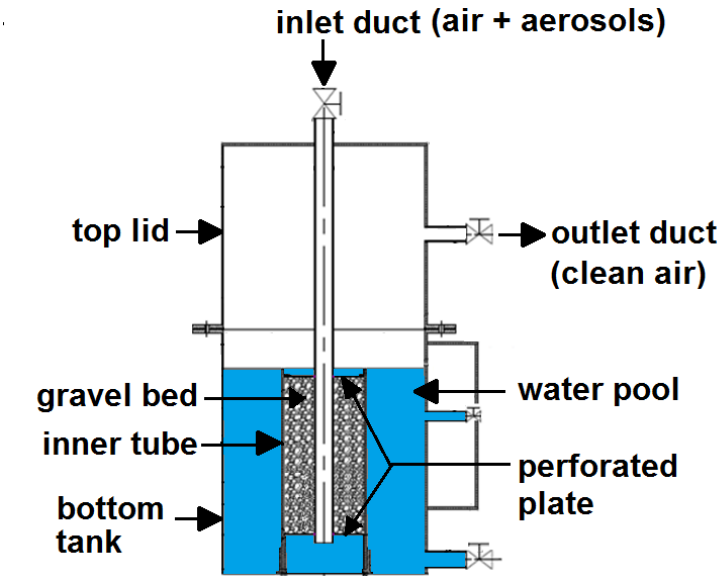

Fig. 6.1 Submerged gravel bed scrubber schematic

Theoretically, the SGBS efficiency was evaluated to date using semiempirical correlations available for packed bed scrubbers. The Calvert's model (Jackson and Calvert, 1966) is given by the following equation:

$$\frac{E(\%)}{100} = \left(1 - exp\left[-\frac{\pi Z K_p}{2(j + j^2)(\varepsilon - H)d_R}\right]\right) \tag{6.1}$$

$$K_p = \frac{V_g d_p^2 \rho_p}{9\mu_g d_R} \tag{6.2}$$

where, j = 0.192 is empirical constant relating channel width to packing diameter, ε = 0.45 is bed void fraction and H_d = 0.2 is fraction of bed occupied by liquid. In this chapter an in-house engineering scale model of SGBS is described in detail. The setup is designed, installed and fabricated in-house and experimental test runs were carried out on the scrubber for varying inlet sodium fire aerosol concentrations. Computational fluid dynamic (CFD) simulations are also performed to evaluate aerosol penetration in SGBS. A single channel of gravel packing is considered for the analysis and caps contact approach is used to overcome the difficulties in meshing. Three-dimensional (3-D) numerical simulations are carried out for evaluating aerosol removal efficiency for both nonsubmerged and submerged cases. Computational model used in the present study is validated against Calvert semiempirical correlation (Jackson and Calvert, 1966) available for packed bed scrubbers. The elaborate grid independent sensitivity analyses are carried out to arrive at the appropriate mesh size for the CFD investigation. Parametric studies are carried out to investigate the effect of aerosol diameter, gravel diameter and bed height on aerosol penetration. The study is useful in decreasing the aerosol penetration and enhancing the performance of EACS for SFRs.

Detailed description of the study is presented in the following sections. Section 6.2 explains the experimental setup and its details. Section 6.3 details the computational model setup for evaluating the sodium fire aerosol removal efficiency of SGBS. In section 6.4, the validation of

model with Calvert model is presented and grid independence studies are carried out in section 6.5.

6.2 Setup for experiments

An engineering scale experimental setup of submerged gravel bed scrubber has been setup at Indira gandhi centre for atomic research to evaluate its scrubbing efficiency for sodium fire aerosols. The design details of SGBS installation and experiments carried out towards evaluating its efficiency are described in the following sub-sections.

6.2.1 Design, installation and commissioning details

The SGBS installed at IGCAR is shown in fig. 6.2. A blower with maximum capacity of 50 m^3/h is used to induce gas flow of 2.1 m^3/h through the scrubber. Gas flows from the aerosol source through the SGBS and then through the blower. The technical specifications of installed SGBS are given in table 6.1.

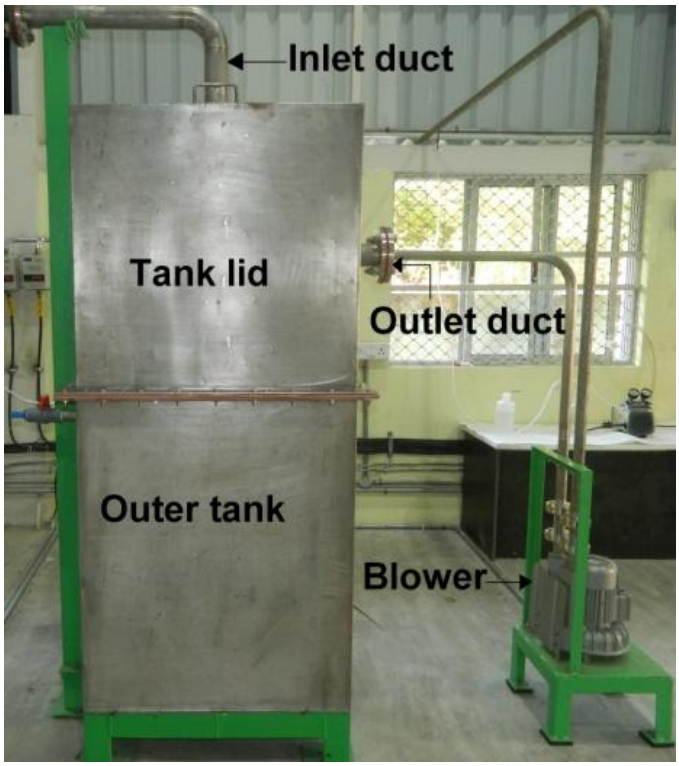

Fig.6.2 Setup of submerged gravel bed scrubber

Table 6.1 Technical specifications of SGBS at IGCAR

Design parameter	**Value**
inlet duct	
gas inlet duct outer diameter	74 mm
gas inlet duct inner diameter	67 mm
gas flow rate	2.1 m^3/h
depth of inlet duct below bottom perforated plate	13 mm
material	stainless steel 304L
gravel Bed	
bed diameter	305 mm
bed height	610 mm
material	blue metal chips (crushed granite stones)
packing material diameter	6.4-10 mm
packing material density	2500 kg/m^3
inner tube	
inner tube diameter	311 mm
inner tube length	762 mm
inner tube thickness	3 mm
material	stainless steel 304L
perforated plates	
top and bottom perforated plate opening	6 mm
number of openings on top and bottom perforated plate	374
perforated plate thickness	3 mm
material	stainless steel 304L
elevation of bottom perforated plate	150 mm
depth of skirt below bottom perforated plate	130 mm
outer tank	
outer tank length	780 mm
outer tank breadth	780 mm
outer tank height	930 mm
tank thickness	4 mm
material	stainless steel 304L
tank lid	
lid length	780 mm
lid breadth	780 mm
lid height	760 mm
lid thickness	4 mm
material	stainless steel 304L
outlet duct	
gas outlet duct outer diameter	74 mm
gas outlet duct inner diameter	67 mm
material	stainless steel 304L

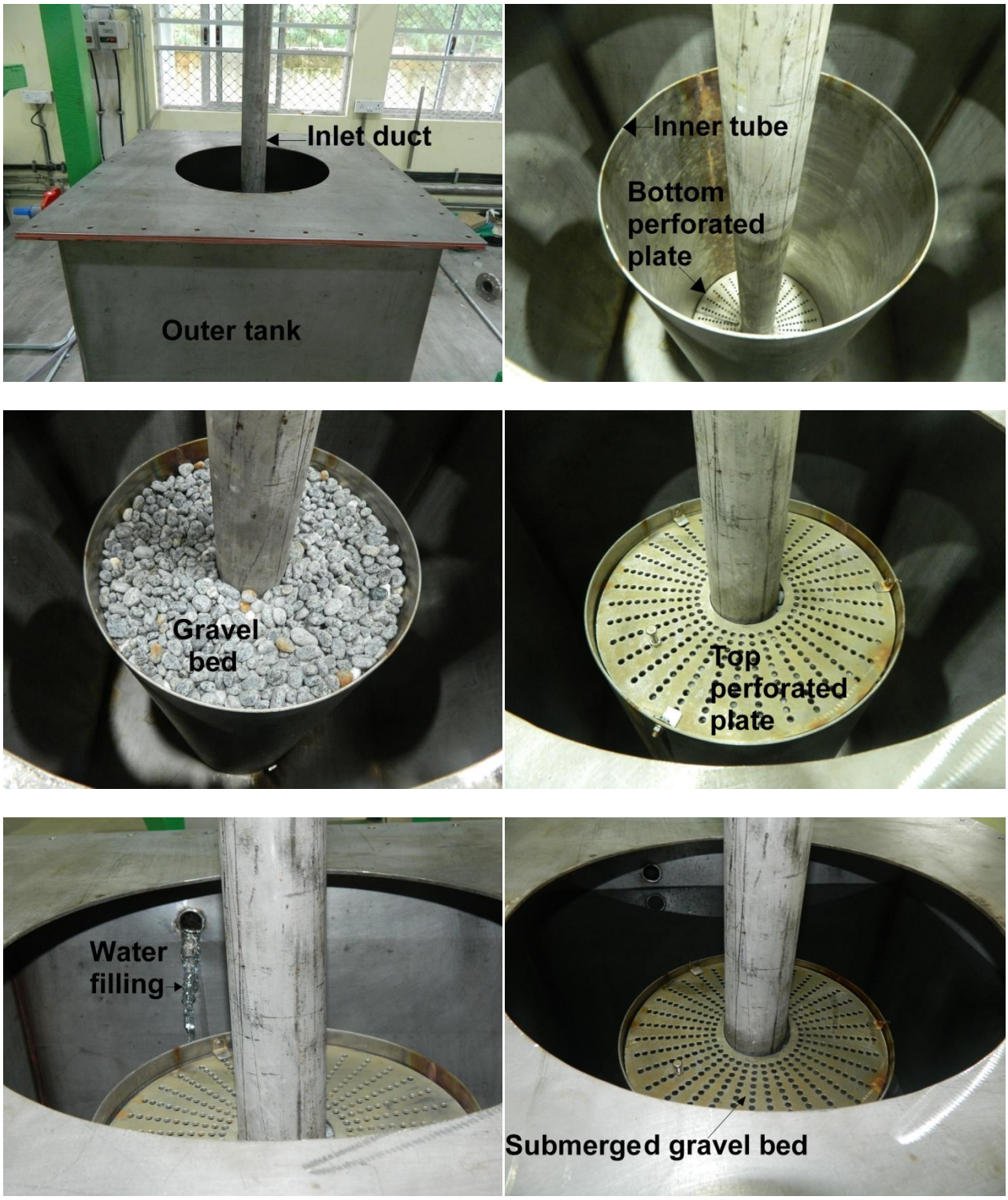

Fig.6.3 Photos of step by step installation of SGBS

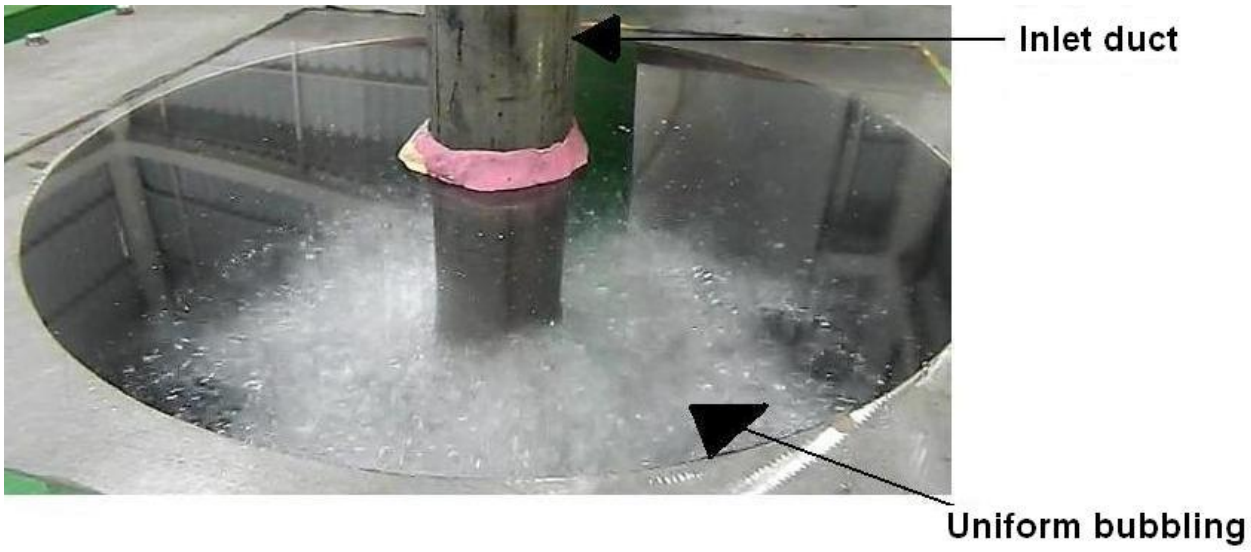

Fig.6.4 Photo of top of SGBS before mounting top lid

The photos of installation of SGBS are given in fig. 6.3. The blower was switched on and observation was made visually from the top of SGBS. The observation confirmed that air bubbled through the wetted packing as expected. The photo of the top of SGBS before mounting lid with blower in operation is shown in fig. 6.4. The bubble flow rate was significant resulting in entrainment of water drops to the region above the water pool. To avoid significant entrainment of drops upto the blower, a top tank lid was installed to provide the air outlet line 500 mm above the free surface of water pool.

6.2.2 Experimental determination of aerosol removal efficiency

To evaluate the effect of aerosol concentration on SGBS efficiency, combustion tests were carried out using different initial sodium masses as shown in table 6.2. Tests are performed using aerosol generated by sodium fire in a 0.0625 m^2 heated pan located in a 1.125 m^3 volume SS 304 chamber. The sodium fires are created by delivering approximately 0.05-1 kg of solid metal to a preheated burn pan at about 250 °C. Correspondingly the inlet mass concentrations of aerosols ranged from 0.04-19.94 g/m^3 for a gas flow rate of 0.0006 m^3/s. The generated aerosol is drawn through 2 meters of 2.5 inch diameter pipe to the scrubber.

Table 6.2 SGBS performance efficiency tests at various aerosol inlet concentrations

Test	**Mass of sodium (kg)**	**Inlet aerosol concentration (g/m^3)**	**Efficiency (%)**
1	0.05	0.017	13.77
2	0.2	0.28	85.7
		1.02	96.57
3	0.31	0.04	75
		0.72	93.75
		0.42	94.05
4	0.29	0.32	89.06
		0.38	90.79
		0.26	94.23
		0.18	86.11
5	1	0.67	70.15
		2.63	98.73
		3.94	99.66
		19.94	99.93
6	1.043	2.55	97.5
		5.65	99.03
		11.4	99.68

Test runs are carried out with inlet aerosol concentration as a parameter. During each test run 1-6 filter paper samples were taken from both scrubber inlet and outlet ports at specified time intervals. Aerosol samples (filters) are taken from the inlet duct immediately preceding the scrubber and entrance to the outlet duct. The aerosol mass concentrations are determined gravimetrically. Aquarium stone/enamel gravels of size 10-30 mm was used in test 1, which gave lower efficiencies and hence, the packing material was changed to blue metal granite stones of

size range 6.4-10 mm in the further test runs. Figure 6.5 shows the variation of scrubber efficiency.

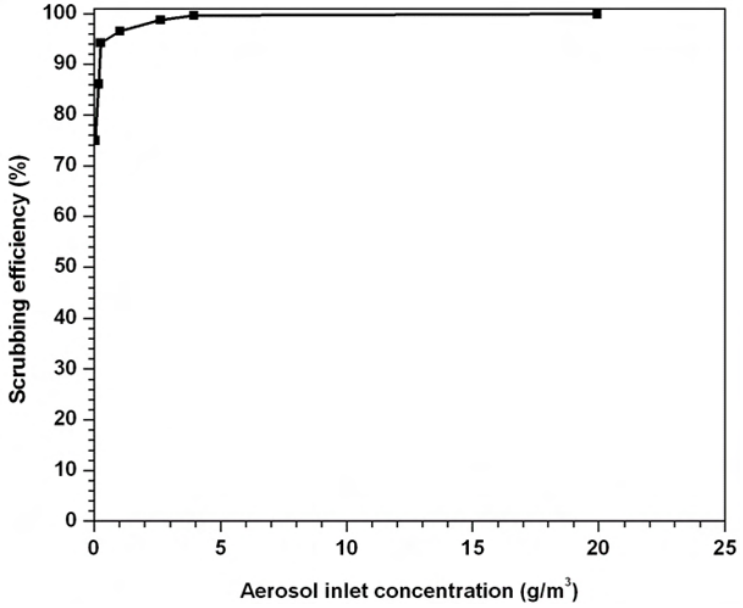

Fig.6.5 Variation of SGBS scrubbing efficiency with inlet aerosol concentration

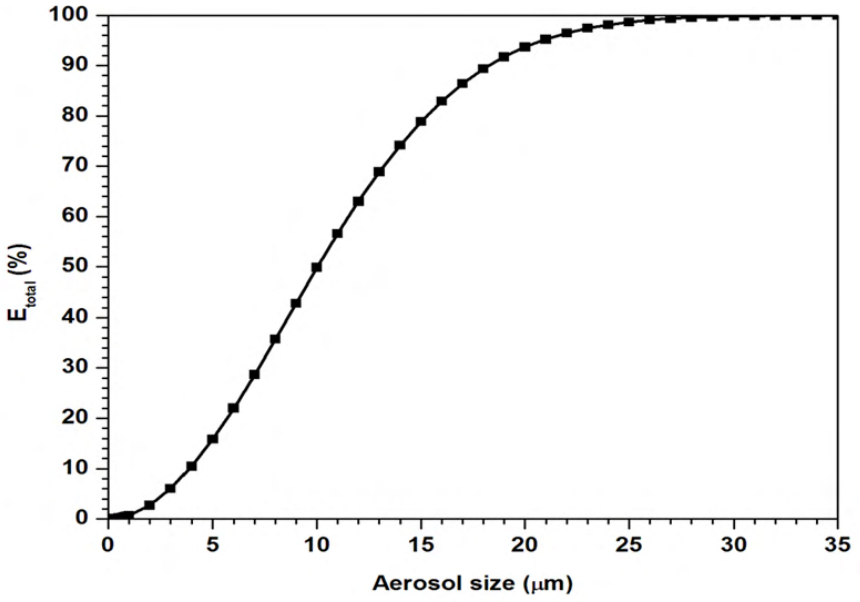

Fig.6.6 Grade efficiency curve from Calvert's model

The study shows that at very low gas flow rate and superficial velocity, the SGBS has the potential to scrub sodium fire aerosols with removal efficiencies of 75-99.93% for inlet aerosol concentrations in the range of 0.04-19.94 g/m^3. The inlet aerosol concentrations corresponded to a size range of 0.7-5.2 μm based on Kitani correlation (Kitani *et al*., 1973). Hence, higher the aerosol mass concentration at the SGBS inlet, higher is its size and removal efficiency. The scrubber provides efficiencies higher than 90 % for inlet concentration greater than 1 g/m^3 even at low gas flow rates of 0.0006 m^3/s. However, the semiempirical Calvert model is found to under predict the scrubber efficiency at low superficial gas velocities as shown in fig. 6.6 for the aerosol size range studied. This brings out the requirement for better theoretical models to capture the SGBS scrubbing efficiency.

6.3. Computational model

The 3-D numerical simulations are carried out for evaluating aerosol penetration in a packed bed of spheres for both nonsubmerged and submerged cases. A commercial CFD solver is used to solve the governing transport equations involved in the physical process.

6.3.1 Geometry and grid

The study considers a single channel of packed bed column for computational analysis of aerosol penetration in SGBS. The gravels are assumed to be spherical in shape and arranged in cubic type packing. The points of contact between spheres and between the sphere and side wall result in narrow fluid regions and hence, problems in meshing. To avoid difficulty in meshing the sphere-sphere junction and sphere-wall junctions, the caps contact approach (Dixon and Nicholas, 2017) is used. The study uses a gap of 0.5 mm and 0.25 mm between the capped spheres and the capped sphere and side wall respectively. The 3-D gravel bed geometry is

constructed from 20 basic capped sphere units contained within a cuboid. The basic unit of capped sphere used for present study is shown in fig. 6.7.

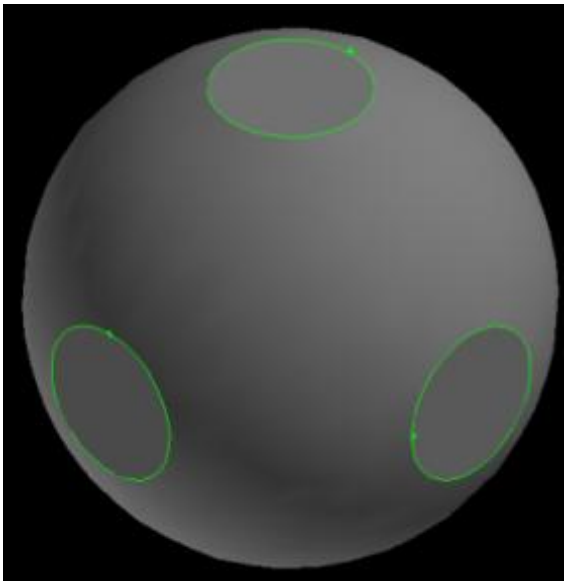

Fig.6.7 Basic capped sphere unit

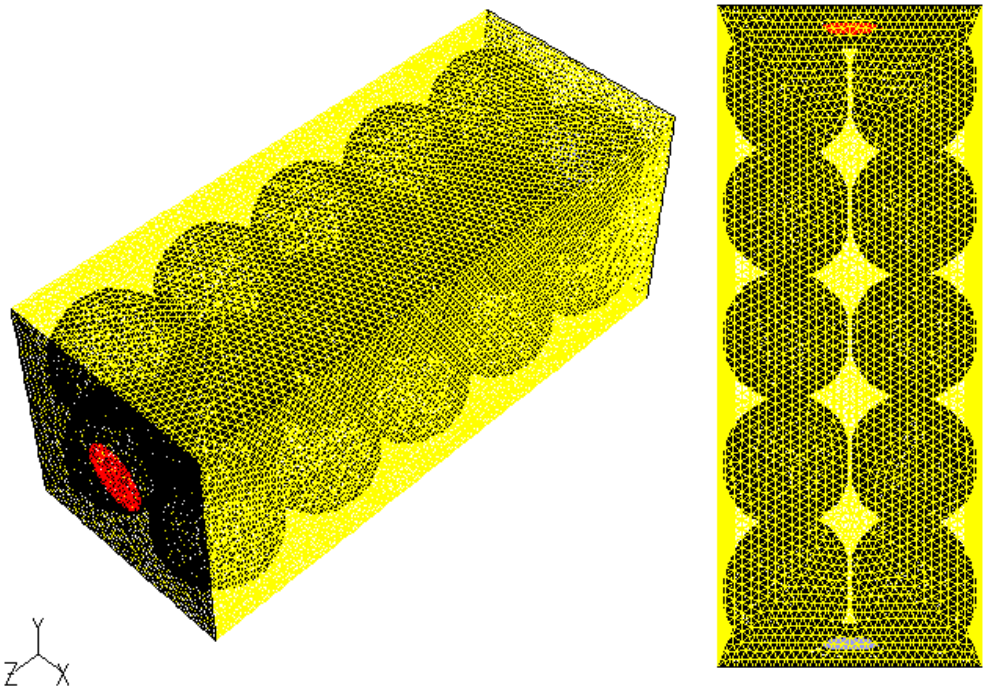

(a) (b)

Fig.6.8 Meshed model (a) isometric and (b) side view

The computational domain has a cuboid shape of dimensions, 20 mm (L) x 20 mm (B) x 50 mm (H), from which 20 capped sphere volumes have been subtracted. Inlet and outlet openings of 6 mm are provided at bottom and top wall respectively for the air flow carrying aerosols. The typical grid used for computational simulations are as shown in fig. 6.8.

6.3.2. Numerical details

The governing equations for mass, momentum, volume fraction and discrete phase are solved using commercial CFD solver in 3-D domain. The equations are as follows.

The continuity equation for continuous phase is given by:

$$\nabla \cdot \vec{u} = 0 \tag{6.3}$$

The conservation equation for momentum is described by:

$$\frac{\partial(\rho\vec{u})}{\partial t} + \nabla \cdot (\rho\vec{u}\vec{u}) = -\nabla \mathrm{p} + \nabla \cdot \{\mu[\nabla\vec{u} + (\nabla\vec{u})^T]\} + F_s + \rho\vec{g} \tag{6.4}$$

For nonsubmerged case

$$F_s = 0 \tag{6.5}$$

For submerged case

$$F_s = \sigma \frac{\rho k F_1}{0.5(\rho_g + \rho_l)} \tag{6.6}$$

where, the volume fraction of fluid is given by:

$$F_1 = \begin{cases} 0 & in\ bubble \\ 0 < F_1 < 1 & interface \\ 1 & in\ liquid \end{cases} \tag{6.7}$$

The interface surface curvature, *k* is given by:

$$k = -(\nabla \cdot \hat{n}), \text{where } \hat{n} = \frac{\vec{n}}{|\vec{n}|} \tag{6.8}$$

The mixed density, viscosity and velocity of fluid are described as:

$$\rho = F_1\rho_1 + [1 - F_1]\rho_2 \tag{6.9}$$

$$\mu = F_1\mu_1 + [1 - F_1]\mu_2 \tag{6.10}$$

$$\vec{u} = \vec{u}_1 \tag{6.11}$$

The volume fraction (F_1) of phase 1 is obtained by solving the conservation equation given by:

$$\frac{\partial(F_1)}{\partial t} + \nabla \cdot (\vec{u}F_1) = 0 \tag{6.12}$$

The packed bed Reynolds number is given as follows:

$$Re^* = \frac{d_R V_g \rho_g}{\mu_g(1-\varepsilon)} \tag{6.13}$$

The flow regimes can be classified based on packed bed Reynolds number as laminar (Re^*<1), transitional (1<Re^*<2000) and turbulent (Re^*>2000). The packed bed Reynolds number for flow through packed beds considered in the present study is in the transitional regime. This brings in the requirement for usage of a turbulence model with low Reynolds number effects to model the flow situation. The present study uses RNG *k-ε* turbulence model, which takes care of the low Reynolds number effects based on a differential formula for effective viscosity.

The renormalized group (RNG) *k-ε* turbulent model is derived from instantaneous navier stokes equations and uses renormalization group theory of Yakhot and Orszag (1986).

$$\frac{\partial}{\partial t}(\rho k) + \frac{\partial}{\partial x_i}(\rho k u_i) = \frac{\partial}{\partial x_j}\left[\alpha_k \mu_{eff}\frac{\partial k}{\partial x_j}\right] + G_k + G_b - \rho\varepsilon - Y_M + S_K \tag{6.14}$$

$$\frac{\partial}{\partial t}(\rho \varepsilon) + \frac{\partial}{\partial x_i}(\rho \varepsilon u_i) = \frac{\partial}{\partial x_j}\left[\alpha_\varepsilon \mu_{eff}\frac{\partial \varepsilon}{\partial x_j}\right] + C_{1\varepsilon}\frac{\varepsilon}{k}(G_k + C_{3\varepsilon}G_b) - C_{2\varepsilon}\rho\frac{\varepsilon^2}{k} - R_\varepsilon + S_\varepsilon \tag{6.15}$$

The model uses effective viscosity obtained from RNG theory, which accurately defines the variation of effective turbulent transport with effective Reynolds number required for low-Re flows and is given by,

$$d\left(\frac{\rho^2 k}{\sqrt{\varepsilon\mu}}\right) = 1.72\frac{\hat{v}}{\sqrt{\hat{v}^3 - 1 + C_v}}d\hat{v} \tag{6.16}$$

where, C_v = 100

$$\hat{v} = \frac{\mu_{eff}}{\mu} \tag{6.17}$$

For high Reynolds numbers, the effective viscosity is given as follows:

$$\mu_t = \rho C_\mu \frac{k^2}{\varepsilon} \tag{6.18}$$

where, the coefficient, C_μ = 0.0845, $C_{1\varepsilon}$=1.42 and $C_{2\varepsilon}$=1.62 are derived using RNG theory.

The aerosol trajectory is evaluated by stepwise integration of the aerosol equation of motion. The aerosol force balance in the *z*-direction of cartesian coordinate is given as follows:

$$\frac{du_p}{dt} = F_D\left(u - u_p\right) + g_z \frac{\left(\rho_p - \rho\right)}{\rho_p} + F_z \tag{6.19}$$

where, F_D is the time constant for momentum transfer due to drag force and F_z is the additional force per unit aerosol mass arising from those required to accelerate the fluid surrounding aerosols and fluid pressure gradient.

$$F_D = \frac{18\mu C_D Re}{24\rho_p d^2} \tag{6.20}$$

$$Re = \frac{\rho_g d\left|u_p - u\right|}{\mu} \tag{6.21}$$

$$F_z = \frac{1}{2}\frac{\rho}{\rho_p}\frac{d}{dt}\left(u - u_p\right) + \left(\frac{\rho}{\rho_p}\right)u_p \frac{\partial u}{\partial z} \tag{6.22}$$

$$u = \bar{u} + u' \tag{6.23}$$

The discrete random walk model is used to determine the instantaneous gas velocity (u'). Time integration of Eq. 6.19 gives the instantaneous aerosol velocity along its trajectory, which is predicted using the following equation.

$$\frac{dz}{dt} = u_p \tag{6.24}$$

The aerosol trajectory Eqs. 6.19 and 6.24 are similarly solved for each coordinate direction to predict the trajectories of discrete aerosols.

For given air and aerosol flow rates at domain inlet as inputs, the solver computes the aerosol inlet concentration (C_{in}). The aerosol outlet concentration (C_{out}) at the domain outlet is computed after the numerical simulation reaches steady state, i.e. no more variation in aerosol outlet concentration. Aerosol removal efficiency for the packed bed domain is evaluated in the present model as:

$$E_{total}(\%) = \left(1 - \frac{C_{out}}{C_{in}}\right) \times 100 \tag{6.25}$$

The aerosol penetration is evaluated in the present model as:

$$Pt = 1 - \frac{E_{total}(\%)}{100} \tag{6.26}$$

6.3.3 Computational details

Pressure-velocity coupling is carried out using SIMPLE algorithm. For spatial discretization, the pressure staggering option (PRESTO) scheme is chosen for pressure and first order upwind scheme for momentum.

6.3.4 Boundary conditions

The bottom wall, gravel surfaces and top wall are assigned with noslip boundary conditions and symmetry boundary conditions for cuboid sides. The “trap” boundary condition is assigned to the gravel surfaces, “escape” boundary condition to inlet, outlet surfaces and “reflect” to bottom, top walls for discrete phase modeling. The “trap” and “escape” surface boundary conditions terminate the trajectory calculations, once the aerosol position encounters corresponding surface. The “escape” boundary condition is typically used for flow boundaries. The “reflect” surface boundary condition rebounds the aerosol off from the corresponding surface with momentum

change defined by coefficient of restitution (*COR*). The present model assumes elastic collision and hence, *COR*=1.

6.4 Grid independence study

The present study considers a sodium combustion aerosol density of 1000 kg/m^3 and size of 1 μm. Gravel diameter of 10 mm is considered in the model. The air and aerosol mass flow rates of 1.87x10^{-6} kg/s and 1.36 x 10^{-9} kg/s are considered at inlet. The carrier air mass flow rate of 1.87 x 10^{-6} kg/s at inlet 6 mm opening corresponds to an overall flow rate of 37 liter/minute flowing through various channels of gravel bed in the SGBS design. The aerosol mass flow rate of 1.36 x 10^{-9} kg/s at inlet 6 mm opening corresponds to an aerosol inlet concentration of 727 ppmw/0.073 wt% to the scrubber.

The elaborate grid independence test is carried out by simulating nonsubmerged and submerged cases for three different uniform mesh sizes. The results of studies for various mesh sizes are compared in tables 6.3 and 6.4.

Table 6.3 Grid independence study for nonsubmerged case

Mesh	Efficiency	% deviation
141812	95.8 %	-
195316	94.9 %	-0.98 %
301207	94.3 %	-0.55 %

Table 6.4 Grid independence study for submerged case

Mesh	Efficiency	% deviation
141812	97.2 %	-
195316	95.4 %	-1.88 %
301207	96.1 %	0.66 %

In table 6.3, it can be seen that the deviation of aerosol removal efficiency for 195316 mesh size as compared to a case of 141812 mesh is -0.98 %. However, the change in predictions of aerosol

removal efficiency is less than -0.55% for the mesh size of 301207 as compared to 195316 mesh case. Therefore, the mesh of 195316 is chosen for further analysis in nonsubmerged case. In table 6.4, it can be seen that the deviation of aerosol removal efficiency for 195316 mesh case from 141812 mesh case is -1.88 %, but only 0.66 % for 301207 mesh case from 195316 mesh case. Hence, the mesh of 195316 is chosen for the submerged case in subsequent analysis.

6.5 Validation

The numerical verification of present model is carried out by comparing the grade efficiency curve with results of Chang (2003) for a dust cleaning packed bed scrubber operating at 53 liter/minute air flow rate (9.14×10^{-5} kg/s) and 2 liter/minute water flow rate. Chang (2003) studied dust removal grade efficiency curve for the packed bed scrubber using fluent 5. The cuboid considered in packed bed model of Chang (2003) was 20.1 mm in width, 20.1 mm in length and 55.2 mm. Eight droplets on each solid sphere corresponded to the total volume of liquid droplets (liquid holdup) on a single solid sphere and were affixed with boundary condition for trapping dust particles. Chang (2003) also experimentally studied the grade efficiency curve for a packed bed scrubber of height 19 cm and diameter 7.8 cm operating at an air flow rate of 53 liter/minute and water flow rate of 2 liter/minute. Comparison of the present model is also carried out using semiempirical model of Jackson and Calvert (1966).

In present study, we consider a packed bed model of 20 mm width, 20 mm length and 50 mm height. The packed bed Reynolds number for validation study is ~220 and hence flow through the packed bed is in transitional regime. This brings in the requirement for usage of RNG k- ε turbulence model that works well for low Reynolds number flows encountered in the transition regime. The present study using RNG k- ε model evaluates pressure drop of 1.62 Pa/cm across

the packed bed scrubber compared to values of 1.87 Pa/cm and 2.06 Pa/cm predicted by Chang (2003) numerical and experimental studies respectively.

Figure 6.9 shows comparison between grade efficiency evaluated from the present CFD study and Chang's numerical study for a packing height of 50 mm. A comparison is also provided in fig. 6.9 between RNG *k*- ε model and standard *k*- ε model for modeling the flow field in present validation case study. The computational time taken by RNG *k*- ε model to converge for the 5 μm case is 3 hours 16 minutes and that for standard *k*- ε model is 4 hours in an Intel core i5 processor with 8 GB RAM. The RNG *k*- ε model slightly underpredicts the scrubber efficiency compared to standard *k*- ε model with a maximum deviation of ~1.3 % at 3 μm aerosol size and is hence insignificant. The comparison shows that both *k*- ε models gives similar results, with RNG *k*- ε model being faster to converge than standard *k*- ε model and hence proves its validity for usage in low Reynolds number turbulent flows in packed beds.

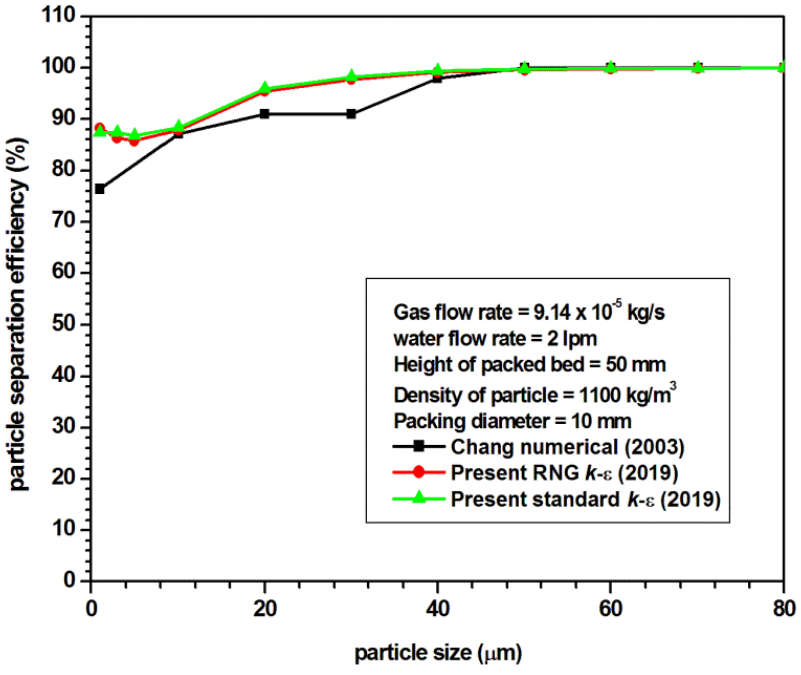

Fig. 6.9 Verification of present CFD model

The present CFD study is observed to better predict the grade efficiency curve compared to Calvert model for particle sizes in the range from 3-10 μm as can be seen in Fig. 6.10 for a packing height of 190 mm. The deviation of scrubbing efficiency for 3 μm aerosol size from experimental value is ~3% for present model and -64% for Calvert model. Similarly, the deviation of scrubbing efficiency for 10 μm aerosol size from experimental value is ~0.9% for present model and ~0.2% for Calvert model. The limits of separation (x_{98}) predicted by both present numerical study and Calvert model are within 10 μm and in close agreement with the experimental value due to the higher superficial velocity of 0.179 m/s in the validation case. This proves the validity of present numerical study for studying the scrubbing efficiency for aerosol sizes typically expected at the scrubber inlet during sodium fire in SFR containment.

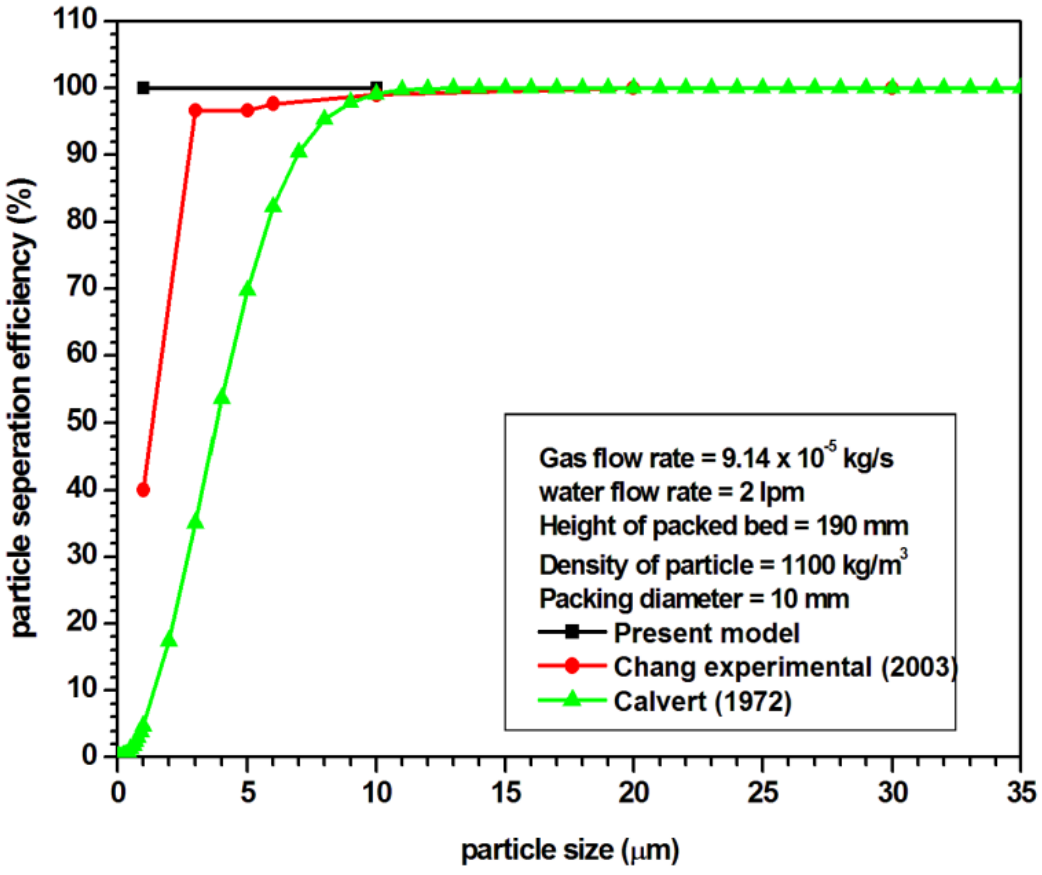

Fig. 6.10 Validation of present CFD model

6.6 Results and discussion

This study deals with investigation on the sodium fire aerosol removal efficiency in a SGBS. The gap between adjacent gravels and gravel and side wall is maintained as 0.5 mm and 0.25 mm respectively. Simulations were carried out for nonsubmerged and submerged cases. Figure 6.11 shows the CFD derived velocity contour for air mass flow rate, M_g of 1.87 x 10^{-6} kg/s at inlet.

In the nonsubmerged case, the air flow field is observed to cover the entire void volume available in gravel bed as shown in fig. 6.11a, thus increasing the gravel surface area available for aerosol removal but decreases the superficial velocity required for inertial impaction. However, in submerged condition, the air flow field is confined to rise trajectories of air bubbles above the inlet opening as shown in fig. 6.11b, thus reducing the gravel surface area available for aerosol removal but increases the superficial velocity required for inertial impaction. The overall penetration of 1 μm aerosols with mass flow rate of 1.36 x 10^{-9} kg/s for nonsubmerged case is illustrated in fig. 6.12a. The aerosol penetration is determined in terms of the ratio of outlet aerosol concentration to inlet aerosol concentration. Figure 6.12b shows the CFD derived volume fraction contour of submerged case for air mass flow rate, M_g of 1.87 x 10^{-6} kg/s at inlet.

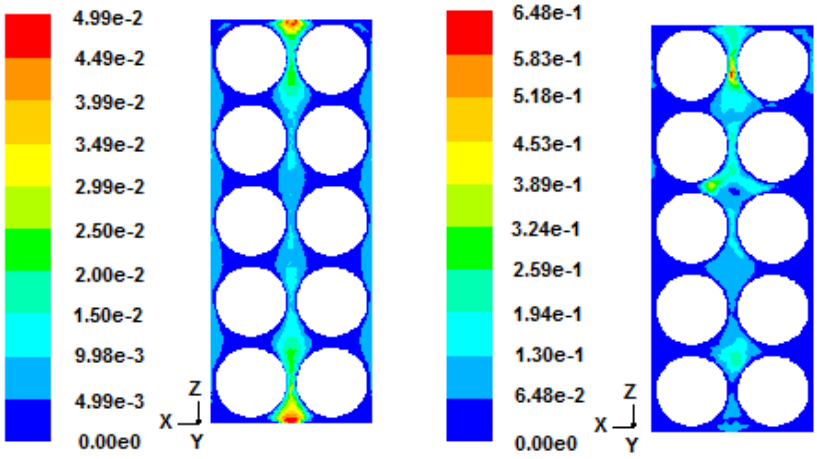

(a) (b)

Fig.6.11 Velocity contours (m/s) (a) nonsubmerged (b) submerged

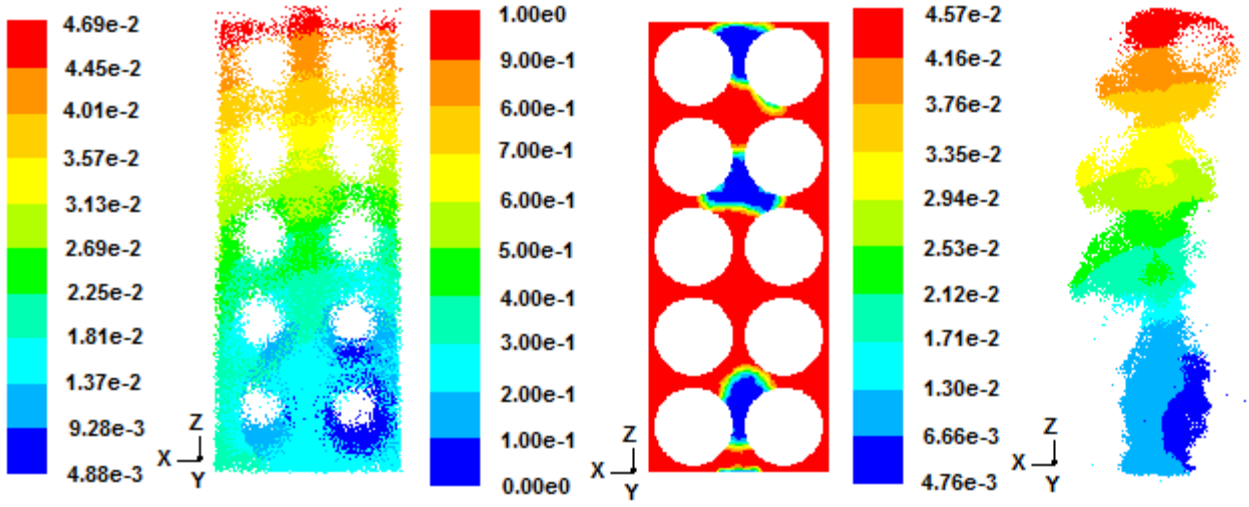

(a) (b) (c)

Fig.6.12 CFD model prediction (a) nonsubmerged case aerosol penetration (b) submerged case water volume fraction contour (c) submerged case aerosol penetration

The overall penetration for 1 μm aerosol with mass flow rate of 1.36 x 10^{-9} kg/s for submerged case is illustrated in fig. 6.12c. The values of aerosol penetration are comparable for both nonsubmerged and submerged cases (fig. 6.12). For air flow rate at 1.87 x 10^{-6} kg/s, the overall aerosol separation efficiency E_{total} is obtained for different gravel-gravel gap, aerosol size, gravel diameter and bed heights. The results are illustrated in the following sub-sections.

6.6.1 Gravel-gravel gap

Numerical simulations are carried out to understand the effect of gravel-gravel gap on sodium fire aerosol removal efficiency in a SGBS. The packed bed height considered for the study is 50 mm. The gap between adjacent gravels and between gravel and side wall is varied from 0.25-0.75 mm and 0.125-0.5 mm respectively. The variation of E_{total} with gravel-gravel gap is given in fig. 6.13.

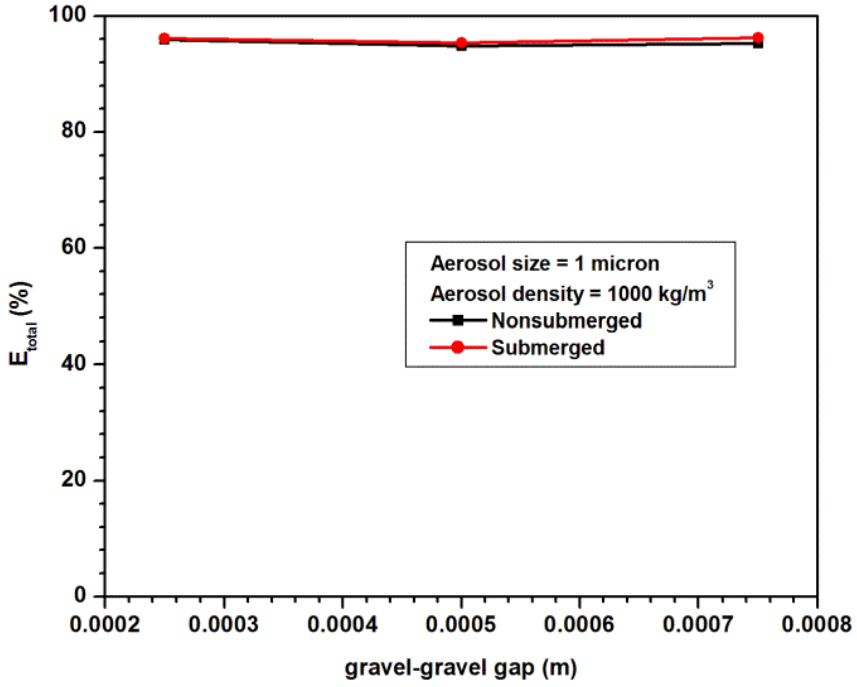

Fig.6.13 Variation of E_{total} with gravel-gravel gap

The variation is observed to be almost linear, showing the independence of scrubbing efficiency with gravel-gravel gap in the study range considered. Hence, a gap of 0.5 mm between adjacent gravels and 0.25 mm between gravel and side wall is sufficient for evaluation of aerosol removal efficiency in a PBS. The study also shows the validity of caps contact approach for packed bed flow problems and is in line with the observations made by Dixon and Nicholas (2017).

6.6.2 Aerosol size

Numerical simulations are carried out to understand the effect of aerosol size on sodium fire aerosol removal efficiency in a SGBS. The packed bed height considered for the study is 50 mm. Figures 6.14 and 6.15 show the tracks of 20 μm and 80 μm size aerosols respectively in terms of residence time inside the scrubber. It is clear from figs. 6.14 and 6.15 that no penetration occurs for aerosols in nonsubmerged case and very small penetration happens in submerged case due to the air bubble carrying aerosols reaching the scrubber top.

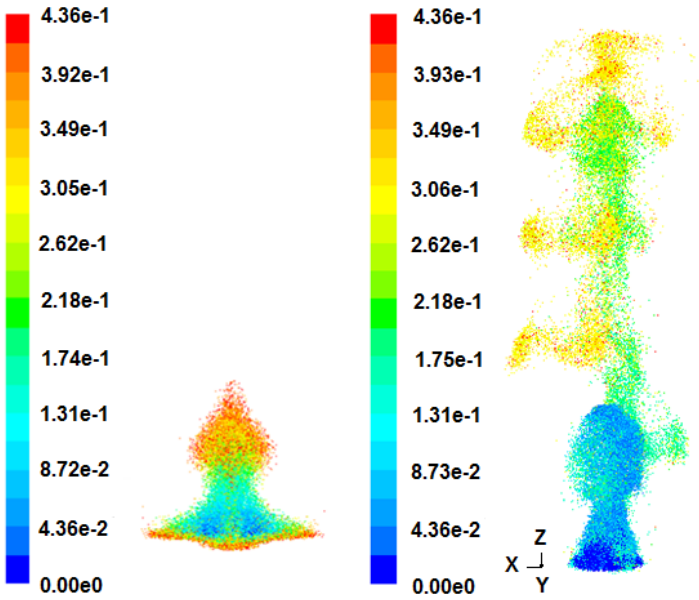

(a) (b)

Fig.6.14 CFD model predicted residence time (s) of 20 μm aerosols (a) nonsubmerged (b) submerged

The variation of E_{total} with aerosol size (fig. 6.16) is essentially the grade efficiency curve. E_{total} is observed to increase with increase in aerosol size. As the aerosol size increases, its mass increases and hence, improves the inertial deposition of aerosol, i.e. there is a greater deviation of aerosols from the air streamlines to impact on the capped gravel spheres. It is clear from this figure that the CFD study predicts a limit of separation (x_{98}) of ~12 μm and ~61 μm for the nonsubmerged and submerged cases respectively. However, the Calvert semiempirical model (Jackson and Calvert, 1966) predicts x_{98} value of ~84 μm. The predicted grade efficiency curves for both nonsubmerged and submerged scrubbers are in concurrence with the experimental value of cut diameter (x_{50}) for typical SGBS, which is below 1 μm as predicted by Owen (1980). Differences observed between the experimental and CFD derived limit of separation can be due to lower height of packed bed considered for the CFD study. Hence, the present CFD study is

observed to better predict the grade efficiency curve compared to Calvert model (Jackson and Calvert, 1966) for sodium fire aerosols at low air flow rates.

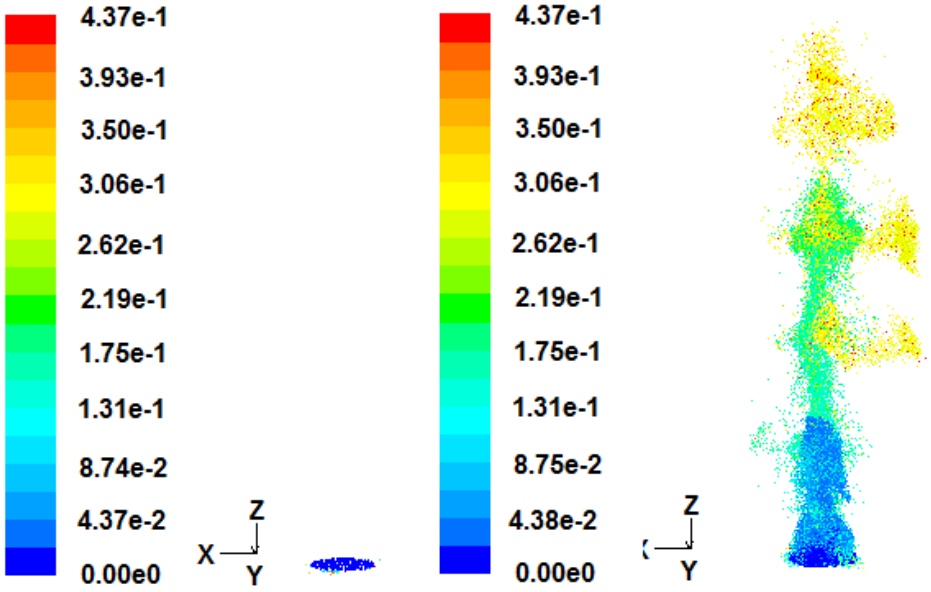

(a) (b)

Fig.6.15 CFD model predicted residence time (s) of 80 μm aerosols (a) nonsubmerged (b) submerged

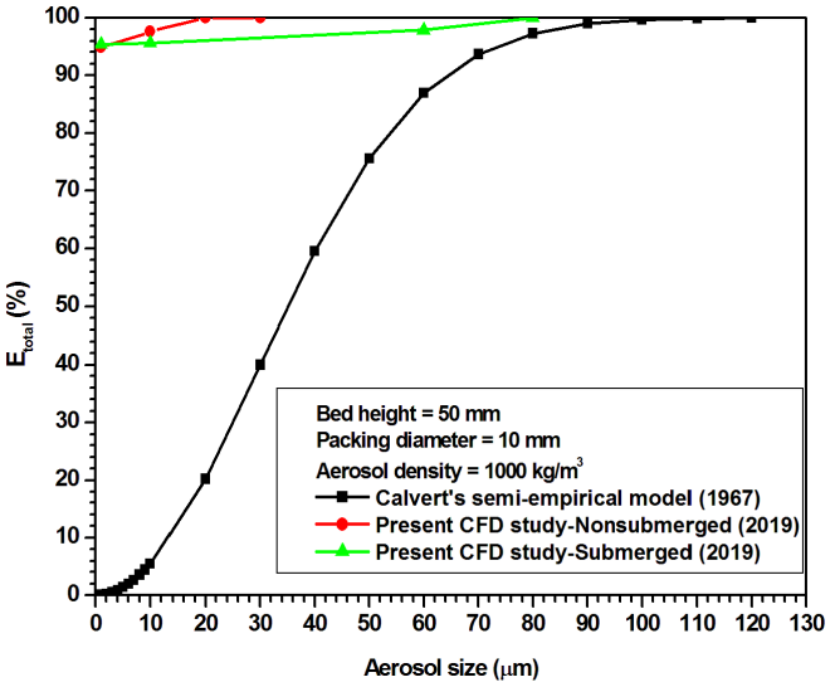

Fig.6.16 Variation of E_{total} with aerosol size

6.6.3. Gravel diameter

The sensitivity of gravel diameter (d_R) as a parameter on sodium fire aerosol removal efficiency of SGBS is studied. The packed bed height considered for the study is $5d_R$ and the gravel diameter is varied from 6-15 mm. The decrease in gravel diameter improves the E_{total} as shown in fig. 6.17. The decrease in sphere diameter increases the inertial impaction parameter, which results in increased aerosol impaction on spheres and hence scrubbing efficiency. However, the increase is much small as compared to predictions made from semiempirical Calvert model as observed in table 6.5 due to the lower prediction of SGBS cut diameter (x_{50}) by the present study. The Calvert model predicts an increase of 125 % on decreasing the gravel diameter by 60 % from an initial diameter of 15 mm for the similar conditions.

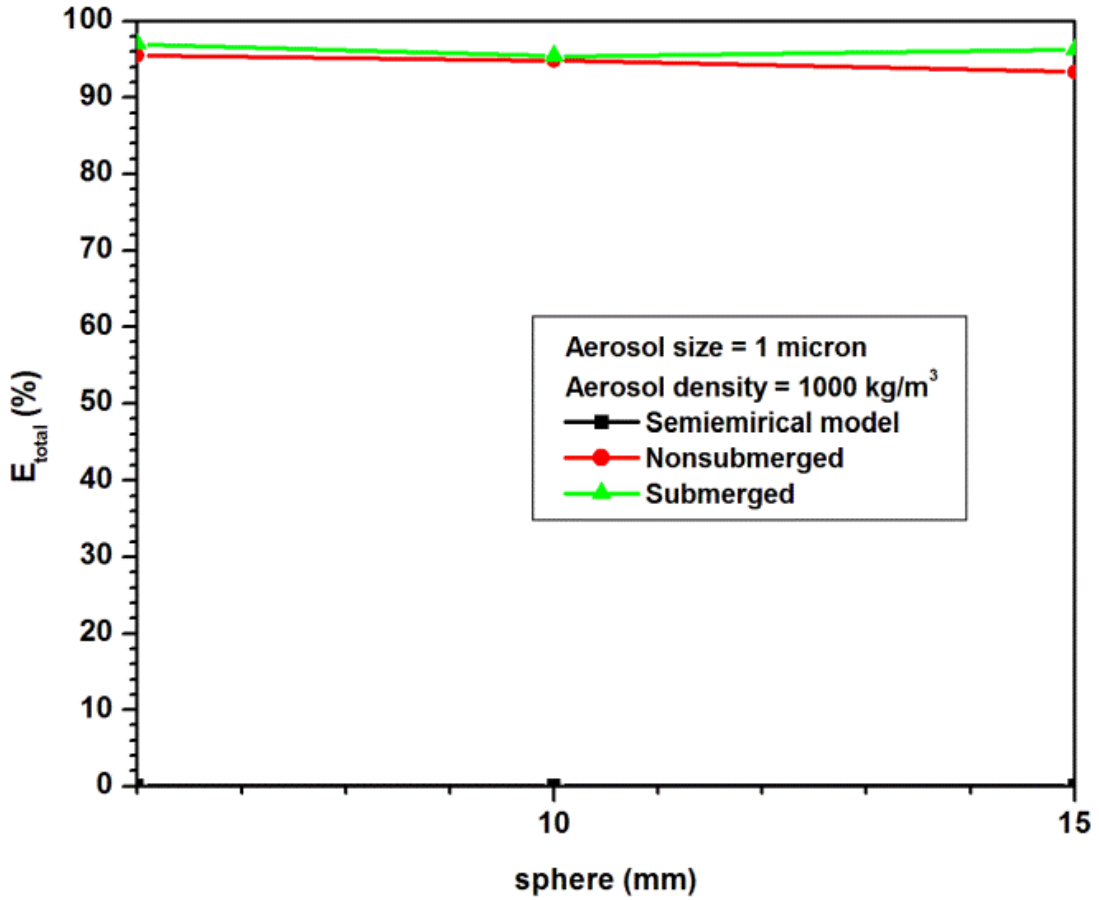

Fig.6.17 Variation of E_{total} with sphere diameter

Table 6.5 Effect of sphere diameter on scrubbing efficiency

Sphere diameter (mm)	Efficiency (Calvert)	Efficiency (nonsubmerged)	Efficiency (submerged)
6	0.09 %	95.5%	97.0%
10	0.06 %	94.9%	95.4%
15	0.04 %	93.3%	96.2%

6.6.4. Bed height

Numerical simulations are carried out to understand the effect of bed height on sodium fire aerosol removal efficiency in a submerged gravel bed scrubber. The packed bed height considered for the study is varied from 50-150 mm. The increase in bed height also improves the E_{total} as shown in fig. 6.18 and table 6.6.

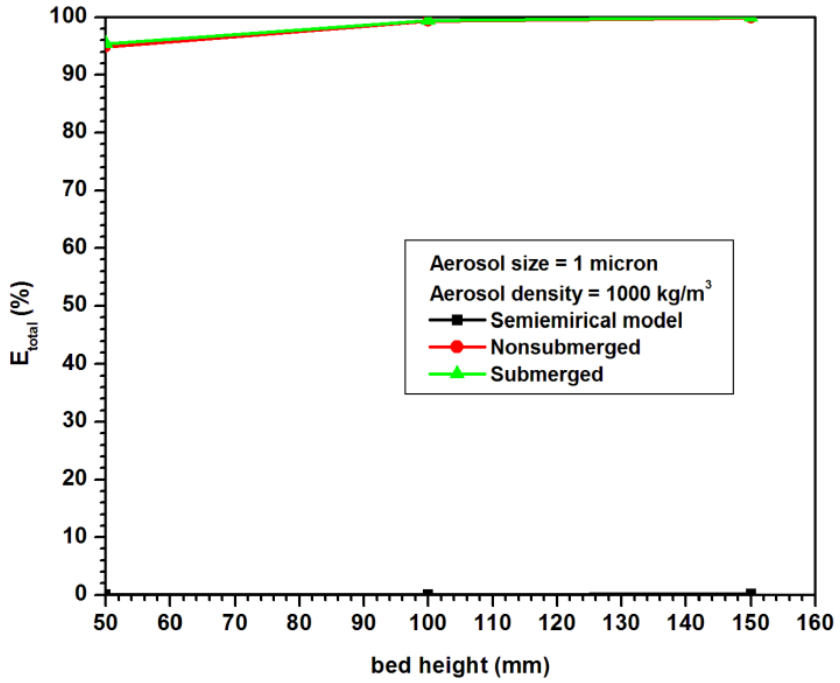

Fig.6.18 Variation of E_{total} with bed height

The increase in bed height increases the aerosol inertial impaction on spheres and hence, scrubbing efficiency. The scrubbing efficiency is observed to increase by 4.7 % and 5.3 % on

doubling and tripling the bed height respectively from the initial height of 50 mm for the studied geometry and flow conditions of scrubber under nonsubmerged condition. Similarly, the scrubbing efficiency increases by 4.3 % and 4.8 % on doubling and tripling the bed height respectively in submerged case.

Table 6.6 Effect of bed height on scrubbing efficiency

Bed height(mm)	**Efficiency (Calvert)**	**Efficiency (nonsubmerged)**	**Efficiency (submerged)**
50	0.06 %	94.9%	95.4%
100	0.11 %	99.3%	99.5%
150	0.17 %	99.9%	99.9%

Chang (2003) developed a mathematical relation to evaluate the scrubbing efficiency of packed bed with height 'n' times the height of packed bed for which the scrubbing efficiency is known.

$$E_{ntotal} = \left[1 - \left(1 - \frac{E_{total}}{100}\right)^{n}\right] \times 100\% \qquad (6.27)$$

Based on the scrubbing efficiencies evaluated using the present CFD model for 50 mm high gravel bed for both nonsubmerged and submerged cases, the efficiencies for bed heights of 100 mm and 150 mm were evaluated using Eq. 6.16 and were found to be in close agreement with data obtained in present study.

6.7 Closure

This chapter details the investigation on efficiency of submerged gravel bed scrubber (SGBS) in removing sodium fire aerosols. The wet scrubber is designed and installed to reduce the aerosol concentration in vented air to permissible limits under the event of sodium fire inside combustion chamber. The functionality of SGBS in generating uniform bubbles was visually tested from the scrubber top during its commissioning. The performance of SGBS is also studied experimentally for sodium fire aerosol removal by generating test aerosols inside sodium fire chamber. The

sodium fire aerosols removal efficiency of SGBS is experimentally measured to be in the range from 75-99.93 % for inlet aerosol concentrations in the range of 0.04-19.94 g/m^3 at low gas flow rate of 0.0006 m^3/s. The semiempirical Calvert model is found to underpredict the scrubber efficiency at lower superficial gas velocities. This brings in the requirement for better theoretical models for capturing the scrubbing efficiency of SGBS. Computational fluid dynamic (CFD) simulations are performed to evaluate aerosol penetration in a SGBS. A single channel of gravel packing submerged in liquid is considered for the analysis and caps contact approach is used to overcome the difficulties in meshing. Commercial CFD solver is used to solve the transport equations for mass, momentum, volume fraction and discrete phase modeling for path trajectories of aerosols. The model validation is carried out with data available in literature for packed bed scrubbers. Parametric studies using gravel-gravel gap shows validity of caps contact approach used in the CFD study. The simulations are carried out at a low inlet air flow rate of $1.87x10^{-6}$ kg/s to prove the passiveness of SGBS for both nonsubmerged and submerged conditions. Increasing the bed height from 50 mm to 150 mm increases the scrubbing efficiency of 1 μm aerosols by 5.3 % and 4.7 % in nonsubmerged and submerged cases respectively at an inlet concentration of 727 ppmw. It is also found from the grade efficiency curves obtained for nonsubmerged and submerged cases that the SGBS cut diameter is below 1 μm as observed in literature. Both submerged and nonsubmerged cases predict similar results for SGBS scrubbing efficiency, but considering the computation time involved in modeling two-phase flow the nonsubmerged case is proposed for simulating SGBS. The study is useful to understand the scrubbing phenomena in SGBS for sodium fire aerosols and also overcomes the deficiencies posed by Calvert model at low air flow rates. Next chapter is dedicated to the broad conclusions drawn from these studies presented in this thesis and the future scope of the work.

REFERENCES

References

1. Adelsberger, J., Esser, P., Griebel, M., Groÿ, S., Klitz, M., and Rüttgers, A. 3D incompressible two-phase flow benchmark computations for rising droplets. In proceedings of the 11th world congress on computational mechanics (WCCM XI), Vol. 179, Barcelona, Spain, 2014.

   http://www.featflow.de/en/benchmarks/cfdbenchmarking/bubble/bubble_reference.html.

2. Aggarwal, P. K., Pandey, G. K., Malathi, N., Arun, A. D., Ananthanarayanan, R., Banerjee, I., Sahoo, P., Padmakumar, G., Murali, N. Investigation of free level fluctuations in a simulated model of a sodium cooled Fast Breeder Reactor using pulsating conductance monitoring device. Annals of Nuclear Energy 41, 87-96, 2012.

3. Albadawi, A., Donoghue, D. B., Robinson, A. J., Murray, D. B., and Delaur´e, Y. M. C. Influence of surface tension implementation in volume of fluid and coupled volume of fluid with level set methods for bubble growth and detachment. In: International Journal of Multiphase Flow 53, 11–28, 2013.

4. Apostolakis, G., Driscoll, M., Golay, M., Kadak, A., Todreas, N., Aldmir, T., Denning, R., and Lineberry, M. Risk-informed balancing of safety, nonproliferation, and economics For the SFR. No. DOE/ID/14888-20. Massachusetts institute of technology, 2011.

5. Ashok, G. V. S., Venkata Subramani, C. R., Kumar, R., Sivakumar, S., Murugan, S., Varadharajan, S., Sureshkumar, K. V., Ananthasivan, K., Joseph, M., and Srinivasan, G. Design, installation and preliminary flux measurements at the fast flux experimental

facility (FFEF) of the fast breeder test reactor (FBTR). Journal of Radioanalytical and Nuclear Chemistry 320(1), 255-263, 2019.

6. Atomics International, Quarterly Technical Progress Report. AEC unclassified programs July-September 1965, NAA-SR-11650, 1965.
7. Azhagarason, B., Poorankumar, P., Chennakeshava, B. K., and Babu, V. R. Challenges during Manufacture of reactor components of PFBR. In proceedings of international conference on fast reactors and related fuel cycles: next generation nuclear systems for sustainable development (FR17), 2017.
8. Babu, V. R., and Roy, K. Lessons and strategies from PFBR to future fast breeder reactors. In proceedings of international conference on fast reactors and related fuel cycles: next generation nuclear systems for sustainable development (FR17), 2017.
9. Ballif, J. L., Ford, B., and Davis, U. I. Liquid metal fire control engineering hand book, 1979.
10. Barreca, J. R., and McCormack, J. D. Sodium fire aerosol loading capacity of several sand and gravel filters. No. HEDL-SA-2128. Hanford Engineering Development Laboratory, 1980.
11. Beghi, I., Lind, T., and Prasser, H. M. Experimental studies on retention of iodine in a wet scrubber. Nuclear Engineering and Design 326, 234-243, 2018.
12. Begley, R. J. Liquid sodium absorbs gaseous iodine. Nucleonics (US) ceased publication 20(10), 1962.
13. Behar, C. Technology roadmap update for generation IV nuclear energy systems. In OECD Nuclear Energy Agency for the Generation IV International Forum, 2014.

14. Bharasi, N. S., Pujar, M. G., Das, C.R., John Philip, Thyagarajan, K., Paneerselvi, S., Moitra, A., Chandramouli, S., Karki, V., and Kannan, S. Microstructure, corrosion and mechanical properties characterization of AISI type 316L (N) stainless steel and modified 9Cr-1Mo steel after 40,000 h of dynamic sodium exposure at 525° C. Journal of Nuclear Materials 516, 84-99, 2019.

15. Boehm, L., Jordan, S., and Schikarski, W. Experiments on filtration of sodium aerosols by sand bed filters. No. CONF-740401-P1, 1974.

16. Boehm, L., and Jordan, S. On the filtration of sodium oxide aerosols by multilayer sand bed filters. Journal of Aerosol Science 7(4), 311-318, 1976.

17. Brackbill, J. U., Kothe, D. B., and Zemach, C. A continuum method for modeling surface tension. Journal of Computational Physics 100, 335-354, 1992.

18. Brady, D., and MacKinlay, C. Overview: Canada's generation IV international forum (GIF) participation and national program. JOM 68(2), 454-455, 2016.

19. Bucknor, M., Farmer, M., Grabaskas, D. An assessment of fission product scrubbing in sodium pools following a core damage event in a sodium cooled fast reactor. Argonne National Laboratory (ANL), 2017.

20. Chandran, K., Clinsha, P. C., Lavanya, M., Anthonysamy, S., and Gnanasekar, K. I. Chemical interaction of D9 alloy clad with B4C in liquid sodium: studies employing XPS, XRD, and SEM. Journal of the American Ceramic Society 102(5), 2932-2947, 2019.

21. Chang, B. F. A non-wetting packed bed gas scrubber. PhD dissertation, University of Sheffield, 2003.

22. Chetal, S. C., Chellapandi, P., Raghupathy, S., Selvaraj, P., Natesan, K., Rajan, V. N., Raj, B. Storage and Management of Spent Fuel of Fast Reactors in India. In Management of Spent Fuel from Nuclear Power Reactors. Proceedings of an International Conference, 2015.

23. Clift R., Grace, J. R., and Weber, M. E. Bubbles, drops and particles. Academic Press: New York, 1978.

24. Cunnane, J. C., Kuhlmann, M. R., Oehlberg, R. N. The scrubbing of fission product aerosols in LWR water pools under severe accident conditions-experimental results. Proceedings of fission product behavior and source term research, 1984.

25. Cunnane, J. C., Bishop, T.A., Collier, R. P., Cudnik, R. A., Flanigan, L. J., Gieseke, J. A., Kuhlman, M. R., and Paul, D. D. Scrubbing of aerosols by water pools, volume 1: quencher orifice injection. EPRI NP-4890SP, 1986.

26. Davies, R. M., Taylor, G. The mechanics of large bubbles rising through extended liquids and through liquids in tubes. In Proceedings of the Royal Society of London A: Mathematical, Physical and Engineering Sciences 200, 375-390, 1950.

27. De Cuy, G. D. Sodium Oxide Aerosol Filtration. International working group on fast reactors 192, 1978.

28. Dehbi, A., Suckow, D., and Guentay, S. Aerosol retention in low-subcooling pools under realistic accident conditions. Nuclear engineering and design 203(2), 229-241, 2001.

29. Demitrack, T., and Moody, F. J. Planetary ellipsoid bubble model for fission product scrubbing. Transactions of American nuclear society, (United States) 45, no. CONF-831047, 1983.

30. Dickinson, D. R., and Nunamaker, F. H. LMFBR source term iodine attenuation test of bubble breakup/coalescence in LMFBR outlet plenum following large fission gas release. No. HEDL-TC-537, Hanford Engineering Development Lab., Richland, Wash. (USA), 1975.

31. Diffey, H. R., Rumary, C. H., Smith, M. J. S., and Stinchcombe R. A. Iodine clean-up in a steam suppression system. In CONF-65047, vol. 1. 1965.

32. Dixon, A. G., and Nicholas, J. M. Computational fluid dynamics simulations of gas-phase radial dispersion in fixed beds with wall effects. Fluids, 2(4), 56, 2017.

33. Damián, S. M. Description and utilization of interFoam multiphase solver. final work, computational fluid dynamics, 2012. http://infofich.unl.edu.ar/upload/3be0e16065026527477b4b948c4caa7523c8ea52.pdf.

34. Eckardt, B., and Losch, N. Filtered containment venting system designs-development features qualification applications. NRC meeting on containment venting systems, Rockville, 2012.

35. Findlay, T. The Future of nuclear energy to 2030 and its implications for safety, security and nonproliferation: part 3–nuclear security. Centre for International Governance Innovation (CIGI), 2010.

36. Fink, J.K., Leibwitz, L. Thermodynamic and transport properties of sodium liquid and vapour. ANL/RE-95/2IL, Argonne National lab., United States, 1995.

37. Fischer, K., Kuhlmann, M. R., Kogan, V. Fission product pool scrubbing data and modeling assessment. ACEX TR-A-01, Vol. 1, 1996.

38. Fischer, K., Kuhlmann, M. R., Kogan, V. Fission product pool scrubbing data and modeling assessment. ACEX TR-A-02, Vol. 2, 1997.

39. Fuchs, N. A. The mechanics of aerosols. Pergamon Press, 1964.

40. Furrer, M., Passalaqua, R. SPARTA project: scoping test results and comparison with pool scrubbing codes predictions. ENEA-CRE Casaccia, 1992.

41. Gnanasekaran, S., Padmanaban, G., Balasubramanian, V., Kumar, H., and Albert, S. K. Correlation between travel speed, microstructure, mechanical properties and wear characteristics of Ni-based hardfaced deposits over 316LN austenitic stainless steel. High Temperature Materials and Processes 38(2019), 16-29, 2019.

42. Grace, J. R. Shapes and velocities of bubbles rising in infinite liquids, Transactions of the Institution of Chemical Engineers 51, 116-120, 1973.

43. Greenshields, C. J. OpenFOAM user guide, 2016.

44. Guézennec, A. G., Huber, J. C., Patisson, F., Sessiecq, Ph., Birat J. P., and Ablitzer, D. Dust formation by bubble-burst phenomenon at the surface of a liquid steel bath. ISIJ international 44(8), 1328-1333, 2004.

45. Güntay, S. Experiment POSEIDON: elemental iodine retention in water pools. Transactions of the American Nuclear Society 62, 1990.

46. Güntay, S. Experiment POSEIDON: pool scrubbing effect on iodine decontamination. paper presented at the ENC'90, ENS/ANS-Foratom conference Lyon, 1990.

47. Güntay, S. Proceedings of the 4. CSNI workshop on the chemistry of iodine in reactor safety. No. PSI--97-02. Paul Scherrer Inst.(PSI), 1996.

48. Gupta, G., Jalaldheen, S., Chellapandi, P., and Chetal, S. C. Advanced structural mechanics design of 500 MWe commercial SFRs. In proceedings of international conference on fast reactors and related fuel cycles: safe technologies and sustainable scenarios; Paris (France), 2013.

49. Gupta, S. N. V. M. S., Nayak, A. K., Misra, U. B., Yarasi, B. R., Babu, C. P., and Kalyanakrishnan, G. A simple and rapid method for determination of boron in fast breeder reactor components. Journal of Radioanalytical and Nuclear Chemistry 313(3), 571-579, 2017.

50. Han, Z., and Holappa, L. Bubble bursting phenomenon in gas/metal/slag systems. Metallurgical and Materials Transactions B. 34B, 525-532, 2003.

51. Haroun, Y., Legendre, D., Raynal, L. Volume of fluid method for interfacial reactive mass transfer: Application to stable liquid film. Chem. Eng. Sci., 65, 2896–2909, 2010.

52. Haroun, Y., Raynal, L., Legendre, D. Mass transfer and liquid hold-up determination in structured packing by CFD. Chem. Eng. Sci., 75, 342–348, 2012.

53. Hashimoto, K., Soda, K., Uno, S., Nakatani, H., and Tateoka. H. Effect of pool scrubbing of insoluble aerosol in two phase flow in a pipe. In Severe accidents in nuclear power plants, 1988.

54. Hashimoto, K., Soda, K., and Uno, S. High pressure pool scrubbing experiment for a PWR severe accident. In proceedings of the international topical meeting on safety of thermal reactors, 740-745. 1991.

55. Hasty, R. A., Can. J. Chem. 46, 163, 1968.

56. Heisler, M. P., Johnson, R. P., Otter, J. M., Nelson, C. T., Specht, E. R., Guderjahn, C., and Vaughan, E. U. Characterization of sodium fires and fission products. Progress report, October-December 1975.[LMFBR]. No. DOE/SF/75010-T6. Rockwell International Corp., Canoga Park, CA (USA), 1975.

57. Hillary, J. J., Taylor, J. C., Abbey, F., Diffey, H.R. Iodine removal by a scale model of the SGHW reactor vented steam suppression system. UKAEA, TRG report 1256 (W), August 1966.

58. Hilliard, R. K., Mccormack, J. D., and Posthma, A. K. Submerged gravel scrubber demonstration as a passive air cleaner for containment venting and purging with sodium aerosols-CSTF tests AC7-AC10. No. HEDL-TME 81-30, Hanford site (HNF), Richland, WA, United States, 1981.

59. Hilliard, R. K., McCormack, J. D. and Postma, A. K. Evaluation of air cleaning system concepts for emergency use in LMFBR plants. No. HEDL-TME-76-41. Hanford Engineering Development Lab., Richland, Washington (USA), 1976.

60. Hilliard, R. K., McCormack, J. D., Postma, A. K., and Owen. R. K. Containment air cleaning for LMFBRs. No. HEDL-SA--1713-FP. Hanford Engineering Development Laboratory, 1979.

61. Hilliard, R. K., and Muhlestein, L. D. Air-cleaning systems for sodium-fire-aerosol control. No. HEDL-SA-2698-FP, Hanford Engineering Development Laboratory, 1982.

62. Hirschfelder, J. O., Bird, R. B., and Spotz, E. L., Viscosity and Other Physical Properties of Gas Mixtures, Trans. ASME, vol. 71, 921-937, 1949.

63. Hirt, C., W., and Nichols, B. D. Volume of fluid (VOF) method for the dynamics of free boundaries. Journal of Computational Physics 39, 201-225, 1981.

64. Horvath, A., and Rachlew, E. Nuclear power in the 21st century: challenges and possibilities. Ambio 45, no. 1, 38-49, 2016.

65. https://www.powermag.com/india-gears-up-to-expand-fast-breeder-reactor-fleet/

66. https://www.hccindia.com/news/hcc-awarded-igcars-fast-reactor-fuel-cycle-facility

67. Hysing S. R., Turek, S., Kuzmin, D., Parolini, N., Burman, E., Ganesan, S., and Tobiska, L. Quantitative benchmark computations of two-dimensional bubble dynamics. International Journal of Numerical Methods in Fluids 60, 1259-1288, 2009. http://www.featflow.de/en/benchmarks/cfdbenchmarking/bubble/bubble_reference.html

68. Islam, M. T., Ganesan, P., Sahu, J. N., Uddin, M. N., Mannan, A. A Single Air Bubble Rise in Water: A CFD Study. Mechanical Engineering Research Journal 9, 1-6, 2013.

69. Jackson, S., and Calvert, S. Entrained particle collection in packed beds. AIChE Journal 12, 1075-1078, 1966.

70. Kale, R. D., Sreedhar, B. K., and Sreedharan, K. V. The history of liquid metal pump development in India. Current Science 114(2), 292, 2018.

71. Kestin, J., Ro, S. T., Wakeham, W.A. Viscosity of the noble gas in the temperature range 25 – 700 °C. The Journal of Chemical Physics 56, 4119-4124, 1972.

72. Kitani, S., Matsui, H., Uno, S., Murata, M., and Takada, J. Behavior of sodium oxide aerosol in a closed chamber. Journal of Nuclear Science and Technology 10(9), 566-573, 1973.

73. Klostermann, J., Schaake, K., and Schwarze, R. Numerical simulation of a single rising bubble by VOF with surface compression. International Journal of Numerical Methods in Fluids 71, 960-982, 2013.

74. Knaus, Z. C. 105-DR Large Sodium Fire Facility decontamination, sampling, and analysis plan. No. WHC-SD-EN-AP-186, Westinghouse Hanford Corporation, 1995.

75. Krishna, R., and Baten, J. M. V. Rise characteristics of gas bubbles in a 2D rectangular column: VOF simulations vs experiments. International Communications in Heat and Mass Transfer, 26(7), 965-974, 1999.

76. Krovvidi, S. C. S. P. K., Punniyamoorthy, R., Sreedhar, B. K., Chandramouli, S., Padmakumar, G., Raghupathy, S., and Selvaraj, P. Testing in sodium and qualification of the bearings used in inclined fuel transfer machine of prototype fast breeder reactor. International Journal of Nuclear Energy Science and Technology 12(1), 1-18, 2018.

77. Kunkel, W. P. Fission-product retention in sodium: a summary of analytical and experimental studies at atomics international. No. NAA-SR-11766, Atomics International, Canoga Park, California, 1966.

78. Kuhlman, M. R., Gieseke, J. A., Merilo, M., and Oehlberg, R. Scrubbing of fission product aerosols in LWR water pools under severe accident conditions. In Source term evaluation for accident conditions, 1986.

79. Lee, J. Y., and Choi, Y. S. Lift force of large bubble in high reynolds condition, 346–357, 2014.

80. Levich, V.G. Physiochemical hydrodynamics. Englewood cliffs, New Jersey, Prentice hall, 1962.

81. Lewis, W. K., and Whitman, W. G. Principles of gas absorption. Industrial & Engineering Chemistry 16(12), 1215-1220, 1924.

82. Lineberry, M. J., and Allen, T. R. The sodium-cooled fast reactor (SFR). No. ANL/NT/CP-108933. Argonne National Lab., IL (US), 2002.

83. Malathi, N., Sahoo, P., Ananthanarayanan, R., Murali, N., Level monitoring system with pulsating sensor-Application to online level monitoring of dashpots in a Fast Breeder Reactor. Review of Scientific Instruments, 86, 025103, 2015.

84. Marcos, M. J., Gomez, F. J., Melches, I., Martin, M., López, J. LACE-España experimental programme on the retention of aerosols in submerged beds Final report. CIEMAT, ITN/TS-08/DP-93, 1993.

85. McCormack, J. D., Dickinson, D., and Allemann, R. T. Experimental results of ACE vent filtration, pool scrubber tests. AA1-AA4 and DOP1-DOP5, ACE-TR-A1, 1989.

86. Mendelson, H. D. The prediction of bubble terminal velocities from wave theory. AIChE Journal 13(2), 250-253, 1967.

87. Merilo, M. Scrubbing of aerosols in water pools under LWR severe accident conditions. handouts from a lecture, 1986.

88. Miyahara, S., Shimoyama, K. Transport phenomena of iodine and noble gas mixed bubbles through liquid sodium. In liquid metal systems, 27-33, 1995.

89. Miyagi, K., and Miyahara, S. Development of in-vessel source term analysis code, TRACER. Technical committee meeting on evaluation of radioactive materials release and sodium fires in fast reactor, IWGFR/92, O-arai, Japan, 1996.

90. Miyahara, S., Sagawa, N., and Shimoyama, K. Iodine mass transfer from xenon-iodine mixed gas bubble to liquid sodium pool, (I) experiment. Journal of nuclear science and technology, 33(2), 128, 1995.

91. Miyahara, S., Sagawa, N., and Shimoyama, K. Iodine mass transfer from xenon-iodine mixed gas bubble to liquid sodium pool, (II) development of analytical model. Journal of nuclear science and technology, 33(3), 220, 1995.

92. Miyahara, S., Sagawa, N., and Shimoyama, K. Experimental and analytical studies of iodine mass transfer from xenon-iodine mixed gas bubble to liquid sodium pool.

Technical committee meeting on evaluation of radioactive materials release and sodium fires in fast reactor, IWGFR/92, O-arai, Japan, 1996.

93. Nakagiri, T., Toyohara, D., and Miyahara, S. In-vessel source term analysis code version 1.0 user's Manual. JNC TN9520 2000-003, Japan Atomic Energy Agency, 2000.

94. Narayanan, M. M., Anish K., Thirunavukkarasu, S., and Mukhopadhyay, C. K. Detection of service-induced damage in steam generator tubes of PFBR using ultrasonic guided waves. NDE 2018 conference and exhibition of the society for NDT (ISNT), Mumbai, India, 2018.

95. Nelson, C. T., Johnson, R. P., Vaughan, E. U., Guderjahn, C. A., Morewitz, H. A. Some potential reductions in the release of radioactivity under LMFBR accident conditions. Proceedings of international meeting on fast reactor safety and related physics, Chicago, 1976.

96. Owczarski, P. C., Schreck, R. I., and Postma, A. K. Technical bases and user's manual for the prototype of a suppression pool aerosol removal code (SPARC). NUREG/CR-3317, 1985.

97. Owczarski, P. C., and Burk, K. W. SPARC-90, a code for calculating fission product capture in suppression pools. Division of regulatory applications, office of nuclear regulatory research, US Nuclear regulatory commission, 1991.

98. Owen, R. K. Development of an emergency air-cleaning system for liquid-metal reactors. HEDL-6859, Hanford Engineering Development Laboratory, Richland, WA, USA, 1980.

99. Owen, R. K., and Postma, A. K. Development of a passive, self-cleaning scrubber for containment venting applications. Proceedings of 16th DOE nuclear air cleaning conference, 1980.

100. Park, S.H., Park, C., Lee, J., Lee, B. A Simple parameterization for the rising velocity of bubbles in a liquid pool. Nuclear Engineering and Technology 49, 692-699, 2017.

101. Paul, D. D., Flanigan, L. J., Cunnane, J. C., Cudnik, R. A., Collier, R. P., and Oehlberg, R. N. Radionuclide scrubbing in water pools-gas-liquid hydrodynamics. No. EPRI-NP--4113-SR. 1985.

102. Pawar, T. V., Sudha, A. J., Ponraju, D., Nashine, B. K., and Selvaraj, P. An effective conductivity model for jet ablation of a solid substrate. In IOP Conference Series: Materials Science and Engineering 402(1), IOP Publishing, 012057, 2018.

103. Perumalsamy, G., Visweswaran, P., Joel Jose, Joseph Winston, S., and Murugan, S. Quintic interpolation joint trajectory for the path planning of a serial two-axis robotic arm for PFBR steam generator inspection. In Machines, Mechanism and Robotics, Springer, Singapore, 637-648, 2019.

104. Peyres, V., Espigares, M. M., Polo, J., Escudero, M. J., Herranz, L. E., and López-Jiménez, J. Pool scrubbing and hydrodynamic experiments on jet injection regime. No. CIEMAT-785, Centro de Investigaciones Energeticas Medioambientales y Tecnologicas (CIEMAT), 1995.

105. Polo, J., Herranz, L. E., Peyres, V., and Escudero, M. Removal of volatile iodine from gas bubbles rising in water pools: review and assessment of pool scrubbing codes. No. PSI-97-02, 1996.

106. Postma, A.K. Passive self-cleaning aerosol scrubber. GB patent document 2074893/A, 1981.

107. Postma, A. K., and Hilliard, R. K. Evaluation of air cleaning systems for FFTF containment margins. HEDL-TME 79-79, Hanford Engineering Development Laboratory, Richland, Washington, 1980.

108. Powers, D. A., and Brockmann, J. E. Radionuclide release and aerosol generation during core debris interactions with concrete. No. SAND-86-2678C; CONF-860911-22, Sandia national laboratories, Albuquerque, NM (USA), 1986.

109. Powers, D.A., Sprung, J. L. A simplified model of aerosol scrubbing by a water pool overlying core debris interacting with concrete. NUREG/CR-5901, 1992.

110. Praveen, K., Rajiniganth, M. P., Arun, A. D., Ananthanarayanan, R., Malathi, N., Sahoo, P., Murali, N. High-performance differential pressure monitoring devices using pulsating sensors for a sodium-cooled fast breeder reactor. Nuclear plant operations and control 176, 127-137, 2010.

111. Puthiyavinayagam, P., Devan, K., Aithal, S. R., Athmalingam, S., Vijayashree, R., Raghupathy, S., Velusamy, K., Theivarajan, N., Usha, S., and Bhaduri, A. K. Advanced design features of MOX fuelled future indian SFRs. In proceedings of international conference on fast reactors and related fuel cycles: next generation nuclear systems for sustainable development (FR17), 2017.

112. Puthiyavinayagam, P., Natesan, K., and Raghupathy, S. Safety design criteria of indian sodium cooled fast reactors: current status, 2018.

113. Puthiyavinayagam, P., Selvaraj, P., Balasubramaniyan, V., Raghupathy, S., Velusamy, K., Devan, K., Nashine, B.K., Kumar, G.P., Varatharajan, S., Mohanakrishnan, P. and Srinivasan, G. Development of fast breeder reactor technology in India. Progress in Nuclear Energy, 101, 19-42, 2017.

114. Raees, F., Heul, D. R. V. D., and Vuik, C. Evaluation of the interface-capturing algorithm of OpenFOAM for the simulation of incompressible immiscible two-phase flow, Report, Department of Applied Mathematical Analysis, Delft University of Technology, 2011.

115. Raghupathy, S., Varghese, J., Surendran, C. S., Sakthivel, R., Arumugam, S., Kumar, S., and Puthiyavinayagam, P., Component handling system: prototype fast breeder reactor (PFBR) and beyond. In proceedings of international conference on fast reactors and related fuel cycles: next generation nuclear systems for sustainable development (FR17), 2017.

116. Raja, R. India's nuclear programme: A study of adjacent areas of the nuclear plants. International Journal of Academic Research and Development, 3(1), 119-122, 2018.

117. Ramsdale, S. A., Bamford, G. J., Fishwick, S., and Starkie, H. C. Status of research and modelling of water-pool scrubbing. No. EUR—14566, commission of the european communities, 1992.

118. Ramsdale, S. A., Güntay, S., and Friederichs, H. G. BUSCA-JUN91 reference manual, No. PSI-95-05, Paul Scherrer Institute (PSI), 1995.

119. Rangasamy, R. G., Sudha, B., Chennakeshava, B. K., Babu, V. R., Pasha, A., and Roy, K. Challenges during construction of sodium piping systems for 500 MWe prototype fast breeder reactor. In proceedings of international conference on fast reactors and related fuel cycles: next generation nuclear systems for sustainable development (FR17), 2017.

120. Raymond, F., and Rosant, J. M. A numerical and experimental study of the terminal velocity and shape of bubbles in viscous liquids. Chemical Engineering Science 55(5), 943-955, 2000.

121. Sagayama, Y. SFR systems R&D activities. In GIF-INPRO/IAEA Interface Meeting, 2017.

122. Sahoo P., Malathi N., Praveen K., Ananthanarayanan R., Arun A. D., Murali N., Swaminathan P. High performance conductivity monitoring instrument with pulsating sensor. Review of Scientific Instruments 81, 065109, 2010.

123. Sarangapani, R., Jaffar, I., Srinivsan, T .K., Mitra, A., Bajeer Sultan, K., Delli Ganesh, K., Annadurai, P. M. A new method for the localisation of gas leaker fuel subassemblies in fast breeder reactors. Annals of Nuclear Energy 107109, 2019.

124. Sarathy, U. P., Velusamy, K., Selvaraj, P., Chellapandi, P., Chetal, S. C., and Bhoje, S. B. Thermal hydraulic studies for PFBR using PHOENICS." In Proceedings of 10th international PHOENICS Users' Conference, 2004.

125. Selvaraj, P., Puthiyavinayagam, P., Venkatesan, A., and Bhaduri, A. K. Sodium testing of fast reactor components. In proceedings of international conference on fast reactors and related fuel cycles: next generation nuclear systems for sustainable development (FR17), 2017.

126. Shevchenko, N., Boden, S., Eckert, S., Borin, D., Heinze, M., and Odenbach, S. Application of X-ray radioscopic methods for characterization of two-phase phenomena and solidification processes in metallic melts. The European Physical Journal Special Topics 220(1), 63-77, 2013.

127. Srinivas, M., Ravi Shankar, A., George, R. P., Ningshen, S., John Philip, and Amarendra, G. Pitting corrosion studies on fusion zone of shielded metal arc welded type 316LN stainless steel weldments. Transactions of the Indian Institute of Metals 72(12), 3089-3105, 2019.

128. Srinivasan, G., Sureshkumar, K. V., and Ramalingam, P. V. Two decades of operating experience with the fast breeder test reactor. No. IAEA-CN—156. In international conference on research reactors: safe management and effective utilization, Sydney, 2007.

129. Štrubelj, L., Tiselj, I. and Mavko, B. Simulations of free surface flows with implementation of surface tension and interface sharpening in the two-fluid model. International Journal of Heat and Fluid Flow 30(4), 741-750, 2009.

130. Sundaran, M. N., Vijayashree, R., Raghupathy, S., and Puthiyavinayagam, P. Experimental seismic qualification of diverse safety rod and its drive mechanism of prototype fast breeder reactor. In proceedings of international conference on fast reactors and related fuel cycles: next generation nuclear systems for sustainable development (FR17), 2017.

131. Talaia, M. A. Terminal velocity of a bubble rise in a liquid column. World Academy of Science, Engineering and Technology 28, 264-268, 2007.

132. Taylor, T. D., and Acrivos, A. On the deformation and drag of a falling viscous drop at low Reynolds number. Journal of Fluid Mechanics 18, 466-476, 1964.

133. Taqieddin, A., Modeling of Bubbles Hydrodynamics and Mass Transfer in Electrochemical Gas-Evolving Systems. PhD diss., Northeastern University, 2018.

134. Toyahara, D., Nakagiri, T., Hamada, H., Miyahara, S. In-vessel source term analysis code TRACER version 2.0 user's manual. JNC TN9520 2002-002, Japan Atomic Energy Agency, 2002.

135. Toyahara, D., Nakagiri,, T., Hamada, H., Miyahara, S. In-vessel source term analysis code TRACER version 2.3 user's Manual. JNC TN9520 2004-004, Japan Atomic Energy Agency, 2005.

136. Umbel, M., Containment source terms for sodium-cooled fast reactor accidents. Master of science thesis, the ohio state university, 2011. https://etd.ohiolink.edu/!etd.send_file?accession=osu1306506275&disposition=inline.

137. Van Leer, B. Towards the ultimate conservative difference scheme. V. A second-order sequel to Godunov's method. Journal of Computational Physics 32, 101-136, 1979.

138. Verma, A., Babu, R., and Das, M. K. Modelling of a single bubble rising in a liquid column. In fluid mechanics and fluid power-contemporary research, 1059, 2017.

139. Wang, X. Numerical simulation of two-dimensional bubble dynamics and evaporation. PhD Thesis, KU Leuven Arenberg doctoral school, 2015.

140. Wang, Z., and Tong, A. Y. Deformation and oscillations of a single gas bubble rising in a narrow vertical tube. International Journal of Thermal Sciences 47, 221-228, 2008.

141. Wassel, A. T., Farr, J. L. Jr., and Hoseyni, M. S. SUPRA: A code for simulating removal of radionuclides by water pools under severe accident conditions. EPRI NP 3886-CCMP, 1985.

142. Wassel, A. T., Mills, A. F., Bugby, D. C., and Oehlberg, R. N. Analysis of radionuclide retention in water pools. Nuclear engineering and design 90(1), 87-104, 1985.

143. Welty, J.R., Wicks, C.E., Rorrer, G., Wilson, R.E. Fundamentals of momentum, heat and mass transfer. John Wiley and Sons, 2009.

144. Wilke, C. R., and Lee, C. V., Estimation of Diffusion Coefficients for Gases and Vapours. Ind. Eng. Chem, vol. 47, 1253-1257, 1955.

145. Xu, Y., Ersson, M., and Jönsson, P. Numerical simulation of single argon bubble rising in molten metal under a laminar flow. Steel Research International 86(11), 1289-1297, 2015.

146. Yakhot, V., and Steven A. O. Renormalization group analysis of turbulence. I. Basic theory. Journal of scientific computing 1(1), 3-51, 1986.

147. Yolcu, H. H., and Gürses, A. A. Demonstration of the Sublimation Process and its Effect on Students' Conceptual Understanding of the Sublimation Concept. Turkiye Kimya Dernegi Dergisi Kisim C: Kimya Egitimi 1(2), 67-74, 2016.

148. Zahedi, P., Saleh, R., Moreno-Atanasio, R., Yousefi, K. Influence of fluid properties on bubble formation, detachment, rising and collapse; investigation using volume of fluid method. Korean Journal of Chemical Engineering 31, 1349-1361, 2014.

GLOSSARY

ABWR	Advanced Boiling Water Reactor
ACR	Advanced Candu Reactor
AFR	Advanced Fast Reactor
AGR	Advanced Gas-cooled Reactor
AHX	Air Heat eXchanger
AI	Atomics International
ALFRED	Advanced Lead Fast Reactor European Demonstrator
AMMD	Aerodynamic Mass Median Diameter
AP	Advanced Passive
ASTRID	Advanced Sodium Technological Reactor for Industrial Demonstration
ATMEL	Advanced Technology for MEmory and Logic
BFP	Boiler Feed Pump
BOP	Balance of Plant
BR	Breeding Ratio
BSA	Blanket Sub Assembly
BUSCA	Bubble Scrubbing Analysis
BWR	Boiling Water Reactor
CANDU	Canada Deuterium Uranium
CFBR	Commercial Fast Breeder Reactor
CFD	Computational Fluid Dynamics
CMA	Core Melt Accident
CMSR	Compact Molten Salt Reactor
CORAL	COmpact Reprocessing of Advanced fuel in Lead shielded facility
CRBR	Clinch River Breeder Reactor
DAE	Department of Atomic Energy

DAQ	Data AcQuisition
DFRP	Demonstration Fast breeder Reprocessing Plant
DHRS	Decay Heat Removal System
DHX	Decay Heat eXchanger
DI	DeIonized
DIC	Diagonal Incomplete Cholesky
DiD	Defense-in-Depth
DILU	Diagonal Incomplete-Lower Upper
EACS	Emergency Air Cleaning System
EBR	Experimental Breeder Reactor
ELSY	European Lead SYstem
EM	Electromagnetic
EM^2	Energy Multiplier Module
ESFR	European Sodium Fast Reactor
FB	Fuel Building
FBTR	Fast Breeder Test Reactor
FCVS	Filtered Containment Venting System
FFTF	Fast Flux Test Facility
FP	Fission Product
FreeLIFE	Free-surface LIbrary of Finite Element
FRFCF	Fast Reactor Fuel Cycle Facility
FSA	Fuel Sub Assembly
GACID	Global Actinide Cycle International Demonstration
GCR	Gas-Cooled Reactor
GEN	GENeration
GFR	Gas-cooled Fast Reactor
GIF	Generation IV International Forum

GUI	Graphical User Interface
HCDA	Hypothetical Core Disruptive Accident
HEDL	Hanford Engineering Development Laboratory
HEFD	High Efficiency Fiber Demister
HEPA	High Efficiency Particulate Air
HP	High Pressure
HTTR	High Temperature engineering Test Reactor
HTR	High Temperature gas cooled Test reactor
IAEA	International Atomic Energy Agency
I&C	Instrumentation and Control
ICP-MS	Inductively Coupled Plasma-Mass Spectrometry
IGCAR	Indira Gandhi Centre for Atomic Research
IHX	Intermediate Heat Exchanger
INPRO	INternational PROject on innovative nuclear reactors and fuel cycles
IP	Intermediate Pressure
ISI&R	In-Service Inspection and Repair
JSFR	Japan Sodium-cooled Fast Reactor
KALIMER	Korea Advanced LIquid MEtal Reactor
LFR	Lead-cooled Fast Reactor
LFTR	Liquid Fluoride Thorium Reactor
LGO	Logic Gate Oscillator
LHR	Linear Heat Rate
LOCI	Loss Of Clad Integrity
LP	Low Pressure
LWR	Light Water Reactor
MA	Minor Actinide
MC	Mixed Carbide

MFPR	Metal Fuel Power Reactor
MOC	Material of Construction
MooNMD	Mathematics and object-oriented Numerics in MagDeburg
MSR	Molten Salt Reactor
MST	Mechanistic Source Term
MULES	Multi-dimensional Universal Limiter for Explicit Solution
MV	Main Vessel
MWe	Mega Watt electrical
MWt	Mega Watt thermal
NAA	Neutron Activation Analysis
NEA	Nuclear Energy Agency
NSSS	Nuclear steam supply system
OECD	Organization for Economic Coordination and Development
OGDHR	Operation Grade Decay Heat Removal
OpenFOAM	Open source Field Operation And Manipulation
PBiCG	Preconditioned Bi-Conjugate Gradient
PBMR	Pebble Bed Modular Reactor
PBS	Packed Bed Scrubber
PC	Personal Computer
PFBR	Prototype Fast Breeder Reactor
PHWR	Pressurized Heavy Water Reactor
PISO	Pressure Implicit with Splitting of Operator
ppmw	parts per million by weight
PR&PP	Proliferation Resistant and Physical Protection
PRESTO	PREssure STaggering Option
PSP	Primary Sodium Pump
PWR	Pressurized Water Reactor

RA	Reactor Assembly
R&D	Research and Development
RBMK	Reaktor Bolshoy Moshchnosti Kanalnyy
RCB	Reactor Containment Building
RCC	Reinforced Concrete Containment
RNG	ReNormalization Group
RS	Recommended Standard
RV	Reactor Vessel
RVCG	Reactor Vessel Cover Gas
S&O	Safety and Operations
SCWR	Super Critical Water Reactor
SDC	Safety Design Criteria
SDG	Sustainable Development Goal
SFR	Sodium-cooled Fast Reactor
SG	Steam Generator
SGB	Steam Generator Building
SGBS	Submerged Gravel Bed Scrubber
SGDHR	Safety Grade Decay Heat Removal
SIA	System Integration and Assessment
SIMPLE	Semi Implicit Method for Pressure Linked Equations
SNL	Sandia National Laboratories
SPARC	Suppression Pool Aerosol Removal Code
SRP	System Research Plan
SS	Stainless Steel
SSSB	Spent Subassembly Storage Bay
SUPRA	SUppression Pool Retention Analysis
swak4Foam	swiss army knife for Foam

TG	Turbine Generator
TP2D	Transport Phenomena in 2D
TRACER	Transport Phenomena of Radionuclides for Accident Consequence Calculation of Reactor
TWR	Traveling Wave Reactor
VFP	Volatile Fission Product
VVER	Vodo-Vodyanoi Energetichesky Reaktor

LIST OF SYMBOLS

Latin

A	Area (m^2)
C	Concentration (kg/m^3, $mole/m^3$), Coefficient, Constant
d	Diameter (m)
D	Diffusion coefficient (m/s^2), Density at STP (g/l)
F	Force per unit mass (m/s^2), Source term (kg/m^2s^2), Time constant (1/s)
g	Acceleration due to gravity (m/s^2)
G	Generation of turbulent kinetic energy (kg/ms^3)
h	Height (m)
H	Fraction of bed occupied by liquid
j	Empirical constant relating channel width to packing diameter
k	Turbulent kinetic energy (m^2/s^2), Interface surface curvature
M	Mass flow rate (kg/s)
n	Normal
p	Pressure (N/m^2), Pressure before injection (torr)
q	Mass injected (g)
r	Radial coordinate
R	Radius (m)
S	Partial pressure (torr), Source term (kg/ms^3)
t	Time (s)
T	Temperature (°C)
u	Velocity (m/s)
V	Volume (l), Superficial velocity (m/s)
x	Position, Size (μm)
Y	Fluctuating dilation in turbulence
z	Distance (m)
Z	Bed height (m)

Greek

α	Deposition coefficient, Phase fraction, Inverse effective *Pr*

Δ	Change
ε	Turbulent dissipation rate (m^2/s^3), Bed void fraction
μ	Dynamic viscosity (Pa.s)
ρ	Density (kg/m^3)
σ	Surface tension (N/m)
Superscripts	
n	Ratio of bed heights
T	Transpose
Subscripts	
0	Initial
1	Phase 1
2	Phase 2
50	Cut
98	Limit of separation
a	Aerosol, Aerodynamic
b	Bubble, Buoyancy
c	Center of mass
D	Drag
diff	Diffusion
eff	Effective
g	Gas, Air
i	Inert
in	Injected, Inlet
iner	Inertial
k	Turbulent kinetic energy, Mean velocity gradients
l	Liquid
M	Compressible
ntotal	N times total
out	Outlet
p	Particle
R	Packing

rgh	Dynamic
s	Surface tension
sed	Sedimentation
sod	Sodium
t	turbulent
T	Terminal
total	Total
v	Vapour
w	Water
y	Y direction
z	Z-direction
ε	Turbulent dissipation
Non-dimensional	
AR	Aspect ratio
Ca	Capillary number
COR	Coefficient Of Restitution
DF	Decontamination factor
E	Particle removal efficiency
Eo	Eötvös number
F	Volume fraction
He	Henry number
K_p	Inertial impaction parameter
M	Morton number
Pr	Prandtl number
Pt	Penetration
RF	Retention factor
Re	Reynolds number
SE	Scrubbing efficiency
Ta	Tadaki number
We	Weber number

Thesis Highlights

Name of the Student: Arjun Pradeep
Name of CI: Indira Gandhi Centre for Atomic Research **Enrolment No.:** ENGG02201504006
Thesis Title: Mass transfer from rising mixed gas bubble in quiescent liquid pool of SFR
Discipline: Engineering Sciences **Sub-Area of Discipline:** Chemical Engineering
Date of viva voce: 25/06/2021

Pool scrubbing requires information on bubble dynamics and mass transfer. Since bubbles dynamics controls the phenomenon, it is of interest to study the same using a judicious mix of numerical models and in-house experiments. This necessitates proper choices of system parameters such as bubble diameter and pool height. In addition, mass transfer from bubble requires inclusion of aerosol and vapor transport parameters. The thesis addresses key interesting issues in the field of bubble scrubbing related safety studies in SFRs.

A semi-empirical model is developed to first understand the concept of pool scrubbing. The main phenomena governing the removal of aerosol and vapors from rising bubbles are identified. This is followed by reliable numerical simulation of bubble dynamics using OpenFOAM software to verify the empirical correlations used in the pool scrubbing model. The simulated terminal velocity and shapes of the rising bubble as shown in Fig. 1a were found to agree well with the experimental results (Fig. 1b). In the experimental investigations, an innovative data processing technique was used to measure average bubble rise velocity in large pools of fluids based on in-house developed void sensors as shown in Fig. 1b. Finally, similarity between water and sodium systems on bubble dynamics is brought out to simplify SFR safety studies.

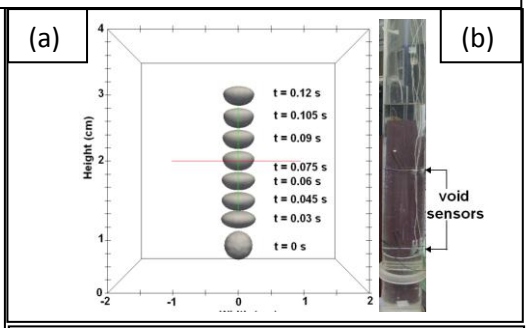

Fig. 1 (a) Experimental setup (b)numerical model for air bubble dynamics in water.

The understanding of bubble dynamics gained from CFD and experimental studies have been extended to analyze mass transfer/scrubbing of vapors and aerosols encountered in liquid pool of SFR systems. An experimental water setup has been installed to study iodine vapor retention in water pool (Fig. 2a). The setup consists of iodine bubble injection system, bubbler tank and bubble collection systems. This work uses iodimetric titration method for the measurement of iodine concentration in water samples. A numerical study on iodine retention in water pool is also carried out as shown in Fig. 2b and is in good agreement with experimental results.

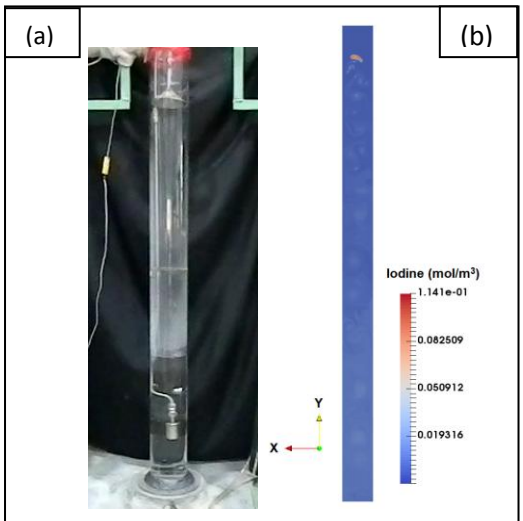

Fig. 2. (a) Experimental setup(b) numerical model for iodine scrubbing in water pool.

Engineering scale model of a wet scrubber (SGBS) is setup as shown in Fig. 3a to study the scrubbing efficiency of sodium fire aerosols during mixed gas bubble rising through water submerged gravel bed. Numerical simulations (Fig. 3b) are also performed to evaluate aerosol penetration in a submerged gravel bed scrubber. At low gas flow rates, semiempirical model underpredicts the removal efficiency for aerosols; however, present CFD study predicts efficiencies as observed during in-house experiments for the typical size range of sodium combustion aerosols, hence, proving the suitability of SGBS as a passive device for sodium combustion aerosol removal.

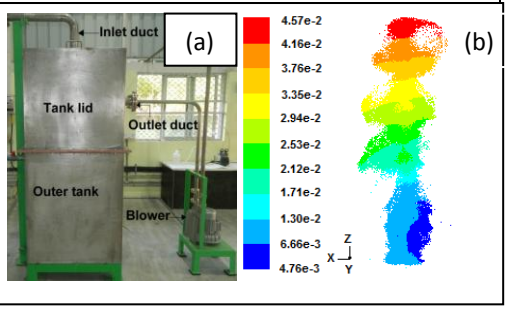

Fig. 3.(a) Experimental setup of submerged gravel bed scrubber and (b) numerical model results for aerosol penetration.